Understanding and predicting changes in North Atlantic Sea Surface Temperature

by

S. G. Yeager

B.A., Dartmouth College, 1993

M.S., Brown University, 1997

A thesis submitted to the

Faculty of the Graduate School of the

University of Colorado in partial fulfillment

of the requirements for the degree of

Doctor of Philosophy

Department of Atmospheric and Oceanic Sciences

2013

This thesis entitled:
Understanding and predicting changes in North Atlantic Sea Surface Temperature
written by S. G. Yeager
has been approved for the Department of Atmospheric and Oceanic Sciences

Baylor Fox-Kemper

Prof. Jeffrey Weiss

Prof. Weiqing Han

Date

The final copy of this thesis has been examined by the signatories, and we find that both the content and the form meet acceptable presentation standards of scholarly work in the above mentioned discipline.

Yeager, S. G. (Ph.D., Atmospheric and Oceanic Science)

Understanding and predicting changes in North Atlantic Sea Surface Temperature

Thesis directed by Prof. Baylor Fox-Kemper

Abstract The mechanisms associated with sea surface temperature variability in the North Atlantic are explored using observation-based reconstructions of the historical surface states of the atmosphere and ocean as well as simulations run with the Community Earth System Model, version 1 (CESM1). The relationship between air-sea heat flux and SST between 1948 and 2009 yields evidence of a positive heat flux feedback at work in the subpolar gyre region on quasi-decadal timescales. Warming of the high latitude Atlantic precedes an atmospheric response which resembles a negative NAO state. The historical flux data set is used to estimate temporal variations in North Atlantic deep water formation which suggest that NAO variations drove strong decadal changes in thermohaline circulation strength in the last half century. Model simulations corroborate the observation-based inferences that substantial changes in the strength of the Atlantic Meridional Overturning Circulation (AMOC) ensued as a result of NAO-driven water mass perturbations, and that changes in the large-scale ocean circulation played a significant role in modulating North Atlantic SST.

Surface forcing perturbation experiments show that the simulated low-frequency AMOC variability is mainly driven by turbulent buoyancy forcing over the Labrador Sea region, and that the decadal ocean variability, in uncoupled experiments, derives from low-frequency variability in the overlying atmospheric state. Surface momentum forcing accounts for most of the interannual variability in AMOC at all latitudes, and also most of the decadal AMOC variability south of the Equator. We show that the latter relates to the trend in wind stress forcing of the Southern Ocean, but that Southern Ocean forcing explains very little of the North Atlantic signal. The sea surface height in the Labrador Sea is identified as a strongly buoyancy-forced observable which supports its use as a monitor of AMOC strength.

The dynamics which characterize the model mean overturning and gyre circulations, and which explain the model response to surface momentum and buoyancy forcing perturbations, are investigated in terms of mean and time-varying vorticity balances. The significant effect of bottom vortex stretching, noted in previous studies, is shown here to play a key role in a variety of time-dependent phenomena, such as the covariation of overturning and gyre circulations, the variation of the barotropic streamfunction in the intergyre-gyre region, and changes in AMOC associated with momentum forcing perturbations. We show that latitudinal changes in the AMOC vorticity balance explains the attenuation of buoyancy-forced signals south of Cape Hatteras, and that the dominant frictional balance near the Equator greatly inhibits the propagation of AMOC variability signals from one hemisphere to the other.

The long persistence of buoyancy-forced, high-latitude circulation anomalies results in significant predictability of SST in the subpolar gyre. This is demonstrated with an analysis of initialized, fully coupled retrospective predictions of the mid-1990s warming in that region. The atmospheric response is shown to be relatively unimportant on timescales of up to 10 years, but skill for longer lead times is inhibited by an incorrect heat flux feedback in the North Atlantic in the coupled CESM1.

Dedication

To my inspirations: Ashley, Jack, and Madeline.

Acknowledgements

First and foremost, I thank my wife Ashley for making this possible by keeping things running smoothly on the domestic front while I pursued quixotic quests, and for providing such an excellent, rejuvenating retreat at the end of each day. Thanks to Baylor, who provided assistance and encouragement from the start and whose mastery of physical oceanography and geophysical fluid dynamics was inspiring throughout this process. Thanks to all my committee members, and in particular to Frank Bryan who provided extremely helpful notes, thoughts, and pointers to key papers which faciliated the development of vorticity diagnostics for the POP ocean model. This dissertation would not have been possible without the support provided by the UCAR Educational Assistance Program as well as the division office of Climate and Global Dynamics at NCAR, and I am very grateful for it. My research was supported by the NOAA Climate Program Office under Climate Variability and Predictability Program grant NA09OAR4310163 and by the National Science Foundation through its sponsorship of the National Center for Atmospheric Research. Computing resources were provided by NCAR's Computational and Information Systems Laboratory and by the Oak Ridge Leadership Computing Facility, which is supported by the Office of Science of the U. S. Department of Energy.

Contents

Chapter

Tables

Table

Figures

Figure

Chapter 1

Introduction

The surface climate of the Earth is strongly influenced by poleward transfers of heat in the atmosphere and ocean which redistribute the incoming radiant energy from the Sun. Our understanding of the relative roles of the atmosphere and ocean in the mean energy balance of the planet has advanced considerably since the advent of satellite measurements of the radiation budget at the top of the atmosphere. This has enabled estimation of the oceanic component of meridional heat transport as a residual (Vonder Haar and Oort, 1973; Trenberth and Caron, 2001; Trenberth and Fasullo, 2008); or, at least in one instance, of the atmospheric component as a residual (Wunsch, 2005). In recent years, improved observing systems have led to a rough convergence of inferred estimates of poleward heat transport in the ocean with those derived from direct measurements (Ganachaud and Wunsch, 2003; Trenberth and Fasullo, 2008; Large and Yeager, 2009). There is mounting evidence that the ocean is responsible for between 1.5-2 PW of northward heat transport in the Northern Hemisphere, much of this in the subtropical Atlantic Ocean. Outside of the Tropics, most of the heat transport implied by the Earth's radiation budget occurs in the atmosphere; it accounts for about 80% of the roughly 5 PW of heat transported poleward at 35°N, according to one estimate (Trenberth and Caron, 2001). While small relative to the atmosphere, the transport of heat associated with the motions of the Atlantic Ocean nevertheless has a profound impact on the climate and hence the biosphere.

Changes in the Earth's energy balance produce surface climate variations. While this variability is even less well understood than the mean budget, a compelling body of evidence suggests

that the peaks in the spectra of surface climate fields on decadal and longer timescales are related to variations in the oceanic component of poleward heat transport and in particular to the strength of the Atlantic Meridional Overturning Circulation (AMOC). On millenial timescales, proxy records show there were large climate shifts associated with cycles of glaciation and deglaciation which can be linked to changes in rates of North Atlantic Deep Water (NADW) formation and AMOC strength (e.g., Rahmstorf, 2002; Clark et al., 2002; Manabe and Stouffer, 1999). Centennial reconstructions of surface temperature in the recent past have led to the identification of a prominent climate mode in the Atlantic with a timescale of approximately 70 years (Fig. 1.1) which has been variously dubbed the Atlantic Multidecadal Oscillation (AMO; Kerr, 2000), or Atlantic Multidecadal Variability (AMV). The AMV is generally interpreted as a signature of AMOC variability because of its low-frequency and the fact that it correlates with AMOC in climate model simulations which can reproduce the observed spatiotemporal patterns of SST variability (e.g., Delworth and Mann, 2000; Sutton and Hodson, 2005; Knight et al., 2005; Danabasoglu et al., 2012b). Direct measurement of the basin-scale meridional volume transport in the Atlantic Ocean is a relatively recent development which has so far yielded less than a decade of AMOC observations and only at one latitude (26.5°N; Kanzow et al., 2010; Johns et al., 2011). Thus, apart from paleo proxies, the evidence supporting the climatic significance of Atlantic circulation variability is primarily based on the behavior of climate models.

Many coupled general circulation models (CGCMs) exhibit a clear relationship between AMOC strength and North Atlantic SST and, as shown in several of the papers cited above, some show pronounced variability on timescales which are consistent with observed records. While coupled climate models are critical tools for investigating AMOC variability and related climate effects, model fidelity and interpretation remain significant issues. The realism of simulated variability is a particularly thorny issue in the Atlantic basin, because CGCMs have large systematic errors in the extratropical Atlantic associated with poorly-represented Gulf Stream (GS) and North Atlantic Current (NAC) pathways (Dengg et al., 1996; Large and Danabasoglu, 2006). The impacts of such mean biases on model temporal evolution are unknown. The dominant timescales

of AMOC variability cited in several different CGCM analyses cover a wide range: 70-100 years (Delworth and Greatbatch, 2000; Vellinga and Wu, 2004)); 70-80 years (Jungclaus et al., 2005); 50 years (Delworth et al., 1993); 35 and 125 years (Timmermann and Latif, 2005); 30 years (Cheng et al., 2004); 24 years (Dai et al., 2005); 21 years (Danabasoglu, 2008); 20 years (Farneti and Vallis, 2009); 50-200 years (Danabasoglu et al., 2012b). Such disparate results likely stem from sensitivity to the details of model explicit and parameterized physics as well as model resolution (e.g., Bryan et al., 2006; Fox-Kemper et al., 2011; Yeager and Danabasoglu, 2012). The magnitude and spectral character of AMOC variance has been found to differ substantially from one version of a model to another (Danabasoglu et al., 2012b), and even from one time segment of a model simulation to another (Kwon and Frankignoul, 2012). Observational records are too short to clearly discriminate realistic from unrealistic model behavior on such timescales.

While it is highly desirable to study climate in general, and AMV in particular, using models which faithfully represent the plethora of physical processes at work in Nature across the full spectrum of space and time scales, such complexity produces results which can be as challenging to understand as the system being simulated. Modelling of course permits experimentation and thorough exploration of covariant relationships, but multicentury coupled climate experiments using full-complexity CGCMs continue to be so computationally expensive that experimentation designed to illuminate multidecadal climate variability is severely limited in practice. In one of few such studies, Yeager and Danabasoglu (2012) (Appendix E) analyzed a pair of long fully-coupled simulations using the Community Climate System Model, version 4 (CCSM4) to evaluate the specific impacts of a Nordic Seas overflow parameterization (Danabasoglu et al., 2010) on AMOC variability. The comparison showed that enhanced abyssal stratification in the North Atlantic associated with a more realistic influx of Nordic Seas overflow waters resulted in a general reduction of AMOC variance (Fig. 1.2), but that the impacts differed with latitude and spectral band. In the vicinity of the RAPID observational array, at 26.5°N, the parameterization produced a slight increase in AMOC variance, concentrated in the lowest frequency band (period $>$ 50-year). The study highlighted the complexity of AMOC variability in coupled model simulations, which is of-

ten analyzed simplistically in terms of the maximum overturning streamfunction at a particular latitude or in terms of artificially-coherent empirical orthogonal functions (EOFs), and it underscored the lack of robustness of multidecadal variability diagnosed from CGCMs. In the simulation without overflows, very strong variability of the maximum AMOC strength in the spectral band 50-200 years was found to derive from probably unrealistic fluctuations in the pathway of the deep western boundary current (DWBC) and its interaction with topography along the Atlantic coast. This variance vanished when overflows were added (Fig. 1.2). The dynamics which underpin such AMOC behavior, and indeed the overturning circulation in general, are poorly understood and this has provided motivation for some of the work presented herein.

Despite a vast and growing literature on AMOC variability in CGCMs (see Liu, 2012; Srokosz et al., 2012, for recent reviews), a fundamental understanding of the mechanisms even of simulated AMOC variability remains elusive. A recurrent theme, however, on timescales from decadal to millenial, is that AMOC maxima are associated with anomalously strong North Atlantic Deep Water (NADW) formation and deep convection in the subpolar North Atlantic. The formation of NADW appears to depend on the large-scale atmospheric state as represented by the North Atlantic Oscillation (NAO; Hurrell, 1995), but some degree of NAO "persistence" seems to be necessary to generate substantial NADW and hence AMOC variations (Lohmann et al., 2009b,a; Robson et al., 2012a; Yeager et al., 2012; Danabasoglu et al., 2012b). The origins of any redness in the NAO spectrum, either in observations or coupled simulations, is a subject of ongoing research, but insofar as it exists it suggests that AMV may result from the resonance of a coupled ocean-atmosphere mode (Liu, 2012; Timmermann and Latif, 2005; Selten et al., 1999). There is emerging evidence that the interaction between the NAO and Atlantic circulation is two way, with a positive phase of AMOC resulting in a weakening of the NAO (Gastineau and Frankignoul, 2012; Gastineau et al., 2012). This relationship is weak in the current generation of CGCMs, but it is consistent with the conceptual model of NAO-ocean interaction put forth by Marshall et al. (2001a) in which strong ocean heating of the subpolar gyre results in a weakened jet stream and anomalously weak poleward heat transport in the atmosphere. The Marshall et al. (2001a) model is based on the Bjerknes compen-

sation hypothesis (Bjerknes, 1964) which posits that anomalously positive poleward heat transport in the ocean is accompanied by anomalously negative poleward heat transport in the atmosphere, such that the net poleward heat transport remains constant. Evidence for this compensation has been found in CGCM simulations, particularly on multidecadal timescales (Shaffrey and Sutton, 2006). As shown in Marshall et al. (2001a), ocean-atmosphere interaction can give rise to damped oscillatory behavior with preferred decadal timescales in the Atlantic, but this is just one example of a host of studies which have invoked various mechanisms to explain various timescales, many of which do not require strong atmosphere-ocean coupling (e.g., Griffies and Tziperman, 1995; Delworth and Greatbatch, 2000). As summarized by Liu (2012), all that we can comfortably say is known about AMV is that it involves stochastic atmospheric forcing (i.e., random weather noise) together with long AMOC-related timescales.

Insight into the connections between Atlantic variability of the past few decades and AMOC can be gained from forced ocean general circulation model (OGCM) simulations whose fidelity can be tested by direct comparison with available observations. The confidence in mechanisms diagnosed from such simulations depends upon the model's ability to reproduce observed features of the mean and time-varying ocean state. Reliable historical forcing data for OGCMs are only available from about 1950 onwards, and so this technique cannot address the topic of intrinsic multidecadal variability in the absence of strong external radiative forcings, and it provides no information about potentially important ocean-atmosphere feedbacks, but it is useful for identifying important AMOC driving mechanisms. A fairly robust result which emerges from such OGCM hindcast studies is that there was a strengthening of the AMOC and northward heat transport (NHT) over the last few decades of the 20th century, and this decadal-scale spinup of the North Atlantic circulation was associated with changes in NAO-related buoyancy forcing (e.g., Häkkinen, 1999; Eden and Willebrand, 2001; Bentsen et al., 2004; Beismann and Barnier, 2004; Böning et al., 2006; Biastoch et al., 2008; Robson et al., 2012a; Yeager and Danabasoglu, 2013). In these and other studies (e.g., Marshall et al., 2001a; Visbeck et al., 2003; Brauch and Gerdes, 2005; Lohmann et al., 2009b), the slow AMOC variations are interpreted as delayed baroclinic adjustments to the

quasi-decadal changes in NAO in the recent past (Hurrell and Van Loon, 1997). The associated increase in oceanic NHT has been identified as a key factor in an abrupt warming of the Atlantic subpolar gyre (SPG) which occurred in the mid-1990s, and it accounts for the significant skill at predicting high latitude North Atlantic SST in several nascent decadal prediction systems (Grist et al., 2010; Robson et al., 2012a,b; Yeager et al., 2012) (Appendix F).

There are far-reaching climate effects associated with the AMV which have spurred efforts not only to understand it but to predict it. Links have been established between the variations in North Atlantic SST and decadal-scale climate fluctuations from the Americas to India, including variations in summertime climate in North America and Europe, drought in the Sahel, and modulation of Atlantic hurricane activity (e.g., Sutton and Hodson, 2005; Knight et al., 2006; Zhang and Delworth, 2006; Delworth et al., 2007, provides a nice review). Promising results in studies of potential predictability of simulated low frequency AMOC and associated SST variations (Griffies and Bryan, 1997; Collins et al., 2003; Msadek et al., 2010) have led to organized coupled decadal prediction efforts in which emphasis is placed on improved ocean, and in particular AMOC, initialization (Hurrell et al., 2006; Taylor et al., 2009; Meehl et al., 2009, 2013). Early results are encouraging in the North Atlantic sector (Smith et al., 2007; Keenlyside et al., 2008; Pohlmann et al., 2009; Yeager et al., 2012) with indications of potential for predicting not only SST, but also related climate impacts such as hurricane frequency (Smith et al., 2010a). However, a problematic aspect of intialized decadal climate prediction predicated on AMOC prediction, or at least persistence, is that the connection between AMOC and SST only emerges on decadal and longer timescales, whereas direct heat flux forcing of SST appears to dominate on shorter, interannual timescales (Bjerknes, 1959, 1964; Cayan, 1992; Deser and Blackmon, 1993; Kushnir, 1994; Battisti et al., 1995; Delworth et al., 2007). The transition from flux-dominated SST variability to transport-dominated SST variability merits further investigation, particularly in the context of understanding and improving prediction systems.

1.1 Structure and Goals

This thesis has two distinct but complementary aims: 1) to elucidate the forcing dependence of the mean and time-varying large-scale circulation in the North Atlantic Ocean, and 2) to contribute to our understanding of North Atlantic SST variability and its predictability. A unifying theme will be the variability of AMOC and its signature in the surface temperature field. The primary tool will be the Community Earth System Model, version 1 (CESM1), although some experiments used earlier versions of that model. Given the complexity of the model, parts of the work included here are dedicated to understanding model mean and variability, with no pretense that light is being shed on natural phenomena.

Most of the experiments under consideration are forced ocean–sea-ice configurations of the CESM1 model at standard resolution (i.e., global nominal 1° ocean and sea ice models coupled together and forced at the surface with reanalysis fields), but some fully coupled experiments are also examined. We have chosen to focus on forced historical hindcast experiments because they can be directly compared with observations; they make possible a variety of forcing sensitivity experiments which are not tenable in coupled simulations; and they tie in directly to initialized decadal prediction results. The primary experiments are forced at the surface with surface meteorology from 1948 to 2009 derived primarily from the NCEP/NCAR reanalysis of the low-level atmospheric state (Kistler et al., 2001). Specifically, we use a suite of historical atmospheric surface state fields compiled by Large and Yeager (2004, 2009) which the CLIVAR Working Group on Ocean Model Development (WGOMD) has promoted for use in so-called Coordinated Ocean-Ice Reference Experiments (COREs)[1] . This data set includes both interannually-varying (CORE-II) as well as normal year (NYF; a repeating annual cycle) surface fields and fluxes suitable for forcing ocean and sea ice models. The main set of experiments and associated forcings are summarized in Appendix *B*, and a reference for frequently used abbreviations is given in Appendix *A* .

A good portion of the research included in this dissertation has already been published

[1] http://www.clivar.org/organization/wgomd/core

(Yeager and Jochum, 2009; Yeager and Danabasoglu, 2012; Yeager et al., 2012). The published papers are attached as appendices D through F. These can be read independently, but we have also included select results from these works where appropriate in the main body of the thesis, which is primarily recent work. Yeager and Jochum (2009) is an analysis of forced hindcast experiments using the Community Climate System Model, version 3.5 (CCSM3.5), which explores the impacts on North Atlantic gyre circulation of strongly perturbed high latitude buoyancy forcing. A conclusion from that study is that the GS and NAC path in a non-eddy resolving OGCM can be substantially improved, but only through unrealistically strong surface heat flux forcing in the Labrador Sea. As mentioned above, Yeager and Danabasoglu (2012) compares AMOC variability obtained in twin, multi-century, fully coupled CCSM4 simulations, only one of which included a parameterization for Nordic Seas overflows. The AMOC variance in the experiments was analyzed by binning in frequency space. This novel analysis highlighted the latitudes and depths where different processes operating on different timescales dominate overturning variations, and it showed that the impacts of the new parameterization varied substantially with latitude, depth, and spectral band. As in Yeager and Jochum (2009), the interaction of deep flow with bottom topography was found to be key to understanding model behavior. Most recently, Yeager et al. (2012) analyzed the North Atlantic evolution of a set of CMIP5 decadal prediction experiments run with CCSM4. The significant skill in predicting SST change associated with the mid-1990s warming of the SPG was found to derive from correct physical mechanisms, based on a heat budget analysis of the SPG. This study was the first to explicitly demonstrate that skillful North Atlantic SST prediction is explained by the persistence of AMOC-related advective heat transport anomalies, and that loss of skill is explained by poor prediction of surface heat flux anomalies.

In Chapter 2, we provide an overview of historical variability in the North Atlantic inferred from the CORE-II data set. In addition to setting the stage for subequent chapters, this overview is a timely complement to ongoing WGOMD-organized model intercomparison work focused on the North Atlantic. Pairing the CORE-II atmospheric state with observed SST yields a 62-year surface air-sea flux data set. We use this to investigate the relationship between time-varying SST and

surface heat flux in Nature. We identify a positive heat flux feedback at work in the North Atlantic on quasi-decadal timescales which bolsters the case for a coupled mechanism of AMV. The flux data set is then used to derive an observation-based estimate of time-dependent NADW formation over the latter half of the twentieth century. The mean NADW formation rate thus computed provides a new independent metric comparable to hydrographic estimates of NADW strength (Ganachaud and Wunsch, 2000), and its variability, strongly linked to NAO, serves as a useful proxy for variations in the thermohaline circulation (THC). The fidelity of the forced CESM1 hindcast CONTROL simulation is evaluated and its variability assessed relative to available observational time series, including the CORE-II NADW time series. A heat budget of the SPG region from CONTROL provides compelling evidence that the AMV was AMOC-driven over the latter half of the twentieth century.

Parts of Chapter 2 and the entirety of Chapter 3 are from a recently submitted manuscript (Yeager and Danabasoglu, 2013). This paper examines the origins of large-scale North Atlantic circulation variability by considering a set of forcing perturbation experiments which isolate the effects of particular air-sea fluxes in select regions. The separate contributions to AMOC and gyre circulation variability of momentum and buoyancy forcing are thereby revealed. The results are in line with similar published analyses (e.g., Biastoch et al., 2008), but go further to illuminate the relative effects of: thermal vs. haline forcing, turbulent buoyancy forcing, Labrador Sea buoyancy forcing, and Southern Ocean wind forcing. This study highlights the importance of buoyancy forcing over the Labrador Sea in explaining AMOC variability and it identifies SSH in the Labrador Sea as a potential monitor and predictor of THC changes.

In Chapter 4, a newly-developed vorticity diagnostics toolkit for the POP ocean model is applied to the experiments of Chapter 3 to shed light on the dynamics which underpin the mean and time-varying overturning and gyre circulations in the Atlantic. The vorticity diagnostics are developed in some detail in Appendix *C*. The results underscore the profound importance of topographic effects on the large-scale circulation in the Atlantic, in line with previous studies (e.g., Hughes and de Cuevas, 2001) but perhaps not widely appreciated. The mean vorticity balance

helps to explicate the link between overturning and gyre circulations, the strong attenuation of AMOC anomalies at select latitudes, and the factors which determine the position of the model NAC. New and unexpected findings are obtained by considering, from a vorticity perspective, the circulation response to momentum and buoyancy forcing perturbations on various timescales. In particular, we find that buoyancy forcing accounts for almost all of the variability in the intergyre-gyre on decadal timescales and that the vorticity forcing associated with wind stress changes is more related to changes in abyssal flow over bottom topography than to Ekman pumping, in many regions. We argue that the latter effect is important for understanding wind-related AMOC and gyre variations.

The potential for predicting decadal North Atlantic SST evolution is explored in Chapter 5. Improved understanding of the results of Yeager et al. (2012) is developed by contrasting fully coupled prediction experiments with uncoupled versions, and by assessing the air-sea heat flux feedback at work in CESM1. The findings strongly suggest that coupled decadal prediction with CESM1 is currently limited by an incorrect NAO response to slow SST variability in the SPG.

A brief summary is given in Chapter 6.

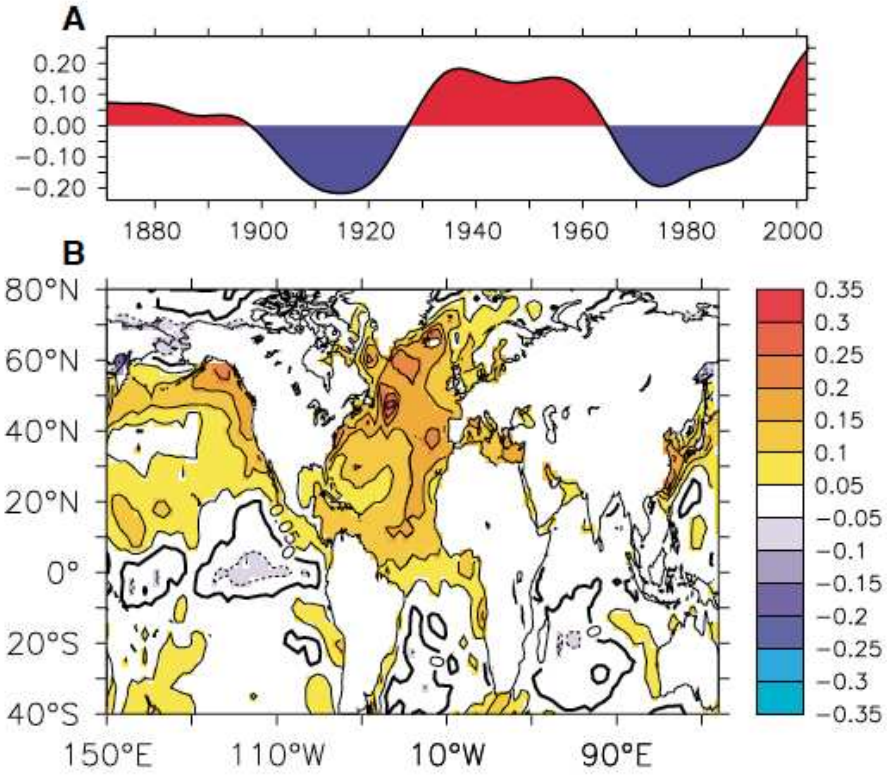

Figure 1.1: Figure 1 from Sutton and Hodson (2005): (a) AMO index (°C) from 1871 to 2003 computed as a detrended, low-pass filtered average of annual SST over the region 0°N-60°N, 75°W-7.5°W; (b) regression of detrended annual SST on the AMO index (°C/s.d.).

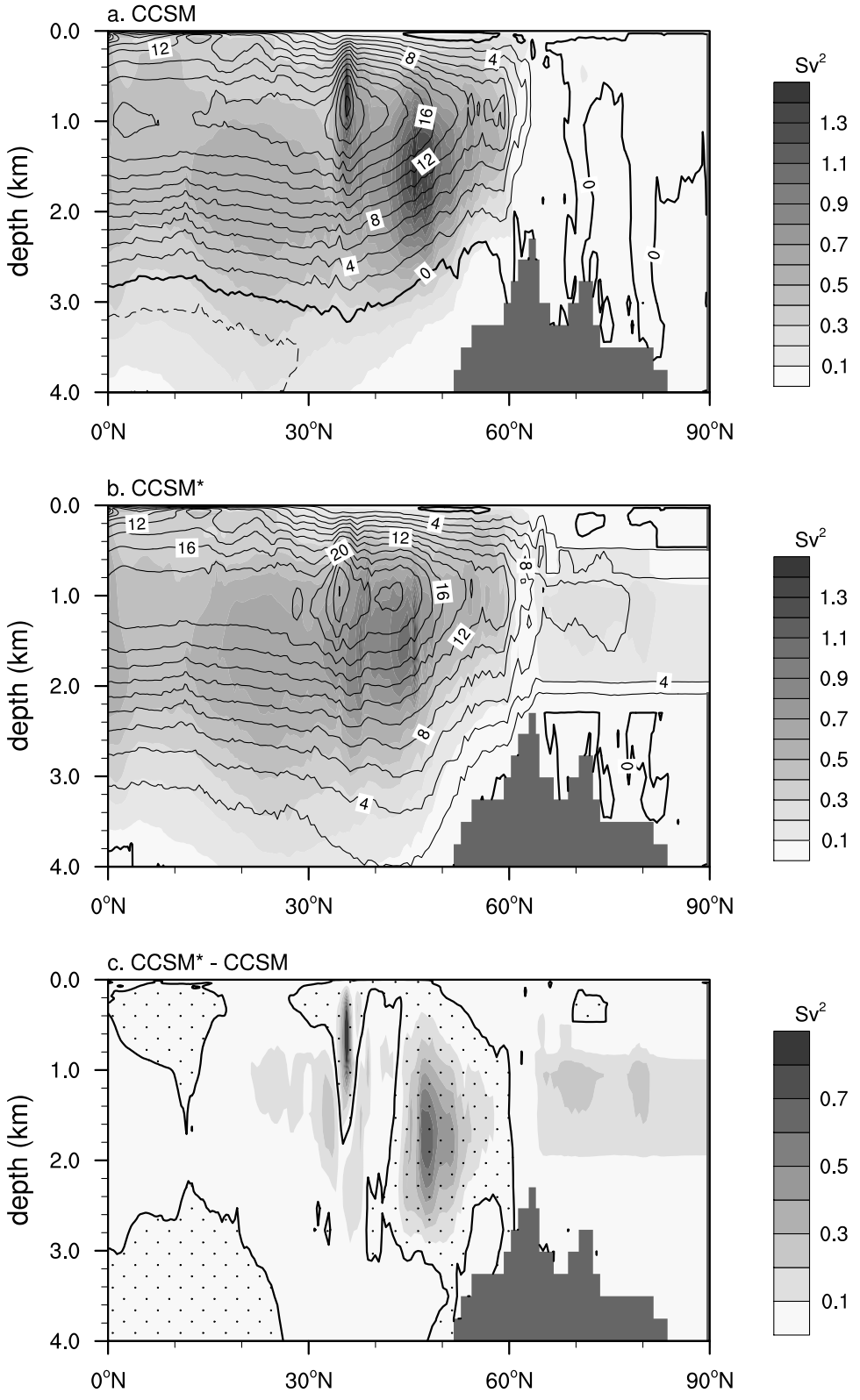

Figure 1.2: Figure 8 from Yeager and Danabasoglu (2012). Total variance (shading, in Sv^2) of 550-year detrended annual AMOC time series as a function of latitude and depth from (a) CCSM (without overflow), (b) CCSM* (with overflow), and (c) the difference (CCSM* - CCSM). Black contour lines in (a) and (b) show respective 550-year mean AMOC streamfunctions (contour interval is 2 Sv). The shading in (c) indicates the magnitude of the difference, with the sign indicated by the zero contour line and stippling for negative values.

Chapter 2

North Atlantic variability in the recent past

The limited observational sampling of the climate system makes it necessary to consider model-based reconstructions of past atmospheric and oceanic states in order to make sense of climate variability on large spatial and temporal scales. In this chapter, we examine reconstructions of historical SST, air-sea fluxes, and ocean state fields to gain insight into the interannual to decadal climate variability in the North Atlantic in the relatively recent past. Taken as a whole, these data sets paint a compelling picture of NAO-forced decadal AMOC variability as a key driver of the AMV in the late twentieth century. Furthermore, historical time series show hints of coupled air-sea interaction on quasi-decadal timescales, with AMV inducing a negative NAO-like response after a few years delay.

2.1 Historical SST variations (1900-2009)

A brief consideration of historical SST variability is warranted, to frame the discussion. Global, gridded reconstructions of SST extend back to the late 19th century (e.g., Rayner et al., 2003; Hurrell et al., 2008). The Atlantic Gulf Stream region and its extension into the subpolar gyre and Labrador and Nordic Seas stands out as one of three major regions of high interannual SST variability (Fig. 2.1a), based on annual mean data from 1900 to 2009. The other two regions of notably high variability are the Kuroshio and its extension into the north central Pacific and the equatorial Pacific, where the signature of El Nino appears as the strongest feature in the interannual standard deviation. If the historical record is first bin-averaged by decade (1900-1909, 1910-1919,

etc), then the regions of highest decadal variability are revealed (Fig. 2.1b). The data have not been detrended, and so if global scale warming of the oceans in response to anthropogenic forcing were the primary cause of decadal variability, then the standard deviation of decadal mean SST would be quite uniform across the globe, but this is not the case. The equatorial Pacific and indeed most of the Tropics and subtropics are relatively quiescent on decadal timescales. The most pronounced variability is seen in western boundary current regions, and the North Atlantic poleward of about 30°N stands out as a region where the low frequency variability of the climate system is focused.

What drives sea surface temperature change? The depth-integral of the heat equation in the upper ocean yields a prognostic equation for the upper ocean heat content, or vertically-averaged temperature, which is found empirically to be a very good proxy for SST (e.g., Stevenson and Niiler, 1983). The evolution of SST can then be expressed succinctly as in Large and Yeager (2012):

$$\frac{\partial SST}{\partial t} = (\rho C_p)^{-1} \frac{Q_{as}}{h} + \frac{R_V}{h} + R_H \tag{2.1}$$

where Q_{as} is the surface air-sea heat flux[1] , h is the depth of the vertical integral, R_H and R_V represent horizontal and vertical ocean heating processes, respectively, ρ is ocean density ($\approx$1026 kg m^{-3}), and C_p is the ocean heat capacity (3996 J kg^{-1} K^{-1}). The R_V term includes vertical heat fluxes due to both entrainment and diffusion across the bottom boundary at h, and the R_H term represents the lateral heat flux convergence associated with horizontal advection and diffusion over the full depth h. The impact on SST tendency of the first two terms on the RHS is in inverse proportion to h, which represents the effective mixing depth but is often defined in practice as a material surface or a constant depth level.

The heat flux term Q_{as} is itself a function of SST through the radiative and turbulent components of the surface heat flux (Appendix B). The partial derivative of Q_{as} with SST is always negative (increased cooling with warmer surface ocean), and this introduces a direct negative feedback on SST tendency. However, this direct effect can be counteracted by changes in the overlying atmospheric state (e.g., humidity, temperature, and wind speed) which accompany the

[1] Here and throughout, fluxes are defined positive into the ocean.

SST change, so that the effective dependence of Q_{as} on SST could vary substantially with region and timescale (Large and Yeager, 2012). The nature of the relationship between $\partial_t SST$ and Q_{as}, and between Q_{as} and SST, on various timescales gets to the heart of the conundrum of coupled climate dynamics. In the Atlantic, observational studies have identified an influence of summer midlatitude SST anomalies on wintertime NAO which results in a positive feedback on the SST anomaly (Czaja and Frankignoul, 1999, 2002). A similar interaction on decadal timescales is emerging in some model simulations (Gastineau et al., 2012; Gastineau and Frankignoul, 2012). Positive SST anomalies in the SPG associated with enhanced AMOC are found to induce a negative NAO state with some delay, consistent with the Marshall et al. (2001a) conceptual model. The negative NAO conditions amount to a positive feedback on high-latitude SSTs (i.e., less vigorous cooling), which at some point leads to a reversal of the AMOC anomaly. These recent studies bolster the case for a coupled mechanism for AMOC variability and AMV. We will now look for evidence of such air-sea interaction in historical heat flux data.

2.2 Historical air-sea flux variations (1948-2009)

If the CORE-II data are paired with an SST field, then a full set of air-sea heat and freshwater fluxes are obtained (Appendix B) at temporal resolutions ranging between 6-hourly and monthly depending on the flux component. In this section, we examine a data set of daily, historical air-sea fluxes constructed by using bulk flux formulae to couple the CORE-II fields together with time-interpolated monthly SSTs ("HadleyOI"; Hurrell et al., 2008) between 1948 and 2009. The air-sea interface is modulated by a time-dependent sea ice fraction which is prescribed using a daily SSM/I satellite product (Comiso, 2000), but this product is only available from 1980 onwards; climatological daily sea ice fraction is used in prior years. No suitable historical data set exists for ice-ocean fluxes and so fluxes under regions of observed sea ice are zero. For a complete listing of the data products used as input, refer to Large and Yeager (2009). Some aspects of the global climatology as well as the regional interannual variability which results from this procedure can be found in that paper and Large and Yeager (2012).

The correlations of monthly net heat flux with ΔSST and SST, after removal of mean seasonal cycles at each grid point, are shown in Figure 2.2 (panels a and b, respectively). The correlation extends over the full time period of the flux data set (1948-2009) and no trends have been removed.[2] The ΔSST for a given month is computed by time-interpolating the mid-month HadleyOI SST field to end-of-month, and then differencing to yield the change over a given month. An equivalent analysis is performed on annual-mean Q_{as} and SST, with ΔSST now defined as the change between successive January 1^{st} values (panels c,d). Finally, correlations are computed for pentadal means, with ΔSST defined as the change between January-mean SST fields 5 years apart (panels e,f). For the pentadal mean analysis, the correlation plotted is the average correlation obtained after using 5 different start years for the analysis (1948, 1949, ..., 1952). While it would be desirable to consider correlations of decadal means, the flux data set is not long enough to do so.

On monthly timescales, deviations from the mean seasonal cycle in Q_{as} correlate positively with anomalous ΔSST throughout the extratropical North Atlantic, although the correlation exceeds 0.5 only in select regions (Fig. 2.2a). Even on monthly timescales, the correlation is remarkably low in regions of strong ocean heat transport in the ocean (i.e., the GS and NAC) and deep mixing. Nevertheless, the surface heat flux clearly plays a non-trivial role in driving month-to-month SST change over much of the basin, and this driving role is even more evident in the winter season (not shown). The correlation of annual Q_{as} with the January-to-January ΔSST is also fairly high over much of the North Atlantic (Fig. 2.2c), consistent with numerous previous studies (e.g., Bjerknes, 1964; Cayan, 1992; Deser and Blackmon, 1993; Kushnir, 1994; Battisti et al., 1995), but we note that the correlations are actually quite low in the regions of greatest SST variance (Fig. 2.1a), along the GS and NAC into the Labrador Sea, where ocean processes are paramount. On monthly timescales, there is no discernible influence of SST on Q_{as} (Fig. 2.2b), but weak feedbacks begin to emerge on interannual timescales (Fig. 2.2d). The mostly negative correlations reflect the direct negative feedback of SST on Q_{as} (see Appendix B; Eqn 10 of Large and Yeager (2012)), but regions of positive feedback are evident, and these become quite strong in correlations of pentadal

[2] subtracting a linear trend from Q_{as} and SST gives qualitatively similar results

means (Fig. 2.2f). We find only weak (and often negative) correlation of pentadal-mean air-sea heat flux with local SST change (Fig. 2.2e), but the influence of SST on Q_{as} is greatly enhanced when considering 5-year means (Fig. 2.2f). The large correlations in Figure 2.2f imply that the ocean is dictating the anomalous air-sea heat exchange. Thus, the nature of ocean-atmosphere interaction in the North Atlantic appears to change significantly as the timescale is lengthened, transitioning from atmosphere driving the ocean on short (monthly) timescales to ocean driving the atmosphere on longer (quasi-decadal) timescales.

Positive correlation of SST with Q_{as} is indicative of SST-driven changes in the atmospheric surface state which tend to reinforce the ocean temperature anomaly. Our observation-based surface flux data set would thus appear to offer confirmation of the hypothesis that slow, AMOC-driven SST anomalies in the SPG induce a positive SST feedback by weakening the NAO and thus reducing the turbulent extraction of heat from the ocean in the SPG. This effect is generally interpreted as a modulation of storm track activity associated with the SST-driven change in the meridional temperature gradient in the atmosphere (Marshall et al., 2001a; Gastineau et al., 2012). It is interesting that the correlation pattern in Figure 2.2f bears some resemblance to the classic tripole pattern obtained when regressing SST or heat flux on the NAO index (Marshall et al., 2001b). The tripole pattern emerges more clearly, and the positive correlation of Q_{as} with SST becomes stronger, when Q_{as} lags SST by several years (Figure 2.3). The lag correlations were computed by staggering the start years of respective pentadal means. This result is strong observation-based evidence that slow SST variations in the Atlantic (i.e., the AMV) drive an NAO-like response in the atmosphere with some time-delay which acts as a positive feedback on the SST anomalies. This seems consistent with the model-derived conclusions of Gastineau and Frankignoul (2012) and the idealized mechanism of AMV oscillations advanced by Marshall et al. (2001b).

2.2.1 Time-varying water mass transformation rates in the North Atlantic

The CORE-II air-sea flux data set can also be used to bolster the model-based evidence that AMOC changes factored significantly in driving the observed AMV (see Fig. 1.1) by providing

rough estimates of ocean water mass changes over the latter half of the twentieth century. The surface density flux associated with air-sea fluxes of heat and freshwater is given by (see e.g., Schmitt et al., 1989; Speer and Tziperman, 1992; Large and Nurser, 2001):

$$D_{as} = -\alpha \frac{Q_{as}}{C_p} - \beta F_{as} \frac{SSS}{1 - SSS} \tag{2.2}$$

where Q_{as} and F_{as} are fluxes of heat (W m^{-2}) and freshwater (kg of freshwater m^{-2} s^{-1}), D_{as} is the surface density flux (kg of seawater m^{-2} s^{-1}), SSS is the sea surface salinity (psu or (kg of salt)/(kg of seawater)), and α and β are the coefficients of thermal expansion and haline contraction:

$$\alpha = \frac{-1}{\rho} \frac{\partial \rho}{\partial T}\bigg|_{p,S}, \quad \beta = \frac{1}{\rho} \frac{\partial \rho}{\partial S}\bigg|_{p,T}. \tag{2.3}$$

Again, all fluxes are defined to be positive into the ocean, such that positive heat and freshwater fluxes both result in negative density flux components. We compute daily D_{as} by pairing the daily CORE-II flux data set from the previous section with daily SST (a linear interpolation of monthly HadleyOI SST) and climatological daily SSS. The latter is simply a linear interpolation of the climatological monthly SSS obtained from the World Ocean Atlas 2009 (hereafter WOA09; Antonov et al., 2010). SSD, α, and β are computed from daily SST and SSS using the POP model equation of state (Smith et al., 2010b).

In a seminal paper, Walin (1982) derived relations between the surface heating of the ocean and the thermal circulation which have since been generalized into a theory of water mass transformation driven by surface density flux (e.g., Tziperman, 1986; Speer and Tziperman, 1992; Nurser et al., 1999; Large and Nurser, 2001). We refer readers to the papers just cited for detailed derivations and theory; the intent here is to apply this now common analysis to the CORE-II fluxes in order to investigate the ocean circulation variability implied by the flux data set. First, water mass transformation (WMT) rates can then be obtained by integrating the surface density flux over an isopycnal outcrop area:

$$F(\rho) = \frac{1}{\Delta\rho} \int\limits_{outcrop} D_{as} dA \tag{2.4}$$

where $F(\rho)$ has units of Sv ($= 10^6 m^3 s^{-1}$) and represents the cross-isopycnal volume flux associated with air-sea buoyancy exchange. The integral is performed on the POP model grid over the region bounded by the surface outcrops of $\rho - \frac{\Delta\rho}{2}$ and $\rho + \frac{\Delta\rho}{2}$ with $\Delta\rho$ =0.1 kg/m^3. In the limit of weak diapycnal mixing and negligible interior sources, $F(\rho)$ is the primary factor contributing to the formation of distinct ocean water masses. The water mass formation (WMF) in the range $\Delta\rho$ about ρ is then given by the convergence in density space of the surface transformation:

$$M(\rho)\Delta\rho = -\frac{\partial F}{\partial \rho}\Delta\rho \tag{2.5}$$

Climatological (1958-2007) North Atlantic WMT rates for the winter (JFM) and summer (JAS) seasons as well as for the annual mean are shown in Figure 2.5. The area integrals are computed separately for the regions shown in Figure 2.4; the sum over all the regions (denoted ALL) gives the aggregate mean transformation associated with high latitude (north of 50°N) surface buoyancy forcing in the Atlantic. There is a pronounced seasonal cycle, with positive transformation (towards higher density) in winter and negative transformation in summer. The effect of thermal forcing in generating diapycnal mass flux is much more important than haline forcing, but it is important to bear in mind that this analysis excludes the potentially significant effects of sea ice melt and formation. In aggregate, mean surface buoyancy fluxes in the North Atlantic increase the density of surface waters in the range $\sigma = 27 - 28$ kg m^{-3} at a maximum annual mean rate of about 20 Sv at $\sigma = 27.4$ kg m^{-3} (Fig. 2.5e). This value is about 5 Sv higher than many previous estimates of the mean transformation rate at that density (Speer and Tziperman, 1992; Speer et al., 1995; Marsh, 2000; Large and Nurser, 2001), but is in good agreement with a more recent analysis (Brambilla et al., 2008). Reasons for the discrepancy with the earlier studies are unclear and will require further investigation, but likely relate to the use of different flux, SST, and SSS data; integration over different areas; and perhaps most significantly as we show below, by the inclusion of different years in the climatology. Much of the positive mean transformation north of 50°N occurs in the SPG region, but mostly at the lower end of the density range ($\sigma = 27.0 - 27.5$ kg m^{-3}), while the Norwegian Sea is where most of the transformation of densest surface water

occurs ($\sigma = 27.5 - 28.0$ kg m^{-3}). The Irminger and Lab Seas contribute to mean transformation at mid-range densities.

Negative (positive) slopes in Figure 2.5 indicate the formation (destruction) of water masses. The climatological annual mean net WMF (Eqn 2.5) is shown in Figure 2.6. This shows that the mean surface buoyancy forcing over the North Atlantic creates water mass in the approximate density range $\sigma = 27.4 - 28.2$ kg m^{-3} at a rate of approximately 20 Sv:

$$\sum_{\sigma=27.4}^{\sigma=28.2} M(\rho)\Delta\rho \approx 20\,Sv \tag{2.6}$$

The interpretation of this mean volume flux is not obvious, because it represents a subduction rate only in the limit of negligible interior diapycnal mixing. However, Nurser et al. (1999) show that surface diapycnal transformation dominates interior mixing in the extratropical North Atlantic, and Marsh (2000) derived estimates of the mean and time-varying overturning streamfunction in density space from this type of Walin (1982) analysis. It is certainly true that there is some association between surface water mass formation and overturning circulation in the ocean, if not an exact correspondence. The fact that the CORE-II flux data set results in a mean formation rate of the densest North Atlantic waters that is not far off from the observed mean rate of overturning at 26.5°N ($\approx$ 18.5 Sv; Johns et al. (2011)) is encouraging, but we will refrain from interpreting the WMF rates as direct measures of circulation strength given that we do not know the effects of diapycnal mixing below the surface.

The climatological formation in the North Atlantic (Fig. 2.6e) includes relatively light waters ($\sigma <\approx 27.6$ kg m^{-3}) which are normally classed as Subpolar Mode Water (SPMW) rather than North Atlantic deep water (NADW), but Brambilla et al. (2008) argue that positive formation of these waters is likely associated with turbulent entrainment with denser overflow waters. Ganachaud and Wunsch (2000) give an estimate of 15$\pm$2 Sv of NADW formation (which they define as $\sigma > 27.72$ kg m^{-3}) based on a high latitude WOCE hydrographic line which therefore includes mixing effects. The CORE-II data give a comparable mean net formation rate ($\approx$ 15 Sv) if the computation is done over WOCE-era years (1990-1997) and over a similar density range ($\sigma > 27.7$

kg m^{-3}), but it is unclear whether positive formation of SPMW should be included. Mean formation in the Labrador Sea occurs over the density range $\sigma = 27.5 - 27.9$ kg m^{-3}, giving a net rate of Labrador Sea Water (LSW) production of about 1.8 Sv. This is in line with climatological mean production rate of 2 Sv estimated by Yashayaev (2007), but lower than the 4 Sv of LSW (in the range $\sigma = 27.68 - 27.8$ kg m^{-3}) observed flowing south along the Grand Banks shelf between 1993-1995 (Schott et al., 2004). Again, the latter estimate includes entrainment and the discrepancy is also easily explained by the considerable interannual variability of LSW production, as Yashayaev (2007) cite 4.5 Sv of mean formation during the strong NAO years of 1987-1994.

Further work will be needed to carefully vet the CORE-II formation rates against independent estimates, but the main interest here is not the mean formation so much as its variability. Figure 2.7 shows the standard deviation of CORE-II WMF as a function of density class and region over the period 1948-2009. The SPG and IRM regions contribute mainly to high interannual variance in the annual formation of SPMW ($\sigma < 27.6$ kg m^{-3}), while the LAB and NOR regions contribute mainly to the variance maxima in the density ranges $27.6 < \sigma < 27.8$ kg m^{-3} and $27.9 < \sigma < 28.0$ kg m^{-3}, respectively. The interannual variability in Figure 2.7a is a muted reflection of the stronger wintertime (JFM) formation variability shown in Figure 2.7b. A low-pass filtered analysis shows that almost all of the WMF variance of the densest waters ($\sigma > 27.6$ kg m^{-3}) is associated with decadal timescales, and this is particularly true of the winter formation of water generally classed as LSW ($27.6 < \sigma < 27.8$ kg m^{-3}). Nordic Seas overflow water (NSOW; $27.9 < \sigma < 28.0$ kg m^{-3}) and SPMW in the range $27.4 < \sigma < 27.5$ kg m^{-3} also exhibit pronounced decadal variance.

Correlations of the raw WMF time series with the winter (DJFM) NAO index[3] are shown in Figure 2.8. This demonstrates that NAO variations factor significantly in the WMF variability of the LAB and SPG regions, where correlations of both winter and annual formation exceed 0.6. The IRM region shows weaker positive correlations, and the high NSOW variance (Fig. 2.7) actually exhibits a weak negative correlation with NAO. The influence of NAO can be seen most clearly and succinctly if we consider the WMF in NADW density classes which show relatively high

[3] Observed winter NAO index provided by the Climate Analysis Section, NCAR, Boulder, USA, Hurrell (1995).

interannual and decadal variance in the SPG, IRM, and LAB regions: $27.5 < \sigma < 27.8$ kg m^{-3}. The correspondence is shown in Figure 2.9, and the correlation is 0.72. The class of NADW which is most related to NAO forcing spans the density range of classical LSW and includes lighter waters (Stramma et al., 2004). The CORE-II data show weak production of this NADW in the 1950s and early 1960s followed by a long upward trend which reached a climax in the late 1980s, and then a downward trend from the early 1990s to present. Strong NAO+ years (e.g., in the 1970s, 1980s, and 1990s) are clearly associated with enhanced surface formation, and weak NAO years (e.g., the 1960s) with weak surface formation.

Thus, historical air-sea fluxes provide compelling proxy evidence for substantial interannual variability in the Atlantic THC over the late 20th century associated with changes in the NAO. Based on surface data alone, we would expect an increase in AMOC strength between the early 1960s and early 1990s, followed by a decline in strength in more recent years. These results are in line with several previous studies which have investigated the connections between NAO, surface water mass transformation, and overturning circulation (Marsh, 2000; Gulev et al., 2003; Khatiwala et al., 2002), but our analysis extends over a longer time period and, importantly, serves as an observation-based benchmark for prognostic ocean model hindcast simulations forced with the same CORE-II surface fields. We anticipate that this surface transformation data set will also be quite useful for assessing the fidelity of surface buoyancy forcing in coupled CESM1 simulations.

There are several important caveats. The use of time-interpolated monthly SST and SSS data sets introduces errors not only in the high-frequency fluxes (computed at 6-hourly intervals then averaged to daily values), but also in the SSD field used in the WMT integral. Strong episodic heating/cooling events would tend to introduce high-frequency SST changes which would tend to damp the associated flux anomaly. That effect is missing here, as is the potentially significant role of ocean mesoscale eddies in modulating the air-sea density flux and associated transformation rates. As already mentioned, we do not have an interannually-varying SSS data set, and so potentially important modulations in the SSD field are not taken into account. Finally, sea ice melt and growth effects are missing, and yet these are known to have large impacts on both SSD and surface density

flux in regions near the ice edge.

2.2.2 Winter water mass formation

The winter formation of the densest North Atlantic waters is highly sporadic. Intense formation events associated with cold, dry Arctic air outbreaks occur on timescales of days to weeks, and these account for a significant fraction of the total amount of water accumulation in NADW density classes. To illustrate this, consider the formation of LSW in the LAB region during the strong NAO+ winter of 1989 (Fig. 2.10). Latent and sensible heat loss in February drove formation of $\sigma = 27.65$ kg m^{-3} water at daily rates exceeding 10 Sv and reaching as high as 28 Sv. This resulted in the production of more than 30,000 km^3 of water in that density class in about 20 days, according to the Walin analysis. Subsequent storm events in March drove rapid production in the next higher density class.

A variance-preserving power spectrum of net WMF in the LAB, IRM, and SPG regions in the NAO-driven range $\sigma = 27.5-27.8$ (plotted as an annual time series in Fig. 2.9, but here analyzed as a daily time series from 1948-2009) further emphasizes the importance of high frequency processes in the creation and modulation of dense ocean water masses (Fig. 2.11). Most of the total variance in NADW formation is of course associated with the annual cycle and harmonics thereof, but about two-thirds of the remaining variance is associated with periods less than 30 days. Timescales less than 10 days account for about one-third of the non-seasonal variance in WMF. Figure 2.9 highlights the decadal variability, but there is considerably more spectral power at periods less than 10 days than there is over the whole band of periods longer than annual. The impacts of such high-frequency surface transformation, and the ability of CGCMs to simulate it, will be the focus of future work.

2.3 The historical North Atlantic Ocean state (1948-2009)

In this section, we consider prognostic ocean and ocean–sea-ice model simulations which use the CORE-II data set (or a prior version thereof) as time-varying surface boundary conditions. The

primary focus is the CONTROL experiment of Appendix B which is a global, non-eddy-resolving ocean–sea-ice configuration of the Community Earth System Model version 1 (CESM1), forced at the surface with CORE-II fields. This simulation is one of several such experiments recently performed by modelling groups around the world, and it represents the NCAR contribution to several WGOMD-organized intercomparison studies which are presently underway. The CONTROL experiment was also used as the source of ocean and sea ice state initial conditions for historical CMIP5 coupled decadal prediction experiments using CESM1 which will be included in the IPCC AR5 (Yeager et al., 2012). The results of these decadal prediction experiments are examined in Chapter 5. The confidence in mechanisms diagnosed from forced OGCM simulations depends upon the model's ability to reproduce known features of the mean and time-varying ocean state, and so a general assessment of hindcast fidelity is a crucial first step before such model hindcasts can be used to draw meaningful conclusions. Here, the assessment focuses exclusively on the North Atlantic.

2.3.1 An overview of North Atlantic mean and variability from CONTROL

The CONTROL experiment appears to have a reasonable mean overturning circulation, with a maximum strength of roughly 26 Sv in a small recirculation cell centered at about 37°N (Fig. 2.12). Direct comparison with the observed AMOC profile at 26.5°N (RAPID; Cunningham et al., 2007) shows excellent agreement in terms of the mean magnitude and shape of the meridional transport distribution in the upper 2.5 km, but the deep, southward return flow is shallower than in RAPID and there is no discernible Antarctic Bottom Water (AABW) circulation in the zonal integral of abyssal velocity in the model. The strength of the barotropic circulation in the subtropical gyre (STG) is about 40 Sv and it exceeds 40 Sv in the SPG (Fig. 2.12c). The GS transport is quite low compared to available observational estimates (e.g., 113±8 Sv; Johns et al., 1995) due to the coarse model resolution and the correspondingly high horizontal viscosity needed for numerical reasons (Jochum et al., 2008). However, the subpolar gyre circulation strength is actually not much lower than observational estimates of depth-integrated equatorward transport near 55°N

(Pickart et al., 2002) and it is consistent with Xu et al. (2013), who report 37-42 Sv near 53°N. The barotropic streamfunction (BSF) and SST fields exhibit unrealistic spatial structures which are ubiquitous in this class of (non-eddy resolving) model: the too broad Gulf Stream (GS) separates too far north of Cape Hatteras and then remains too zonal, resulting in 4-5°C SST biases of opposite sign along the North American Coast and off the Grand Banks of Newfoundland (Fig. 2.12c,d). The HadleyOI SST climatology (Hurrell et al., 2008) is used here as the observational benchmark. The subpolar seas are characterized by positive SST (and SSS, not shown) biases, which are most pronounced in the Labrador (Lab) Sea.

Notwithstanding these familiar gyre circulation biases, the model maintains a fairly realistic winter sea ice edge compared to satellite observations (SSMI; Comiso (2000)) and the region of most active deep convection is along the ice edge in the western Lab Sea where mixed layer depths (MLDs) in late winter reach to about 1500 m on average (Fig. 2.13). The simulated location and strength of deep mixing is not inconsistent with the limited observations from this region (Marshall et al., 1998; Pickart et al., 2002; Lavender et al., 2002). The interannual variability of the winter MLD is likewise concentrated in the Lab Sea, particularly along the sea ice edge but with a lobe of high variability concentrated in the southeast corner of the Lab Sea Box region (60°W-45°W; 53°N-65°N). The region of greatest variability is thus somewhat displaced from the region of deepest mean mixing, a phenomenon which has been noted in fully coupled simulations of CESM1 (Yeager and Danabasoglu, 2012; Danabasoglu et al., 2012b). A second, weaker and less extensive, center of convective activity is apparent in the Norwegian Sea, off the coast of Svalbard island (Fig. 2.13).

It is difficult to assess the fidelity of the simulated variations in Lab Sea MLD, but other related fields can more readily be evaluated against observed time series to get a sense of the model hindcast skill in this key deep water mass formation region. A straightforward comparison of Lab Sea March sea ice coverage with satellite observations reveals a too weak response of the sea ice component of the model to the intense positive NAO winters of the early 1980's and 1990's (Fig. 2.14). This is probably related to ocean model biases (in particular, the too warm Lab Sea surface waters) which prevent ice growth in this region, but forcing and sea ice model deficiencies are likely

also to blame. The correlation with the observed time series is nevertheless quite high (r=0.86).

Long-term monitoring of the region via repeat hydrographic sections and floats has revealed decadal variations in the T and S properties of central Lab Sea water which have been linked to NAO (Dickson et al., 2002; Yashayaev, 2007; Yashayaev and Loder, 2009). A direct comparison with the observation-based T and S profile time series analyzed in these studies (not shown) mostly highlights the model's mean bias in this region (warm and salty), which are less pronounced in density due to the compensating effects of T and S contributions. A more encouraging correspondence is seen when deviations from the long-term (1960-2007) time mean are compared (Fig. 2.15), although the comparison is rough. As in Yashayaev (2007), we generate the time series by averaging over the central Lab Sea defined using the bathymetric contour of 3300m, but we perform the averaging in depth coordinates rather than density coordinates. As in observations, the variability of area-averaged central Lab Sea T and S in CONTROL is dominated by a decadal-scale evolution from warm/salty conditions in the 1960s and early 1970s to cold/fresh conditions in the 1990s, and then back to warm/salty anomalies in the 2000s. There are many differences in the details: the model generally has weaker T and S anomalies than observed except in the most recent years when it shows much stronger anomalies; the strong anomalies of the mid 1980s are of opposite sign in CONTROL; and there is no model signature of the strong freshening at around 2 km depth seen in the data in the 1990s. Nevertheless, the low frequency density variations are quite well represented, particularly later in the record when the quality of the observed record is highest (Here and throughout, the phrase "low frequency" refers to variations on decadal and longer time scales). The fact that Lab Sea density anomalies in CONTROL are comparable or somewhat weaker than observed helps to allay our concerns about the impacts of anemic sea ice variability (Fig. 2.14) on deep water mass formation. The decadal evolution together with strong densification of central Lab Sea water in the mid-1970s, mid-1980s, and early 1990s is in nice agreement with the CORE-II WMF time series seen above (Fig. 2.9).

A crucial test of any hindcast simulation is its ability to reproduce observed spatiotemporal patterns of SST variability. This is not guaranteed in simulations driven by bulk flux formulae

without temperature restoring, particularly in regions where ocean heat transport is a significant component of the upper ocean heat budget. The CONTROL hindcast does quite well at reproducing the observed AMV pattern over the latter half of the 20th century (Fig. 2.16), which we define here as the first empirical orthogonal function (EOF) of detrended North Atlantic annual mean SST. The HadleyOI product shows the familiar pattern (see Fig. 1.1) of basin-wide anomalies of a single sign with variance concentrated in four high latitude regions: the Lab Sea, the Irminger Sea, north of Iceland, and east of Newfoundland. The simulated AMV is also dominated by a broad, single-signed pattern with largest amplitude in the subpolar gyre, but differences are apparent, including the region of excessive variability in the central gyre and the region of large opposite-signed anomalies in the region of the northern recirculation gyre (NRG) just south of Nova Scotia (Fig. 2.16b). The latter is presumably associated with incorrect GS separation. Despite these differences, the pattern correlation of the two EOFs is 0.9 and the temporal correlation of the principle component (PC) time series is 0.95. In fact, the CONTROL simulation has one of the best representations of the AMV out of all the models participating in a CORE-II intercomparison (not shown).

Point-by-point correlations with observed SST from 1949-2009 provide another perspective on model behavior (Fig. 2.17). These show that the model does an excellent job of reproducing observed SST variations in the high-variance SPG and Lab Sea regions on both interannual and pentadal timescales, but the GS and NRG stand out as problem areas. Figure 2.1 shows that there is very little SST variance south of Cape Hatteras on interannual and longer timescales, and so the negative correlations in Figure 2.17b are not as worrisome as the low correlations in the high-variance NRG.

2.3.2 The SPG warming of the mid-1990s

The observed AMV is dominated by large decadal changes in the upper ocean heat content of the SPG. Gridded analyses of North Atlantic hydrographic data compiled by Ishii and Kimoto (2009) and Levitus et al. (2009) show a large, sudden warming of the high latitude upper ocean

in the mid-1990s (Fig. 2.18), which has been linked to similarly abrupt shifts in observed North Atlantic surface circulation and sea surface height (Flatau et al. (2003); Häkkinen and Rhines (2004)), marine fauna (Hatun et al., 2009), and Greenland glacier melt (Holland et al., 2008). The abrupt warming was preceded by anomalously cool conditions in the SPG region (50-10°W, 50-60°N; see Fig. 2.18), and growth of anomalously warm conditions in the subtropical gyre (STG) region (70-30°W, 32-42°N), between about 1981 and 1995. The CONTROL simulation reproduces the overall pattern and magnitude of observed pentadal-mean 275-meter heat content change in the late 20^{th} century (Fig. 2.18 i-l). The simulated warming in the 1996-2000 pentad is too strong, but the discrepancies with observed hydrography are roughly the same magnitude as the uncertainty in the observation-based gridded products.[4]

The time series of regionally-averaged SPG heat content anomaly (Fig. 2.19a) further demonstrates the abruptness of the high latitude warming in the mid-1990s following a long cooling trend. The CONTROL time series matches the observed year-to-year variations in heat content, including the sharp rise in 1996, but shows much more positive anomalies than either of the observed time series from about 1996 onwards. In contrast, the STG region is characterized by a long warming trend between about 1970 and 2000 (Fig. 2.19b), which mirrors the positive trend in the winter NAO index over the same time period (Fig. 2.19f; observed winter (DJFM) NAO index provided by the Climate Analysis Section, NCAR, Boulder, USA, Hurrell (1995)). The strength of the inter-gyre heat content gradient, quantified here simply as the difference of the STG and SPG heat content time series, exhibits an even better correspondence with the winter NAO index (Fig. 2.19c). Positive values of this STG−SPG index indicate that there is an anomalously strong meridional heat content gradient in the North Atlantic, with a dipole structure such as can be seen in the 1991-1995 panels of Figure 2.18. The 1960-2006 correlations of CONTROL heat content with Ishii and Kimoto (2009) are 0.90, 0.85, and 0.82 in Figure 2.19 panels a-c, respectively. The correspondence of CONTROL with observations in the SPG region is even better for SST, which

[4] All heat content anomalies are expressed as mean temperature anomalies (°C) relative to a 1957-1990 climatology that is computed separately for each individual data set.

clearly reflects the upper ocean heat content variations (Fig. 2.19d). The 1960-2006 correlations of CONTROL SST with fields from Ishii and Kimoto (2009) and Hurrell et al. (2008) are 0.93 and 0.96, respectively. All of these correlations are significant at the 95% confidence level based on a two-sided Student's t-test with autocorrelation taken into account. Thus, the verisimilitude of CONTROL on regional scales in the Atlantic is quite a bit better than might be surmised from the basin-scale, statistical comparison of Figure 2.16.

The dipolar heat content anomaly that preceded the late 1990s warming reached maximum strength in the early 1990s (Fig. 2.19c) and is generally understood to be the ocean signature of persistent positive NAO (NAO+) forcing in the years leading up to the shift (Marshall et al. (2001a); Eden and Willebrand (2001); Lozier et al. (2008); Lohmann et al. (2009b); Lohmann et al. (2009a); Robson et al. (2012a)). Our CONTROL simulation results are consistent with many of the ideas advanced in these studies: increasingly strong winter NAO conditions from the early 1970s through 1995 (Fig. 2.19f) resulted in a decades-long spin-up of the AMOC and subpolar gyre barotropic streamfunction (BSF) strength (Fig. 2.19e) and anomalously cool conditions at subpolar latitudes initially (Fig. 2.19a). The increase in northward heat transport associated with a strengthening AMOC contributed to the steady warming of the STG region (Fig. 2.19b), and thus enhancement of the STG−SPG heat content dipole (Fig. 2.19c). The SPG warming was triggered abruptly in 1996 when winter NAO conditions weakened dramatically, but Lohmann and coauthors (Lohmann et al., 2009b,a) contend that strong ocean preconditioning (reflected here in the dipole strength index) made significant SPG warming all but inevitable. This is because the enhanced northward heat transport associated with NAO+ at some point overwhelms the surface cooling, leading to a reversal of the high latitude heat content tendency even if NAO remains strong and positive. The implication of the Lohmann et al. results is that the large magnitude warming of the high latitude North Atlantic Ocean in the 1990s was highly predictable, given the state of the Atlantic Ocean in the early 1990s.

A heat budget of the SPG region (to 275-m depth) from the CONTROL simulation provides further insight into the physical mechanisms that account for the rapid late 20^{th} century SPG

warming (Fig. 2.20). Imbalances between the net surface heat flux (SFLX), which cools the SPG box on average, and the net advective and diffusive fluxes (ADV and DIFF), both of which warm the SPG box on average, generate non-zero heat content tendency: TEND = SFLX + ADV + DIFF.[5] The 1961-2007 averages are 1, -60, 47, and 14 W m^{-2} for TEND, SFLX, ADV, and DIFF, respectively, and so there is a slight upward trend in SPG temperature during the 47-year period being analyzed. The heat budget components in Figure 2.20 are plotted as anomalies from the time-mean over this time period.[6] . The increasingly strong NAO+ forcing of the 1980s and early 1990s (Fig. 2.19f) gave rise to opposing trends in the SFLX and ADV terms, such that the heat content tendency remained quite low from the mid-1970s up until the mid-1990s. By the early 1990s, very anomalous surface cooling was largely balanced by unusually strong advective and diffusive heating of the SPG box (Fig. 2.20a). The weak NAO in the winter of 1996 coincided with an extreme, positive heat content tendency in the SPG because the surface cooling was suddenly insufficient to match the strong advective heating that had been established over the preceding decades. Thus, both surface and advective heat fluxes played crucial roles in the SPG warming, but the abruptness and timing of the regime shift is attributable to the sudden change in atmospheric state.

The upward trend in ADV from the mid-1970s to the mid-1990s was primarily due to a pronounced increase in heat flux through the south face of the SPG box (Fig. 2.20c). A decomposition of the mean northward heat transport from CONTROL into gyre and overturning components (see for example Eden and Willebrand (2001), Johns et al. (2011)) indicates that, at the southern edge of the box (50°N), the gyre component accounts on average for about 83% of the meridional transport of heat across that latitude (0.55 PW of the the 1961-2007 mean net heat transport of 0.66 PW). Therefore, the trend in heat advection through the south face of the SPG box (Fig. 2.20c) is a direct reflection of the trend in the strength of the subpolar gyre circulation (Fig. 2.19e). However, at 45°N and 40°N, the overturning component accounts for about 60% and more than 100%, respectively, of roughly the same net meridional heat transport. The boundary between the gyres at

[5] In this heat budget analysis, from Yeager et al. (2012), the DIFF term is computed as the residual.

[6] The climatology over 1961-2007 is chosen because this is the period used for defining the bias adjustment factor, $d_i\tau$, required for analysis of decadal prediction experiments (see Chapter 5).

latitudes of 40-50°N is a transition zone between the overturning-dominated heat transport in the subtropics and the gyre-dominated heat transport at subpolar latitudes, and these clearly covary on long timescales (Fig. 2.19e). These decadal variations are primarily driven by NAO-related buoyancy forcing (Robson et al., 2012a).

While CONTROL shows a notable surge in heat transport through the south face of the box following the NAO+ to NAO− switch, which contributed to the elevated ADV and TEND (see curve S in Fig. 2.20c), this northward flux reached a maximum about a year after TEND reached a maximum in early 1996 and it was largely compensated by increased heat advection out of the north, east, and bottom faces of the box. The dramatic rise in SPG temperature in early 1996 in the CONTROL simulation cannot be attributed primarily to a surge in oceanic heat transport convergence, as Robson et al. (2012a) conclude from their budget analysis. Rather, the CONTROL heat budget indicates a complex evolution of the various forcing terms that resulted in elevated net advective heating of the SPG region throughout the 1990s. The surge in heat content tendency in 1996 is best understood as a sudden loss of balance between strong ADV heating and SFLX cooling when NAO weakened suddenly.

The slow changes in advective ocean heat transport convergence which led, inexorably, to the pronounced increase in SPG heat content and SST in the late 20th century in CONTROL are related to the multidecadal spin up of the large scale overturning and high latitude gyre circulations (Fig. 2.19e). As we will show clearly in the next chapter, these are both elements of the buoyancy-driven, or thermohaline, Atlantic circulation. The link between basin-scale thermohaline circulation variations and high latitude decadal SST variability, strongly implied by the above heat budget, is also suggested by a comparison of the PC time series of the dominant AMOC and SST EOFs (Fig. 2.16). The AMOC variance in CONTROL is dominated by a large-scale decadal evolution from relatively strong overturning in the early 1950s, to weak conditions in the late 1970s, and back to strong in the early 1990s. This decadal variance is most pronounced in mid-latitudes, between about 30°N and 50°N, as Yeager and Danabasoglu (2012) found in coupled CESM1 simulations. The AMOC strengthening leads the recent increase in subpolar SST (Fig. 2.16d), with maximum

correlation when the AMOC principle component leads the model AMV time series by 5 years (not shown). In the next chapter, we will identify the forcing components which are responsible for the decadal AMOC variability in CONTROL.

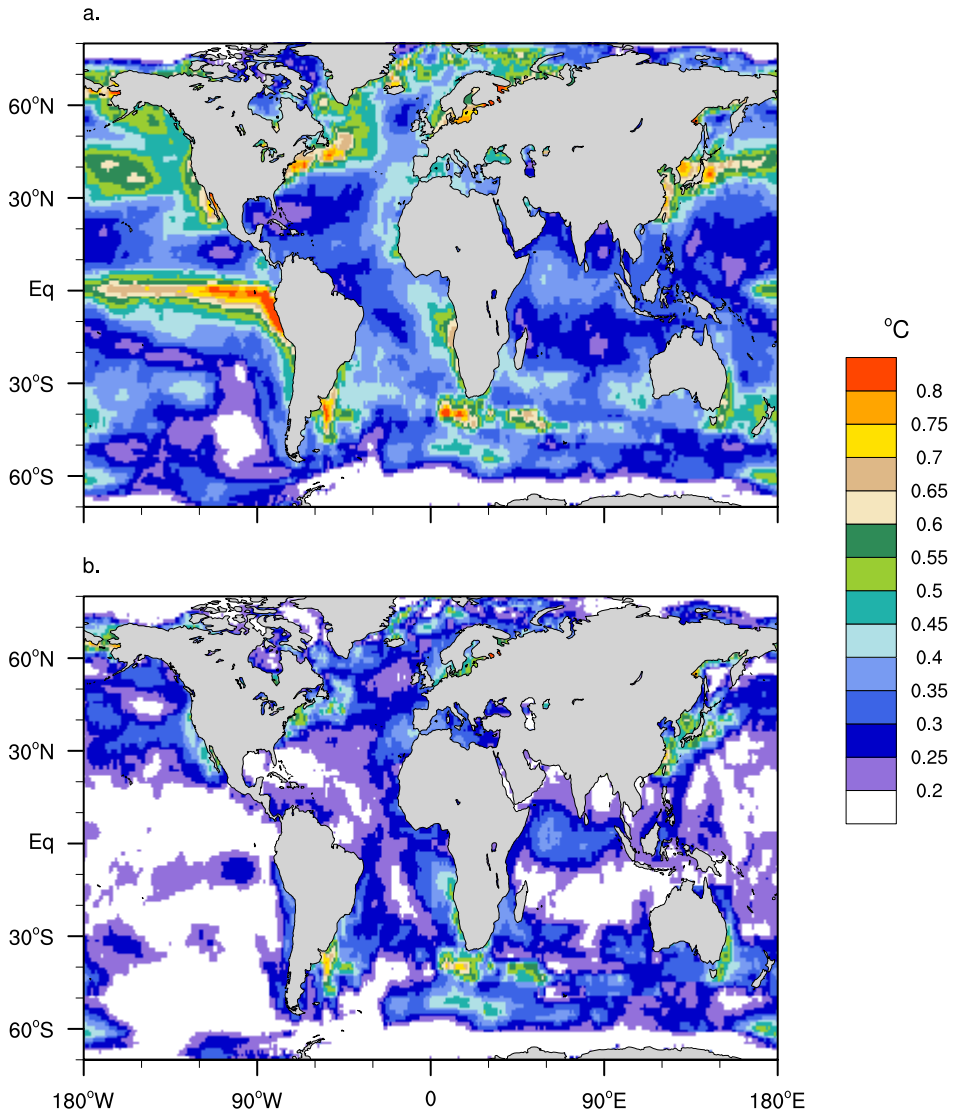

Figure 2.1: Standard deviation of historical (1900-2009) SST (°C) computed from (a) annual means, (b) decadal means (1900-1909, 1910-1919, etc). The monthly, gridded (1°x1°) HadleyOI SST product (Hurrell et al., 2008) was used.

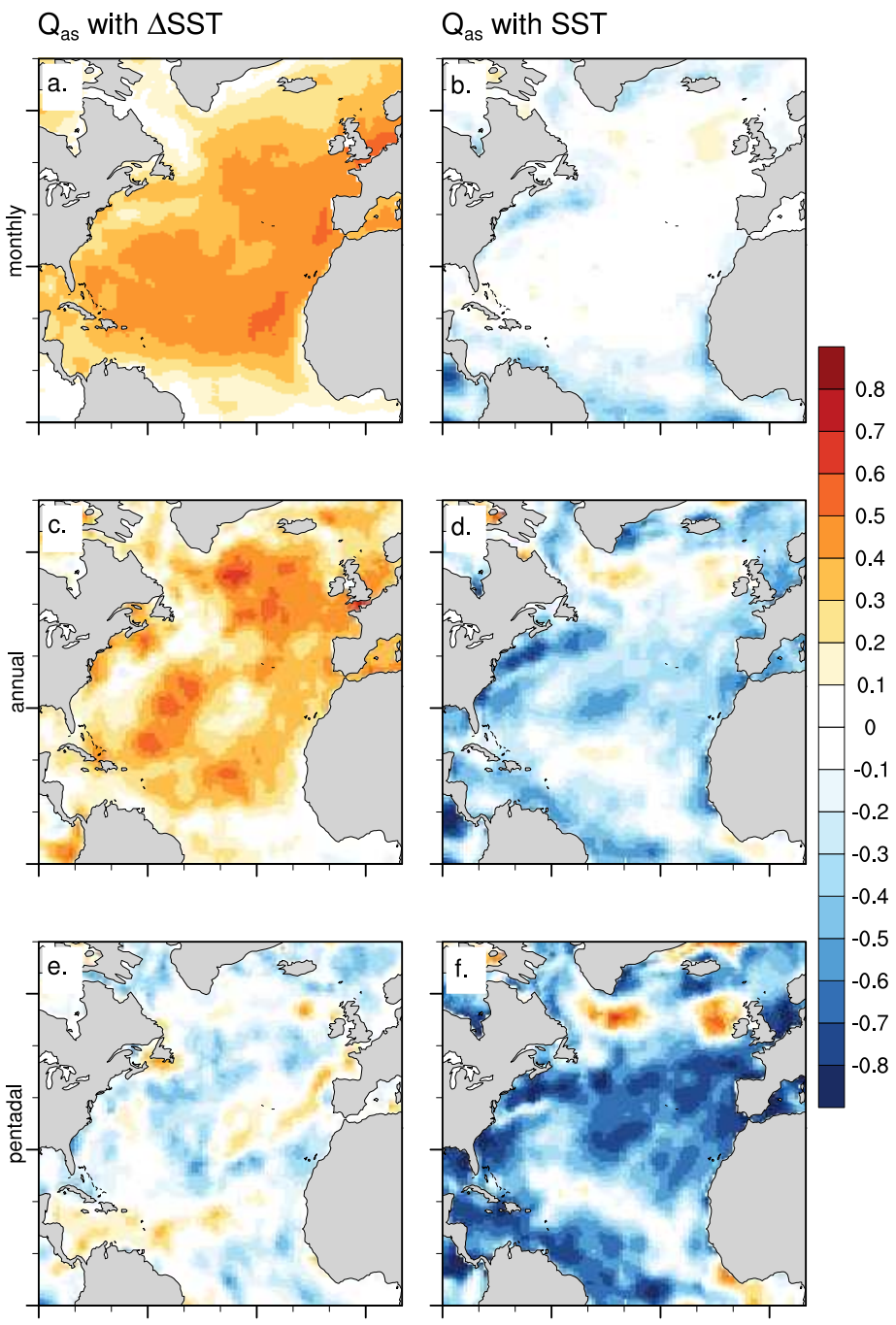

Figure 2.2: Correlations (1948-2009) of net air-sea heat flux derived from COREII meteorological fields with ΔSST and SST for various time-averaging intervals: (a) monthly Q_{as} with ΔSST, (b) monthly Q_{as} with SST, (c) annual Q_{as} with ΔSST, (d) annual Q_{as} with SST, (e) pentadal Q_{as} with ΔSST, and (f) pentadal Q_{as} with SST. A mean seasonal cycle has been removed prior to the computation shown in panels (a),(b). The latitude range is 0°N-70°N and the longitude range is 90°W-10°E, with tick marks plotted at 10° intervals.

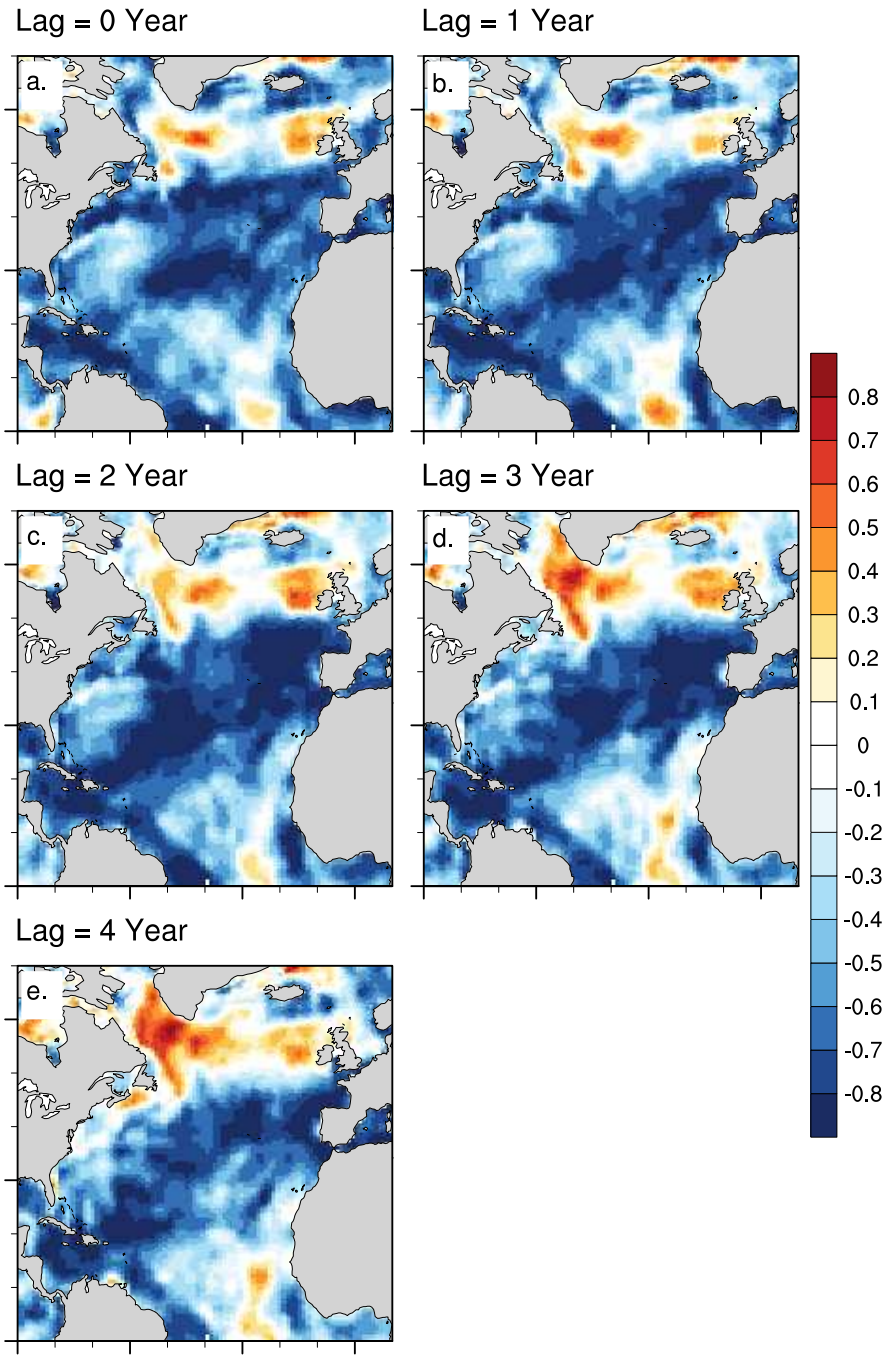

Figure 2.3: As in Figure 2.2f, correlations of pentadal Q_{as} with SST but for various lags: (a) Q_{as} lags SST by 0 years, (b) by 1 year, (c) by 2 years, (d) by 3 years, and (e) by 4 years. The lag corresponds to the mid-point of the respective pentadal means. Panel (a) differs somewhat from Figure 2.2f because an average lag-0 correlation was plotted in the latter.

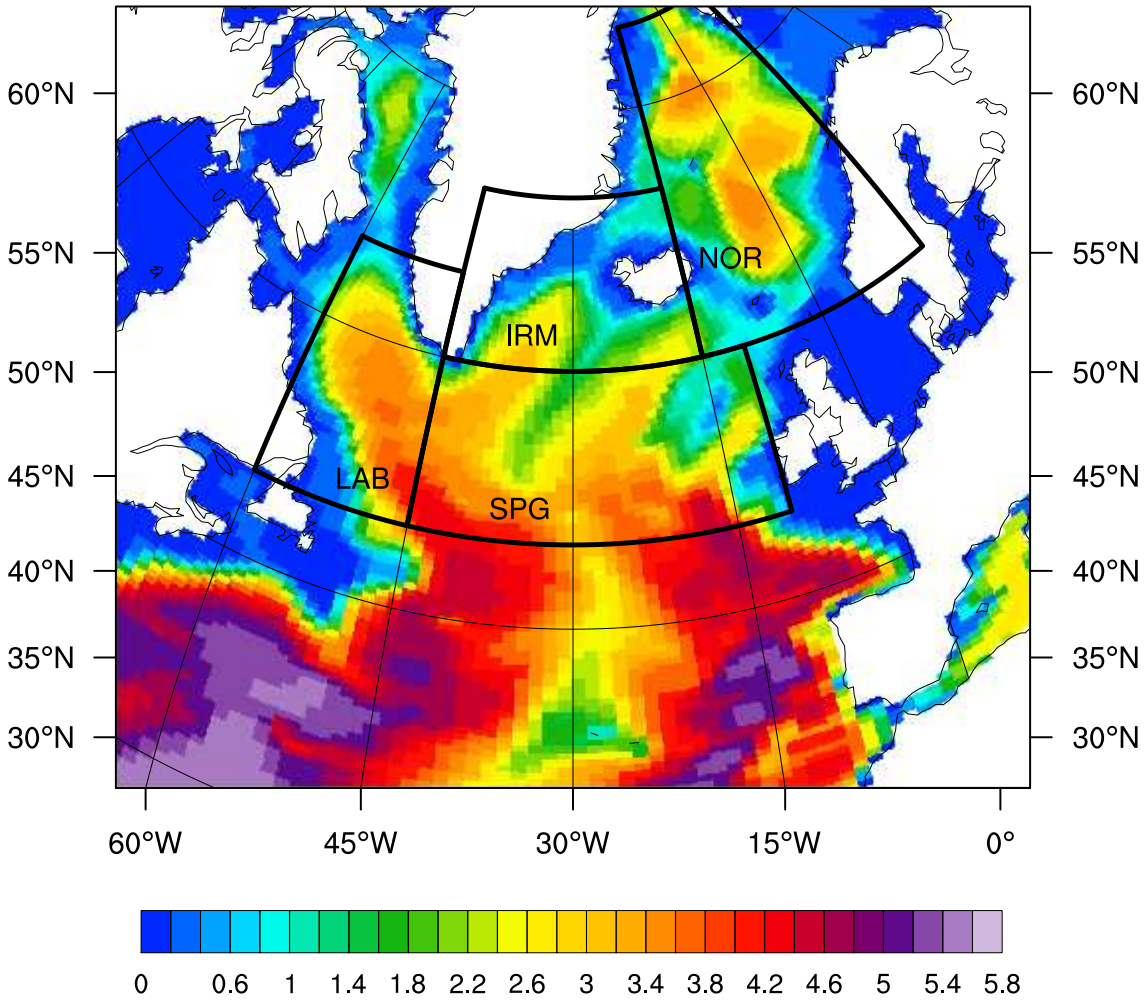

Figure 2.4: Box regions used in the analysis of high-latitude Atlantic water mass (trans)formation, overlayed on North Atlantic bathymetry (km) from the 1° POP ocean model. The regions are as follows: Labrador Sea (LAB), Subpolar gyre (SPG), Irminger Sea (IRM), and Norwegian Sea (NOR). The lower boundary of the LAB and SPG boxes is at 50°N.

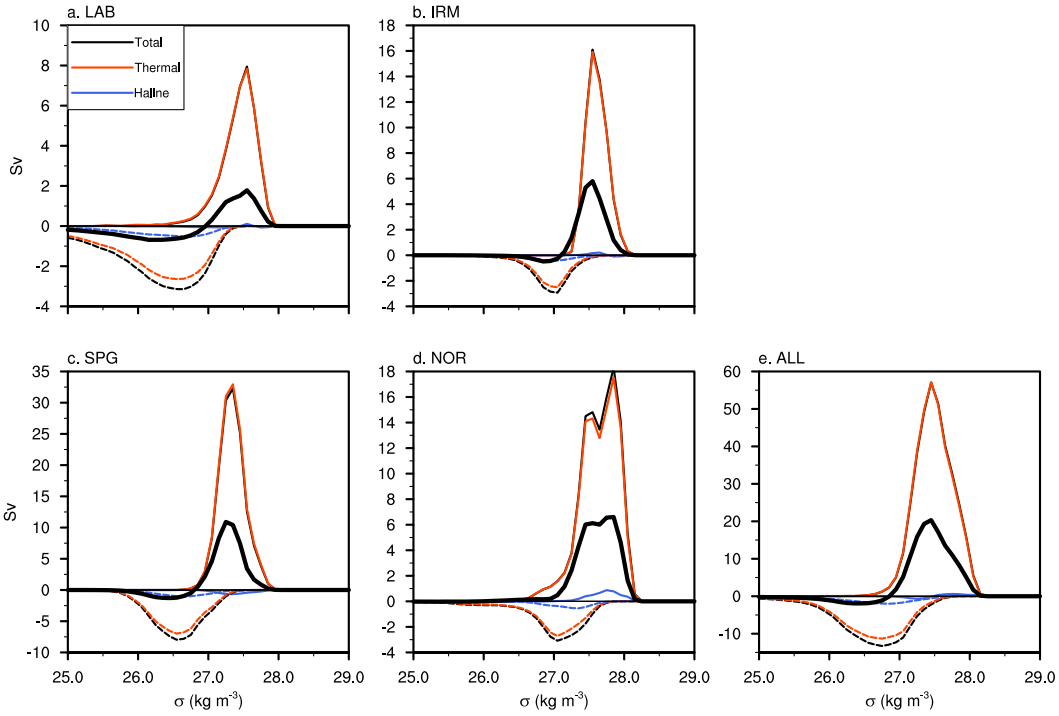

Figure 2.5: Climatological (1958-2007) winter (JFM, solid lines), summer (JAS, dashed lines), and annual mean (thick black line) water mass transformation rates as a function of ocean surface density for the regions shown in Figure 2.4 computed from CORE-II meteorological fields paired with HadleyOI SST. Thermal and haline components are plotted for the seasonal means but not for the annual mean. Panel (e) shows the sum over all regions. Note that panels have different y-ranges.

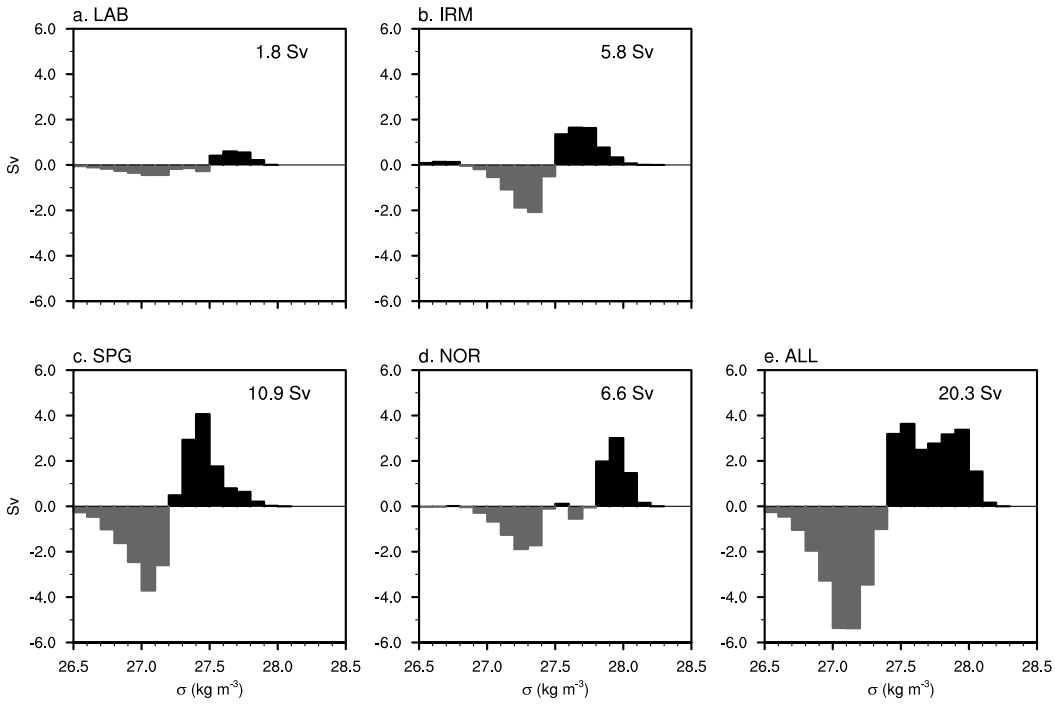

Figure 2.6: Climatological (1958-2007) annual mean net water mass formation (WMF) as a function of ocean surface density for the regions shown in Figure 2.4 computed from CORE-II meteorological fields paired with HadleyOI SST. Panel (e) shows the sum over all regions. The net rate of dense water formation (Sv) is given for each region, corresponding to the integral over density bins of positive WMF. Note that the net formation in ALL is not the sum of the numbers in each region because water formed in one region can be destroyed in another.

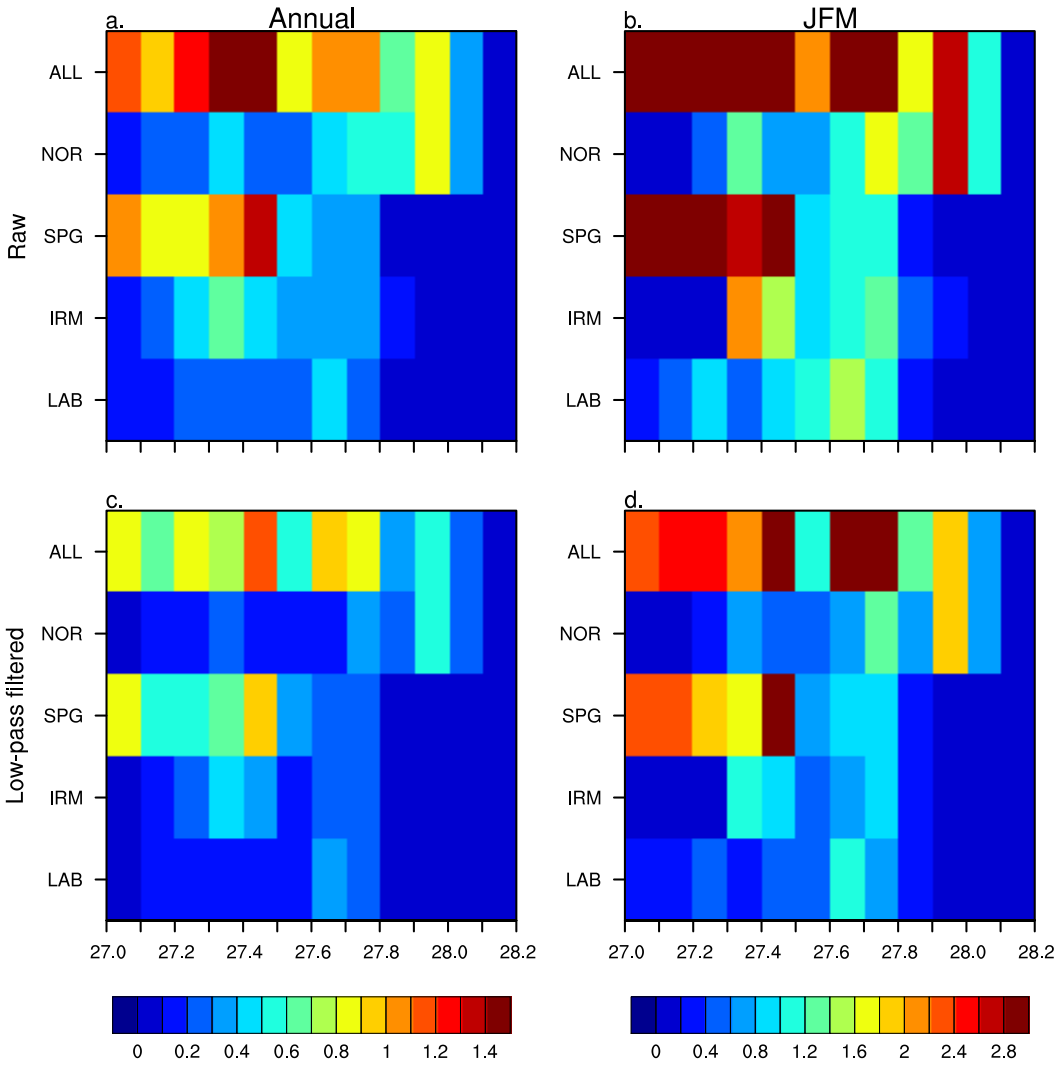

Figure 2.7: Standard deviation (Sv) of CORE-II North Atlantic WMF by region and density class computed from: (a) raw annual means, (b) raw winter (JFM) means, (c) low-pass filtered annual means, and (d) low-pass filtered winter means. A 15-point lanczos filter with cutoff period of 7 years is used for (c),(d).

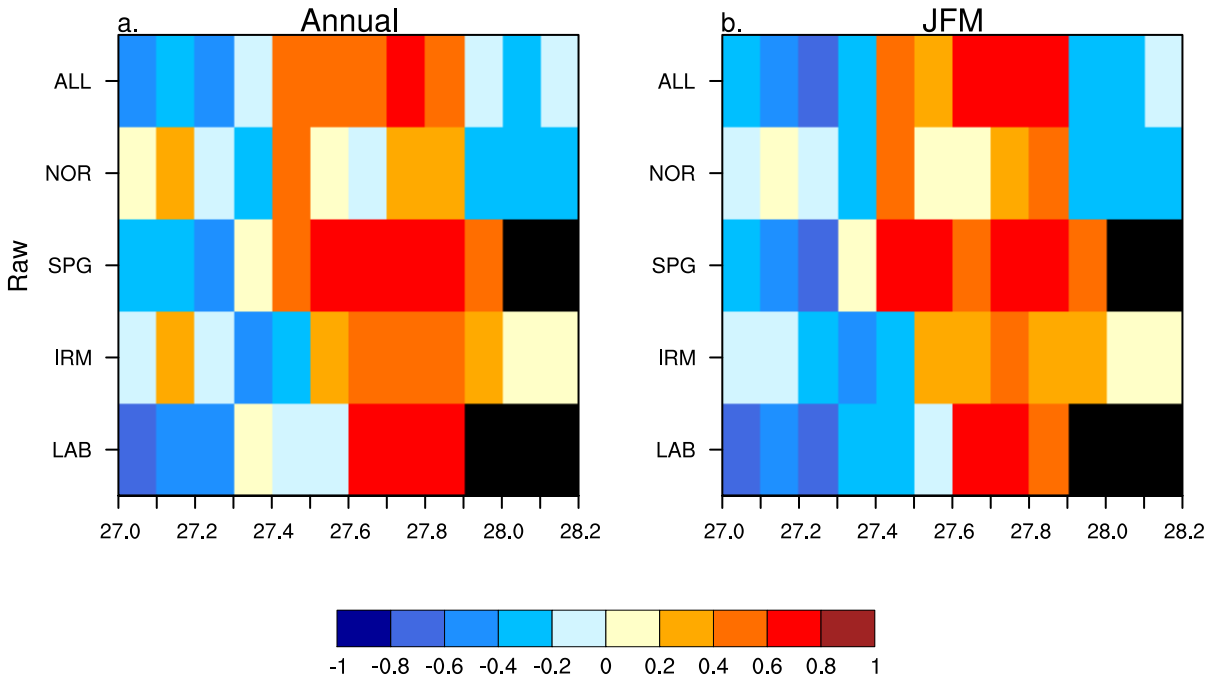

Figure 2.8: Correlations of (raw) CORE-II North Atlantic WMF by region and density class with the observed winter (DJFM) NAO index: (a) annual means, (b) winter (JFM) means. Black fill indicates zero formation of water in a particular density class over the time period 1948-2009.

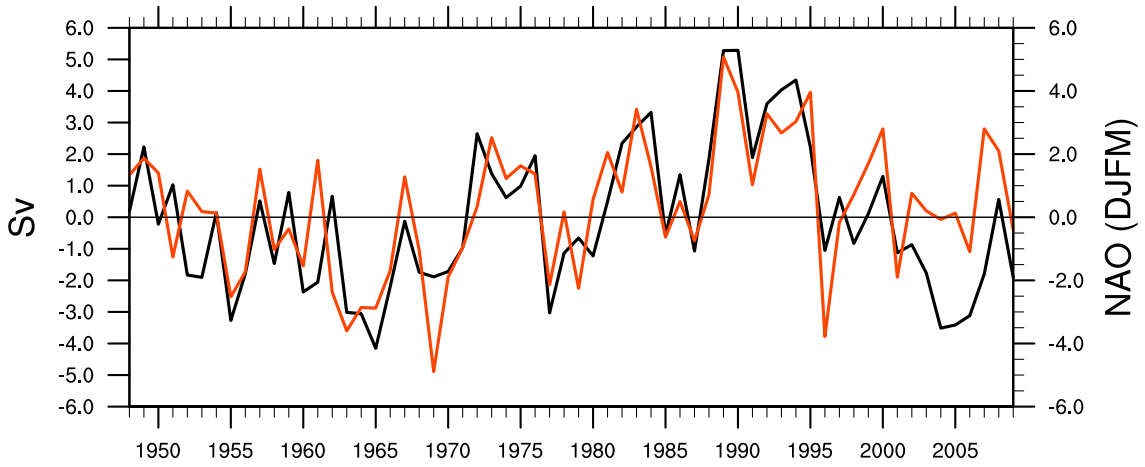

Figure 2.9: Anomalous annual surface formation of NADW in the density class $\sigma = 27.5 - 27.8$ kg m^{-3} aggregated over the LAB, IRM, and SPG regions (black curve) together with the observed winter (DJFM) NAO index (red curve). The correlation is 0.72. Anomalies are computed with respect to the 1958-2007 climatology.

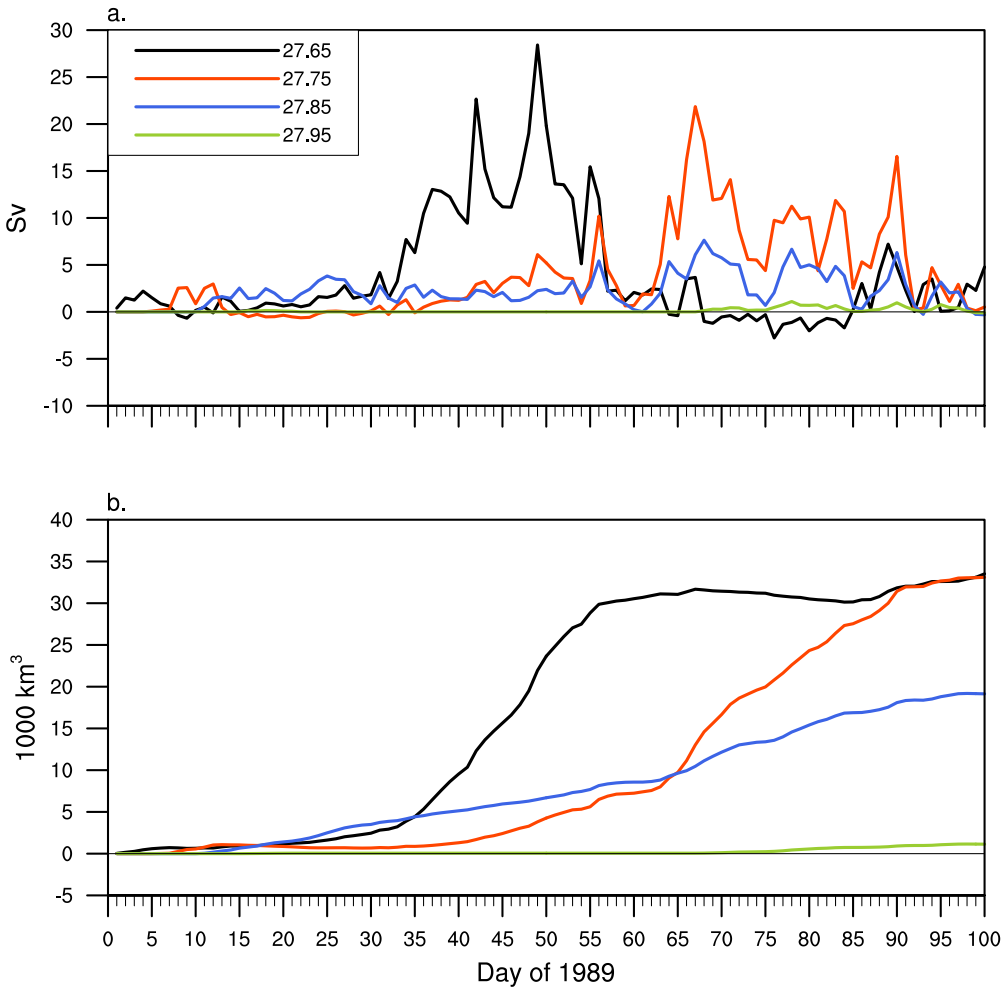

Figure 2.10: Water mass formation in the LAB region for 4 density classes during the early months of 1989 (which corresponded to a high NAO index): (a) daily surface formation rates and (b) associated water mass accumulation.

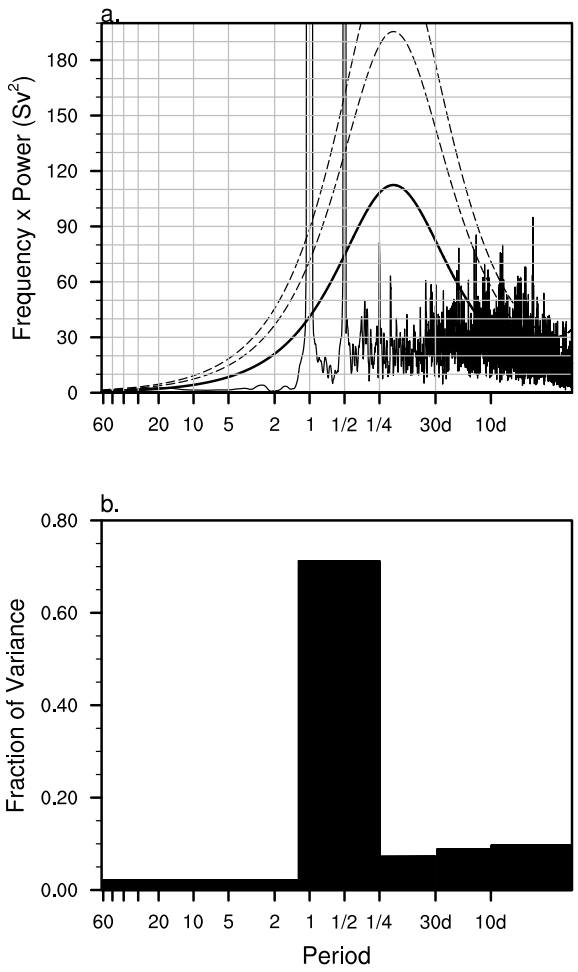

Figure 2.11: Variance-preserving power spectrum of daily WMF in the density range $\sigma = 27.5-27.8$ kg m^{-3} summed over the LAB, IRM, and SPG regions (plotted as an annual mean time series in Fig. 2.9) for the period 1948-2009. Panel (b) shows the fraction of variance explained by integrating the curve in (a) over 5 spectral bands. The x-axis of both panels is the period in either years or days (denoted with "d"). The standard deviation of the daily time series is 18.8 Sv.

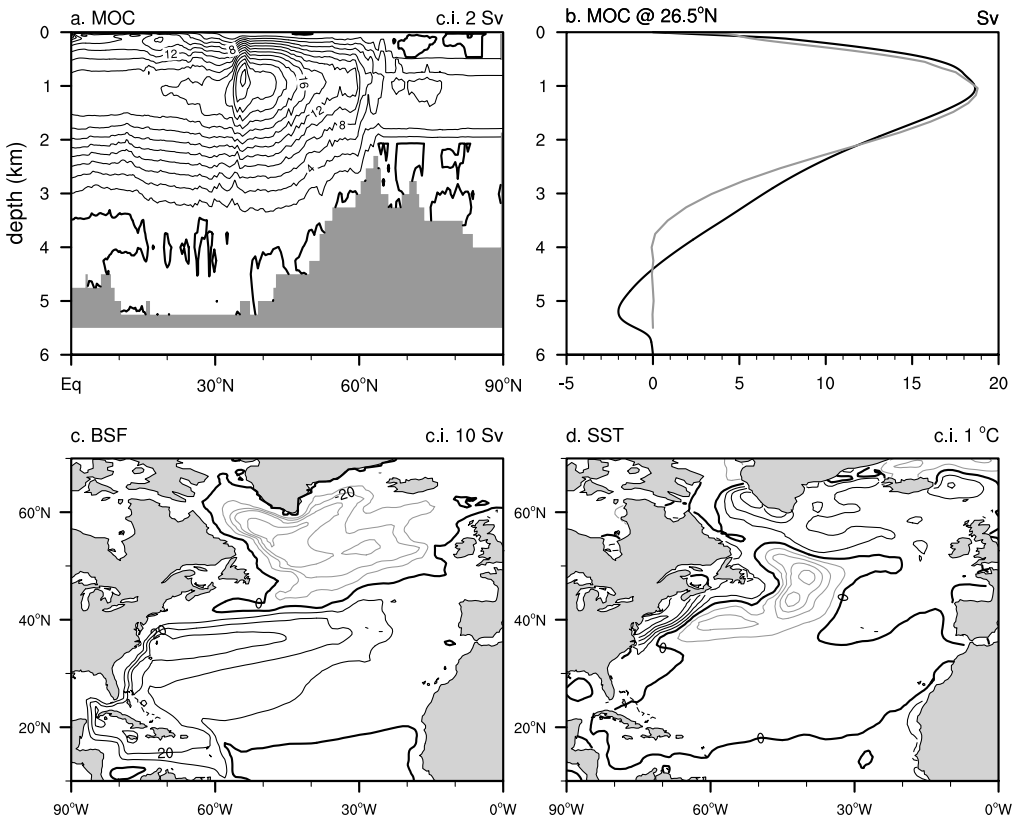

Figure 2.12: Figure 1 from Yeager and Danabasoglu (2013). Time-mean fields from CONTROL: (a) AMOC; (b) AMOC at 26.5°N (grey) compared to RAPID observations (black); (c) barotropic streamfunction; and (d) SST difference from the MergedHadleyOI (see text) dataset. Panels (a),(c), and (d) are 1988-2007 averages; panel (b) is an average from 4/2004-12/2007. Black and grey contour lines denote positive and negative, respectively.

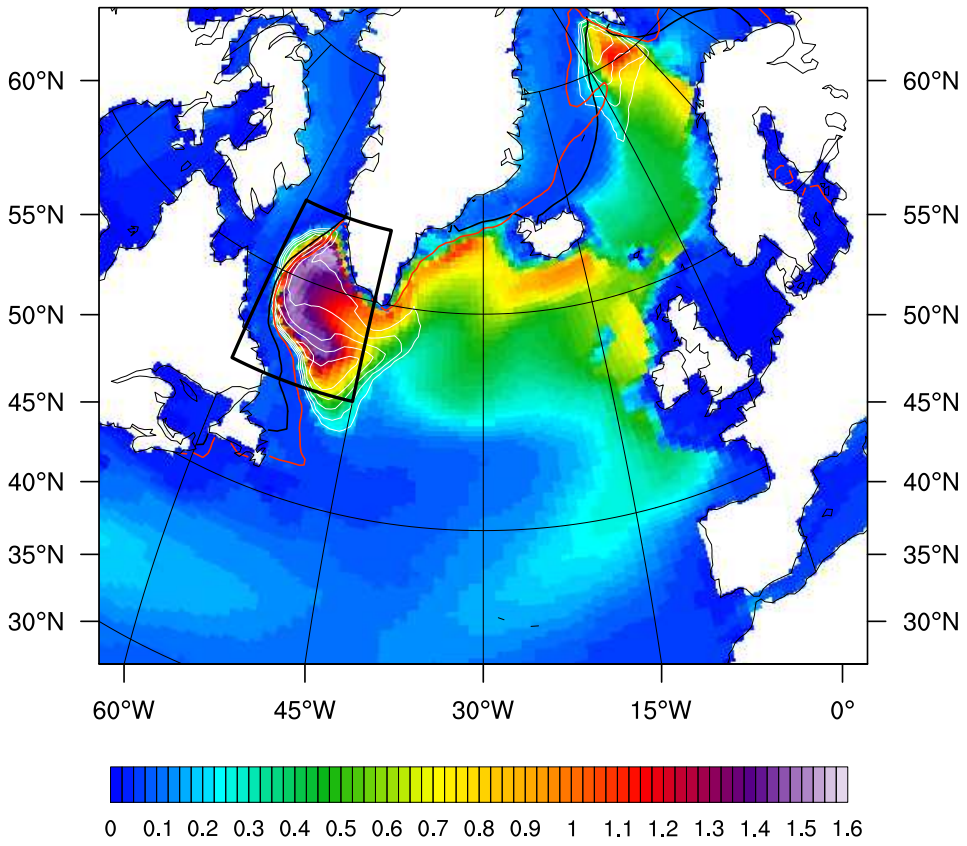

Figure 2.13: Figure 2 from Yeager and Danabasoglu (2013). Time-mean (1988-2007) March MLD (color shade; in km) and sea ice edge (black contour, corresponding to an ice fraction of 15%) from CONTROL. Observed mean sea ice extent from SSMI is also shown (red contour). Root mean square March MLD (computed over the 50 years 1958-2007) from CONTROL is overlayed in white contours (contour interval 0.1 km, starting at 0.2 km). Thick black lines demarcate the Lab Sea Box region (60°W-45°W; 53°N-65°N) referred to in the text.

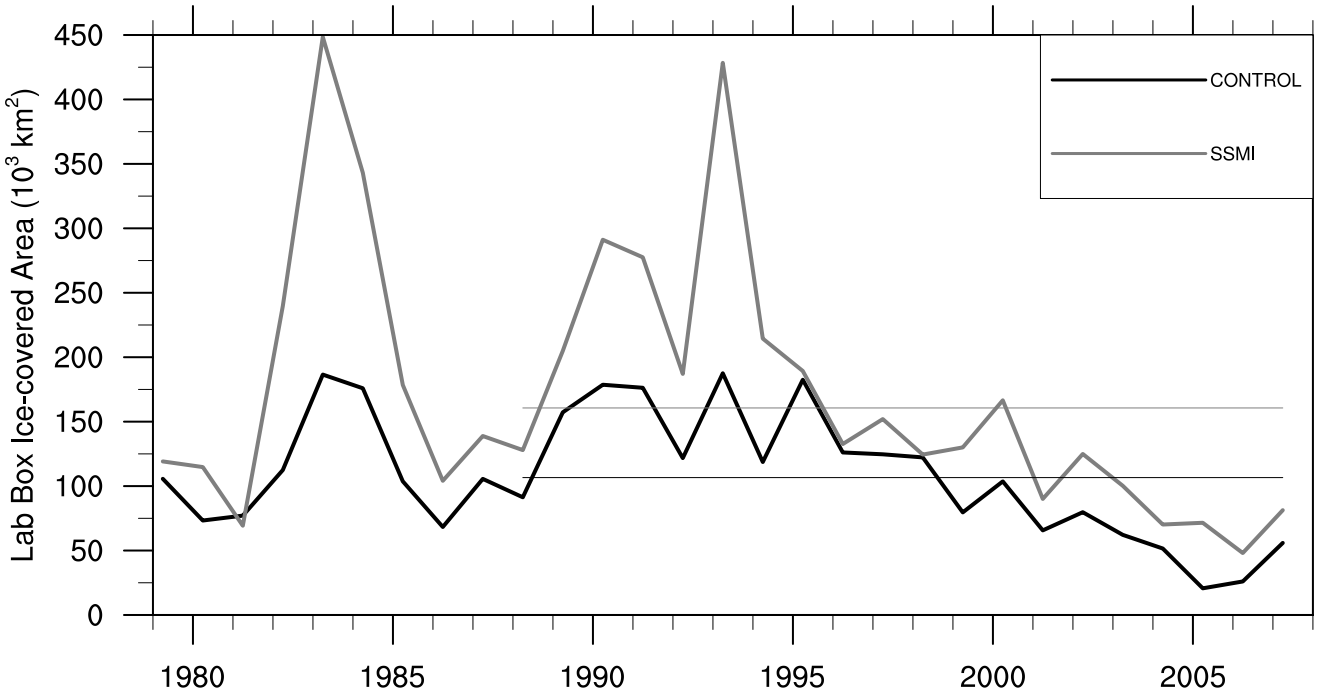

Figure 2.14: Figure 3 from Yeager and Danabasoglu (2013). Time series of March ice-covered area within the Lab Sea Box from CONTROL and SSMI observations. Thin horizontal lines show the 1988-2007 mean values corresponding to the ice edge plotted in Figure 2.13.

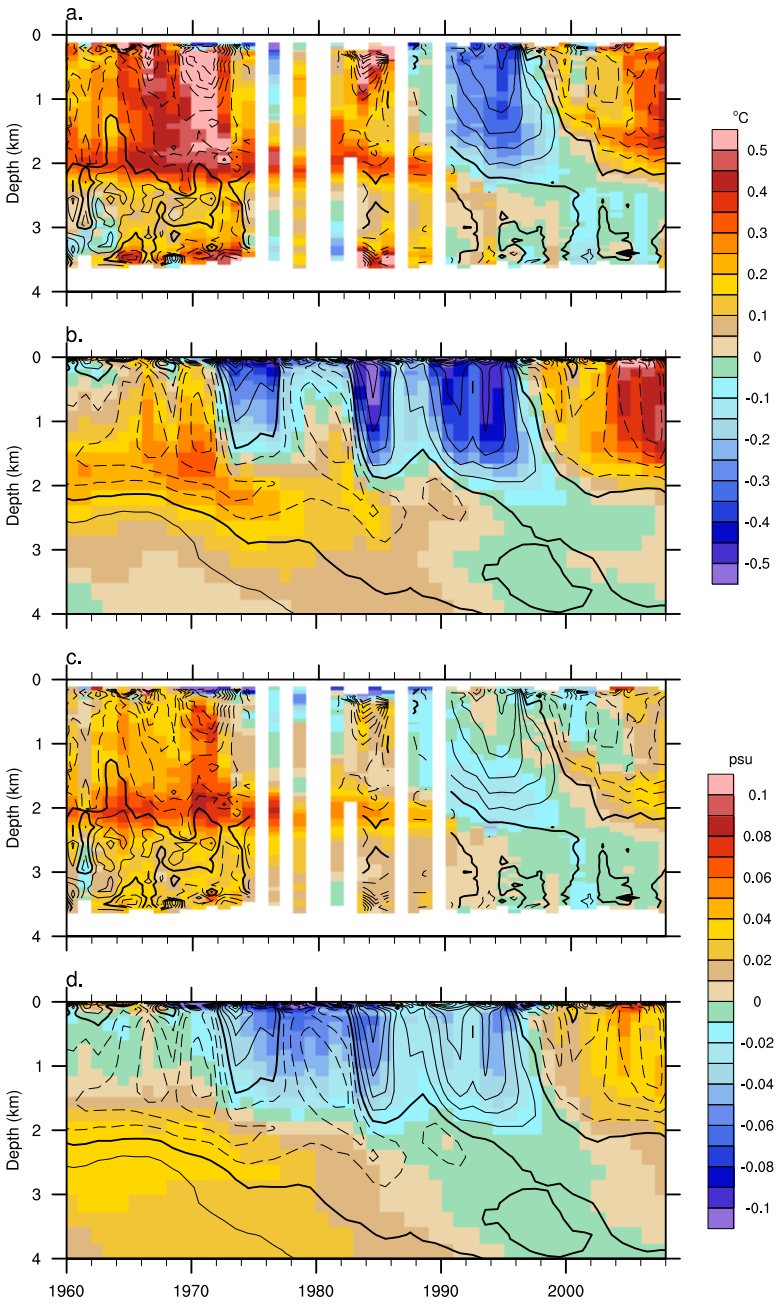

Figure 2.15: Figure 4 from Yeager and Danabasoglu (2013). Time series of anomalous potential temperature (shading) and potential density (σ_2, contoured at 0.01 kg m^{-3}; dashed lines for negative values) within the central Lab Sea from (a) a compilation of hydrographic observations (Yashayaev, 2007; Yashayaev and Loder, 2009) and (b) from CONTROL. Panels (c) and (d) are identical to (a) and (b) but for anomalous salinity. The anomalies are computed relative to the 1960-2007 climatology at each depth level. CONTROL area averages were computed on depth levels within the box region (56°W-49°W; 56°N-61°N) in the vicinity of the AR7W hydrographic section and include only grid cells where the bathymetry exceeds 3300 m. Model output from May of each year is used, to reflect the spring timing of hydrographic measurements, although the difference from annual mean output is small.

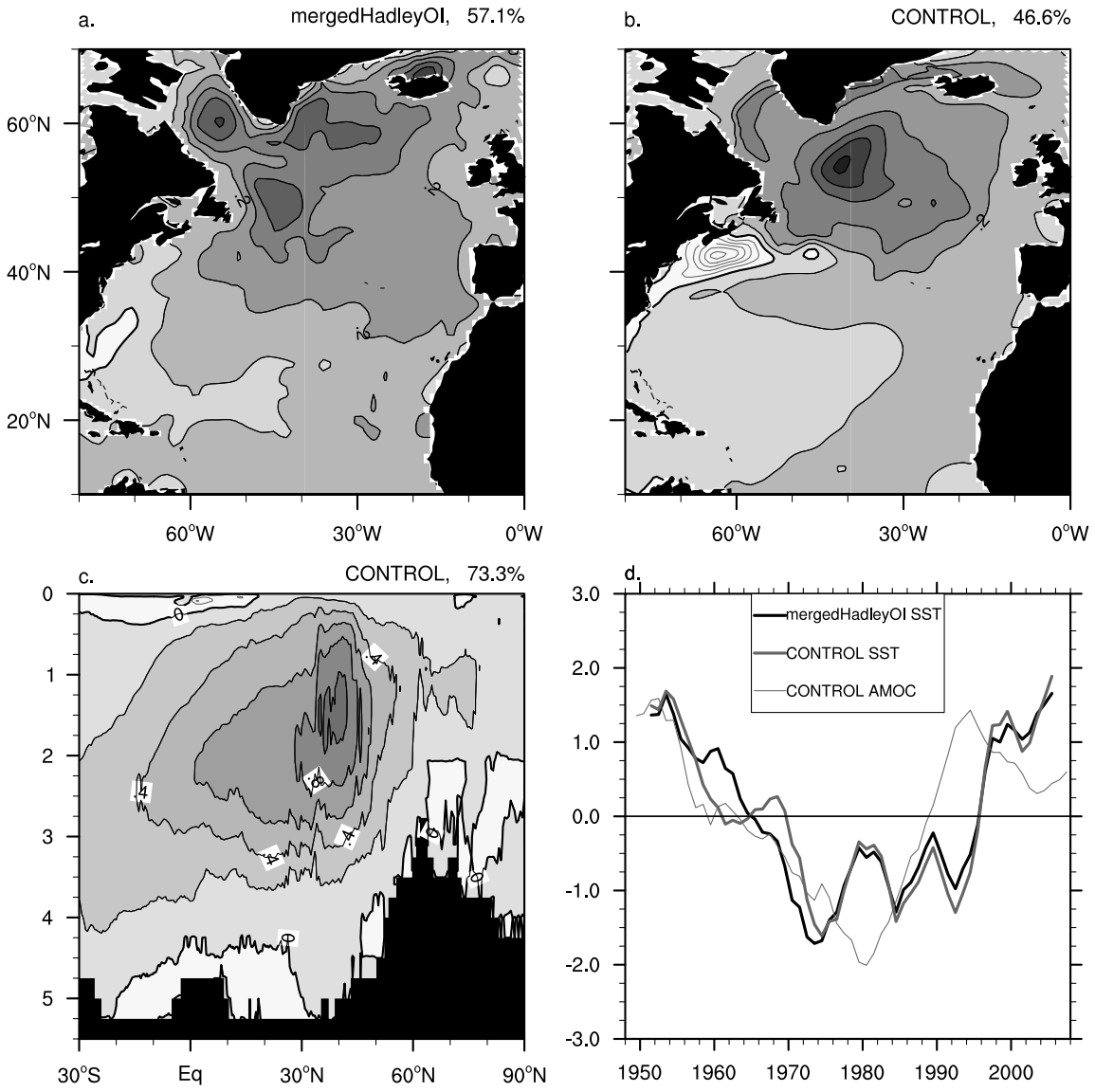

Figure 2.16: Figure 5 from Yeager and Danabasoglu (2013). First empirical orthogonal function (EOF 1) of (a) HadleyOI SST (c.i. = 0.1°C), (b) CONTROL SST (c.i. = 0.1°C), and (c) CONTROL AMOC (c.i. = 0.2 Sv). Grey shading is used for positive contours. The associated normalized principle component time series are plotted in (d). The domain used for computing the EOFs is the same as the region plotted (80°W-0°W; 10°N-70°N for (a),(b)). All fields were first linearly detrended and smoothed with a 5-year boxcar filter before the EOF computation. Percentage of total variance explained (of the smoothed field) is given for each EOF.

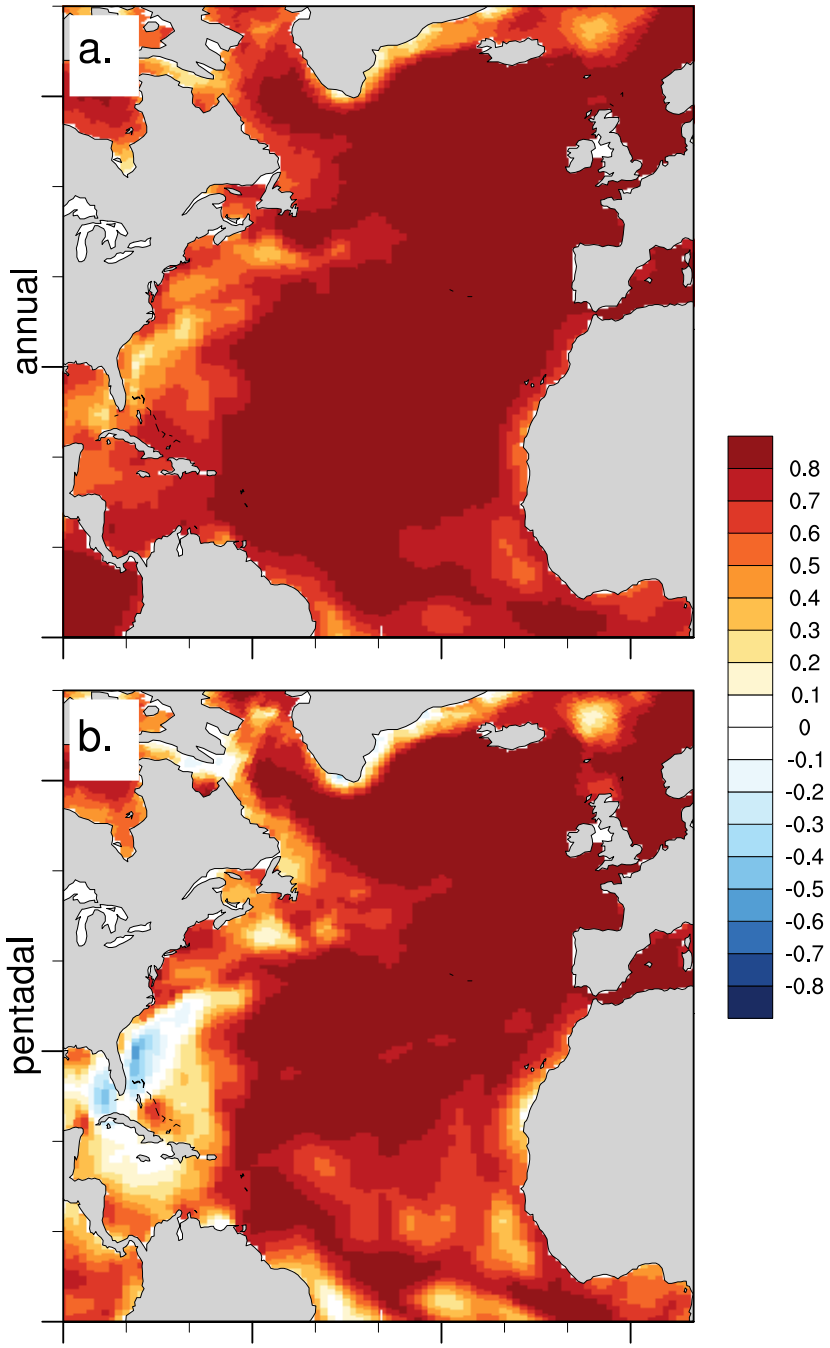

Figure 2.17: Local correlations (1949-2009) of HadleyOI SST with CONTROL SST for various time-averaging intervals: (a) annual, and (b) pentadal. The data have not been detrended, but this does not greatly impact the results.

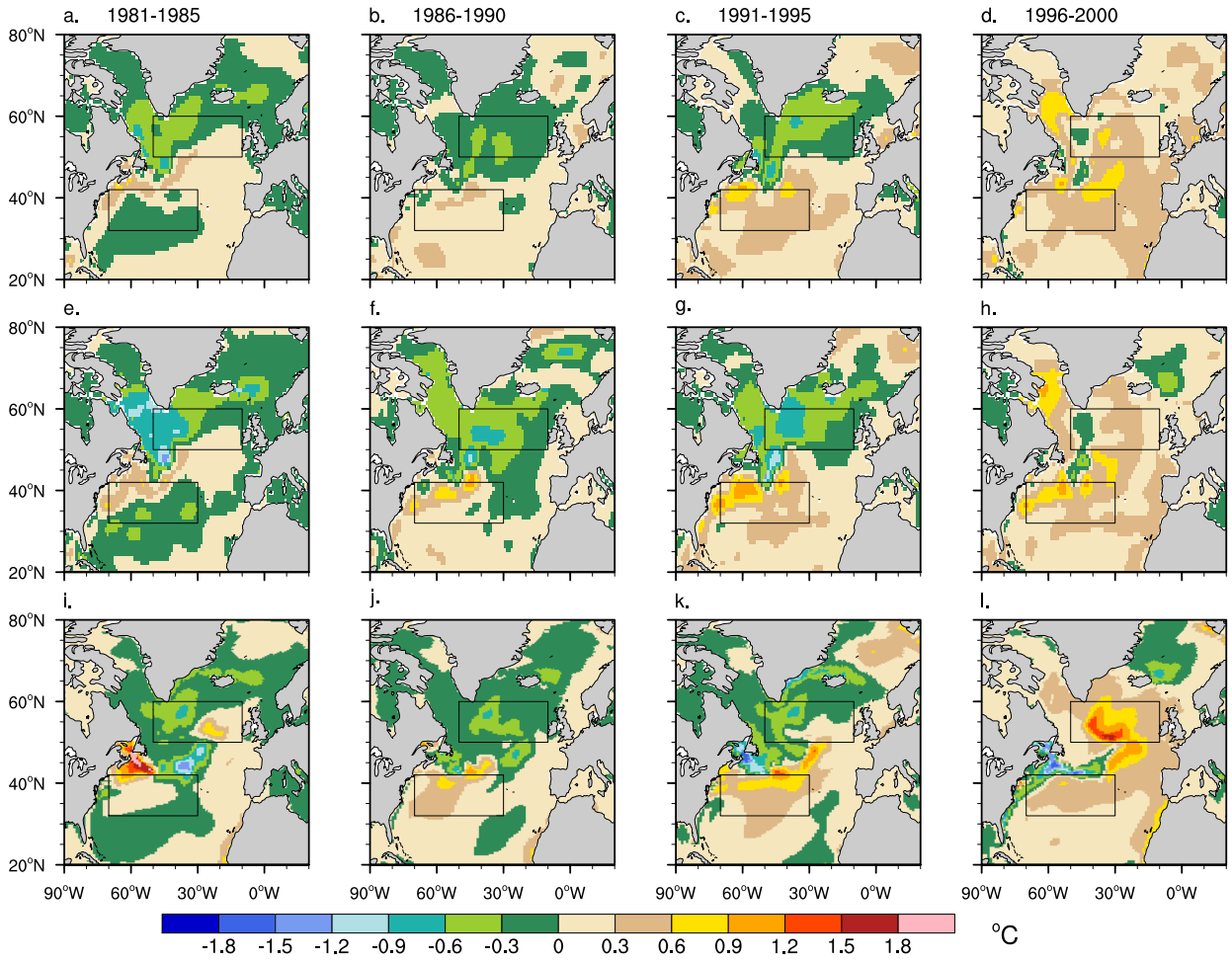

Figure 2.18: Figure 1 from Yeager et al. (2012). Pentadal-mean heat content anomalies expressed as the 275-m depth-averaged temperature anomaly relative to 1957-1990 climatology from (a)-(d) Ishii and Kimoto (2009), (e)-(h) Levitus et al. (2009), and (i)-(l) CONTROL. The boxes in each panel demarcate the SPG (50°-10°W, 50°-60°N) and STG (70°-30°W, 32°-42°N) regions.

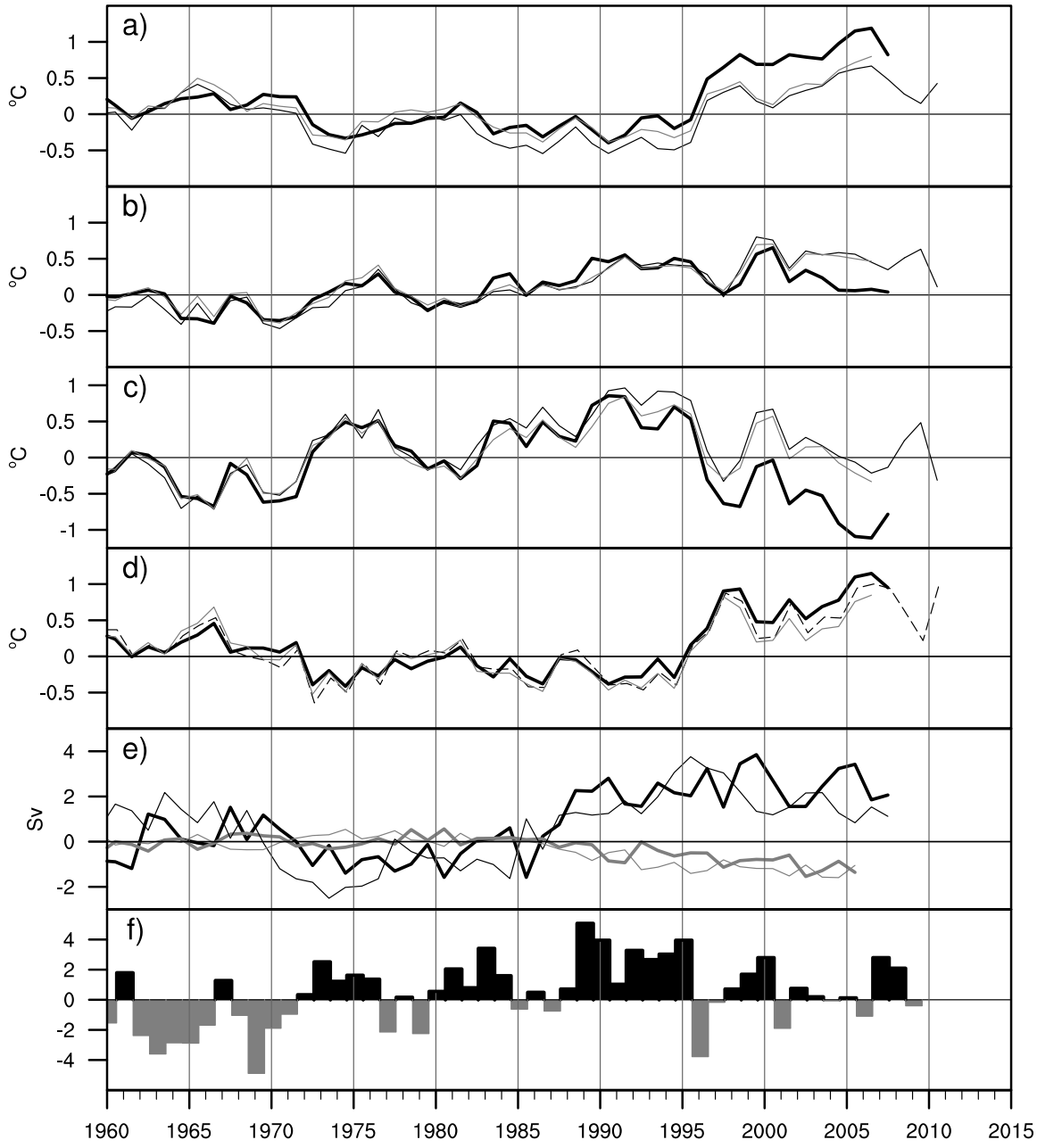

Figure 2.19: Figure 2 from Yeager et al. (2012). Annual mean time series of (a) 275-m heat content anomaly in the SPG box (SPG, °C), (b) 275-m heat content anomaly in the STG box (STG, °C), (c) heat content dipole strength (STG - SPG, °C), (d) SST anomaly in SPG box (°C), (e) AMOC strength at 37.5°N and 900-m depth (thick curves) and mean barotropic streamfunction in the SPG box (thin curves) (Sv $\equiv 10^6 m^3 s^{-1}$), and (f) observed winter (DJFM) NAO index. In panels (a)-(d), the thick black curve is CONTROL and the thin curves are from the following observational data sets: Levitus (thin solid black), Ishii and Kimoto (thin solid grey), and Hurrell (thin dashed black). See text for references. In panel (e), the black curves are from CONTROL, the grey curves are from the 20C ensemble, and the barotropic streamfunction anomaly has been multiplied by -1 so that positive values indicate anomalously strong circulation.

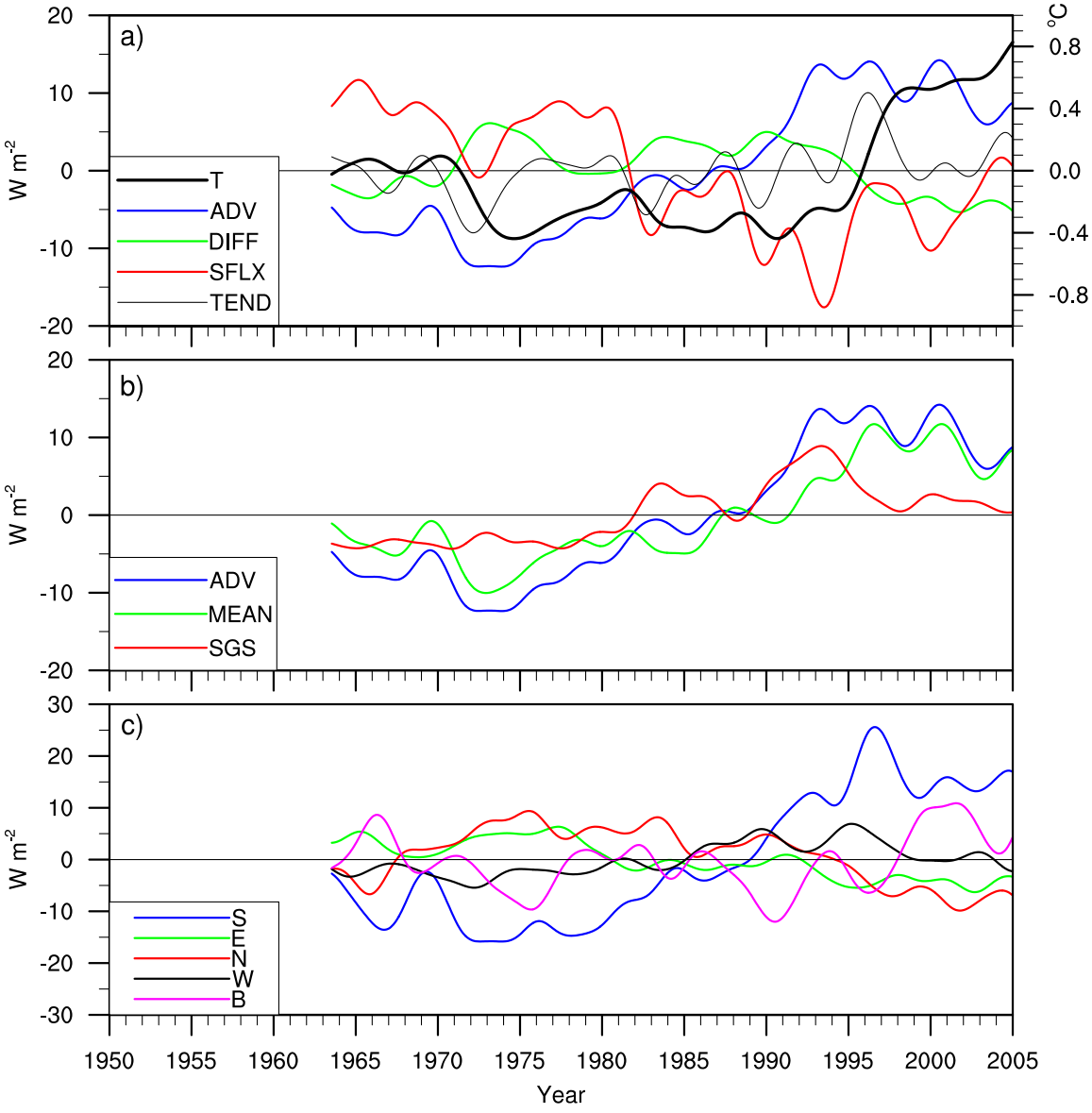

Figure 2.20: Figure 3 from Yeager et al. (2012). Time series of 275-m heat budget terms from CONTROL in the SPG box, with positive values indicating heat gain by the box. In panel (a), the net advective (ADV), diffusive (DIFF), and surface (SFLX) heat fluxes are plotted together with the heat content tendency (TEND) and mean SPG heat content (expressed as the volume-average temperature and referring to scale on right). In panel (b), ADV is replotted together with its decomposition into mean (MEAN) and sub-gridscale (SGS) components. In panel (c), the components of ADV through the south (S), east (E), north (N), west (W), and bottom (B) faces of the SPG box are plotted. All curves are based on monthly mean data low-pass filtered with a 5-year cutoff frequency. To get units of W m^{-2}, the terms have been scaled by the surface area of the SPG box, and they are plotted as anomalies from 1961-2007 climatology.

Chapter 3

What drove decadal ocean circulation changes in the North Atlantic in the late 20th century?

This chapter contains the main body of Yeager and Danabasoglu (2013), which has been submitted to *Journal of Climate*. It is an analysis of the suite of ocean–sea-ice experiments, CONTROL plus a set of perturbed forcing experiments, which are described in Appendix B.

3.1 Introduction

While it seems evident that North Atlantic thermohaline forcing is an important driver of changes in NADW properties and hence of AMOC variations, the relative impacts of various remote and local wind and buoyancy forcings on the AMOC remains unclear. In the limit of weak interior diapycnal mixing, energetic considerations suggest a dominant role for winds, particularly Southern Ocean winds, in sustaining the global overturning circulation (e.g., Toggweiler and Samuels, 1995, 1998; Wunsch and Ferrari, 2004; Kuhlbrodt et al., 2007). GCM experiments indeed show dramatically weakened overturning when the momentum flux into the ocean is completely switched off (Timmermann and Goosse, 2004; Saenko and Weaver, 2004). Based on its importance in the steady-state energy budget of the ocean, it has been hypothesized that mechanical forcing variations may also play a significant role in driving transient AMOC changes with important climate implications on long (glacial-interglacial) timescales (Wunsch, 2006), and this is supported by idealized model studies which indicate that AMOC scales linearly with the magnitude of Southern Ocean zonal wind stress (Nikurashin and Vallis, 2012). On the decadal time scales of interest here

(far shorter than the equilibration time scale of the global overturning circulation), the role of remote mechanical forcing in driving AMOC variability is presumably less important. However, one recent OGCM study (Lee et al., 2011) finds that most of the AMOC-driven increase in North Atlantic upper ocean heat content since the mid-20th century was caused by the strengthening of Southern Ocean zonal winds associated with the recent trend in the Southern Annular Mode (SAM; Thompson and Solomon, 2002).

The aim of this chapter is to systematically probe the origins of AMOC variability. We use forcing perturbation experiments to identify the key forcing elements which explain the simulated historical variability of the large-scale North Atlantic circulation between 1948 and 2007. A multi-model comparison of CORE-II experiments (Danabasoglu et al. (2013)) highlights several common features of simulated interannual-decadal variability, such as the aforementioned AMOC increase over the last three decades of the 20th century and an associated slow spinup of the cyclonic subpolar gyre circulation (Fig. 2.19), which we now seek to explain.

A powerful technique for probing mechanisms in OGCM simulations is to perform sensitivity experiments in which the variability of certain fluxes (e.g., wind, buoyancy) is selectively suppressed (e.g., Eden and Willebrand, 2001; Böning et al., 2006; Biastoch et al., 2008; Robson et al., 2012a). We adopt this approach and extend it to systematically assess the relative impacts on AMOC of year-to-year changes in various atmospheric forcing components (such as fluxes of heat, freshwater, and momentum) and subcomponents (such as the latent and sensible heat fluxes), and in particular examine the impacts of atmospheric state variability in two key regions: the Labrador Sea and the Southern Ocean. The NAO-related air-sea fluxes which have the greatest impact on AMOC are thus identified and their effects contrasted with those associated with the observed SAM trend. The present study is similar in many respects to Biastoch et al. (2008), who used an earlier version of CORE forcing, and this permits some direct comparison with their findings, but it is worth enumerating some salient differences: (1) we use entirely different ocean and sea ice models, both of which have somewhat coarser resolution than theirs; (2) we apply a much weaker global sea surface salinity restoring (relaxation time scale of 4 years as opposed to their 180 days); (3) we do

no restoring of model temperature or salinity anywhere below the surface (in contrast to their use of a "robust diagnostic" method to prevent polar water mass drift); (4) our experiments should include any effects arising from variations in the Nordic Seas overflows because the model has an overflow parameterization (Danabasoglu et al., 2010) and there is no suppression of high latitude water mass variability (#3); and finally (5) the scope of our sensitivity analysis is considerably broader, since we aim to quantify the relative influence of various forcing subcomponents and geographic regions on AMOC variability.

The model and experimental setup is given in Appendix B, and we have already demonstrated the fidelity of the hindcast CONTROL simulation in Chapter 2. The relative contributions of buoyancy and wind forcing to Atlantic Ocean variability on interannual and longer time scales are examined next. We then assess the impacts of regional forcing variations over the Lab Sea and Southern Ocean. After establishing the dominance of Lab Sea forcing in driving AMOC variations of the late twentieth century, we turn to an examination of the origins of Lab Sea flux variability.

3.2 Buoyancy- and Momentum-forced variability

Consistent with several other recent ocean hindcast studies (e.g., Böning et al., 2006; Biastoch et al., 2008; Robson et al., 2012a), we find that the late 20th century AMOC variability in CONTROL can, to an excellent degree of approximation, be understood and analyzed as a linear superposition of anomalies associated with time-varying momentum and buoyancy forcing (isolated in experiments M and B, respectively; see Table B.1), and that the low frequency component of North Atlantic AMOC variability is primarily a response to high-latitude buoyancy forcing anomalies. Hovmuller diagrams of annual-mean AMOC strength (the maximum in depth of the AMOC streamfunction) as a function of latitude and time show that, consistent with the first AMOC EOF (Fig. 2.16), the AMOC variability of CONTROL is dominated at all latitudes by the transition to relatively strong overturning beginning in the mid-1980s following relatively weak overturning in the preceding decades (Fig. 3.1a). Computing AMOC strength at a fixed depth level (e.g., 1000 m) gives qualitatively similar results. North of the equator, the low frequency variability in

CONTROL appears most associated with buoyancy forcing (Fig. 3.1d) while much of the higher frequency (interannual) variability at all latitudes is most associated with momentum forcing (Fig. 3.1b). The linear superposition of M and B anomalies explains almost all the AMOC variability of CONTROL (Fig. 3.1c). Note that the M anomalies have had the NYF drift signal (Fig. 3.8c) removed as explained in Appendix *B*.

The relative contributions of momentum (M) and buoyancy (B) forcing to late twentieth century variations in AMOC strength are quantified as a function of latitude in Fig. 3.2, as correlations with and root-mean-square (rms) differences from the AMOC strength in CONTROL. When interannual fluctuations are included in the analysis, both metrics show a dominant influence of B north of about 35°N, except for the 50-60°N latitude band, while M explains most of the total variance south of 35°N (Fig. 3.2a,c). The variance maximum at 35°N (Fig. 3.1a) is a feature of this model associated with DWBC interaction with topography off Cape Hatteras whose realism is unclear. The introduction of the Nordic Seas overflow parameterization greatly reduces the prominence of this variance maximum, but does not eliminate it (Yeager and Danabasoglu, 2012). This behavior is discussed further in the next chapter. The model circulation response does not cleanly split into momentum- and buoyancy-forced perturbations at this location, resulting in a relative minimum/maximum of the M+B correlation and rms distributions (Fig. 3.2). Temporal smoothing with a decadal filter (Fig. 3.2b,d) confirms the visual impression obtained from the Hovmuller diagrams regarding the low frequency AMOC behavior: B largely explains the decadal variability in AMOC north of the equator, while M accounts for most of the decadal variability south of the equator.

The B experiment suggests a southward propagation of AMOC anomalies originating in the high northern latitudes with latitudinally-dependent propagation speeds (Fig. 3.1d). The positive anomalies which emanate from close to 60°N in 1973, 1984, and 1990 correspond to the formation of anomalously dense water in the central Lab Sea in those years (Figs. 2.9, 2.15), while the opposite is true for the negative anomalies identified in 1970 and 1979. The relatively slow propagation between about 45°N-35°N presumably reflects the existence of interior advective

pathways of NADW between Newfoundland and Cape Hatteras, with fast coastal wave processes dominant elsewhere, as discussed in Zhang (2010) who analyzed AMOC in density space from a coupled climate simulation. The conclusions drawn from Fig. 3.1 are not much changed when AMOC strength anomalies from CONTROL, M, and B are computed in density, rather than depth, coordinates (Fig. 3.3). As Zhang (2010) explains, AMOC in density space has a maximum north of 45°N because the strong (horizontal) subpolar gyre circulation, which largely cancels in the zonal integral in depth coordinates, is now tallied as part of the "overturning." It follows that the AMOC variance maximum shifts from subtropical to subpolar latitudes, but we still find that buoyancy forcing accounts for most of the decadal AMOC variability north of the equator (Fig. 3.3). To the extent that AMOC in density space corresponds to horizontal gyre circulation north of about 45°N, it follows from Fig. 3.3 that low frequency variations in the strength of the subpolar gyre circulation are largely buoyancy driven, rather than wind driven, with bottom pressure torque playing a significant role in the barotropic vorticity balance. A vorticity budget of the CONTROL simulation shows that this is indeed the case, as will be demonstrated in the following chapter.

Changes in the large-scale horizontal gyre circulation of CONTROL can likewise be reconstructed quite accurately as the simple linear superposition of momentum- and buoyancy-forced anomalies. The interannual variance of CONTROL BSF, sea surface height (SSH), and upper ocean flow strength is shown in Fig. 3.4, together with the covariances of those CONTROL fields with corresponding anomalies from the M and B simulations. The sum of the covariances is very nearly equal to the total variance in CONTROL (not shown) which supports the linearity of the gyre response to momentum and buoyancy forcing perturbations. Momentum forcing accounts for most of the variance in the depth-integrated and near surface horizontal circulation at subtropical latitudes (south of about 35°N). The 35°N-45°N latitude band appears to be a transition region where both forcing components contribute about equally to the high horizontal flow variability. At higher latitudes (throughout the subpolar gyre and in the GS extension region), buoyancy forcing becomes the dominant contributor to CONTROL variance in SSH and upper ocean flow strength, and in particular, it largely accounts for the variability in the model NAC. On interannual timescales, the

variance in the subpolar gyre BSF is attributable to variations in both momentum and buoyancy forcing (Fig. 3.4), but when time filtering is used to isolate longer (decadal) timescales, the dominance of buoyancy forcing of the SPG barotropic circulation becomes apparent (see next chapter). The time scale dependence of the momentum and buoyancy contributions to horizontal circulation variability can be readily seen in regionally-averaged time series from the western edge of the basin where the gyre flow is strongest (Fig. 3.5). Fluctuations in the BSF and SSH are largely decadal and buoyancy-driven in the SPG, and largely interannual and momentum-driven in the STG. Again, the sum of M and B anomalies nicely reproduces the CONTROL anomalies. Thus, the principal forcing components which drive anomalous gyre circulations are found to vary with latitude and time scale in much the same way as for the overturning circulation (Figs. 3.1, 3.2).

To the extent that low frequency overturning and subpolar gyre circulation variations are both primarily driven by changes in surface buoyancy forcing and associated water mass formation, there may be potential for monitoring and predicting AMOC variations by tracking high latitude gyre circulation indices, as has been suggested by Böning et al. (2006). While those authors find that wind stress contributes significantly to gyre transport and SSH changes in the Lab Sea, which would diminish the usefulness of those fields as easily-observable proxies for Lab Sea deep convection and AMOC, their conclusion was based on the fact that interannual heat flux forcing could not fully explain the variability in those fields in their experiments. In contrast, we find that buoyancy forcing (which includes both heat and freshwater forcing perturbations) accounts for almost all of the interannual variations in SSH in the Lab Sea in our CONTROL experiment, with only a small momentum-forced residual (Figs. 3.4, 3.5), and there is a correspondence between the buoyancy-driven variations in BSF and SSH in the Lab Sea (Fig. 3.5 a,c), and buoyancy-driven AMOC variations, viewed either in depth-space (Fig. 3.1d) or in density-space (Fig. 3.3d). Positive SSH anomalies in the Lab Sea circa 1970 and 1980 (Fig. 3.5c) were associated with weak barotropic cyclonic circulation especially in the western SPG (Fig. 3.5a; note that positive anomalies correspond to weaker cyclonic circulation), and the opposite was true in the early 1970s, mid 1980s, and early 1990s. These SSH and gyre transport anomalies in the Lab Sea correspond to

the development of AMOC anomalies in depth-space which subsequently propagated equatorward (Fig. 3.1d; note the years indicated by black/grey circles). Furthermore, these buoyancy-forced anomalies are all clearly associated with the temperature-driven density anomalies in the central Lab Sea (Fig. 2.10), which we and others have linked to winter NAO variations (Curry and McCartney, 2001; Yashayaev, 2007).

This result suggests that it may indeed be possible to monitor slow, buoyancy-driven AMOC variations by observing Lab Sea SSH changes, with clear potential for advance prediction of slow AMOC change at lower latitudes. In CONTROL, variations in SSH in the central Lab Sea correlate reasonably well ($r > 0.6$) with AMOC strength when the former leads the latter, with the lead time increasing as latitude decreases, consistent with southward propagation of density anomalies (Fig. 3.6). South of about 35°N, the correlation structure becomes more complex, with distinct correlation maxima at lead times of about 5 years and 9 years which may reflect different propagation mechanisms. As expected, the correlation of Lab Sea SSH with AMOC is much stronger in experiment B which does not have the "noise" associated with time-varying momentum forcing. In that experiment, Lab Sea SSH is a strong predictor of AMOC variations at all northern hemisphere latitudes ($r > 0.8$), with the correlation at subtropical latitudes maximized at a lead time of about 4 years. The explanation for the different correlation structures evident in Fig. 3.6, which imply different propagation speeds of density anomalies with and without wind variations, will be explored in future work.

3.3 Identifying the key components of NAO-related forcing

The decadal variability in AMOC north of the equator in CONTROL is primarily due to decadal variation in Lab Sea water properties which are set by large-scale, high latitude atmospheric variations; that is, the atmospheric variability represented by the NAO. This finding is in line with numerous other studies already mentioned which have analyzed the ocean response to NAO. In this section, we seek to further elucidate the most salient aspects of NAO-related forcing by examining the relative roles of various flux components and the roles of local versus non-local forcing of Lab

Sea deep convection.

First, we note that the buoyancy forcing used in experiment B is dependent on the surface wind speed because this term appears in the turbulent fluxes of evaporation and latent and sensible heat flux (Eqn $B.2$). To what extent are NAO-related wind speed variations driving the buoyancy flux variations implicated in the recent decadal circulation changes of the North Atlantic? To answer this question, we have run an experiment B* (not listed in Table $B.1$) which is equivalent to B except that NYF wind speed is used in the computation of all turbulent fluxes (e.g., $\boldsymbol{Q_E} = \boldsymbol{Q_E}(\boldsymbol{\rho}, \boldsymbol{\Delta q}, |\Delta\vec{U}|)$, etc). The resulting AMOC signal (in depth-space, Fig. 3.7a) shows only minor differences from the experiment with full variability in buoyancy fluxes (compare to Fig. 3.1d). We conclude that NAO-related wind speed variations are relatively unimportant as drivers of the decadal AMOC signals of interest. This is in line with the findings of Seager et al. (2000) who conclude that north of 40°N, the impact of wind speed variations on the turbulent heat fluxes is considerably less than the impact of wind direction changes (the latter being most associated with changes in the advection of temperature and moisture).

Both heat and freshwater fluxes would appear to be important contributors to the buoyancy-forced variability in CONTROL. As expected given the nonlinearity of the equation of state, splitting the buoyancy forcing into separate thermal and haline components in experiments B.Q and B.F, respectively, results in AMOC anomaly signals whose sum is weaker than in the total response from experiment B (Fig. 3.7; compare Fig. 3.7c to Fig. 3.1d). Nevertheless, the correspondence is sufficient to draw some conclusions from this decomposition. Changes in heat and freshwater forcing in the high latitude North Atlantic are about equally important in driving slow changes in ocean dynamics and there tends to be constructive interference of thermal- and haline-forced signals such that the strength of AMOC anomalies in B is quite a bit larger than those in either B.Q or B.F individually. This suggests a particularly important role for evaporation which drives same-signed contributions to density in both the temperature and salinity equations. The low frequency decadal variability in B seems most associated with the freshwater forcing of B.F (Fig. 3.7d), while the episodic generation of high latitude AMOC anomalies in certain years (i.e., those

identified in Fig. 3.1d) seem to be associated with the time-varying heat fluxes of B.Q (Fig. 3.7b).

Experiments B.1 and B.2 are designed to hone in further on the most important components of high latitude buoyancy forcing. All of the essential characteristics of low frequency AMOC variability from experiment B are captured in B.1, which uses interannually-varying forcing only for the turbulent buoyancy fluxes (Fig. 3.8a). The B.1 anomalies are somewhat larger than in B, implying that variability in the other heat and freshwater fluxes (P, R, Q_S, Q_L) tend to damp the Lab Sea density variations induced by evaporation and the latent and sensible heat fluxes. The correspondence between B.1 and B also demonstrates that the use of climatological precipitation and downward radiation fluxes prior to 1979 and 1984 does not significantly effect the variability simulated in B; these are relatively inconsequential fluxes compared to E, Q_E, and Q_H for driving large scale circulation variations. Experiment B.2 is identical to B.1 except that flux variability is confined to the Lab Sea box region, with NYF applied elsewhere. Most of the aforementioned variability features are still evident in the AMOC anomaly time series (Fig. 3.8b), but with somewhat reduced amplitude. The reduced amplitude is not surprising, given that NAO correlates with LSW formation in the Irminger Sea and central SPG (Fig. 2.8). Comparing B.1 and B.2 (or B.1 and B) gives a sense of the impact of local, turbulent flux forcing of water mass transformation and deep convection with and without the "preconditioning" of Lab Sea waters by surface forcing variations over the larger Atlantic basin. The preconditioning is presumably mainly associated with surface formation in nearby regions which tends to enhance Lab Sea water mass anomalies, but we find this to be a second order effect compared to local buoyancy forcing variations over the Lab Sea region. We conclude that most of the decadal variability in AMOC over the last half of the 20th century can be traced to variations in the turbulent heat and freshwater forcing over the Lab Sea alone.

3.4 The role of Southern Ocean Winds

We now turn to the question of the relative role of Southern Ocean (SO) wind variability on low frequency AMOC changes in the recent past. The trend in the Southern Annular Mode

(SAM) over the last few decades of the 20th century (Thompson and Solomon, 2002) is present in the NCEP/NCAR reanalysis surface winds used in CORE-II, and it can clearly be seen in a hovmuller plot of the zonally-averaged zonal wind stress which drives the CONTROL simulation (Fig. 3.9). The positive wind stress trend is most pronounced poleward of 40°S in the region of the Antarctic Circumpolar Current (ACC). The hypothesis that SO wind variations may have a controlling influence on rates of overturning in the Atlantic has been explored in numerous recent studies, with mixed results (e.g., Delworth and Zeng, 2008; Klinger and Cruz, 2009; Sijp and England, 2009; Farneti and Delworth, 2010; Wolfe and Cessi, 2010; Lee et al., 2011). The impact of SO wind variations appears to depend critically on the fidelity of the model representation of mesoscale eddies (Farneti and Delworth, 2010; Farneti and Gent, 2011; Gent and Danabasoglu, 2011), which contributes to the diversity of sensitivities found in the literature. In particular, the use of a constant coefficient in the ocean eddy parameterization induces a too strong response in the Northern Hemisphere AMOC to changes in Southern Ocean winds. Another potential source of confusion, however, is that studies focused on SO effects often employ idealized models and rarely place the results in context by comparing to AMOC variability resulting from realistic high latitude Northern Hemisphere buoyancy flux variations.

As noted in the discussion of Figs. 3.1 and 3.2, momentum forcing accounts for most of the AMOC variance south of about 30°N, and most of the decadal variance south of the Equator. Experiment M.SO looks specifically at the non-local impacts of the trend in Southern Ocean wind stress, with interannual variations in atmospheric surface winds applied only south of 35°S. The effect of this forcing is clearly discernible on AMOC north of 30°S, with northward propagating anomalies reflecting the sign of the SO zonal wind stress anomalies (Fig. 3.8d). This signal explains a large fraction of the low frequency variability in M south of the Equator which in turn dominates the decadal variability in CONTROL at those latitudes. However, the signal is greatly attenuated north of the Equator and is far weaker than buoyancy-driven AMOC signals north of about 20°N. It is interesting to note that the positive AMOC trend induced by SO wind forcing is more or less coherent with the positive trend induced by Lab Sea buoyancy forcing over all latitudes south

of about 20°N; we return to this point in the discussion. We conclude that the recent decadal variations in SO wind forcing were much less important than NAO-related buoyancy forcing in driving recent changes in the North Atlantic AMOC, but that south of the Equator (and certainly at 30°S), SO wind variations were at least as important as SPG buoyancy forcing in driving decadal AMOC variability.

3.5 The origins of Lab Sea flux variability

We have shown with experiment B.2 that most of the decadal AMOC variability in the North Atlantic between 1958 and 2007 can be traced to turbulent fluxes of heat and freshwater in the Lab Sea. An examination of the fluxes in this region offers further clues about the origin of the decadal time scale of AMOC in CONTROL. We are interested in the relative impacts on surface buoyancy of the various flux components, and so we have converted monthly Q_{as} and F_{as} terms to surface buoyancy fluxes following Large and Nurser (2001). Year-to-year variations in wintertime (January through March mean) air-sea buoyancy flux in the Lab Sea Box region are clearly dominated by changes in sensible heat loss, with changes in the latent heat loss contributing significantly as well (Fig. 3.10). Changes in surface freshwater flux, which impact SSD by altering SSS, are less significant in this region, but evaporation is found to be the third most important contributor to the interannual changes in the net surface buoyancy flux. It is important to note that precipitation variability is lacking prior to 1979 and there is no representation of the potentially significant Greenland glacier melt in the CORE-II forcings. In the vicinity of the sea ice edge, ice-ocean freshwater fluxes (in particular, buoyancy fluxes related to ice melt) dominate the buoyancy flux (e.g., Yeager and Jochum, 2009), but our focus here is on the factors which influence deep convection in the open ocean of the Lab Sea, away from the sharp halocline near the ice edge. We find that, to first order, variations in deep convection result from changes in the net local air-sea buoyancy flux (B_{as}; Fig. 3.10c): episodes of intense Lab Sea mixing were contemporaneous with anomalously strong buoyancy loss from the surface.

Because anomalous evaporation is always accompanied by anomalous latent cooling, the E

and Q_E fluxes are perfectly correlated in terms of their contributions to the net surface buoyancy flux; furthermore, anomalies of Q_H over the Lab Sea are highly correlated with the evaporative buoyancy fluxes (Fig. 3.10b). The high correlation between Q_E and Q_H follows from the Clausius-Clapeyron relation: anomalously cold air is anomalously dry, and vice versa. The three turbulent buoyancy fluxes thus work in tandem to generate large surface diapycnal volume flux anomalies which explain much of the simulated variability in SSD and MLD in the Lab Sea (Fig. 3.10c). Of course, to fully account for variations in Lab Sea SSD and MLD, one must take into account the subsurface processes which set the deep density structure, but we find that the gross features of MLD variability in our CONTROL hindcast are largely dictated by local B_{as} variations. This is in agreement with our findings from experiment B.2. The negative AMOC anomalies which originated circa 1970 and 1979 (Fig. 3.1d) can be traced to negative MLD and SSD anomalies in the Lab Sea following winters of particularly weak surface density forcing due to weaker than normal surface heat loss. The three positive AMOC anomalies which originated circa 1973, 1984, and 1990 (Fig. 3.1d) can be traced to positive MLD and SSD anomalies which apparently resulted from strong surface density transformation during cold, dry air outbreaks in winter months of those years. As we showed in Figure 2.10, winter storm events can generate huge volumes of LSW on the order of days to weeks, and so we interpret the Lab Sea MLD maxima as a reflection of intense storm forcing during high NAO winters. While we cannot rule out the possibility that model error may contribute to the dominance of air-sea forcing of convection in this region, especially given the role that unresolved eddies might be expected to play in mixing buoyant shelf waters into the Lab Sea interior (Danabasoglu et al., 2012b), the correspondence of the flux time series of Fig. 3.10 with both the simulated and observed temperature and density profiles in the central Lab Sea (Fig. 2.15) and with the CORE-II WMF and NAO time series (Fig. 2.9) should be noted.

The turbulent buoyancy fluxes are functions of both the atmospheric and oceanic states (Eqn $B.2$), but the interannual variability of winter E, Q_E, and Q_H over the Lab Sea, and thus the variability in B_{as}, is almost entirely driven by changes in atmospheric surface temperature (θ) and humidity (q). The correlations of seasonal- and regionally-averaged θ and q with B_{as} over the Lab

Sea are 0.92 and 0.93, respectively (Fig. 3.11). Low-pass filtering of these time series reveals that a pronounced downward trend in buoyancy flux (i.e., upward trend in density flux) into the surface ocean between the early 1960s and mid 1990s was driven by corresponding trends in atmospheric temperature and humidity over this region (Fig. 3.11b). The slowly changing atmospheric state induced trends in net heat and freshwater fluxes into the Lab Sea region which tended to increase SSD by decreasing SST and increasing SSS over multiple decades in the late twentieth century. We conclude that the ultimate source of the enhanced AMOC in the late 1980s and 1990s in CONTROL is the multidecadal trend towards colder and drier atmospheric conditions over the Lab Sea in winter.

3.6 Discussion

We have explored the forcing contributions to decadal variations in the large-scale overturning and gyre circulations in a CORE-II coupled ocean–sea-ice hindcast simulation run with the latest version of the CESM1. As shown in Chapter 2 and in Yeager et al. (2012), there are many quite realistic features of the mean and variability of this CONTROL solution which support its use as a tool to study mechanisms of ocean variability in the recent past. There are also many known (and no doubt unknown) inadequacies of the model which will necessarily qualify any conclusions drawn from it.

First, mesoscale eddies are parameterized in the model, and while the parameterization used is state-of-the-art (Danabasoglu et al., 2012a), the Lab Sea and Southern Ocean are two regions which are particularly sensitive to the representation of eddies (Chanut et al., 2008; Farneti and Gent, 2011; Danabasoglu et al., 2012b). A CORE-II simulation using the eddy-resolving version of CESM1 is planned, but not available at this time for comparison with CONTROL. The studies by Farneti et al. (2010) and Farneti and Delworth (2010) suggest that, if anything, our model underestimates the eddy-induced overturning response to SO wind increase, and thus overestimates the SO wind impact on AMOC. Another caveat related to model resolution is the perennial issue of a poor North Atlantic Current (NAC) representation which could prolong the time scale of AMOC

variability by eliminating the relatively quick advective feedback of warm/salty/buoyant NAC water into the central Lab Sea following intense convection and gyre spinup. Work is underway to assess the impacts of this bias on model variability. We speculate that this may explain some of the discrepancy with the observed AMV pattern (Fig. 2.16) and with the observed temperature and density anomalies in the central Lab Sea, particularly in the mid-1980s (Fig. 2.15). However, the general agreement between model and observations in this region gives us confidence that model shortcomings are not catastrophic.

Another important caveat pertains to the underestimation of mean and variability of simulated sea ice coverage in the Lab Sea (Figs. 2.13, 2.14). This results in reduced insulation of ocean surface waters from the extremely cold, dry Arctic air, and therefore greatly increases the buoyancy flux out of the ocean. In previous CCSM hindcasts which had a more severe sea ice bias in the Lab Sea, this resulted in excessive surface water mass transformation and an overly strong AMOC mean and variance (Yeager and Jochum, 2009). The fact that CONTROL shows an excellent match to the observed AMOC strength at 26.5°N (Fig. 2.12b) suggests that the sea ice bias in the Lab Sea may be tolerable.

The finding that historical AMOC variability in the North Atlantic can be quite cleanly split into momentum- and buoyancy-forced components which are characterized predominately by interannual and decadal time scales, respectively, with the latter associated with NAO-driven deep convection in the Lab Sea is in line with previous work done with a variety of models (Eden and Willebrand (2001), Böning et al. (2006), Biastoch et al. (2008), and Robson et al. (2012a)). In this study, we have further investigated the spatial dependence of AMOC and gyre circulation variability on surface forcing constituents and find that buoyancy forcing is the dominant driver of decadal AMOC variability north of the Equator and of horizontal gyre variability north of about 40°N. Given that most of the variance in the high latitude gyre and AMOC circulations derive from this common forcing, we have explored the potential for monitoring AMOC using Lab SSH variations as a proxy for the strength of the thermohaline circulation. Going beyond the buoyancy/momentum decomposition, the forcing perturbation technique has been used here to

systematically assess the relative impacts on AMOC of heat and freshwater forcing, wind speed variations, the trend in Southern Ocean zonal winds, turbulent buoyancy fluxes, and Lab Sea atmospheric conditions. The fidelity of our results is supported by the good correspondence of our CONTROL with available observations and by the fact that, in contrast to the previous studies cited, our model includes a parameterization for Nordic Seas overflows which is known to impact AMOC variability (Danabasoglu et al., 2010; Yeager and Danabasoglu, 2012). Furthermore, our use of NYF allows us to filter the power spectrum of forcing fields more effectively than doing simple time-averaging to construct climatological forcing; with NYF, mean variance at annual and higher frequencies is retained.

The analysis has led us to the following conclusions:

- High northern latitude buoyancy-forcing accounts for almost all of the decadal variability in AMOC and subpolar gyre strength over the period 1958-2007, including the positive trend in North Atlantic overturning and gyre strength in the 1980s and 90s which contributed to the large SST increase north of 45°N.

- Both heat and freshwater forcing play important roles in driving recent decadal AMOC changes, and in particular the turbulent buoyancy fluxes (evaporation and sensible and latent heat flux) account for almost all of the buoyancy-driven variability.

- Variations of atmospheric surface temperature and humidity over the Lab Sea region drive the variations in turbulent winter buoyancy loss; in turn, these local surface buoyancy fluxes largely determine the variations in SSD, deep convection, and water mass characteristics which ultimately drive the decadal component of AMOC variability. The preconditioning of Lab Sea water by surface forcing outside of the Lab Sea and the influence of wind speed on the turbulent buoyancy fluxes both appear to be second order effects.

- While NAO-related buoyancy forcing is the dominant driver of decadal AMOC variability north of the Equator, momentum forcing is implicated in the slow variability further south

in the Atlantic. Much of the increasing trend in AMOC in the Southern Hemisphere is related to observed trends in Southern Ocean westerly winds.

- Lab Sea SSH changes are largely buoyancy-driven, and thus may be an excellent proxy for monitoring slow AMOC variations.

The ultimate source of most of the decadal AMOC variability in this and other CORE-II simulations appears to be low frequency atmospheric variability associated with the trend in the winter NAO. The downward trend in winter surface air temperature and humidity over the Lab Sea region, in particular, between 1960 and 1990 (Fig. 3.11b) clearly has huge ramifications for ocean dynamics. We argued in Chapter 2 that CORE-II air-sea fluxes bolster the case that the slow variations in SST associated with the AMV result in NAO persistence (Figs. 2.2, 2.3). But, the nature and origins of low-frequency spectral power in NAO remains a subject of ongoing research, with both external forcing and atmosphere-ocean coupling likely playing a role (e.g., Woollings et al., 2012). If anthropogenic forcing of the climate system is most important, it raises the question of why CGCM simulations of the 20th century generally lack the pronounced increase in buoyancy forcing in the Lab Sea which drove the recent AMOC increase. The CONTROL experiment is not coupled and so it only provides information about the oceanic response to atmospheric trends. The "coupling" of the prognostic model SST with the rigid CORE-II meteorology results in a skewed relationship between SST and Q_{as} (Fig. 3.12; compare to Fig. 2.2). This is a very high bar for evaluating the forced CONTROL simulation. Interpreted simply, it indicates that, despite the many successes of the model hindcast, it is not quite getting SST right for the right (coupled) reasons. Further model development and a deeper understanding of model behavior are needed. In the next chapter, we contribute to the understanding of model circulation dynamics.

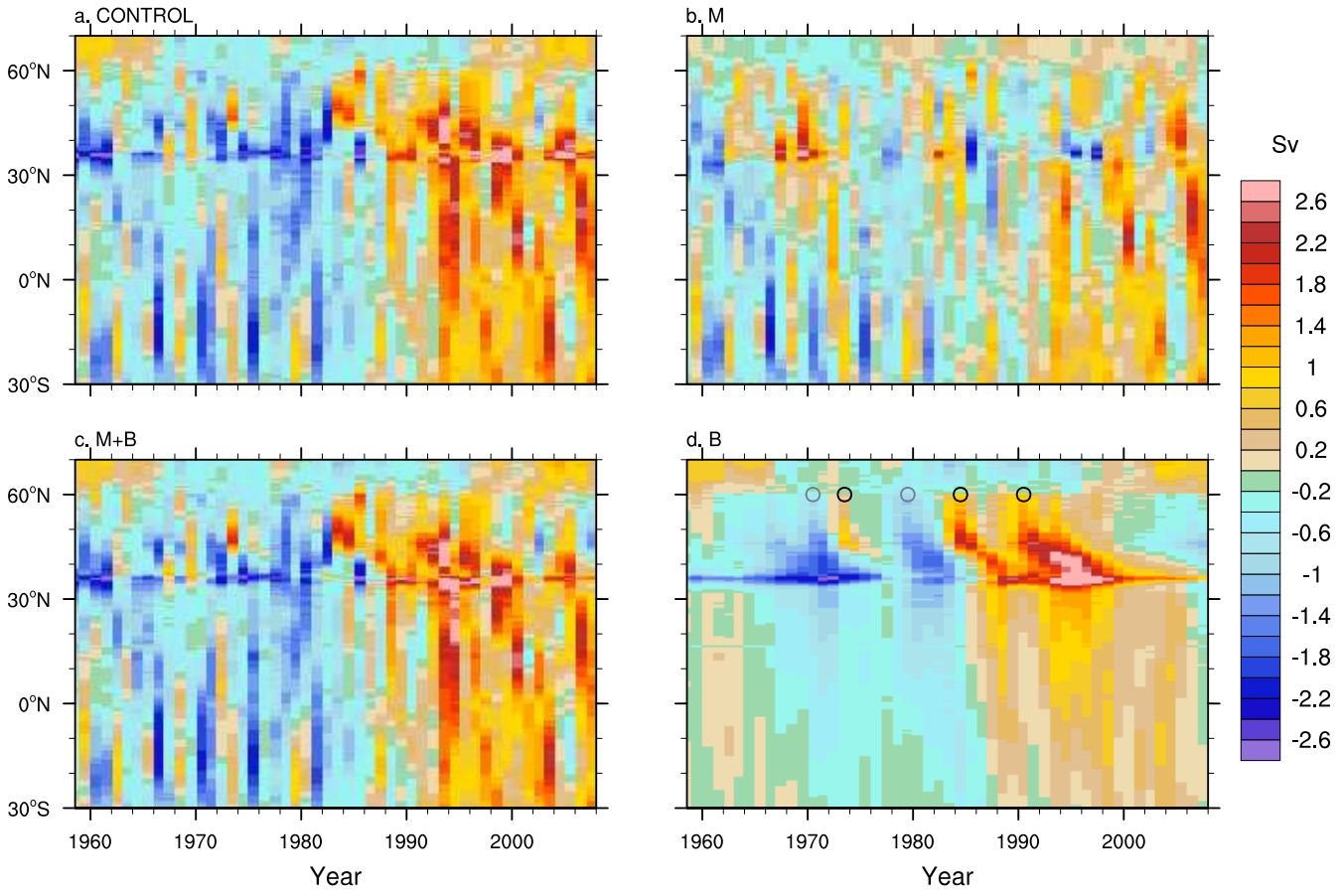

Figure 3.1: Figure 6 from Yeager and Danabasoglu (2013). Hovmuller diagrams of annual AMOC strength anomaly (Sv) as a function of latitude and time from (a) the CONTROL simulation, (b) experiment M, (c) M+B (the sum of anomalies from these experiments), and (d) experiment B. No smoothing has been applied, either in the processing or the plotting. Black/grey circles in panel (d) indicate the approximate origins of positive/negative AMOC anomalies referred to in the text.

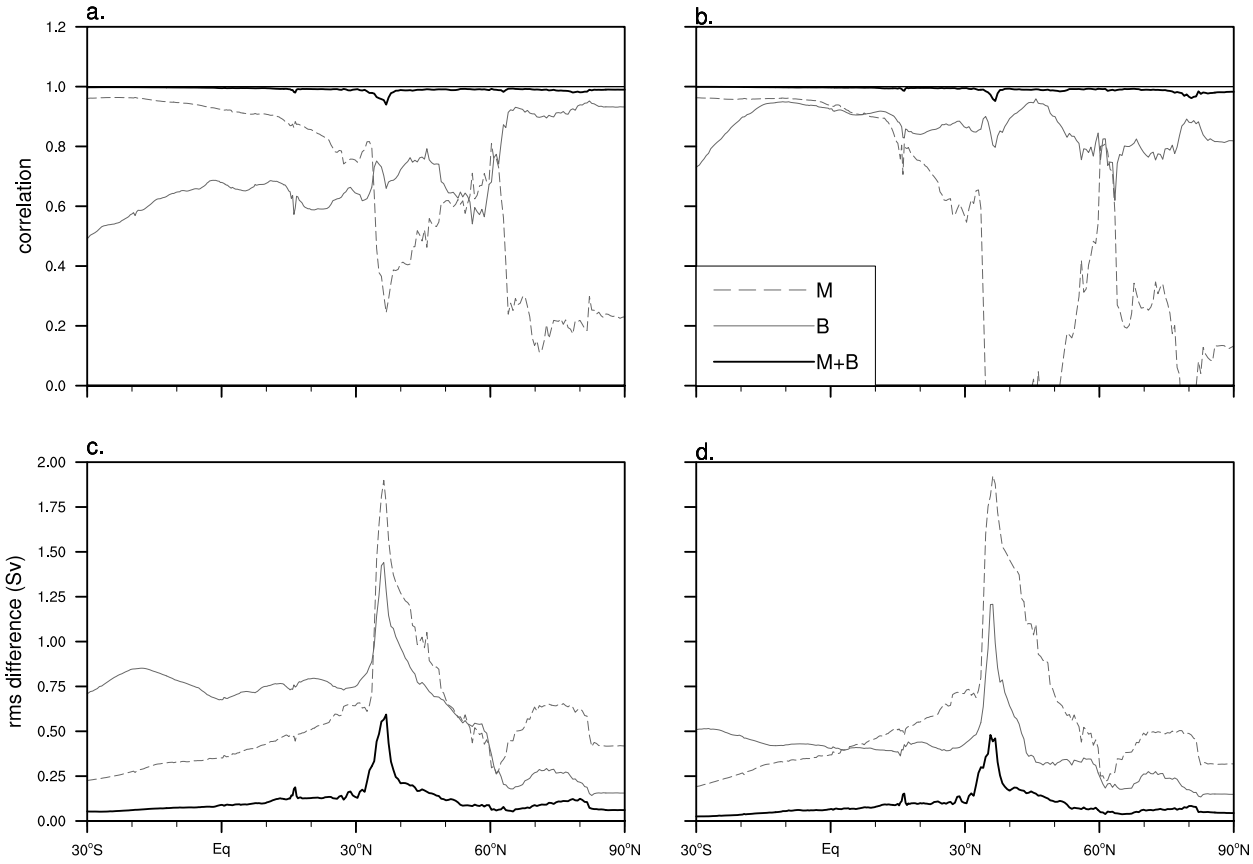

Figure 3.2: Figure 7 from Yeager and Danabasoglu (2013). Comparisons with CONTROL of annual mean AMOC strength as a function of latitude from experiments M and B as well as the sum of their anomalies (M+B), computed from (a),(c) raw annual mean time series, and (b),(d) low-pass filtered time series. Temporal correlations are plotted in (a),(b) and root mean square differences from CONTROL in (c),(d). A 15-point lanczos filter with cutoff period of 7 years is used for the plots on the right.

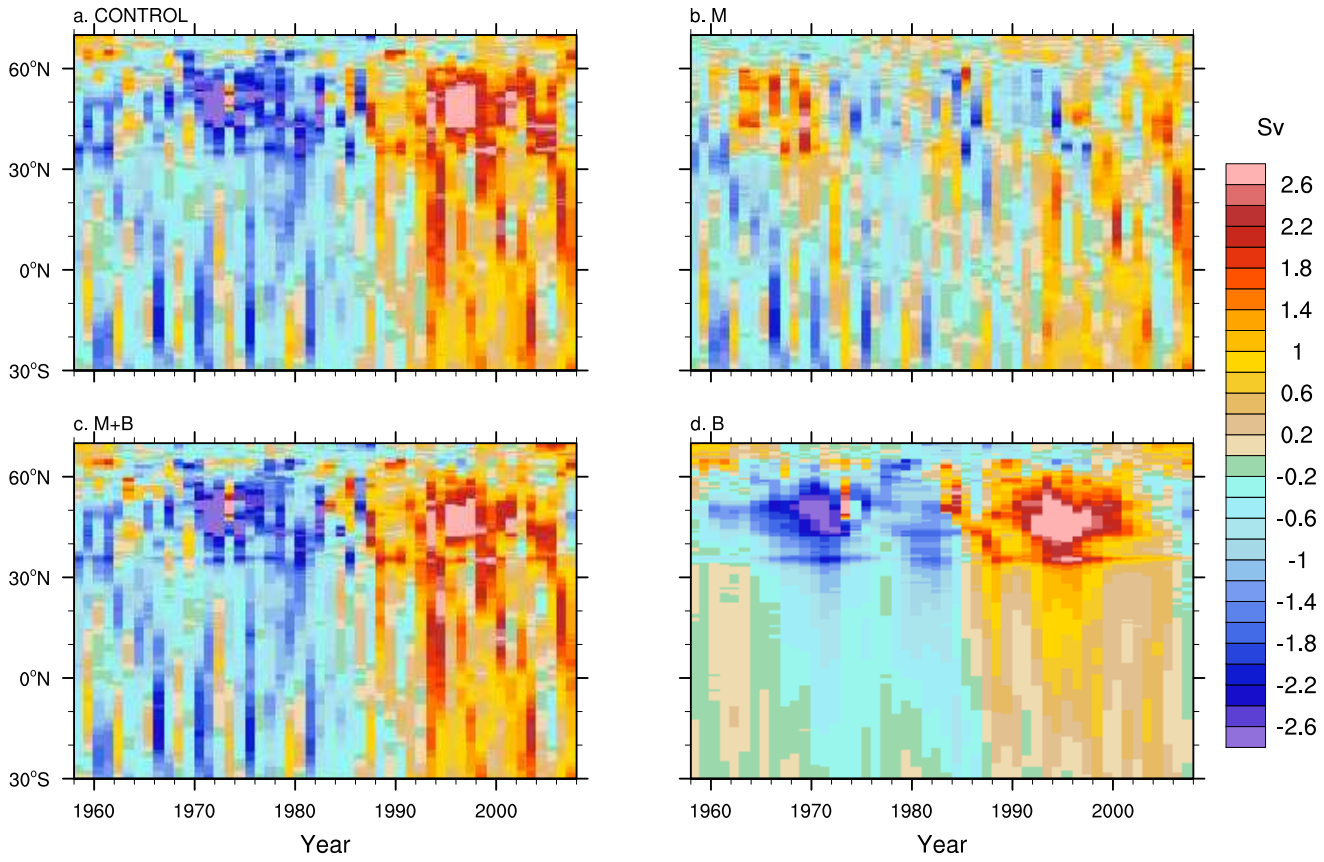

Figure 3.3: Figure 8 from Yeager and Danabasoglu (2013). Same as Figure 3.1, except for AMOC computed in density (σ_2) space, such that the AMOC strength at each latitude is calculated as the maximum in density rather than depth prior to the anomaly calculation.

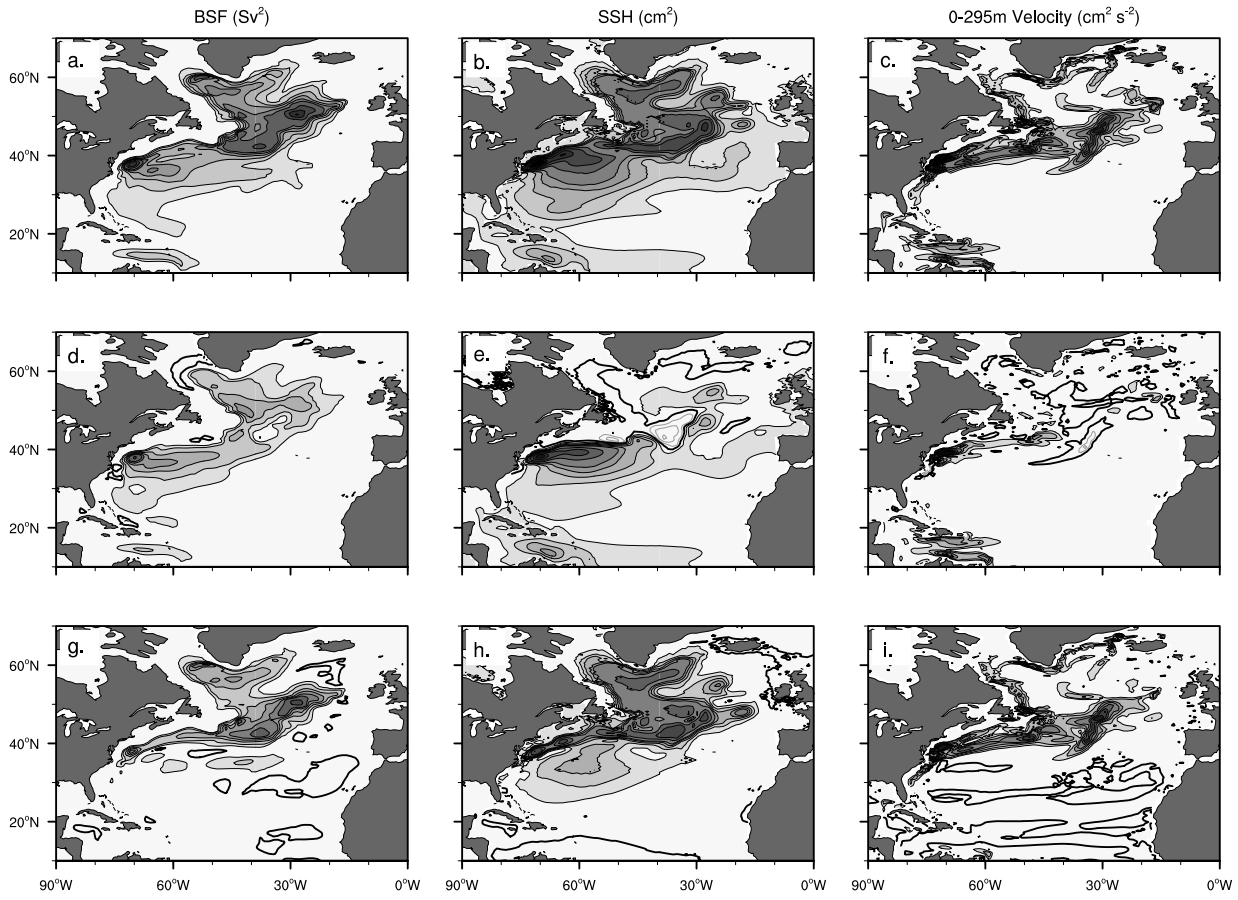

Figure 3.4: Figure 9 from Yeager and Danabasoglu (2013). Variance of annual mean time series from CONTROL of (a) barotropic streamfunction (BSF), (b) sea surface height (SSH), and (c) depth-averaged upper ocean (0-295 m) current speed. The remaining panels show the covariances of the same fields (by column) between M and CONTROL (panels d-f) and between B and CONTROL (panels g-i). To a very good approximation, the sum of covariances plotted in the second and third rows equals the total variance from CONTROL plotted in the first row. The contour levels are as follows: BSF (0,1,2,4,6,8,10,15,20,25,30 Sv^2); SSH (0,2,4,6,8,10,15,20,30,40,50 cm^2); velocity (0,0.5,1,2,3,5,7,10,15 cm^2 s^{-2}). Values are shaded above the first non-zero contour.

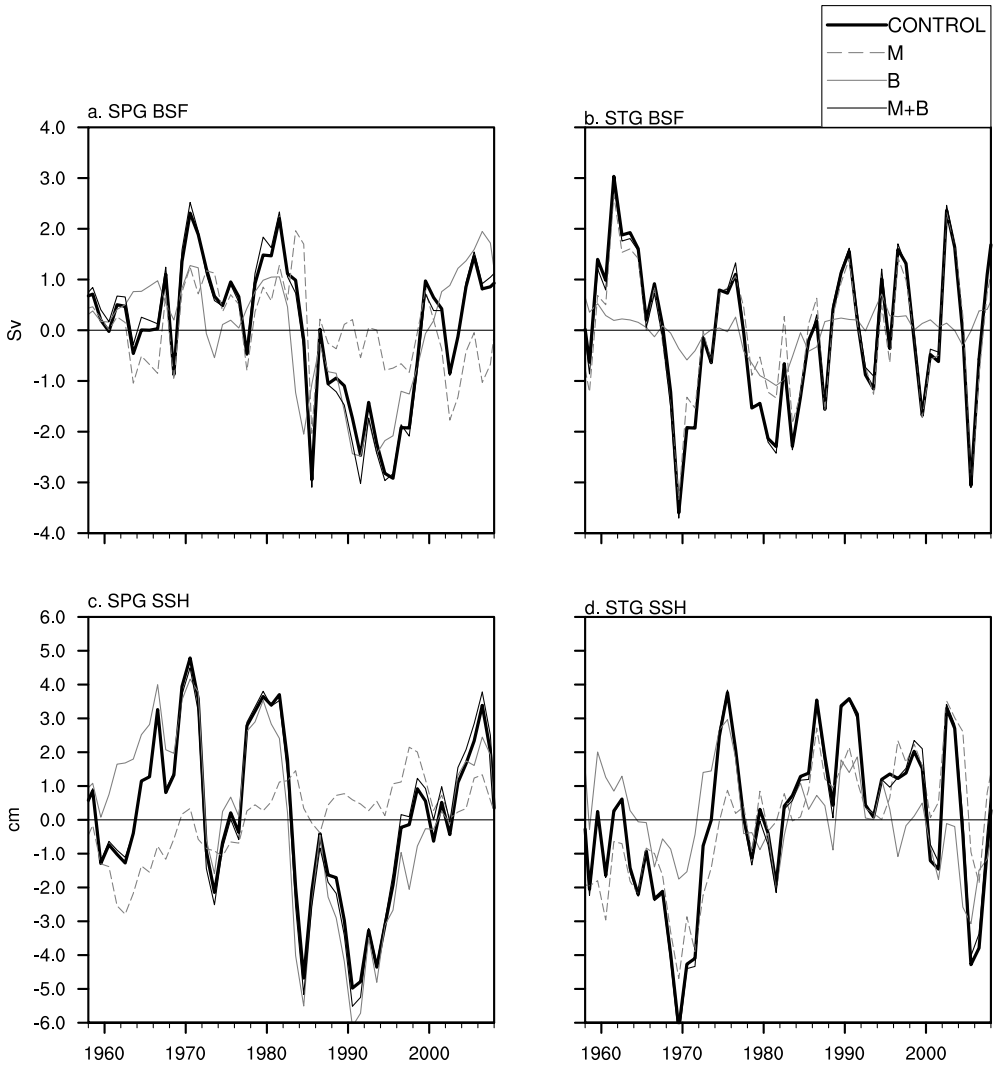

Figure 3.5: Figure 10 from Yeager and Danabasoglu (2013). Annual mean time series of regionally-averaged barotropic streamfunction (BSF) and sea surface height (SSH) anomalies from CONTROL, M, B, and the sum of anomalies M+B. The subpolar gyre (SPG) region is the same as the Lab Sea Box (see Fig. 2.6); the subtropical gyre (STG) region is defined as 80°W-65°W; 26°N-38°N. No smoothing has been applied.

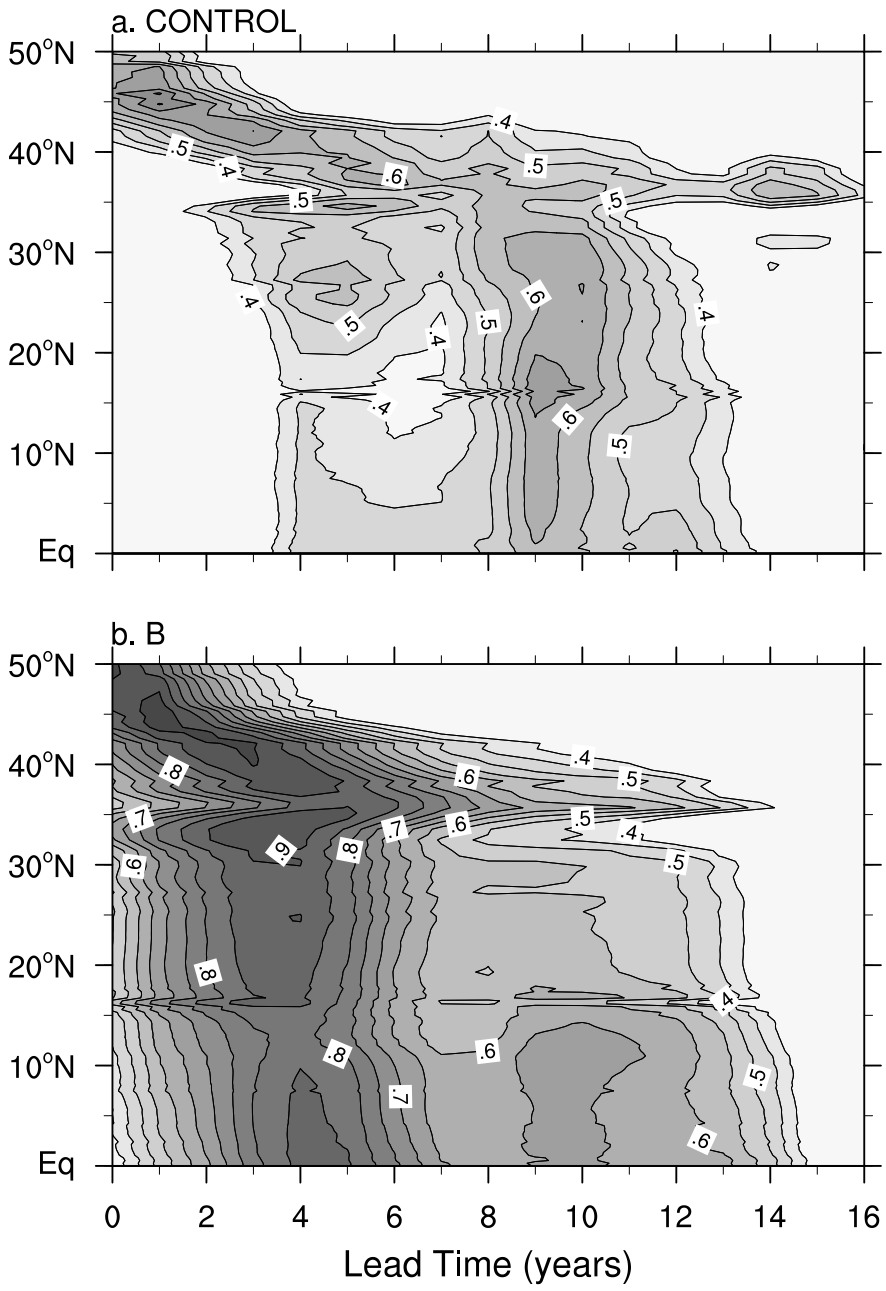

Figure 3.6: Figure 11 from Yeager and Danabasoglu (2013). Lag correlations as a function of latitude of annual mean Lab Sea SSH (regionally-averaged within the box 55°W-50°W; 55°N-60°N) with AMOC strength (computed as the maximum in depth) from (a) CONTROL, and (b) experiment B. No time-filtering has been used. Lead time is positive when Lab SSH precedes AMOC. The contour interval is 0.05 and values below 0.4 are not plotted.

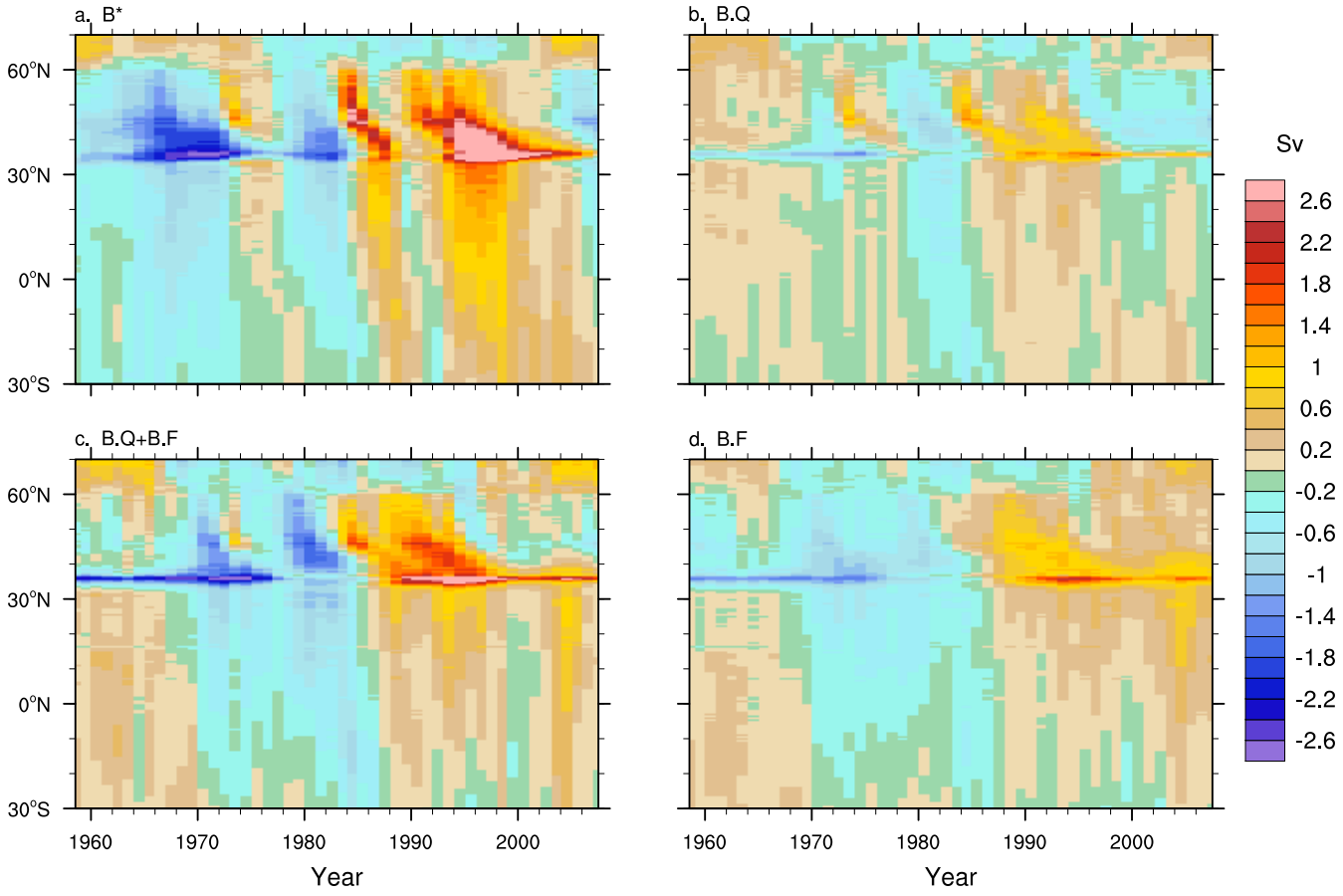

Figure 3.7: Figure 12 from Yeager and Danabasoglu (2013). Same as Figure 3.1, except for (a) experiment B*, (b) experiment B.Q, (c) B.F+B.Q (the sum of anomalies from these experiments), and (d) experiment B.F. Experiment B* is identical to B, except that normal year winds are used for the computation of all turbulent fluxes (see text).

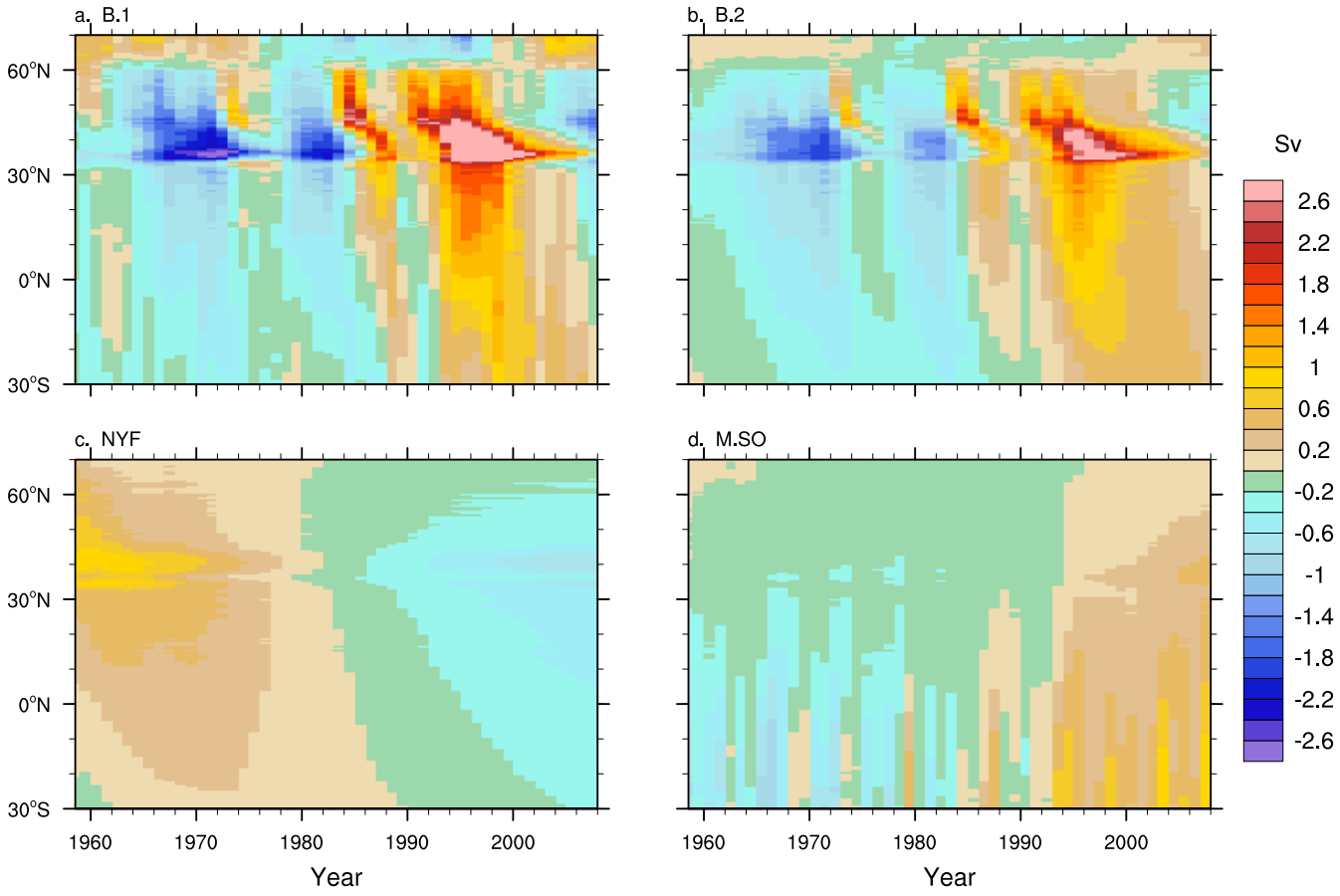

Figure 3.8: Figure 13 from Yeager and Danabasoglu (2013). Same as Figure 3.1, except for (a) experiment B.1, (b) experiment B.2, (c) experiment NYF, and (d) experiment M.SO.

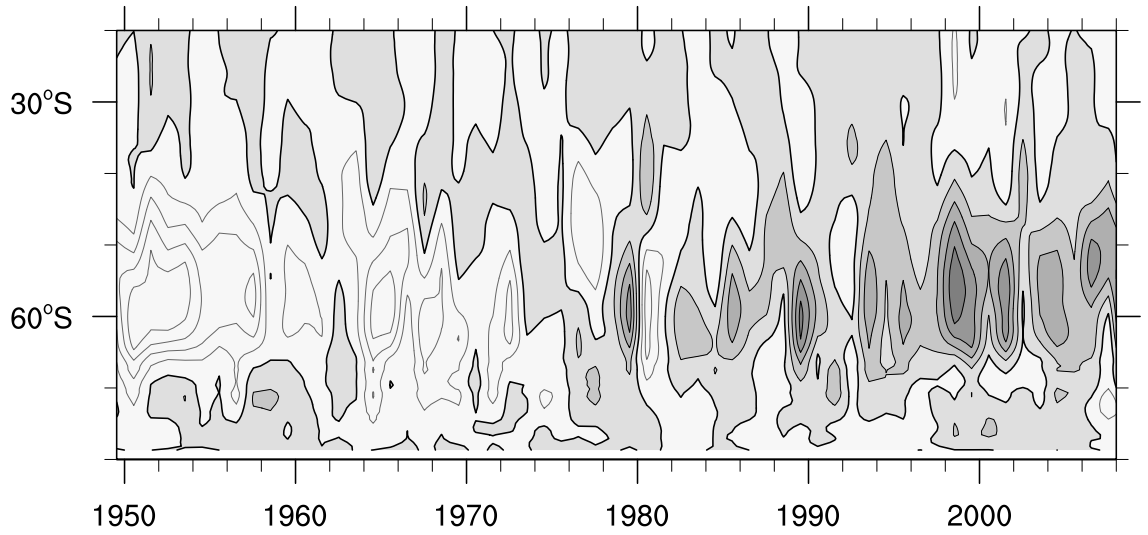

Figure 3.9: Figure 14 from Yeager and Danabasoglu (2013). Anomalous annual mean zonally-averaged zonal wind stress (τ_x) in the Southern Hemisphere from CONTROL. Units are N m^{-2} and the contour interval is 0.01 with positive/negative anomalies contoured in black/grey with grey shading for positive values.

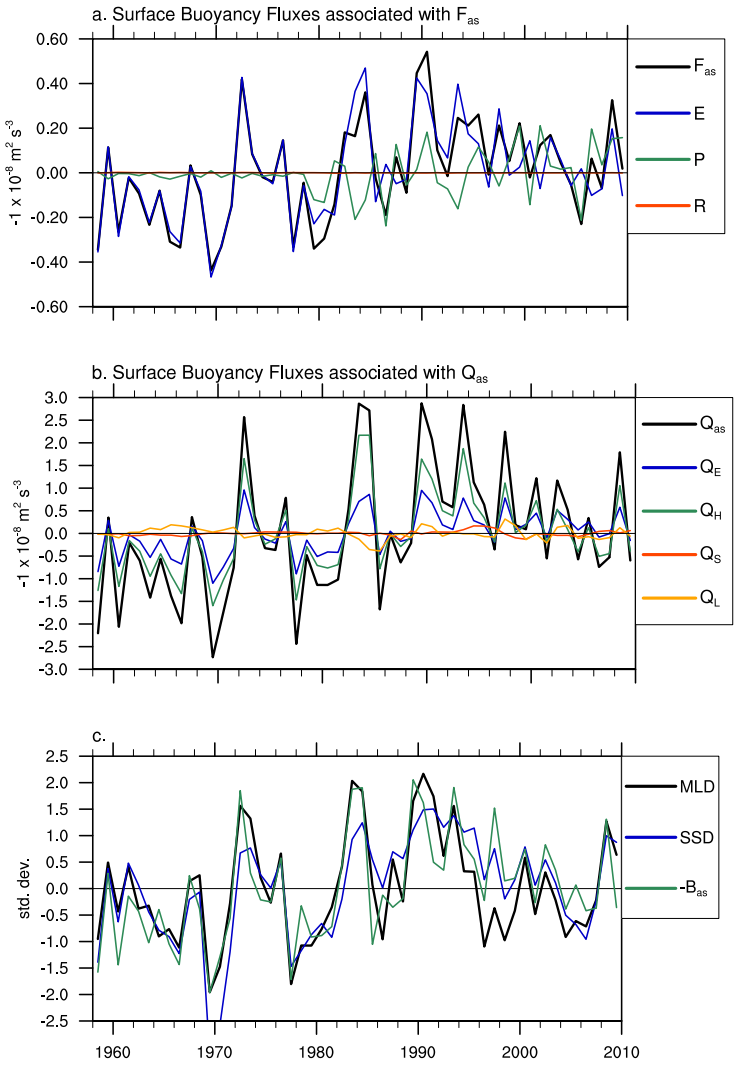

Figure 3.10: Figure 15 from Yeager and Danabasoglu (2013). Anomaly time series of winter fields from CONTROL regionally-averaged over the Lab Sea Box region: (a) JFM-mean net air-sea freshwater flux and components converted into surface buoyancy fluxes (-1 x 10^{-8} m^2 s^{-3}), (b) same as (a) but for JFM-mean net air-sea heat flux and components, and (c) March mean MLD, March mean sea surface density (SSD), and JFM-mean net surface buoyancy flux (-B_{as}; the sum of heat and freshwater components). All fields are averaged over the ice-free ocean as determined by the March mean ice fraction. Panel (c) is plotted in units of standard deviation of the respective time series. The anomalies are relative to the 1958-2007 time-average. Buoyancy fluxes are multiplied by -1 so that positive values indicate buoyancy loss from the surface ocean.

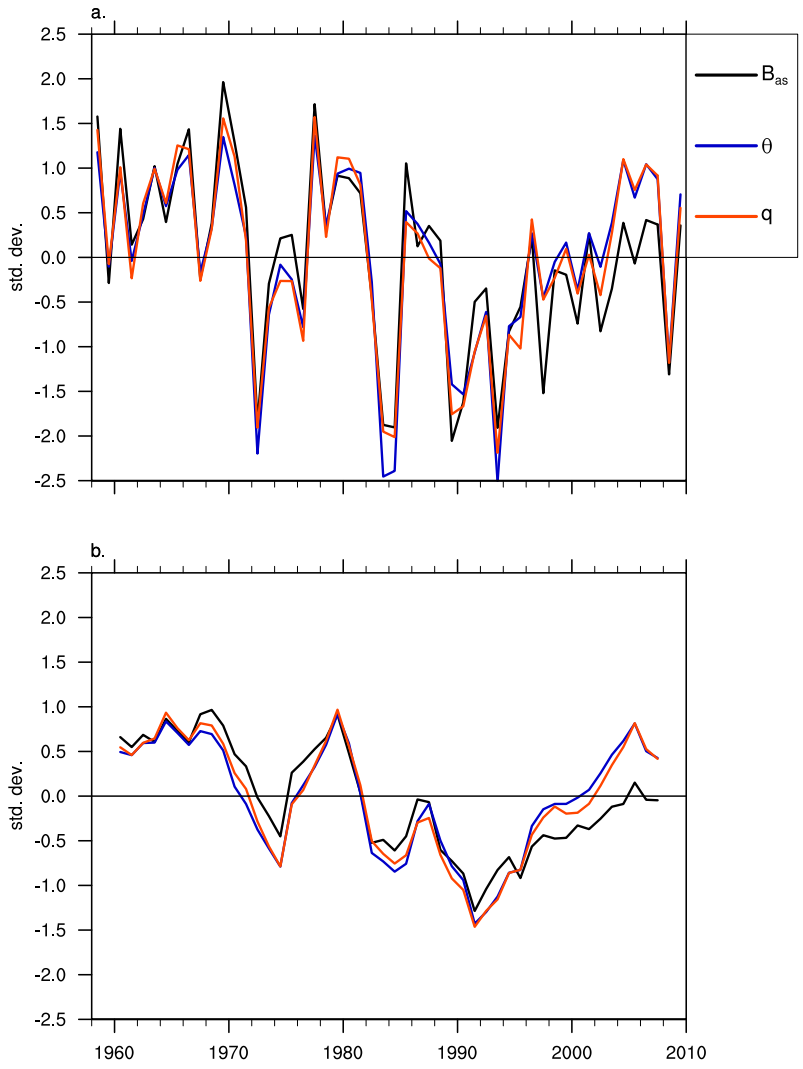

Figure 3.11: Figure 16 from Yeager and Danabasoglu (2013). Anomaly time series of JFM-mean fields from CONTROL regionally-averaged over the Lab Sea Box region: (a) the 10m atmospheric potential temperature (θ) and specific humidity (q) together with the net surface buoyancy flux (this differs from the curve in Figure 3.10c by a factor of -1); (b) identical to (a), but after smoothing with running 5-year boxcar filter. All curves are normalized by the standard deviations of the respective unfiltered time series. The regional averages of θ and q are computed over the entire Lab Sea Box region.

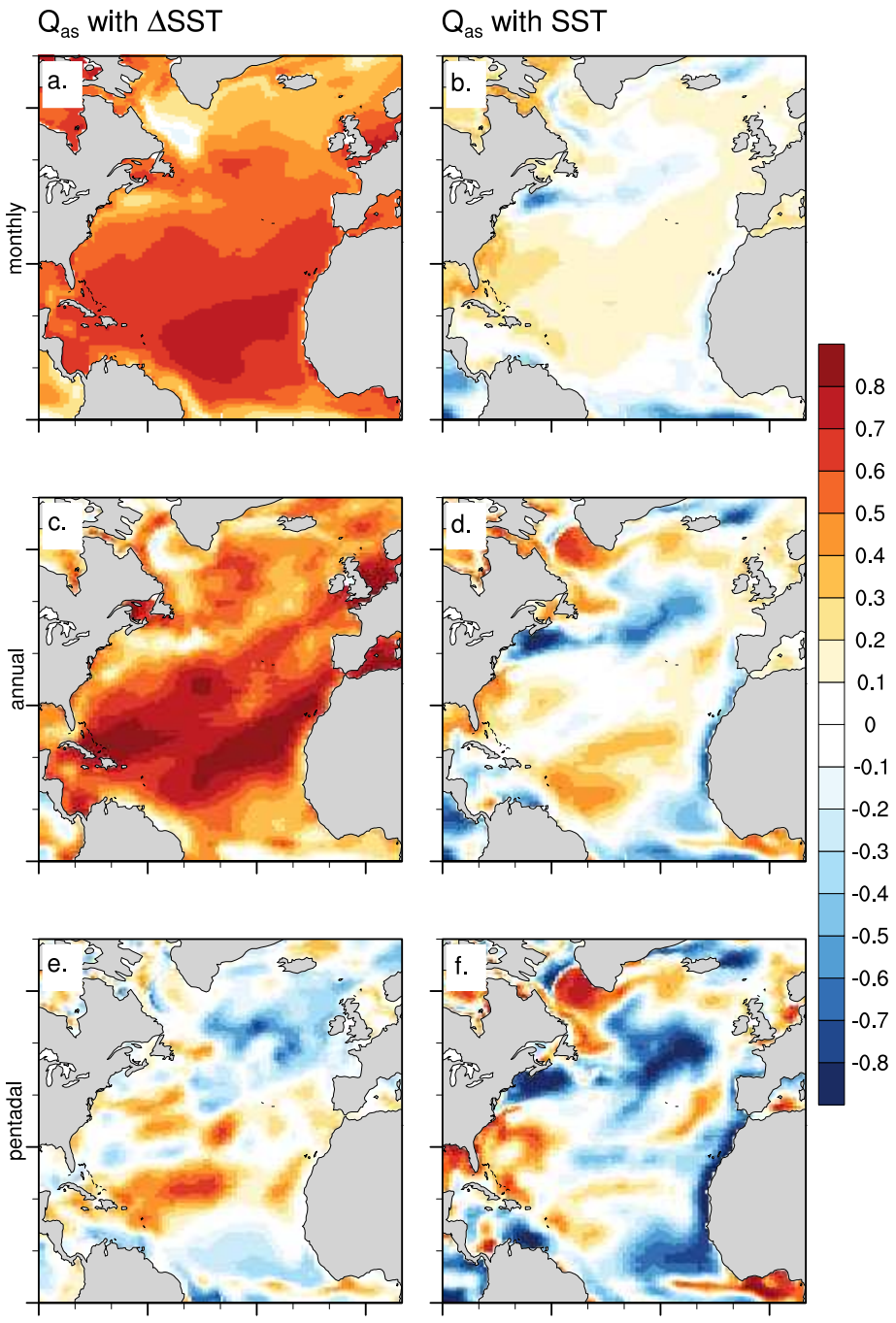

Figure 3.12: As in Figure 2.2, but computed from CONTROL SST and Q_{as}.

Chapter 4

The dynamics of large-scale circulation in the Atlantic

In this chapter, we seek a deeper understanding of the dynamical balances which underpin the mean large scale circulation of the POP ocean model and how those balances change as a result of surface forcing perturbations, reflecting (and driving) temporal variations in the overturning and gyre circulations. We hope, but do not presume, that a deeper understanding of model behavior might translate into insight about how Nature operates. The last two chapters, and the papers in the appendices, have raised several questions which we attempt to shed light on in this section: What are the dynamics which explain the mean and variability of the AMOC, in general, and the NAC, in particular? How do buoyancy forcing perturbations drive the gyres and how does wind forcing drive the overturning? What is the nature of the coupling between the overturning and gyre circulations?

This chapter relies heavily on newly-developed vorticity diagnostics for the POP ocean model which are described in detail in Appendix C. Some explicit references are made to the auxiliary material presented there, but for the sake of concision, it is expected that this chapter be read in conjunction with Appendix C. We consider first the mean vorticity balance. This section largely reiterates the findings of numerous previous studies which have called attention to the role played by bottom pressure torque in the large-scale circulation (e.g., Holland, 1973; Bell, 1999; Hughes and de Cuevas, 2001; Zhang and Vallis, 2007; Spence et al., 2012); we contribute to this literature an analysis of the POP model forced with CORE-II forcing and an evaluation of the mean vorticity balance of AMOC. Novel insights are obtained by considering the time-varying vorticity balance

and its dependence on momentum and buoyancy forcing, separately.

An important caveat of the analysis presented in this chapter which must be borne in mind throughout is that the 1° POP model considered here does not resolve ocean mesoscale eddies, and its dynamics are only weakly nonlinear. The maximum Rossby number of the model mean flow field over the entire North Atlantic basin north of 5°N is about 0.3, and it reduces to about 0.1 for latitudes north of 20°N. The model Rossby number is computed at each grid cell location as

$$\mathcal{R} = \frac{U}{f\Delta L} \tag{4.1}$$

where U and ΔL represent the flow speed and grid cell dimension in either the grid-x or grid-y direction, and f is the Coriolis parameter. The model is incapable of representing the highly ageostrophic ($\mathcal{R} \to 1$) flow features which appear to be ubiquitous in western boundary current regions of the Atlantic. For example, observations of the Florida Current at 25°N give local Rossby numbers in excess of 1 (Brooks and Niiler, 1977). While the verisimilitude of the 1° model dynamics is certainly questionable, there is no doubt that a deeper understanding of model behavior based on the underlying vorticity dynamics is valuable in and of itself.

4.1 The mean vertically-integrated vorticity balance of CONTROL

The time-mean vertically-integrated vorticity (VIV) balance of the CONTROL ocean–sea-ice hindcast simulation (Appendix B) is shown in Figure 4.1. Perhaps the most striking feature of the barotropic[1] balance in the POP model is that strong meridional flow in the North Atlantic is associated locally with strong bottom vortex stretching (BVS, corresponding to $-fw_I$) resulting from flow over topography. The barotropic signatures of the Gulf Stream, NAC, subpolar gyre (SPG), and DWBC are all readily apparent in the $\beta \int v$ term, and their mean strengths are clearly mostly related to the magnitude of colocated BVS. This is not what one would expect from a classical, local Sverdrup balance for a flat-bottom ocean (e.g., Pedlosky, 1996, page 9):

$$\beta \int v = \frac{1}{\rho_o} \nabla \times \tau_s, \tag{4.2}$$

[1] The term barotropic is used although in fact the integral extends only to the bottom of the ocean interior; see Appendix C, Eqn $C.25$.

in which the local wind stress curl sets the depth-integrated meridional transport at each point. In fact, it has been known for some time that available observational evidence calls into question the validity of the Sverdrup balance in the subtropical Atlantic (Wunsch and Roemmich, 1985; Roemmich and Wunsch, 1985).

The surface wind stress curl appears in Figure 4.1 in the $\int F_{V\xi}$ term, which is the integral over the ocean interior of the vertical divergence of the curl of viscous vertical transfer of horizontal momentum (Eqn $C.25$). It differs from the wind stress curl at the surface by a term associated with the horizontal shear near the top of model bathymetric steps (between model topographic and interior ocean grid cells):

$$\int_{z=-z_I}^{0} \nabla \times \overline{\mathbf{F}_V(\mathbf{u})} \quad = \quad \nabla \times \left[\overline{\tau_s} - (\overline{\mu \partial_z \mathbf{u}})|_{-z_I} \right] / \rho_o \tag{4.3}$$

The wind stress curl dominates this term throughout the basin interior (Fig. 4.2), but the second term on the RHS of Eqn 4.3 dominates in shelf regions where strong flow over topography results in considerable vertical shear as a result of the no-slip boundary conditions. Comparing Figures 4.1 and 4.2 shows that the subsurface shear term is a significant contributor to $\int F_{V\xi}$ along the North American coast, as well as along the perimeter of the SPG where it generally tends to counteract the wind stress forcing except along the Labrador coast and in the Grand Banks. Note that because we are considering only the interior ocean, Figure 4.2 excludes ocean cells which are adjacent to land points. We suspect that the positive wind stress near the European and African continents is due to an effect of the land boundary on the surface vorticity forcing of the model.[2] More work will be needed to assess the ramifications of land boundary effects on the vorticity dynamics of POP model solutions, but for now we simply note that it is a potential source of model error. Wind stress curl forcing clearly explains the broad southward flow in the subtropical gyre (STG) interior, as expected, and the northward flow to the southeast of Nova Scotia and in the central subpolar gyre, but otherwise it is difficult to identify regions where $\beta \int v$ is primarily related to the

[2] The model wind stress curl, like other components of vorticity, can be amplified by no-slip boundary conditions which impose zero momentum tendency for velocity points at the ocean-land interface (see Appendix C, discussion of Eqn $C.21$). Heightened wind stress curl will be most pronounced where the wind vector has a large component parallel to the model coastline (e.g., the Eastern Atlantic). The model will feel this wind stress curl, realistic or not.

local wind stress curl.

To clarify the nature of the second term on the RHS of Eqn 4.3 (Fig. 4.2), consider the region of positive $\int F_{V\xi}$ just south of Cape Hatteras which is clearly associated with subsurface shear (Fig. 4.1). An idealized schematic helps to illustrate how topographic shear gives rise to barotropic vorticity forcing at this location in the model (Fig. 4.3). Gulf Stream flow above and adjacent to a bathymetric step associated with the continental shelf is assumed to be uniform in the grid-y direction. The shear term in Eqn 4.3 will take the form:

$$\begin{aligned} \frac{1}{\rho_o}\hat{k}\cdot\nabla\times(-\mu\partial_z\mathbf{u})|_{-z_I} &= -\frac{1}{\rho_o\Delta y}\partial_x(\overline{\mu(\partial_z v)\Delta y}^{y}) + \frac{1}{\rho_o\Delta x}\partial_y(\overline{\mu(\partial_z u)\Delta x}^{x}) \\ &\approx \frac{\mu v}{\rho_o\Delta x\Delta z} \end{aligned} \tag{4.4}$$

which is positive and considerably greater than the wind stress curl at this location. Thus, the vertical shear at the base of the model Gulf Stream in the vicinity of Cape Hatteras generates a positive, steady state barotropic vorticity forcing which helps facilitate the movement of water parcels northward towards regions of higher planetary vorticity. This bottom-friction effect helps to close the gyre circulation, as in the Stommel model (Stommel, 1948), but we note that the BVS term as defined in Eqn $C.24$ includes most of the effect of bottom drag, which is small compared to bottom pressure torque (Fig. $C.4$). Other terms in the VIV balance such as the BVS and viscous torque ($\int F_{H\xi}$) are more important sources of positive vorticity in this location, and so the strong northward flow which is evident along the whole Atlantic east coast, even north of Cape Hatteras, is due to a combination of forcing factors, both local and non-local (as discussed below). The above example is simply intended to illustrate the ramifications of no-slip-induced topographic shear on the model vorticity budget.

The western boundaries of the North Atlantic gyres are largely characterized by fast, barotropic jets which project strongly in the direction of the planetary vorticity gradient. The vorticity forcing needed to accomplish this meridional motion in the model comes primarily from BVS, with $\int F_{H\xi}$ and $\int ADV_{\xi}$ contributing as well but not as systematically (Fig. 4.4). The dominant role of vortex stretching in the western boundary region is surprising given that the model horizontal viscos-

ity formulation is explicitly designed (Bryan et al., 1975; Large et al., 2001; Jochum et al., 2008; Danabasoglu et al., 2012a) for a frictional closure of the gyres at the western boundary (Munk, 1950), as well as for satisfying numerical stability constraints. On the other hand, this result is in line with other modelling studies which have highlighted the significance of BVS in the dynamics of the large-scale Atlantic circulation and western boundary currents (Holland, 1973; Hughes and de Cuevas, 2001; Zhang and Vallis, 2007; Spence et al., 2012).

The relative contributions of the VIV terms in Eqn $C.25$ (Fig. 4.1) to the Atlantic horizontal gyre circulation can be approximated by integrating along the model grid-x direction from the eastern boundary, x_e:

$$\Psi(x) = \int_x^{x_e} dx \int v = -\frac{1}{\beta} \int_x^{x_e} dx \left[\int ADV_\xi - f w_I + \int F_{H\xi} + \int F_{V\xi} - \int R_\xi \right]. \tag{4.5}$$

The resulting fields (in units of Sv $\equiv 10^6\ m^3\ s^{-1}$) are shown in Figure 4.5, with labels reflecting terms in the VIV balance. The integral effect of the weak but large-scale and uniform vorticity forcing by the surface winds accounts for much of the subtropical gyre circulation as well as the northern half of the subpolar gyre circulation (north of about 55°N). The wind-induced circulation is substantially modified by the topographic shear effect (Eqn 4.3), and as a result the $\int F_{V\xi}$ streamfunction is stronger than that due to wind stress alone in the western subtropics and weaker at far northern latitudes.

Converting the local barotropic vorticity forcing into streamfunction components clearly shows that BVS plays a fundamental role in maintaining the model SPG circulation. It accounts for most of the cyclonic circulation between about 40°N and 55°N, consistent with the findings of Zhang and Vallis (2007). Large residuals in the $-fw_I$ term north of 55°N (associated with momentum imbalances arising from the Nordic Seas overflow parameterization; see Appendix C) obscure the streamfunction partition at those latitudes. However, the bottom left panel of Figure 4.5 shows how the BVS streamfunction would look if the residual were identically zero. This demonstrates that BVS contributes significantly to the cyclonic SPG circulation even north of 55°N, although the wind stress curl becomes a more significant driver in the far north.

The strength of the anticyclonic STG circulation north of about 30°N is considerably enhanced by the negative vorticity input[3] from BVS and $\int F_{H\xi}$ in the central Atlantic (compare Figs. 4.1, 4.5). The large negative values in those VIV terms near 30°W and between 35°N-42°N are associated with upslope flow along the mid-Atlantic ridge (MAR). This negative vorticity forcing over the MAR adds to the broad negative vorticity input from the wind field over these latitudes, enhancing the anticyclonic gyre circulation and probably contributing to the poor separation of the model Gulf Stream from the Atlantic coast between 35°N-42°N. The MAR forcing is not necessarily unrealistic. The model simply lacks sufficient positive barotropic vorticity forcing near the western boundary to balance and reverse the integral effects of the negative wind and MAR vorticity forcing at latitudes just north of Hatteras. In Figure 4.5, positive barotropic vorticity forcing appears as negative streamfunction values. Both the BVS and the $\int F_{H\xi}$ terms provide weak positive barotropic vorticity forcing just north of Hatteras, but $\int ADV_{\xi}$ and $\int F_{V\xi}$ are stronger in the other direction. The lack of resolved eddies in the model suggests that $\int ADV_{\xi}$ may not be contributing realistic vorticity forcing, but it is also likely that BVS is too weak north of Cape Hatteras because of an anemic coastal DWBC (see discussion below). Higher resolution modelling with vorticity diagnostics may shed light on the complex dynamics associated with WBC separation, but the importance of far-field and DWBC effects suggests that basin- or global-scale simulations will be required.

Figure 4.5 underscores the point that BVS is the primary term associated with the western boundary closure of the subtropical gyre. This is accomplished through strong bottom downwelling along the continental shelf of the Atlantic east coast (Fig. 4.4) which stretches the overlying fluid column. What mechanism is responsible for this strong time-mean bottom downwelling under the GS? In an analysis of multi-decadal variability in a long coupled CCSM4 simulation, Yeager and Danabasoglu (2012) argued that large BVS variations near Cape Hatteras were related to variations in DWBC convergence onto the Atlantic continental shelf. Stronger southward flow over

[3] By convention, Ψ is positive where the circulation is clockwise, reflecting negative mean relative vorticity within streamline contours.

the model's stepped bathymetry (Fig. 4.6) resulted in stronger bottom downwelling, as expected from the relation:

$$w_B = -\mathbf{u}_B \cdot \nabla H \tag{4.6}$$

where w_B represents the bottom vertical velocity associated with horizontal bottom flow ($\mathbf{u}_B$) across bathymetry ($H > 0$) contours.[4] Anomalous southward DWBC flow might well play a significant role in perturbations of the mean balance in this region, but it does not appear to explain the strong time-mean bottom downwelling which balances the coastal GS flow in CONTROL. Instead, we think that positive barotropic zonal flow ($\int u$) across the shelf accounts for the mean BVS supporting the northward GS. We show in Figure $C.4$ that w_I essentially reflects the the integral effect of pressure torque on model sidewalls, because that term dominates the topographic vorticity equation (Eqn $C.24$). The pressure torque term is the sum of barotropic and baroclinic components, with the former associated with SSH gradients and the latter associated with density gradients (see Eqn $C.3$). The corresponding topographic vorticity equations are:

$$-fw_I^{bt} \approx \int ADV_\xi + -\beta \int v + \int GRADP_\xi^{bt} + \int F_{H\xi} + \int F_{V\xi}, \quad \textit{barotropic} \tag{4.7}$$

$$-fw_I^{bc} \approx \int ADV_\xi + -\beta \int v + \int GRADP_\xi^{bc} + \int F_{H\xi} + \int F_{V\xi}, \quad \textit{baroclinic.} \tag{4.8}$$

The barotropic equation gives the BVS term which would be generated if there were only barotropic pressure gradients (i.e., stretching of the ocean interior due to barotropic bottom flow across bathymetry contours), and similarly for the baroclinic equation. Note that these two terms do not add up to the total BVS, because other terms are retained in each equation. Figure 4.7 shows how these terms compare to the actual BVS computed using the full pressure field. As Holland (1973) pointed out, there is a high degree of baroclinic compensation so that the deep pressure field driving bottom flow is a small residual of large and counterbalancing barotropic and baroclinic pressure terms. The sign of net, time-mean BVS will reflect whichever pressure torque term is larger, as shown in Figure 4.7d. We find that the barotropic pressure field is the dominant term

[4] We distinguish w_B, which here is invoked as a heuristic for the magnitude of bottom vertical velocity, from w_I, which is the bottom vertical velocity which formally appears in the model vorticity balance (Eqns $C.24$, $C.25$).

along the Atlantic shelf, and thus it is barotropic offshore flow that generates the vortex stretching needed to balance the planetary vorticity advection in the GS region. However, the map shows considerable variation from place to place, and below we will examine in more depth the baroclinic flow responsible for BVS in the NAC region and eastern mid-latitude Atlantic. Finally, we note that the dominance of barotropic BVS along the Atlantic shelf is probably related to model bias. A stronger coastal DWBC north of Cape Hatteras would likely result in baroclinic BVS in that region.

We can see, at this point, that the interaction of abyssal flow with bottom topography results in a barotropic vorticity forcing which is key to understanding the mean Atlantic gyre circulations in the POP ocean model, in both the STG and SPG. Regions where strong BVS results from baroclinic flow imply a coupling between the overturning and gyre circulations through barotropic vorticity dynamics. The barotropic balance obscures the depth-dependent flow structure which characterizes the overturning circulation, and so we now examine the mean vorticity balance as a function of depth.

4.2 The mean vorticity balance of the overturning circulation

The zonally-integrated meridional transport in the Atlantic can be conceptually split into a northward flowing upper branch and a southward flowing lower branch, with the demarcation occurring at roughly 1000m depth (Fig. 2.12). We consider now the interior vorticity balances of the two AMOC branches separately by performing partial vertical integrals of the time-mean 3D vorticity balance (Eqn $C.23$) from CONTROL. The upper ocean integral ($\int_{z=-1000)}^{z=0}$) results in two terms: one associated with shelf regions where the the bottom of the ocean interior (see Appendix C) is shallower than 1000m and one where the interior ocean is deeper than 1000m:

$$z_I \leq 1000 : \int R_\xi = \int ADV_\xi - fw_I - \beta \int v + \int F_{H\xi} + \int F_{V\xi}, \quad upper, shelf \tag{4.9}$$

$$z_I > 1000 : \int R_\xi = \int ADV_\xi - fw_{1000} - \beta \int v + \int F_{H\xi} + \int F_{V\xi}, \quad upper, deep. \tag{4.10}$$

The following balance will hold for the lower branch ($\int_{z=-z_I(x,y)}^{z=-1000}$):

$$\int R_\xi \;=\; \int ADV_\xi + (fw_{1000} - fw_I) - \beta \int v + \int F_{H\xi} + \int F_{V\xi}, \quad \textit{lower.} \tag{4.11}$$

The resulting balances are shown in Figures 4.8-4.10, where we now ignore the $\int R_\xi$ terms (they closely resemble that of Figure 4.1).

In continental shelf regions (Fig. 4.8), the upper branch circulation directly feels the bottom bathymetry through the BVS term and the topographic shear, as discussed above.[5] We see again that the northward GS flow along the Atlantic continental shelf is primarily associated with strong bottom downwelling which, we have argued, is due to the eastward component of the depth-integrated shelf current as there is no southward flow on the shelf. The vorticity forcing of the other terms varies considerably from place to place along the western boundary in the subtropics. We leave it for future work to focus in on such local details. A noteworthy feature of the shelf balance is that topographic shear ($\int F_{V\xi}$) greatly facilitates the southward Labrador shelf current by systematically removing vorticity, from Baffin Island all the way to the Grand Banks of Newfoundland, although the net vorticity forcing along this shelf is a complex interplay of all of the forcing terms. North of about 35°N, the shelf flow does not project strongly onto AMOC, because the GS moves into deeper waters.

In the deep ocean region offshore of the Atlantic coast, a weaker southward recirculation is evident on the eastern side of the northward jet. Here, the vorticity balance of the GS is not as dominated by stretching (Fig. 4.9). We now distinguish vortex stretching (VS) from bottom vortex stretching (BVS). The $-fw_{1000}$ term in the Eqn 4.10 balance reflects the net vortex stretching of the fluid between the surface (where $w = 0$) and 1000m, with no direct bottom interaction.[6] Geostrophic flow implies a balance between VS and $\beta \int v$, because the curl of the geostrophic

[5] There clearly are topographic effects associated with the $F_{H\xi}$ and ADV_ξ terms, but these are indirect when considering the vorticity balance of the ocean interior, as we do here.

[6] Note that the stretching of the fluid column between the bottom of the Ekman layer and 1000m will differ from $-fw_{1000}$ due to the effect of wind stress curl, but we opt to keep wind stress curl (i.e., Ekman pumping) separate in our consideration of VIV terms

momentum balance gives:

$$\begin{aligned} \hat{k} \cdot \nabla \times (\mathbf{f} \times \mathbf{u}_g &= -\frac{\nabla p}{\rho_o}) \\ \beta v_g - f\frac{\partial w_g}{\partial z} &= 0 \qquad (4.12) \\ \nabla \cdot \mathbf{u}_g &= -\frac{\beta v_g}{f} \qquad (4.13) \end{aligned}$$

where the subscript "g" indicates the purely geostrophic component of flow. It is clear from the above equation that geostrophic flow is divergent because of the variation of the Coriolis parameter with latitude (the beta effect). In the Northern Hemisphere, northward geostrophic flow is convergent ($\frac{\partial w_g}{\partial z} > 0$, vortex stretching) and southward flow is divergent ($\frac{\partial w_g}{\partial z} < 0$, vortex compression). While ageostrophic effects associated with $\int F_{H\xi}$ and $\int ADV_\xi$ are important in the GS region, the poleward extension of the AMOC upper branch is evidently highly geostrophic, as indicated by the dominant balance of $-\beta \int v$ and $-f w_{1000}$ north of about 40°N (Fig. 4.9). The model NAC (centered around 32°W, 42°N) and its extension into the eastern subpolar gyre region are characterized by strong vertical velocities at 1000m which balance the depth-integrated meridional flow. The downward vertical motions are maximum between 40-60°N and they account for a significant fraction of the high latitude closure of the AMOC streamfunction (Fig. 2.12); the remainder of the vertical transport needed to close the overturning streamfunction occurs along the flanks of the Greenland shelf. The negative vertical velocities at mid- to high-latitudes in the AMOC streamfunction are often erroneously associated with convective sinking motions in the Labrador Sea, but we see from the above discussion that they are essentially a reflection of highly geostrophic NAC flow.

The deep vertical motions which provide the local vorticity balance for the upper layer NAC bear no relation to the overlying wind stress curl ($\int F_{V\xi}$), which generates local vortex stretching (compression) through vertical Ekman suction (pumping) at the base of the surface mixed layer when the wind stress curl is positive (negative) (e.g., Pedlosky, 1996, page 13). We can conclude that the wind stress is probably not a key local factor in NAC dynamics, but the large-scale wind field certainly plays a role in setting up the surface pressure (SSH) field which contributes to NAC flow.

The NAC coincides with the large inter-gyre gradient in the barotropic streamfunction (Fig. 4.5) which has a strong zonal component, indicating strong northward barotropic transport ($\int v = \Psi_x$). The broad region of negative wind stress curl poleward of 40°N in the eastern Atlantic (Fig. 4.2) forces anticyclonic circulation in that region which contributes to the inter-gyre streamfunction gradient (Fig. 4.5). Thus, the NAC is not independent of the wind forcing, and here again, we wonder whether land boundary effects along the complex coastlines of France and the British Isles might be perturbing the wind-related vorticity forcing of the model in consequential ways.

The baroclinicity of the flow in the NAC region is strong evidence that surface buoyancy forcing plays a primary role in setting up the mean pressure gradients which support the NAC. A comparison of the upper and lower interior vorticity balances in this region (Figs. 4.9, 4.10) shows that the primary branches of the southward DWBC are located almost underneath the northward NAC flow between 40°N-50°N. The positive zonal pressure (SSH) gradient which drives northward NAC flow in the upper layer becomes negative in the deep ocean due to the integral effect of the negative zonal density gradient (Eqn $C.3$) in this region. The vorticity signature of this baroclinic geostrophic flow is vortex compression in the lower, DWBC layer between 1000m depth and the bottom of the ocean interior (Fig. 4.10) which largely compensates the stretching in the upper, NAC layer. The compensation is not complete, however, and so considerable bottom downwelling (positive BVS) is also required to balance the barotropic component of the NAC, as we have already seen (Fig. 4.1). The strong bottom downwelling beneath the NAC is associated with the baroclinic pressure field (Fig. 4.7d) and so there is strong coupling between the overturning strength (DWBC strength) and the horizontal gyre strength at this location. The vorticity forcing associated with vertical motion at 1000m ($-fw_{1000}$, Fig. 4.9) is effectively the only term which couples the upper and lower branch vorticity (because $(\int F_{V\xi})|_{z=-1000}$ is very small and there are no other terms shared between Eqn 4.10 and Eqn 4.11). This term is analogous to the stretching term in the PV equation of a two-layer quasi-geostrophic system (e.g., Vallis, 2006, , page 213). This coupling is confined to the western boundary in the STG, but it is large throughout the SPG as well as at inter-gyre latitudes (Fig. 4.9).

The vorticity balance of the deep lower branch of the AMOC is shown in Figure 4.10. The $-\beta \int v$ term shows that only a weak branch of the NADW flows directly southward along the Grand Banks shelf after exiting the Labrador Sea. Some of it recirculates in the SPG, while a large portion flows southward along the eastern and western flanks of the MAR before rejoining the western continental shelf south of Cape Hatteras. Such interior DWBC pathways appear to be realistic (Dickson et al., 1985; Bower et al., 2009; Lozier, 2010) and become more prevalent as model horizontal viscosity is decreased (Spence et al., 2012). The equatorward DWBC flow along the flanks of the MAR is driven by deep density gradients generated by the mean buoyancy forcing (Fig. 4.10). The surface height signature of these deep density gradients diminishes at lower latitudes so that there is little upper layer flow above the MAR equatorward of about 40°N. Between about 30°N-50°N, the highly geostrophic DWBC flow is made possible by vortex compression of the lower layer (between 1000m and the bottom of the ocean interior) associated with upslope flow along the MAR. As in the NAC region, the BVS on the eastern flank of the MAR is a baroclinic effect (Fig. 4.7d), and so the enhancement of the anticyclonic STG circulation associated with BVS at these latitudes which was noted earlier (Fig. 4.5) is another example of strong coupling between the baroclinic overturning circulation and the barotropic gyre circulation. Horizontal viscosity also helps to remove vorticity from DWBC water parcels, particularly on the eastern flank of the MAR, but it plays a much less significant role than BVS along the MAR pathway. In contrast, viscous torque is a key sink of DWBC vorticity along the shelf of the Labrador Sea (between 50°N-60°N), and along the western boundary shelf, south of Cape Hatteras.

The existence of a relatively non-viscous vorticity balance in the mid-latitudes of the Atlantic factors significantly in the model AMOC dynamics. This is perhaps easiest seen when the mean vorticity balance is viewed in the latitude-depth space of the overturning circulation. The zonal integral across the Atlantic basin of the time-mean interior vorticity equation (Eqn $C.23$) is:

$$0 \approx= \frac{1}{\beta} \int_{x_w}^{x_e} dx \left[ADV_\xi + f \frac{\partial w}{\partial z} - \beta v + F_{H\xi} + F_{V\xi} \right] \tag{4.14}$$

where the integral extends across the Atlantic from the western boundary (x_w) to the eastern

boundary (x_w)[7] , $GRADP_\xi$ is zero for the interior balance, and we neglect the residual. The resulting zonally-integrated vorticity (ZIV) terms are shown in Figure 4.11, after conversion to units of volume transport (Sv) by dividing by β and multiplying by grid cell thickness (Δz). The $\beta \int v$ term (plotted as a LHS term) reflects the northward (southward) flows in the upper (lower) layer associated with the mean AMOC streamfunction (Fig. 2.12). The vorticity forcing required for this meridional transport comes essentially from the joint effects of VS and viscous torque: $f\frac{\partial w}{\partial z} + F_{H\xi}$ (Fig. 4.11, lower right panel). The relative contributions of these terms varies with latitude. Between 50°N-60°N, southward DWBC flow along the Labrador shelf is made possibly by viscous extraction of vorticity ($F_{H\xi}$), but $f\frac{\partial w}{\partial z}$ then takes over and supports a relatively inviscid, geostrophic AMOC between about 35°N-50°N. These latitudes correspond to the geostrophic GS/NAC flow in the deep ocean with strong DWBC flow along the MAR, discussed above. South of about 35°N, the AMOC is largely associated with strong western boundary currents along the continental shelf of the Americas. Both stretching and viscous torque are important contributors to the AMOC at latitudes between 25°N-35°N–the western boundary region just south of Cape Hatteras. Horizontal friction becomes the dominant term in the balance of the northward GS south of about 30°N and the dominant term in the balance of the southward DWBC south of about 25°N.

As f approaches zero near the Equator, horizontal friction takes over completely and becomes essentially the sole term providing a vorticity balance for the cross-equatorial meridional AMOC transport. This is not unexpected, because frictional dissipation appears to be an essential element of cross-equatorial flow even at Reynolds numbers which are much more typical of the real ocean than the low values which characterize the weakly nonlinear CONTROL simulation (Killworth, 1991; Edwards and Pedlosky, 1998). In the limit of strongly nonlinear, inviscid dynamics, we would expect eddy fluxes of vorticity into a (thin) frictional boundary layer to play an increasingly important role (Edwards and Pedlosky, 1998; Fox-Kemper and Pedlosky, 2004a,b), but ultimately, frictional dissipation is required for systematic vorticity modification in the absence of stretching.

[7] As in Eqn 4.5, the zonal integral is approximated as the integral along the model grid-x direction

4.3 Interpreting the time-mean balance

We have analyzed a CESM POP hindcast simulation in terms of mean vorticity forcing and dissipation in the Atlantic. This analysis is the first of its kind with this model, and we have presented a fairly comprehensive and detailed overview of preliminary results for the Atlantic basin. We anticipate that future model development will benefit from wider use of the vorticity diagnostics methods outlined in Appendix *C* and comparison with the benchmark analysis shown above.

The time-mean balance helps to shed light on the model dynamical response to historical forcing perturbations described in Chapter 3. First, the strong attenuation of buoyancy-forced AMOC anomalies near 35°N (Fig. 3.1) is related to the transition from relatively inviscid, geostrophic AMOC dynamics to the frictional balance which characterizes GS/DWBC flow near the western boundary. The increasingly viscous vorticity balance in the vicinity of the Equator helps us to understand why buoyancy-forced AMOC anomalies from the Northern Hemisphere and momentum-forced AMOC anomalies from the Southern Hemisphere are greatly attenuated by the time they propagate into the opposite hemisphere (Figs. 3.1, 3.8). The vorticity barrier at the Equator would appear to be an important factor in decadal-scale global climate dynamics.

The dominant influence of buoyancy forcing perturbations on the variability of model SPG and inter-gyre circulations (Fig. 3.4) is clarified by the key role that BVS plays in the mean vorticity balance of those flows. Buoyancy forcing can result in significant barotropic vorticity forcing insofar as it induces flow over bottom topography. Buoyancy-driven abyssal flow can have a strong barotropic component if the surface buoyancy fluxes set SSH, as is largely the case poleward of about 40°N and along the Atlantic continental shelf north of Cape Hatteras (Fig. 3.4). South of 40°N, buoyancy-forced variations in the baroclinic DWBC flow along the MAR also contribute to the variability of the horizontal circulation of the STG.

However, there are perhaps as many questions raised by the analysis as there are questions answered. The vorticity balance, by itself, cannot tell us why the model adjusts to this particular mean circulation. Why does the model NAC migrate to a preferred location which is about 10° too

far east? Why does the STG streamfunction fail to seperate at Cape Hatteras? Clear answers to these questions remain elusive and will likely require a comparison with vorticity diagnostics from more realistic, eddy-resolving models. This is a promising prospect for future work, and we have laid the groundwork for it. Comparisons with observations would also be extremely valuable for identifying model deficiencies in key regions such as the Grand Banks shelf. We are aware of efforts to deploy mooring arrays in this location to measure the vorticity balances associated with NAC flow over the DWBC. Such metrics are sorely needed in order to interpret model mean behavior.

Perturbation experiments can help to identify key factors which influence the model mean vorticity balance, if the perturbations have a large time-mean component. For instance, the impacts on the mean circulation of changes in model bathymetry are currently being investigated by researchers at NCAR and elsewhere. POP vorticity diagnostics will be a useful tool for interpreting those results. Here, we consider an example of the impact of enhanced mean water mass transformation in the Labrador Sea associated with reduced sea ice coverage. The experiment in question was analyzed in Yeager and Jochum (2009), their case "B" (to avoid confusion with the buoyancy-driven experiment B of Appendix B, we will refer to the Yeager and Jochum (2009) experiment as "B_YJ09"). It is a similar configuration to CONTROL (a CORE-forced ocean–sea-ice hindcast) but with crucial differences in model physics which resulted in much lower than observed mean winter sea ice coverage in the Labrador Sea (Fig. 4.12, experiment B). In particular, it was run using an interim version of the CCSM model (CCSM3.5) which lacked several significant physics additions which were later incorporated into CESM1, including: a delta-Eddington shortwave radiative transfer parameterization for sea ice (Holland et al., 2012), a parameterization for density-driven overflows in the Nordic Seas (Briegleb et al., 2010; Danabasoglu et al., 2010), and a parameterization for ocean submesoscale mixing (Fox-Kemper et al., 2008, 2011). As shown in Figure 4.12, persistently low winter ice coverage in B_YJ09 resulted in much too strong positive surface density flux (negative buoyancy flux) into the Lab Sea due to intense surface cooling of waters that are normally insulated by ice. The plot shows how the winter density flux from B_YJ09 compares to that obtained in an ocean-only CORE hindcast which imposes an observed sea ice

fraction (their experiment A) as well as to an estimate of observed winter density fluxes based on Large and Yeager (2009) air-sea fluxes. The unrealistically intense winter cooling in B_YJ09 resulted in very anomalous mean water mass transformation rates in the Labrador Sea (Fig. 4.13).

The B_YJ09 simulation continues to be of considerable interest because its mean gyre circulation (Fig. 4.14) exhibits desirable features which are notoriously hard to achieve even in eddy-resolving OGCMs: a strong, jet-like GS which separates at Cape Hatteras; a strong, cyclonic NRG further north between the GS and Nova Scotia; and a weak but discernible NAC directly offshore of the Grand Banks which turns eastward as it should in the Northwest Corner region (around 40°W, 50°N). We argued in Yeager and Jochum (2009) that BVS associated with an anomalously strong DWBC flow down the Grand Banks shelf explained the unusually realistic GS path in that simulation, in accordance with Zhang and Vallis (2007). We can now use POP vorticity diagnostics to demonstrate this in a more convincing fashion (Fig. 4.15).[8]

The VIV balance from B_YJ09 confirms that, between 40°N-45°N, a very strong NAC is positioned along the southeast flank of the Grand Banks shelf, balanced by intense bottom downwelling there (Fig. 4.15; compare to Fig. 4.4). As in CONTROL, the DWBC in B_YJ09 is driven by the cumulative effect of negative zonal density gradients. It would appear that stronger mean buoyancy forcing in the Labrador Sea generates stronger zonal density gradients along the shelf east of the Grand Banks which allow for a stronger coastal DWBC in B_YJ09 than in CONTROL. A mean barotropic vorticity balance can thus be established more than 10° further west in B_YJ09 between the latitudes of 40°N-45°N. The lack of sea ice and enhanced production of dense LSW are prime suspects in explaining the different mean VIV budget, but we cannot rule out the possibility that the overflow parameterization in CONTROL might have the effect of weakening the coastal DWBC and enhancing the interior DWBC by filling the SPG abyss with dense overflow waters. In B_YJ09, there is more deep southward flow along the continental shelf and west of the MAR than on the eastern flank of the MAR (this is more easily seen in the VIV balance below 1000m, not

[8] The momentum budget terms needed for a closed vorticity budget were not saved in this simulation. Therefore, we computed the vorticity balance for B_YJ09 approximately, as explained in Appendix *C*.

shown here). As discussed above, DWBC flow on the MAR is balanced by the vortex compression associated with upslope flow; this tends to enhance the anticyclonic STG streamfunction by contributing negative barotropic vorticity forcing. The substantial DWBC west of the MAR in B_YJ09 flows downslope. In the relatively inviscid, weakly nonlinear ocean interior, downslope abyssal flow directed southward can only occur as part of a baroclinic flow field whose barotropic component is northward: the vortex compression required for the deep flow results from downwelling from the upper layer which is stronger than the bottom downwelling. This vorticity balance is characteristic of NAC flow in the model and it explains the detached GS in B_YJ09. If we now compute the BSF components from the terms in the VIV balance of the B_YJ09 simulation (Fig. 4.16), we can see that the enhanced bottom downwelling west of the MAR helps to close the streamfunction contours generated by deep flow along the MAR. This results in a cyclonic NRG and a more detached and jet-like GS flow.

We see that the mean vorticity balance of the 1° POP model, and in particular the GS/NAC path, can be substantially altered by a strong and persistent perturbation to the high latitude buoyancy forcing. A question raised by Yeager and Jochum (2009)–why does the model require excessive surface water mass transformation to generate a strong coastal DWBC on the Grand Banks shelf?–remains pertinent and unanswered. We suspect the model simply lacks sufficient resolution (either vertical or horizontal) to maintain the large zonal density gradients needed to balance DWBC flow in this region. It achieves them only when the density is unrealistically high. Progress in improving the mean GS path in the nominal 1° POP model will likely require a dedicated focus on improving the model mean density field on the Grand Banks shelf.

4.4 Historical variability of the large-scale North Atlantic circulation from a vorticity perspective

We showed in Chapter 3 that most of the variance in AMOC, BSF, SSH, and upper ocean flow in the mid- to high-latitude Atlantic over the latter half of the twentieth century was associated with variations in surface buoyancy forcing (Figs. 3.1, 3.4). We are now in a position to delve

deeper into the dynamics which explain this result.

Anomalous fluxes of either momentum or buoyancy at the air-sea interface can generate abyssal flow perturbations which have the potential to produce BVS anomalies when the anomalous flow projects onto the local bathymetry gradient. Thus, we find that the interannual (1958-2011) variance in BVS in CONTROL (Fig. 4.17) has components associated with both momentum and buoyancy forcing (experiments M and B, respectively; see Appendix B). The variance is largest where the time-mean BVS is largest (Fig. 4.1): throughout the SPG and along coastal shelves of the western boundary, as well as over the MAR. Buoyancy forcing accounts for most of the variance in shelf regions and over the ridge of the MAR north of 40°N. Momentum forcing generates more widespread low-level variance, but with heightened effect at the western boundary. Almost all of the BVS variance under the model NAC at 30°W is buoyancy-forced. Temporal smoothing shows that buoyancy forcing explains almost all of the BVS variance on decadal and longer timescales in CONTROL (Fig. 4.17 d-f).

We have already discussed the important role of buoyancy forcing in setting the mean strength and position of the NAC, and a comparison of Figures 4.17 and 4.18 underscores the finding (noted previously in Fig. 3.4) that it dominates the temporal variability of the NAC. Consistent with the dominant balance diagnosed from the mean VIV equation (Fig. 4.1), the local variability of barotropic meridional flow (Fig. 4.18) exhibits a very close match with BVS in terms of overall spatial pattern and the relative contributions of M and B variance in different regions. The correspondence between Figures 4.17 and 4.18 is not surprising for the B experiment because BVS is the only way that buoyancy forcing can drive barotropic flow. However, it is rather surprising to find that the largest $\beta \int v$ variance in M is also related to BVS. Traditionally, we think of winds generating barotropic vorticity forcing exclusively through the wind stress curl and associated Ekman pumping of the interior. The wind stress curl variability dominates the $\int F_{V\xi}$ variance (Figure 4.19), which also includes topographic shear effects.[9] We see that wind stress curl variability

[9] Non-zero covariance in the B experiment is due either to topographic shear, or the surface stress dependence on ocean surface velocity (see Appendix B).

accounts for some of the difference between Figures 4.17 and 4.18, but it is clearly not the driver of the largest, local variations in $\beta \int v$. Note that the choice of scale highlights the regions where local $\beta \int v$ variance is greatest. In short, BVS is the primary driver of $\beta \int v$ variance extrema, even in the M experiment!

Of course, as with the mean wind stress curl, wind variations can have a large cumulative effect on the ocean circulation insofar as they impart small but systematic vorticity forcing over vast regions. Thus, the variance of BSF from CONTROL computed from the VIV balance (Eqn 4.5 shows considerable influence of wind stress curl variations (Fig. 4.20), particularly on interannual timescales. In sharp contrast to the wind, BVS generates extreme vorticity forcing but only on small spatial scales. It contributes significantly to the total BSF variance in CONTROL, particularly on decadal timescales, where it explains most of the variance north of 40°N. The variance in the intergyre-gyre region in particular, between about 40°N-50°N, is strongly influenced by BVS on all timescales, whereas this variance is generally interpreted solely in terms of wind stress curl forcing (Marshall et al., 2001a; Czaja and Marshall, 2001). Note that we have neglected the nonlinear advection and horizontal friction terms in the VIV balance, and so the sum of covariances in this plot only approximates the net variance. To complete the picture, we present the BSF variance breakdown for experiments M and B in Figures 4.21 and 4.22, respectively. We find that wind stress curl is indeed the main contributor to BSF variance in M, but the magnitude of BVS effects on circulation variability in M is still quite remarkable and unexpected. In many regions, such as the intergyre-gyre and SPG, it strongly damps the circulation variability implied by interannual surface wind stress curl anomalies; in others, the BVS effect greatly augments the surface wind-forced variability (i.e., the NRG region, and the intergyre-gyre on decadal timescales). While momentum forcing can generate gyre variability through either surface or bottom vortex stretching, buoyancy forcing can spin the gyres only through BVS (Fig. 4.22). There is very little difference between the interannual and decadal BSF variance in B because it is dominated by the slow propagation of deep density anomalies associated with NADW thickness anomalies. The BVS influence on intergyre-gyre variance (Fig. 4.20) is thus seen to derive largely from the effects of buoyancy forced changes

in ocean density structure on slow timescales.

We now reconsider the forcing factors which account for the AMOC variability in CONTROL. The analysis in Chapter 3 was focused exclusively on the strength of the AMOC streamfunction, but it is revealing to consider the spatial dependence of forcing factors by examining the VIV for the upper and lower layers (above and below 1000m), as was done above.[10] The relative contributions of M and B to CONTROL variance of depth-integrated meridional flow in the (generally) northward and southward branches of AMOC are shown in Figures 4.23 and 4.24, respectively. The dominant role of B, and thus the predominance of decadal scale variability, is even more prominent in the upper layer than in the barotropic plot examined above. It accounts for almost all of the variance north of 40°N, while interannual wind forcing explains most of the GS transport variability south of Cape Hatteras. Both forcing components are implicated in the large variance in GS transport just north of Hatteras which was noted in Figures 3.1 and 3.2 at around 37°N. In the deep layer (Fig. 4.24), we find as expected that B explains almost all of the low-frequency DWBC variance along the MAR pathways as well as along the Atlantic continental shelf, but the interannual variance of abyssal v shows a considerable wind-forced signal in regions where BVS variance is high (Fig. 4.17b).

In contrast to the gyre variability, the wind-induced variability in AMOC appears to be not only influenced by, but indeed primarily related to BVS effects. This can be seen in the covariance of zonally-integrated $f\frac{\partial w}{\partial z}$ between CONTROL and experiments M and B (Fig. 4.25). Surface momentum and buoyancy fluxes drive AMOC by inducing planetary vorticity stretching (Eqn 4.14, Fig. 4.11). AMOC variance largely reflects these forced variations in stretching. Even in the basinwide zonal integral shown in Figure 4.25, most of the wind-forced stretching variance is in the deep ocean below 1000m and therefore is presumably more related to BVS than to Ekman pumping. Considering the covariances of CONTROL with M in Figures 4.20-4.25 suggests the following interpretation. At latitudes south of Cape Hatteras, the zonally integrated meridional flow which yields the AMOC streamfunction is largely dominated by the upper and lower western

[10] In what follows, the upper layer includes the shelf regions.

boundary currents represented by the GS and DWBC. Basin-scale wind stress curl variations result in fast, barotropic adjustment of STG strength (Fig. 4.20b) which in turn induces BVS changes along the Atlantic continental shelf (Fig. 4.17b). To the extent that the wind-forced barotropic flow anomaly induces (anomalous) upslope bottom flow, i.e. positive w_B (Eqn 4.6) and negative BVS, anomalously southward barotropic flow is induced along the shelf. In this way, basin-scale wind stress curl changes project onto the baroclinic AMOC flow via BVS effects in shelf regions. Such topographic interactions are generally not considered when estimating wind-induced overturning and associated heat transport variations (e.g., Jayne and Marotzke, 2001; Kanzow et al., 2010; Johns et al., 2011; Msadek et al., 2013). More work will be needed to ascertain how different the wind-forced overturning variations in experiment M are from the common assumption of barotropic return flow below an anomalous Ekman transport near the surface.

The combination of vorticity budget analysis with forcing perturbation experiments is a powerful technique for probing the mechanisms of large-scale circulation variability. We have also shown that it can help shed light on model mean biases. We anticipate that future use of this type of analysis will contribute both to model development and to the attribution of observed circulation variations.

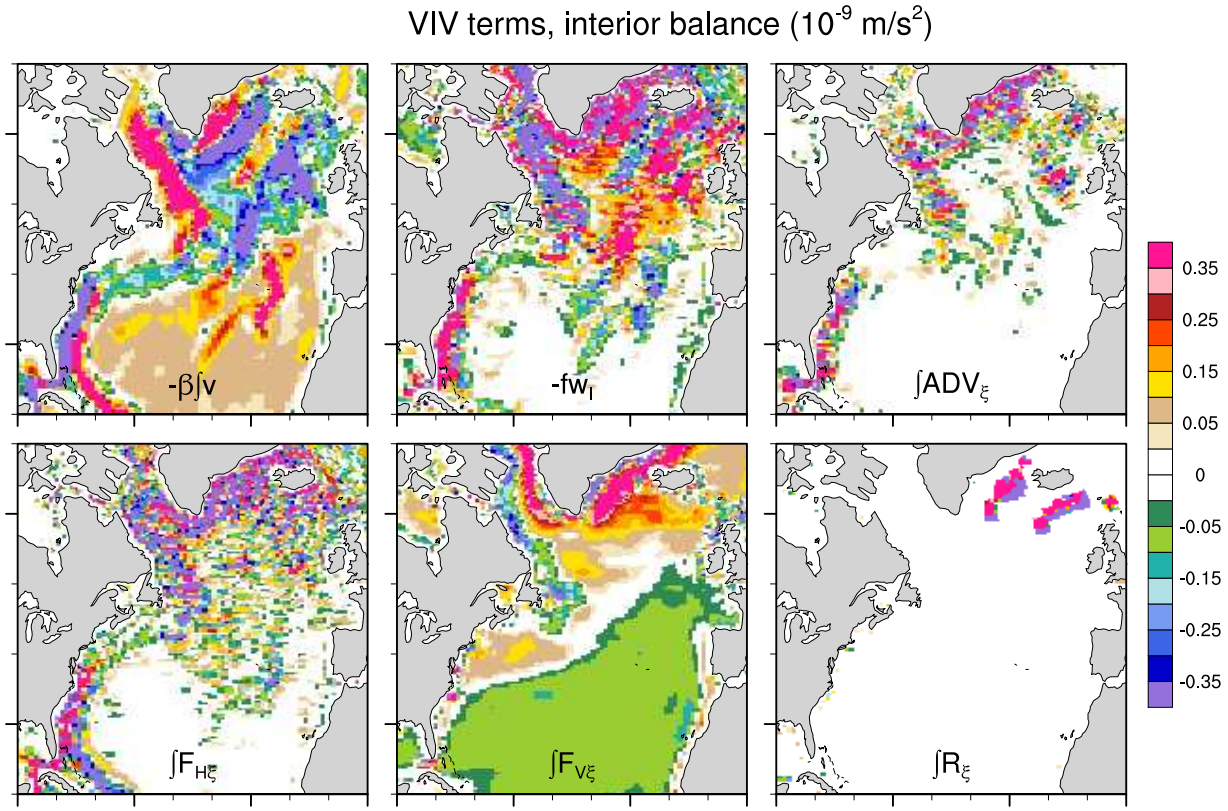

Figure 4.1: Terms in the mean vertically-integrated vorticity (VIV) balance for the ocean interior ($\int_{z=-z_I}^{z=0}$) computed from 50-years of CONTROL (1958-2007). All terms are plotted as RHS values except R_ξ. All fields have been smoothed once with a 9-point spatial filter. The latitude range is 20°N-70°N and the longitude range is 90°W-0°W, with tick marks plotted at 10° intervals.

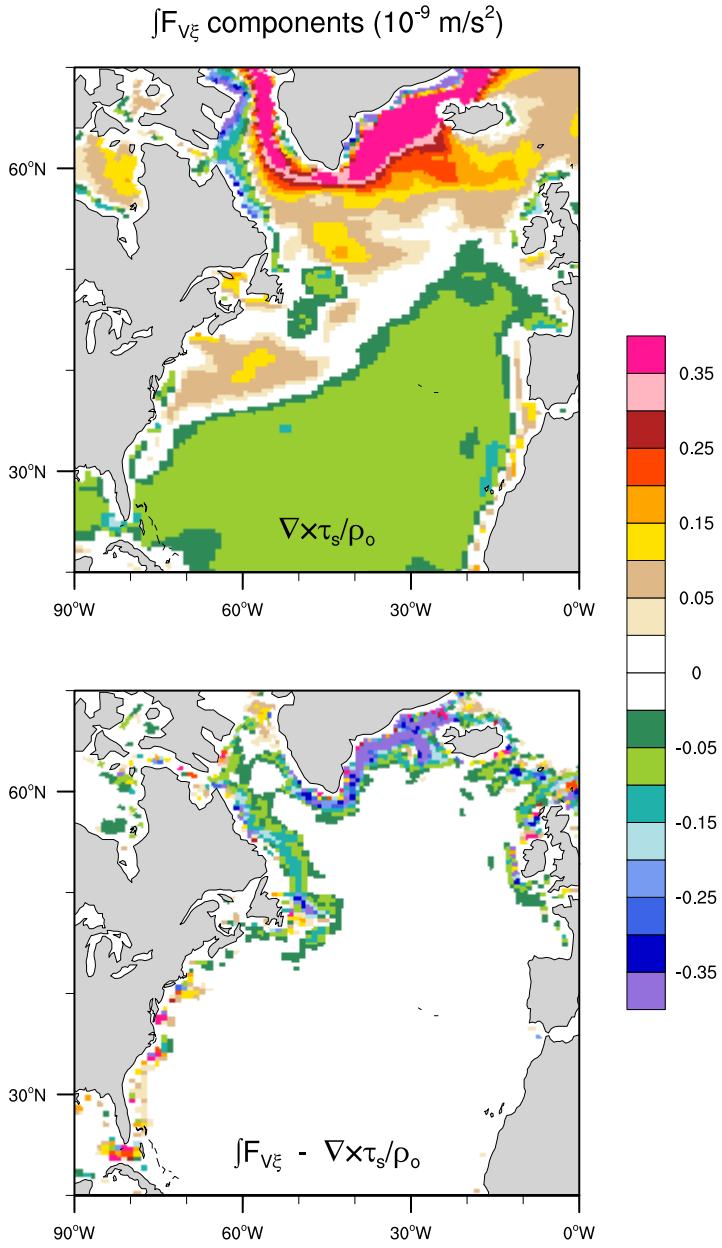

Figure 4.2: Components of the time-mean interior VIV term $\int F_{V\xi}$ from Fig. 4.1: (top panel) surface wind stress curl term ($\frac{1}{\rho_o}\nabla \times \tau_s$); (bottom panel) the topographic shear term ($\nabla \times (-(\overline{\mu \partial_z \mathbf{u}})|_{-z_I})/\rho_o$). See Eqn 4.3.

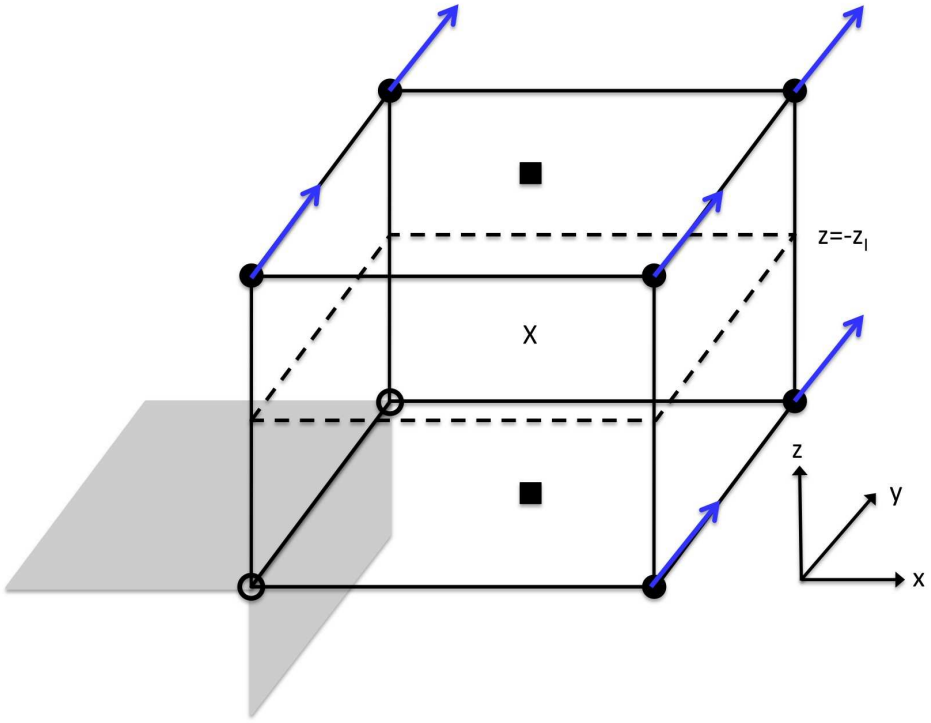

Figure 4.3: Schematic illustrating idealized model Gulf Stream flow in the vicinity of the continental shelf. Circles represent the model U-grid with uniform horizontal velocity $\mathbf{v} = (0, v)$ in the grid-y direction depicted with blue arrows. The open circles (where velocity is zero) represents the ocean-land interface. Vorticity is defined at the T-grid locations indicated by squares, and VIV is defined at the point marked with an X. The dashed square indicates the level defining the bottom of the ocean interior ($z = -z_I$), with BVS ($-fw_I$) and $\nabla \times (\overline{\mu \partial_z \mathbf{u}})|_{-z_I}$ defined at this level at X. Note that the grid cell drawn (solid lines) corresponds to VIV, and that it is centered at the vertical interface between model T-grid cells.

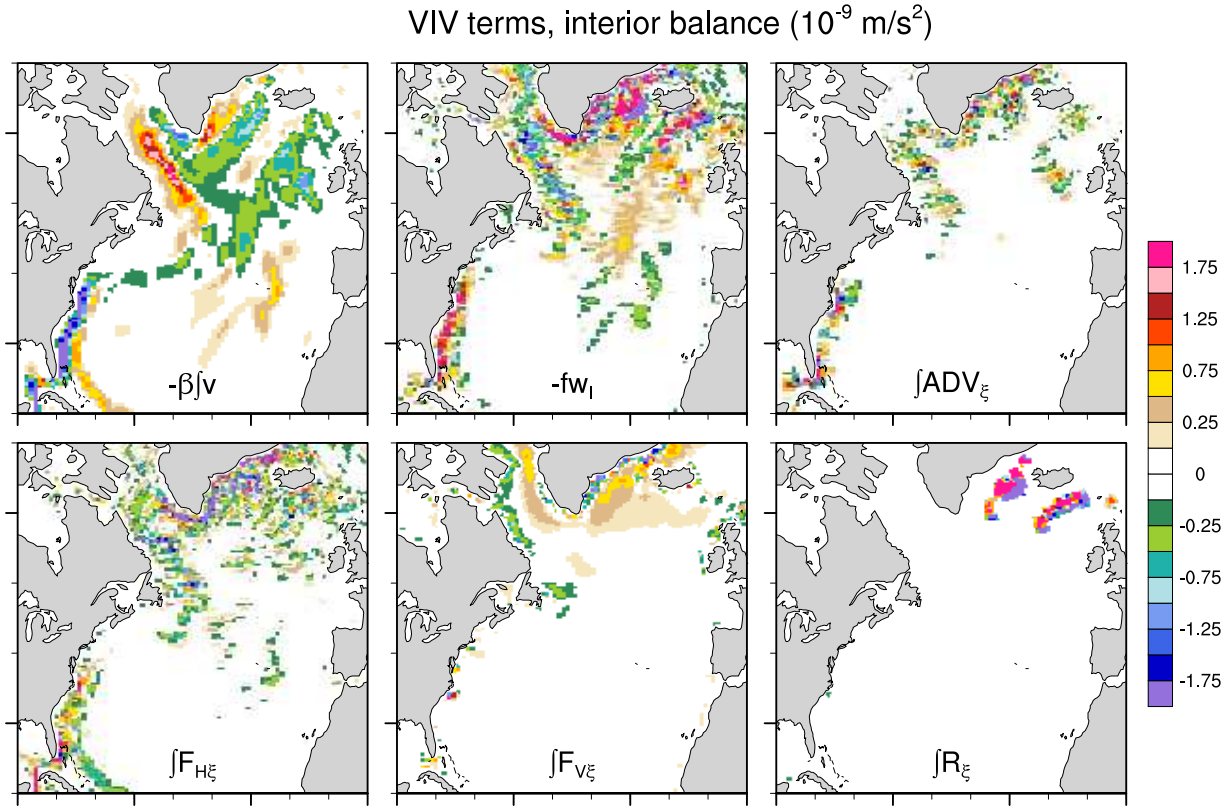

Figure 4.4: Identical to Figure 4.1, but rescaled to highlight large magnitudes.

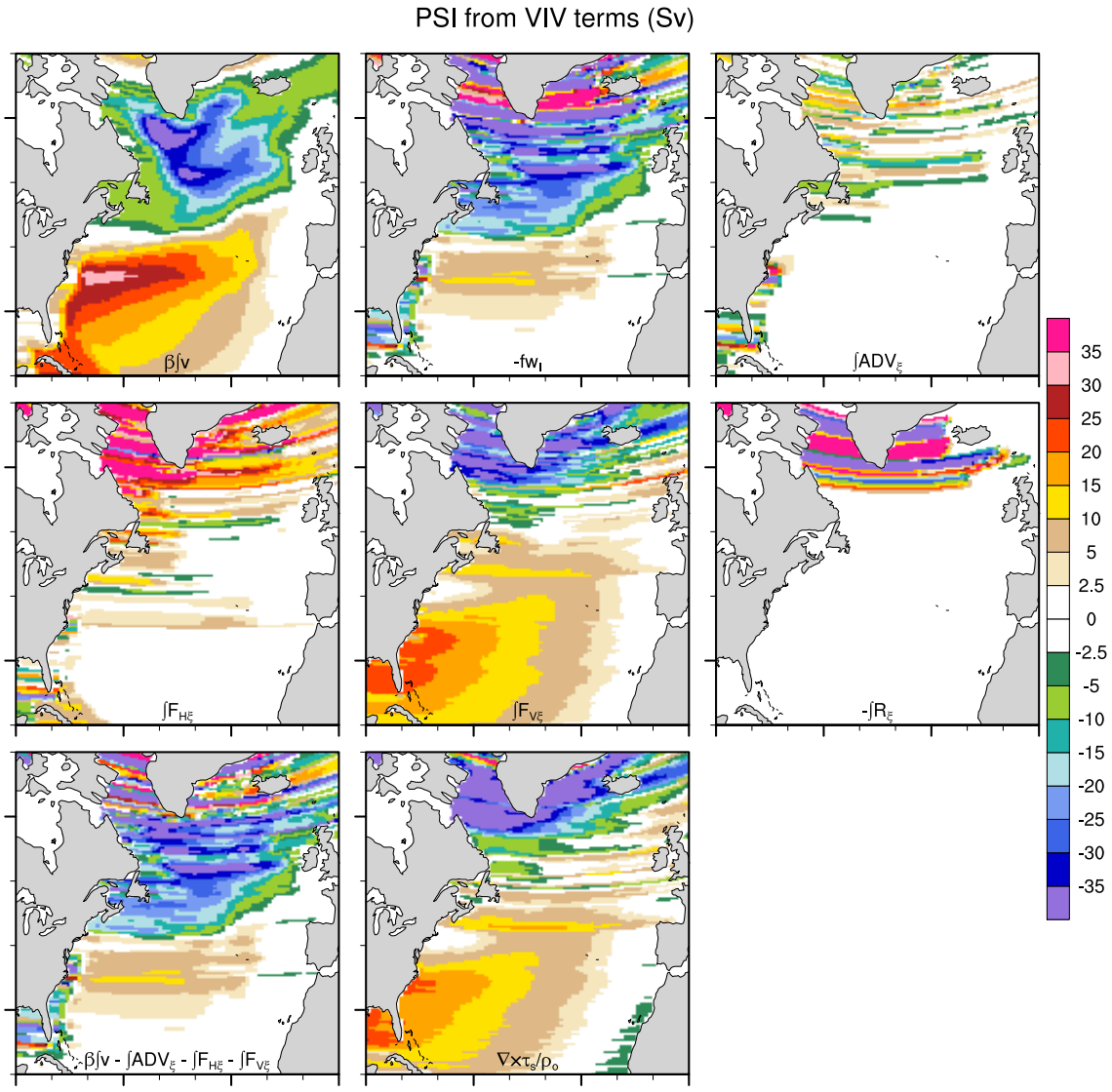

Figure 4.5: Barotropic streamfunction components computed by zonally integrating the VIV terms from Eqn $C.25$ (Fig. 4.1) along the model grid-x direction from the eastern boundary after 3 smoothing passes with a 9-point spatial filter. All terms are RHS except $\beta \int v$. The top six panels show the terms in Eqn 4.5; the lower left panel shows the streamfunction associated with the BVS term $(-fw_I)$ assuming zero residual; and, the bottom right panel shows the component of the $\int F_{V\xi}$ streamfunction associated with surface wind stress curl.

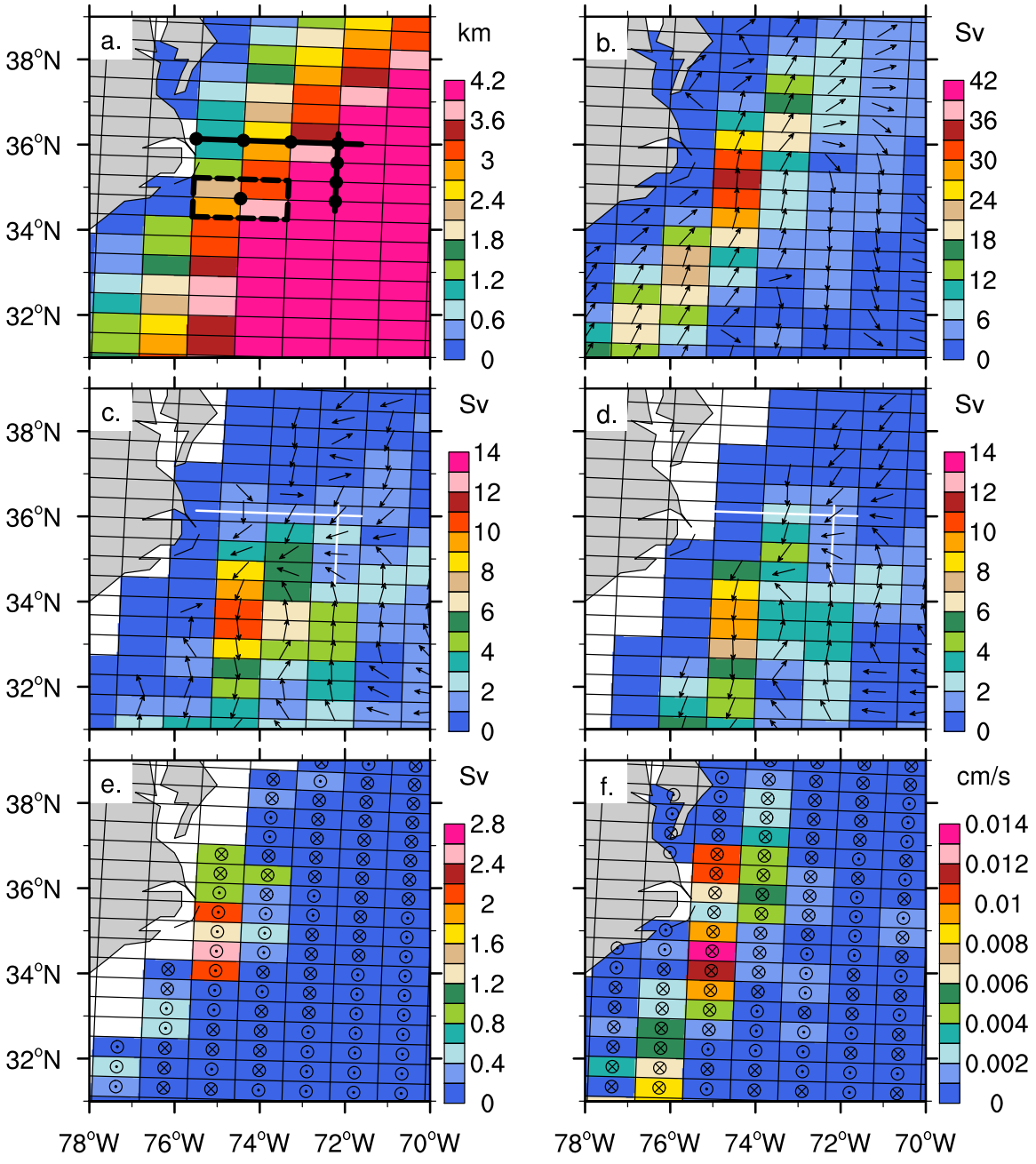

Figure 4.6: Figure 14 from Yeager and Danabasoglu (2012) showing model topography (a) for tracer grid cells in the vicinity of Cape Hatteras (color fill, in km). The black lines indicate tracer cell boundaries, which intersect at model velocity points. The remaining panels are vector plots (magnitude in color and direction given by arrows) of the following time-average fields from a fully-coupled CCSM4 simulation: b) depth-integrated volume transport above 744-m depth (Sv), c) depth-integrated volume transport below 744-m depth (Sv), d) depth-integrated volume transport below 1665-m depth (Sv), e) vertical volume transport at 744-m depth (Sv), f) vertical velocity at the bottom (w_b, in cm s^{-1}). The black lines in panels b-d demarcate model velocity grid cells. The symbols $\otimes$ and $\odot$ indicate downwelling and upwelling, respectively.

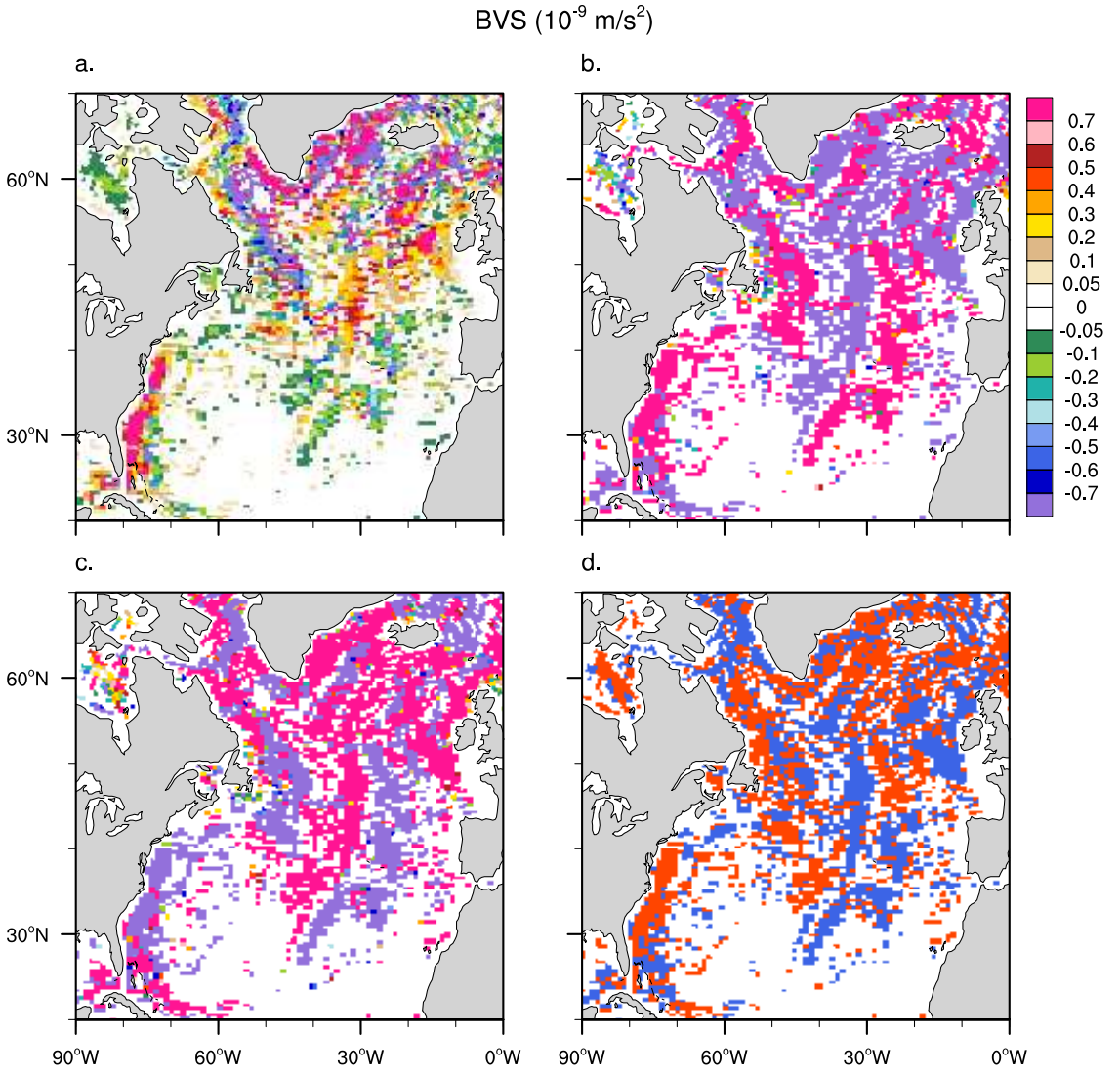

Figure 4.7: Terms from the time-mean vertically-integrated topographic vorticity equation (Eqn *C*.24): (a) BVS ($-fw_I$) (LHS), (b) sum of RHS using barotropic pressure, (c) sum of RHS using baroclinic pressure, (d) map of where barotropic (red) and baroclinic (blue) pressure torque terms dominate and thus determine the sign of time-mean BVS. See text for explanation.

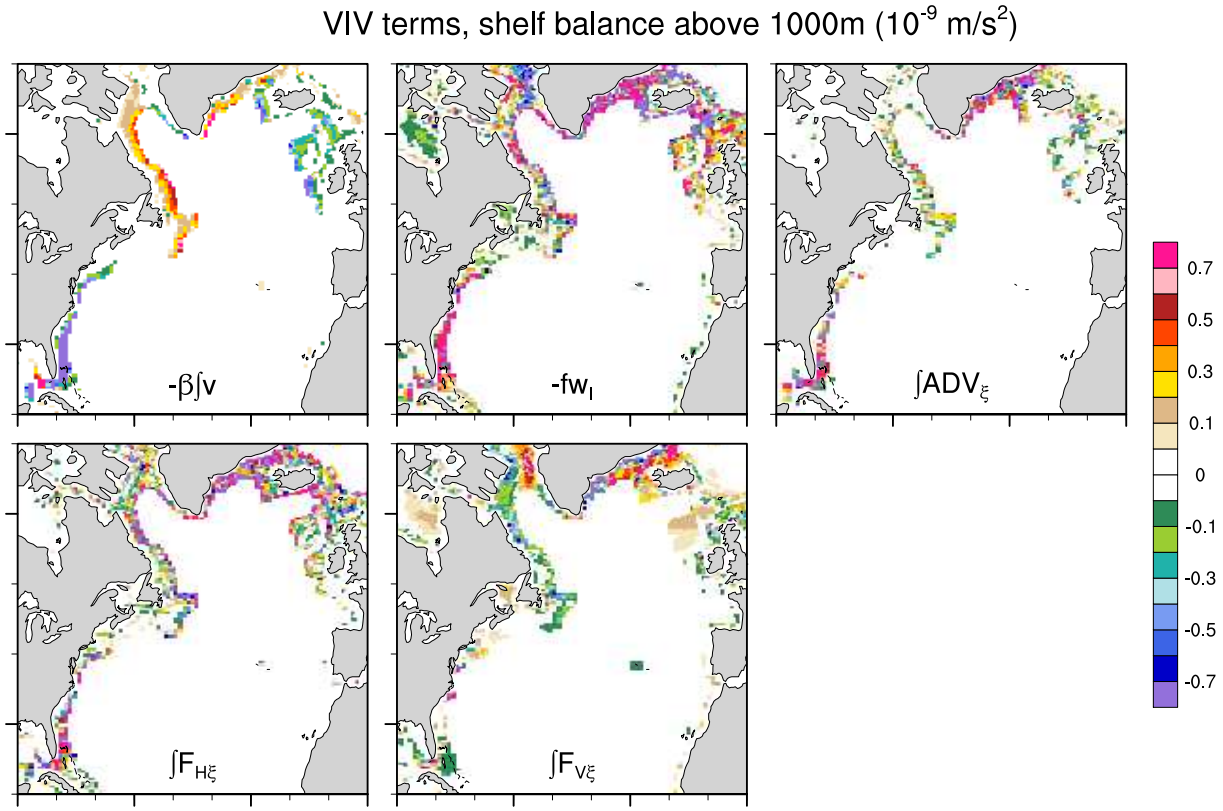

Figure 4.8: Terms in the mean vertically-integrated vorticity (VIV) balance for the ocean interior above 1000m depth along the continental shelf (Eqn 4.9: $\int = \int_{z=-z_I}^{z=0}$, where $z_I \leq 1000m$) computed from 50-years of CONTROL (1958-2007). All terms are plotted as RHS values and we ignore R_ξ. All fields have been smoothed with a 9-point spatial filter.

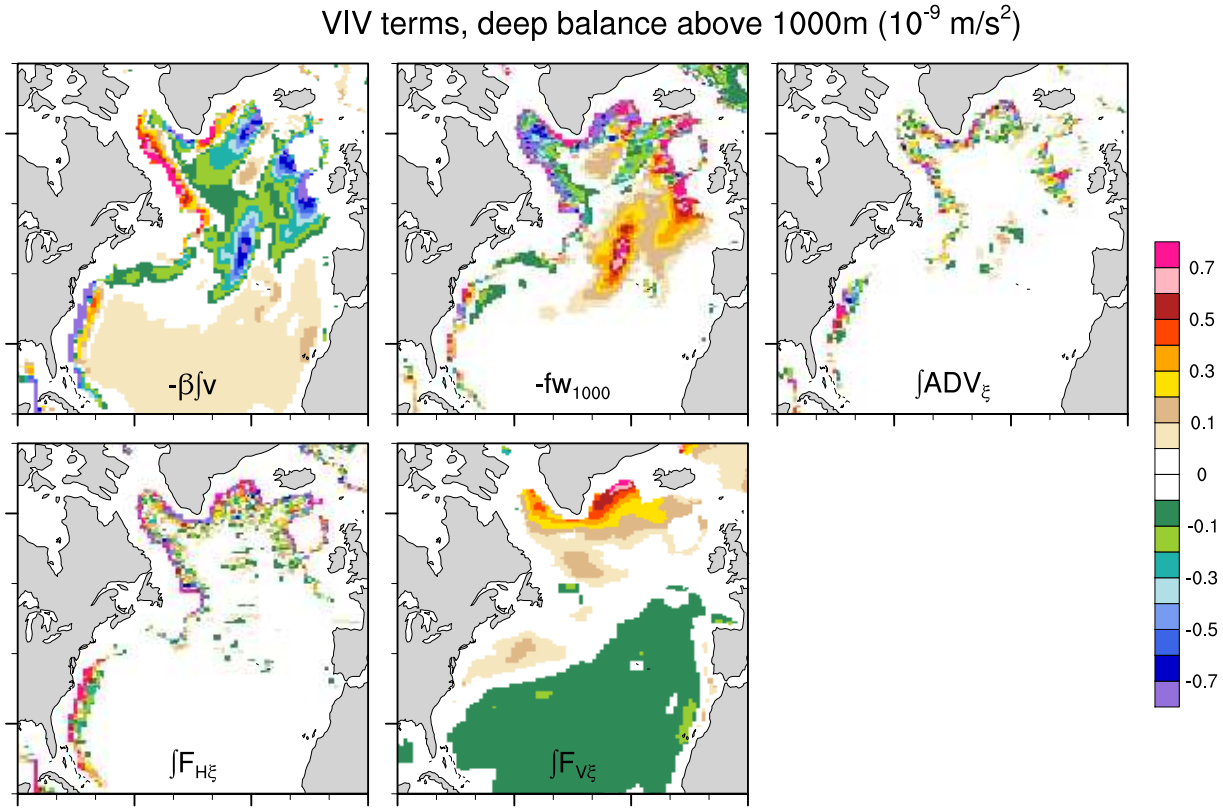

Figure 4.9: As in Figure 4.8, but for the ocean interior above 1000m in deep ocean regions (Eqn 4.10: $\int = \int_{z=-1000}^{z=0}$, where $z_I > 1000m$).

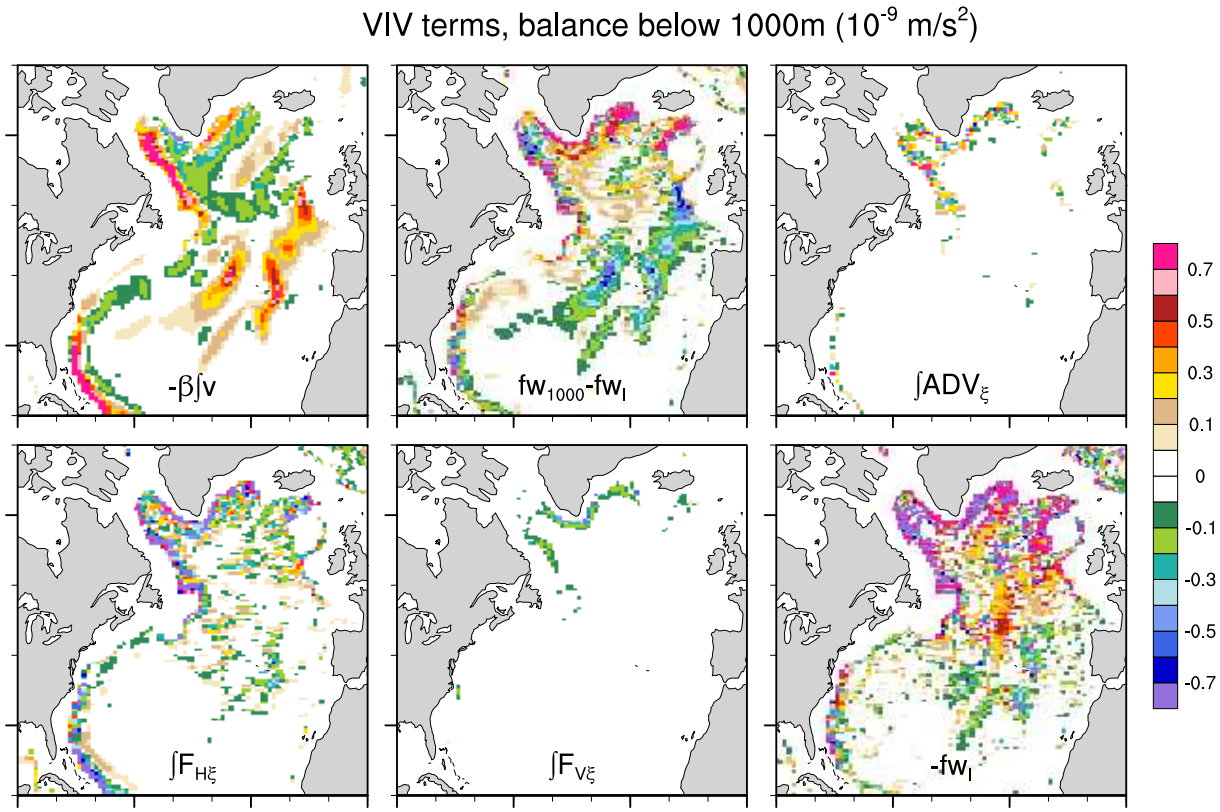

Figure 4.10: As in Figure 4.8, but for the ocean interior below 1000m (Eqn 4.11: $\int = \int_{z=-z_I}^{z=-1000}$, where $z_I > 1000m$). For reference, we show BVS ($-fw_I$) separately for this region.

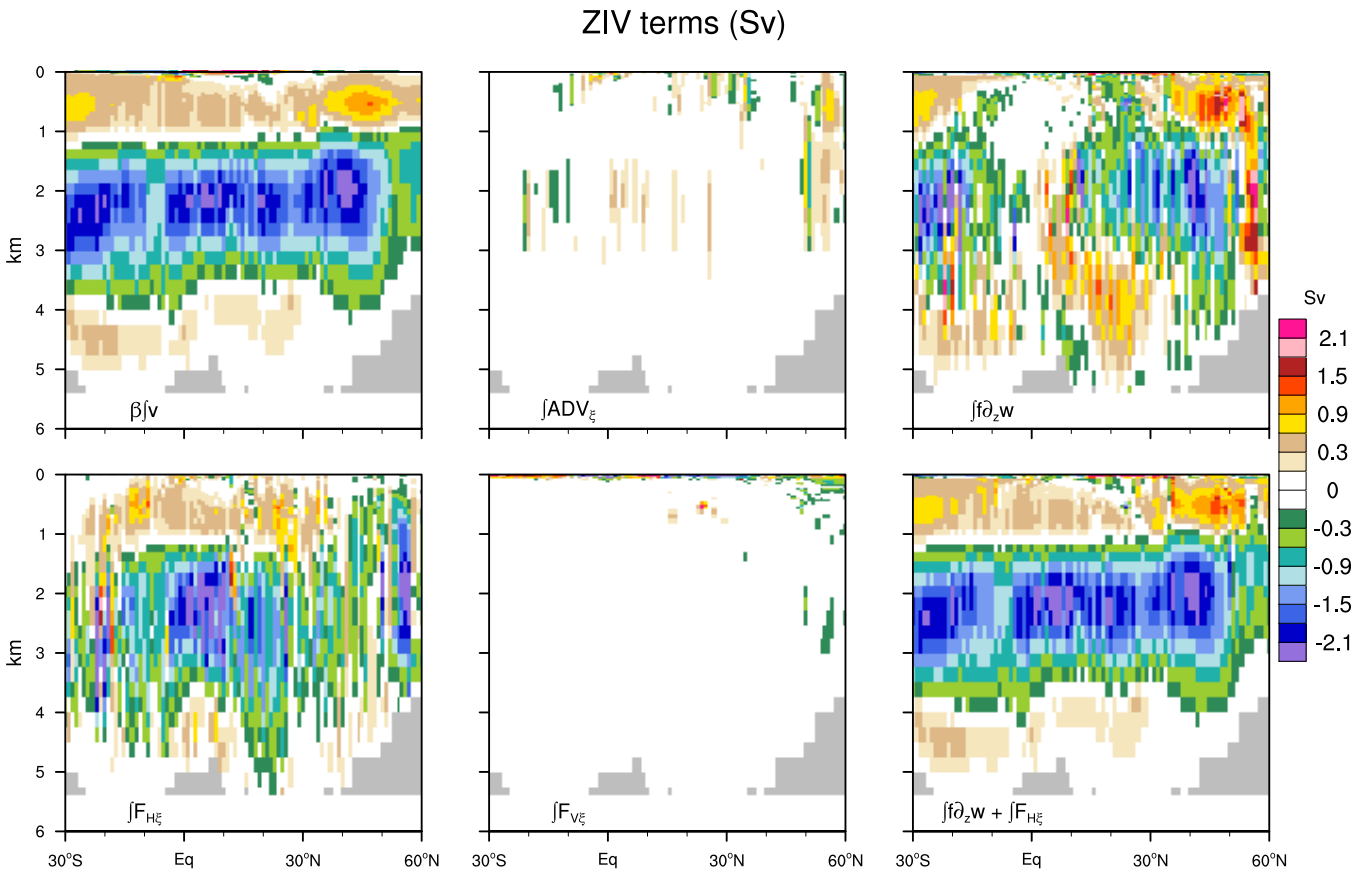

Figure 4.11: Terms in the mean zonally-integrated vorticity (ZIV) balance for the Atlantic ocean interior (Eqn 4.14: $\int = \int_{x=x_w}^{x=x_e}$). All terms are plotted as RHS values except $\beta \int v$ and we ignore R_ξ.

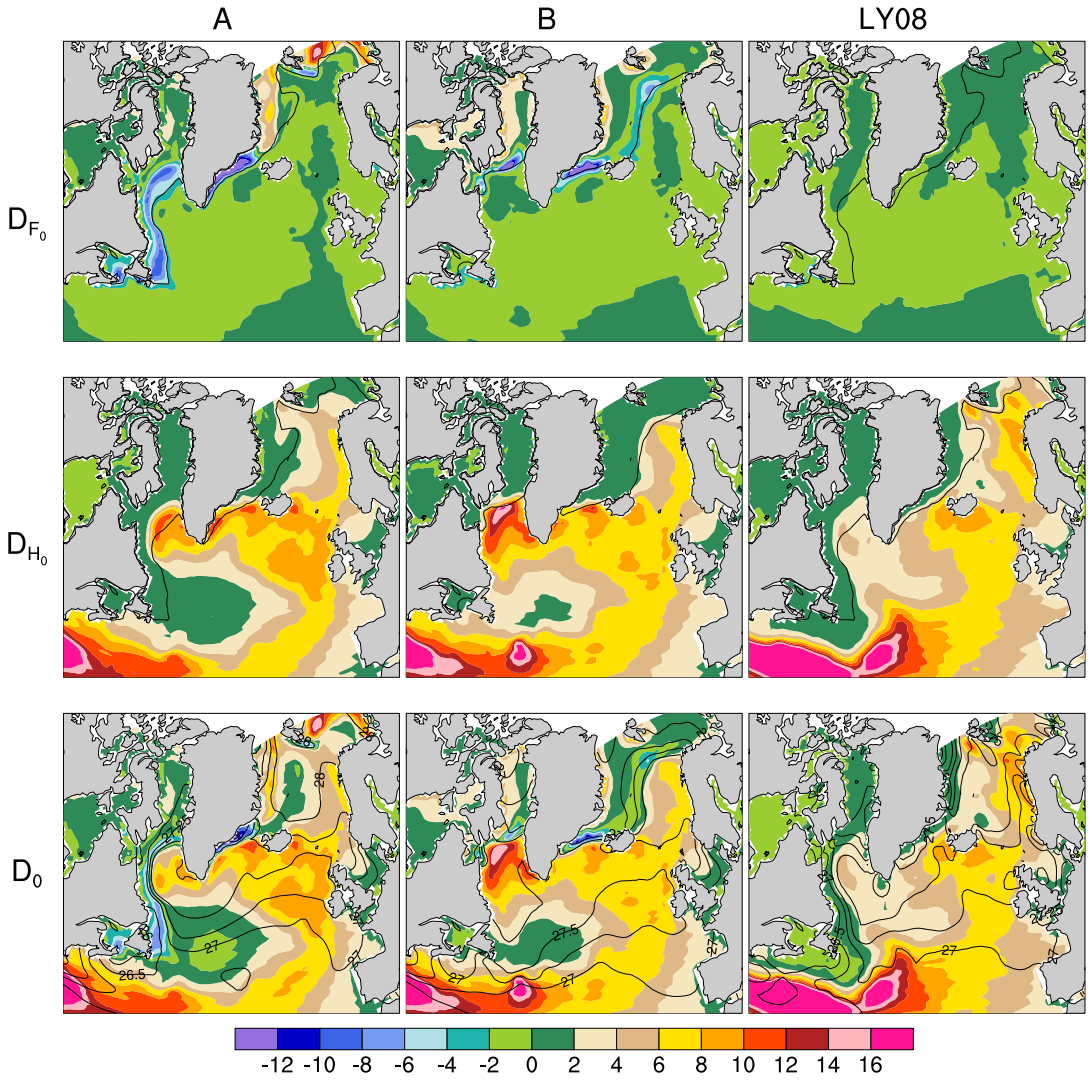

Figure 4.12: Figure 11 from Yeager and Jochum (2009). Mean February surface density flux (averaged over simulation years 16-20, corresponding to historical years 1964-1968) from experiment A (left column; see Appendix *D*), experiment B (middle column; "B_YJ09", see Appendix *D*), and computed from the Large and Yeager (2008) monthly surface flux dataset (right column). The haline and thermal components of the density flux are shown in the top and middle rows, respectively, while the net density flux is shown in the bottom row. Density flux units are kg/m^2/s. The 5-year mean February 15% sea ice fraction contour is overlayed on the plots of D_{F_0} and D_{H_0}. Sea surface density contours (kg/m^3) are overlayed on the D_0 plot.

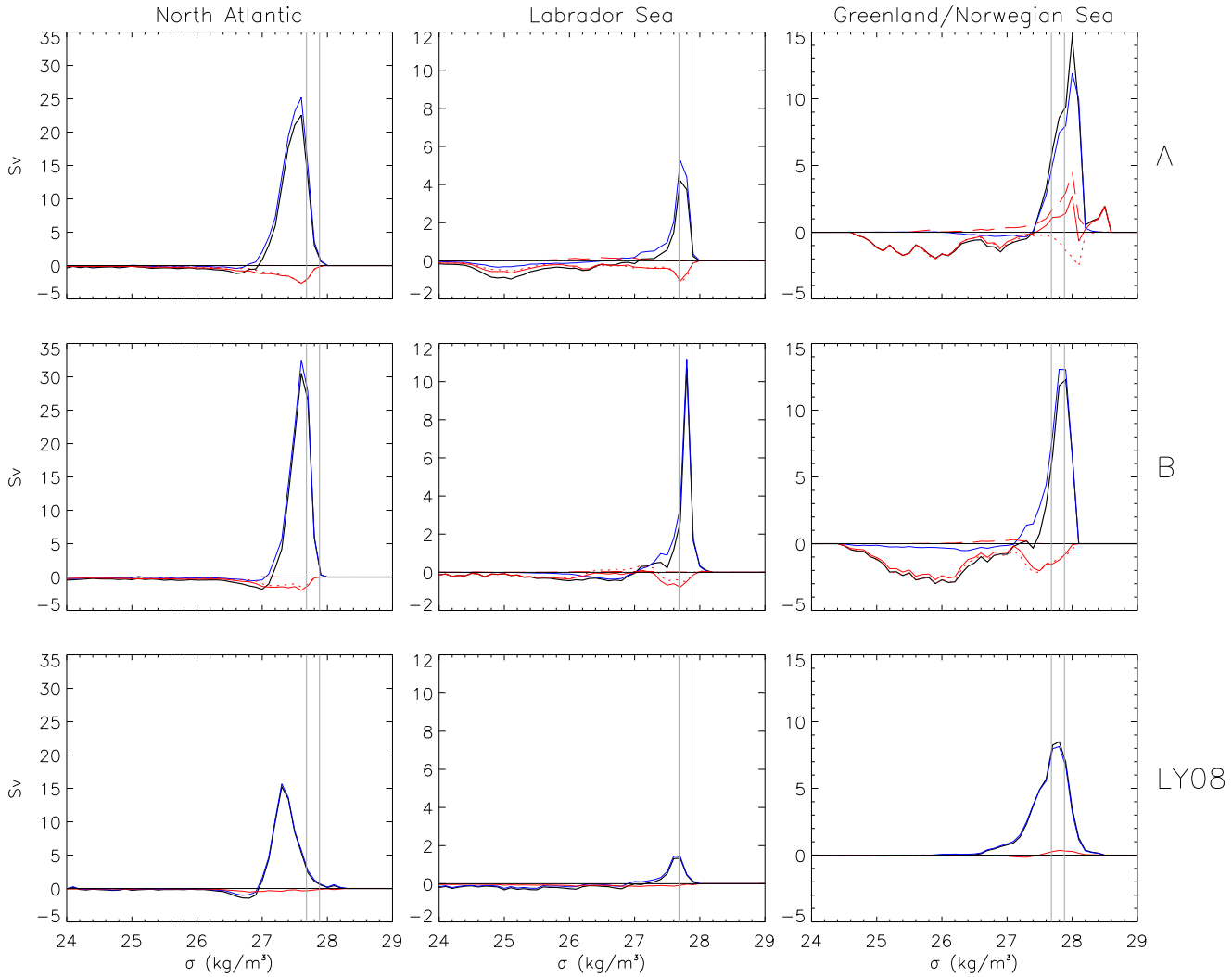

Figure 4.13: Figure 12 from Yeager and Jochum (2009). Mean surface water mass transformation rates computed from years 16-20 (forcing years 1964-1968) of experiment A (top panels), B_YJ09 (middle panels), and the LY08 flux dataset (bottom panels) for 3 regions as a function of sea surface density. The components plotted are as follows: thermal (blue), haline (red), and total (black). The two dominant components of the haline transformation are also shown: melt flux (red, dotted) and frazil ice formation flux, F_F, (red, long dashed). The LY08 surface fluxes exclude ice melt and formation fluxes. The densities σ_0 =27.68 kg/m^3 and σ_0 =27.88 kg/m^3 are marked in grey to indicate the approximate density bounds of observed DWBC flow east of Grand Banks (Schott et al., 2006).

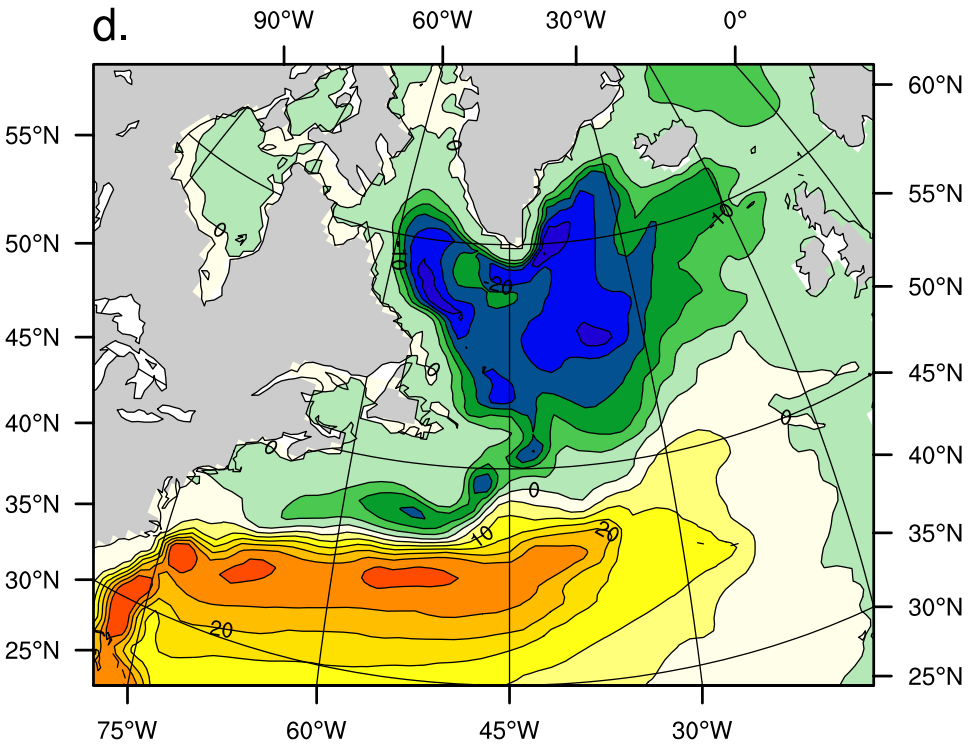

Figure 4.14: Panel from Figure 2 of Yeager and Jochum (2009). Mean barotropic streamfunction (Sv) from experiment B_YJ09 corresponding to simulation years 54-58 (forcing years 2002-2006). The contour interval is 5 Sv.

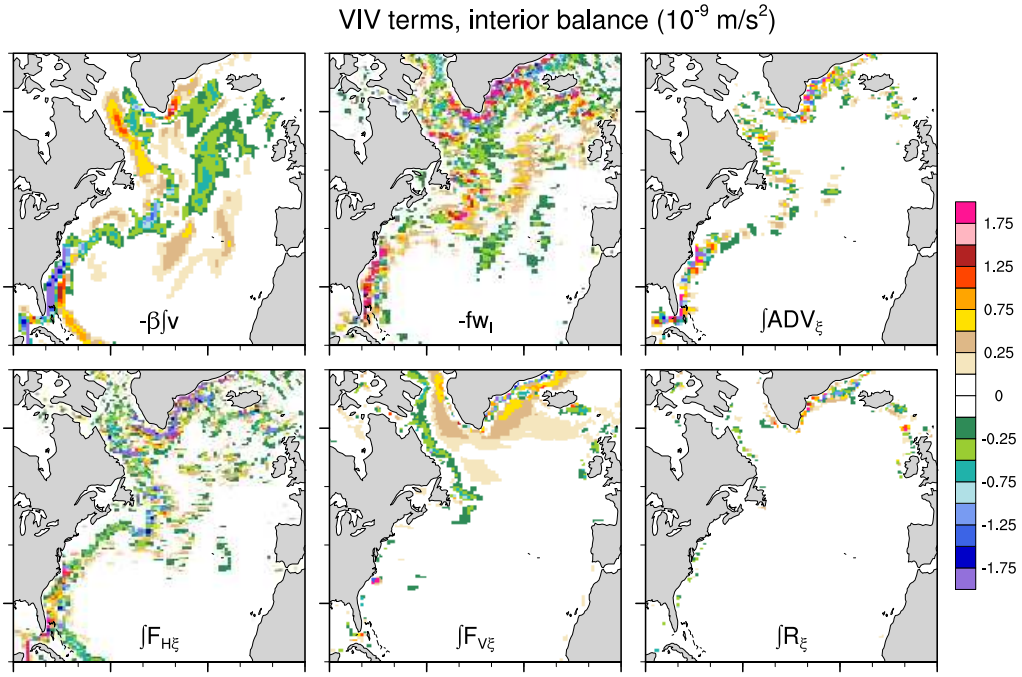

Figure 4.15: As in Figure 4.4 but based on a 5-year (2002-2006) mean from simulation B_YJ09.

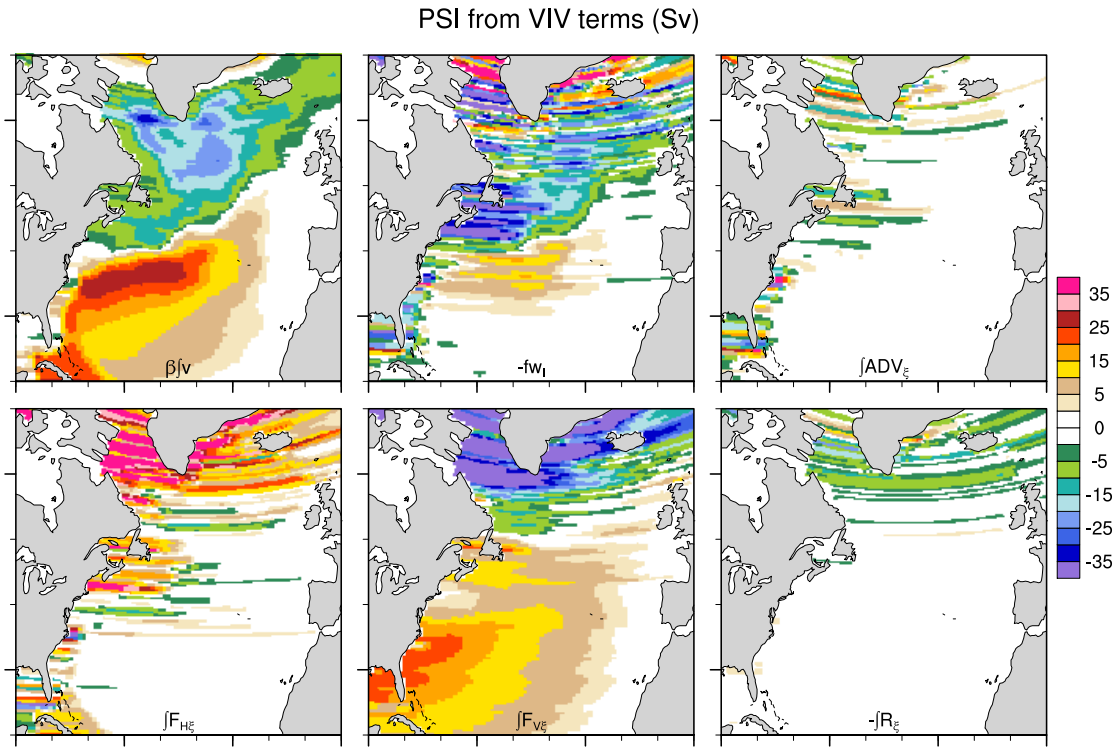

Figure 4.16: As in Figure 4.5 but based on a 5-year (2002-2006) mean VIV from simulation B_YJ09.

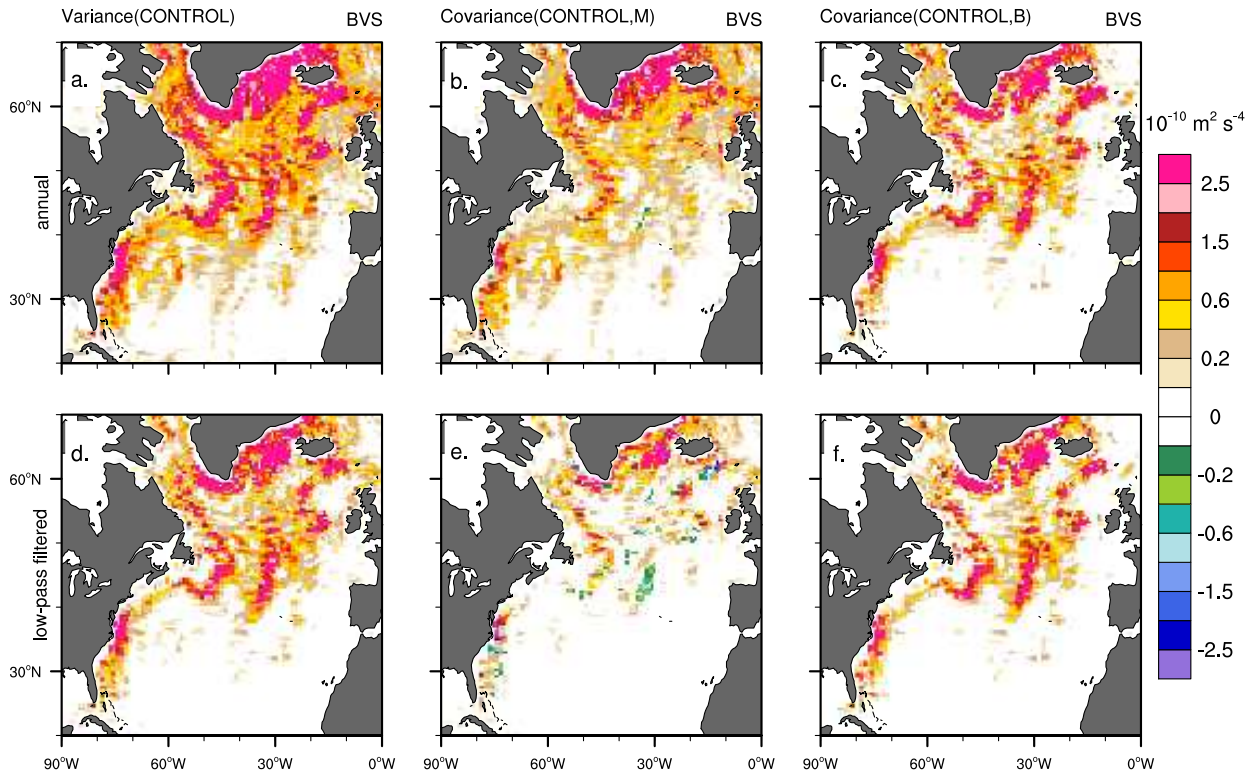

Figure 4.17: As in Figure 3.4, but for the barotropic vorticity forcing associated with vertical velocity at the bottom of the ocean interior, BVS ($-fw_I$): (a) interannual variance from CONTROL, (b) interannual covariance between CONTROL and M, and (c) interannual covariance between CONTROL and B. Panels (d)-(f) are identical, but the fields have been temporally smoothed with a 15-point lanczos filter with cutoff period of 7 years prior to computing (co)variances. The annual variance (a)-(c) includes variance on all interannual timescales. The sum of M and B covariances reproduces the CONTROL variances in (a),(d). The analysis here is based on 54-year time series corresponding to forcing years 1958-2011.

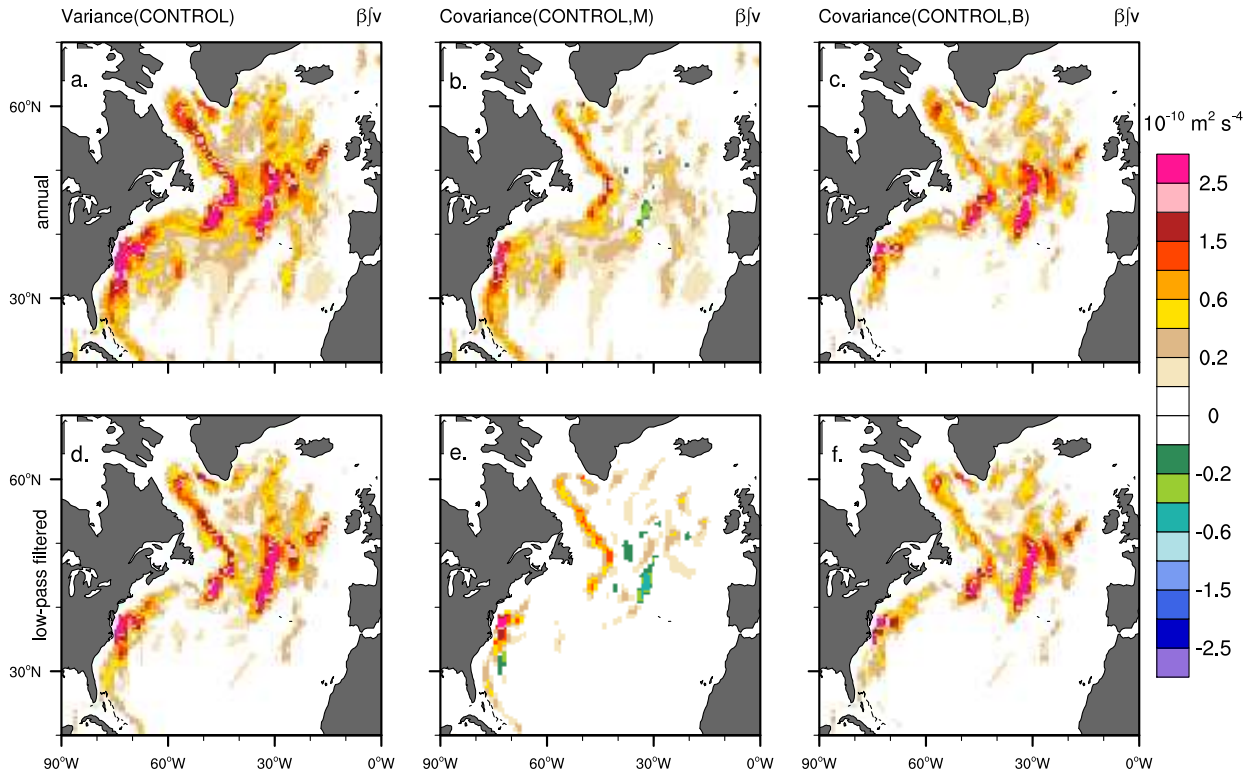

Figure 4.18: As in Figure 4.17, but for the vertically-integrated advection of planetary vorticity: $\beta \int v$.

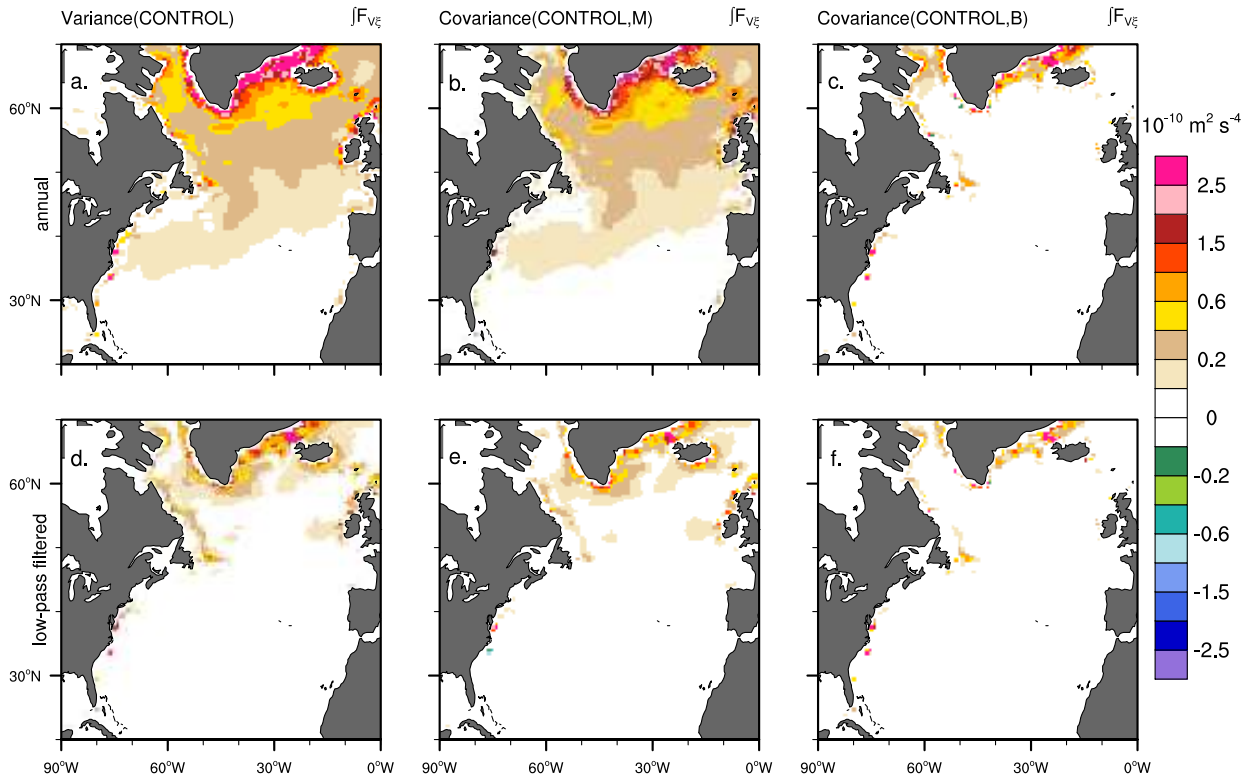

Figure 4.19: As in Figure 4.17, but for the vertically-integrated vorticity term associated (primarily) with surface wind stress curl: $\int F_{V\xi}$.

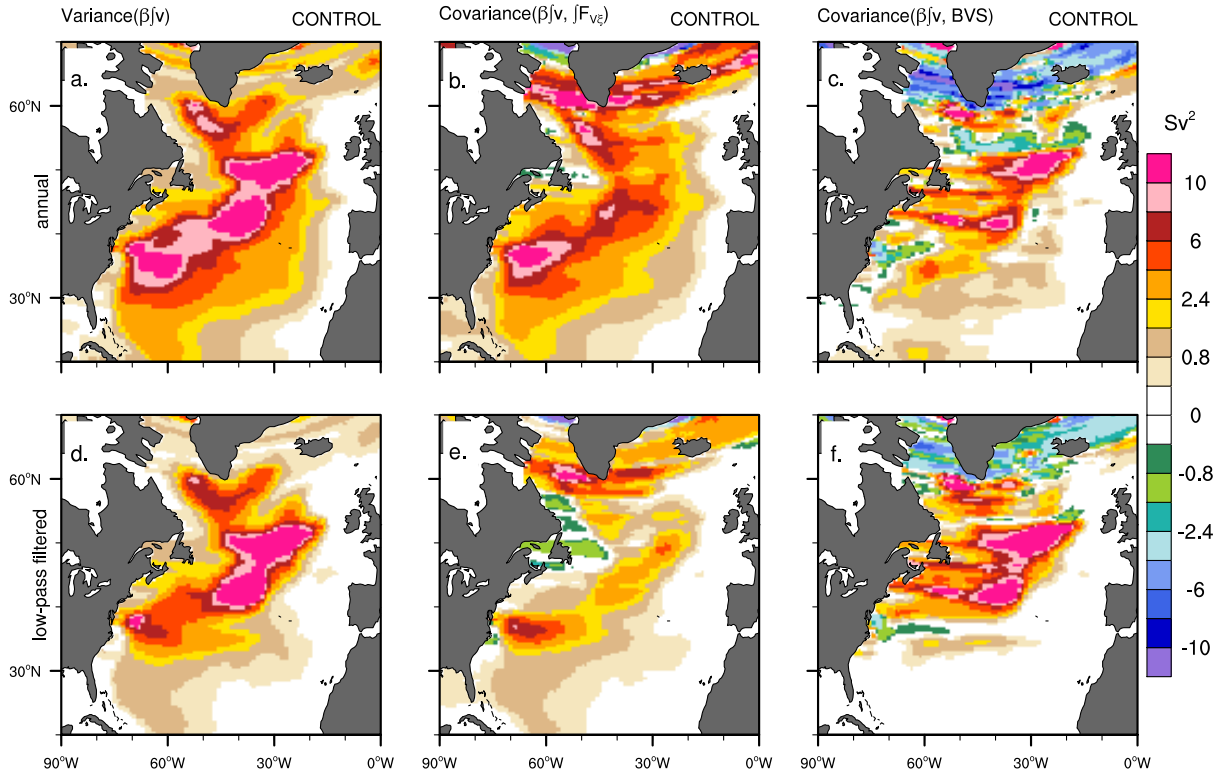

Figure 4.20: Variance of BSF (computed as a zonal integral of VIV) from CONTROL and the dominant contributors to that variance based on Eqn 4.5: (a) interannual variance of BSF computed from $\beta \int v$, (b) covariance of $\beta \int v$ and $\int F_{V\xi}$, (c) covariance of $\beta \int v$ and BVS $(-fw_I)$. Panels (d)-(f) are identical, but the fields have been temporally smoothed with a 15-point lanczos filter with cutoff period of 7 years prior to computing (co)variances.

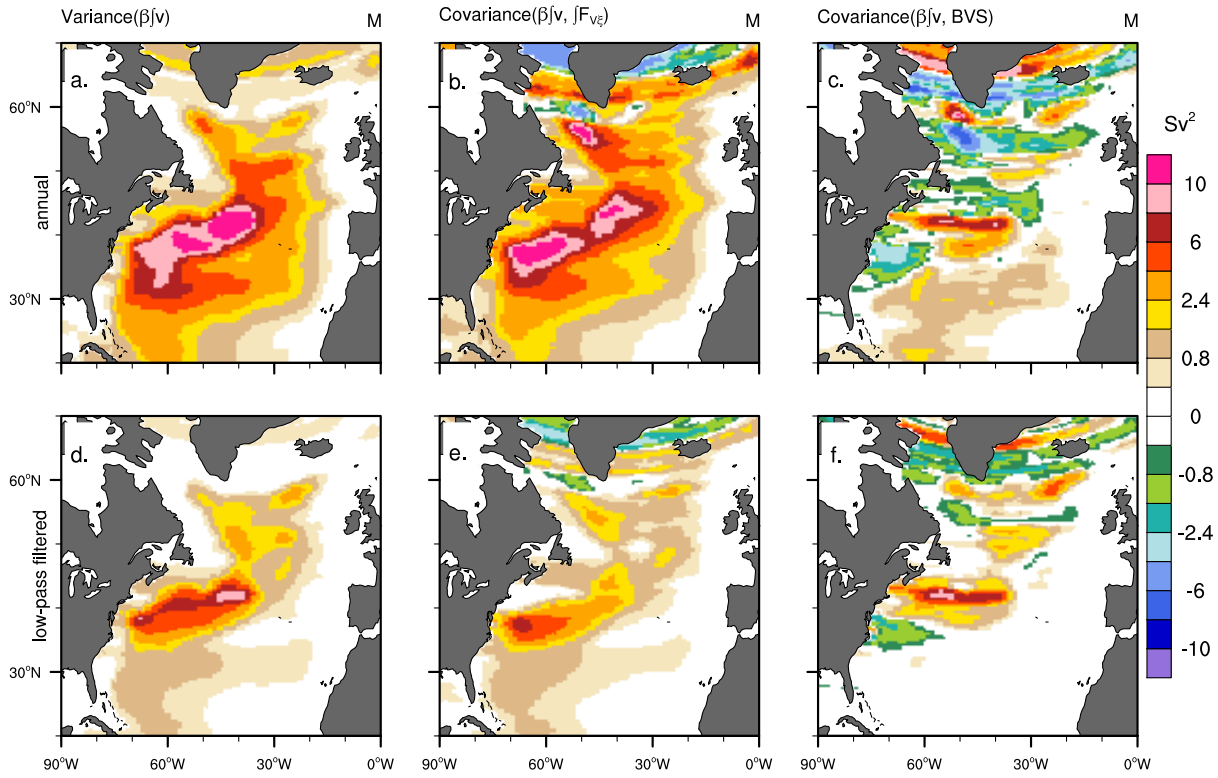

Figure 4.21: As in Figure 4.20, but for experiment M.

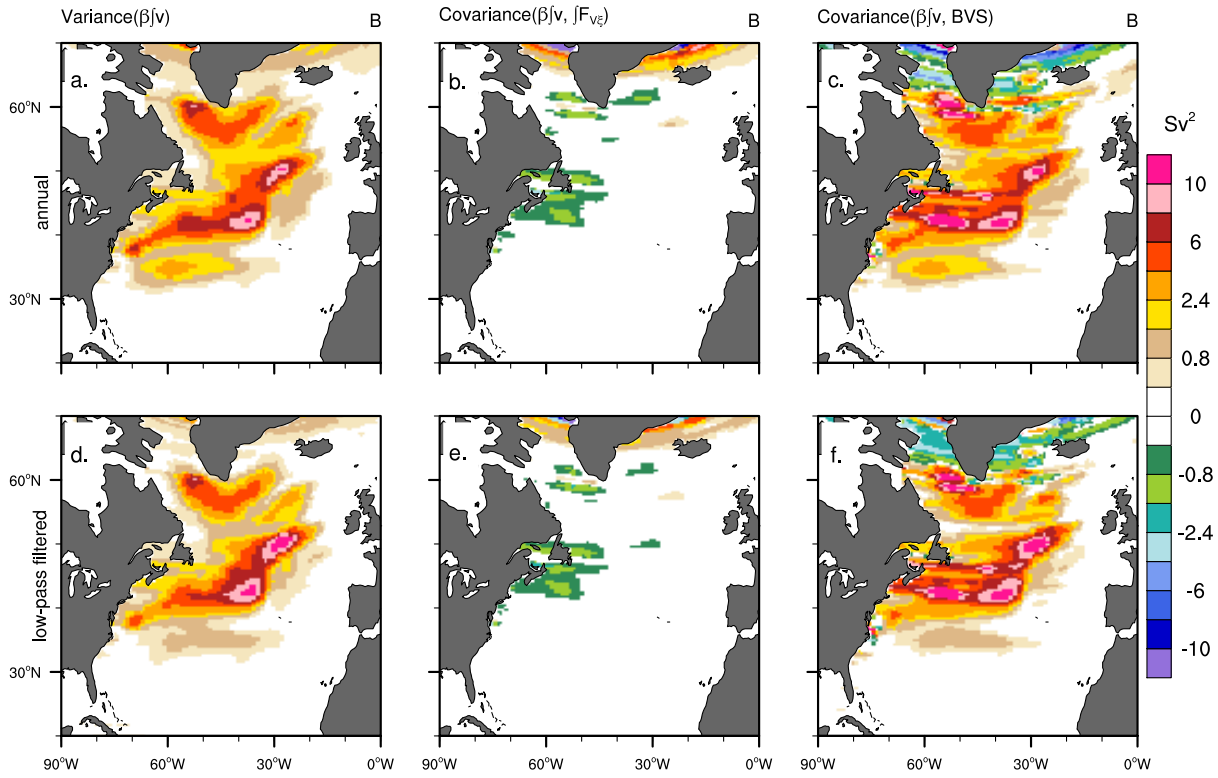

Figure 4.22: As in Figure 4.20, but for experiment B.

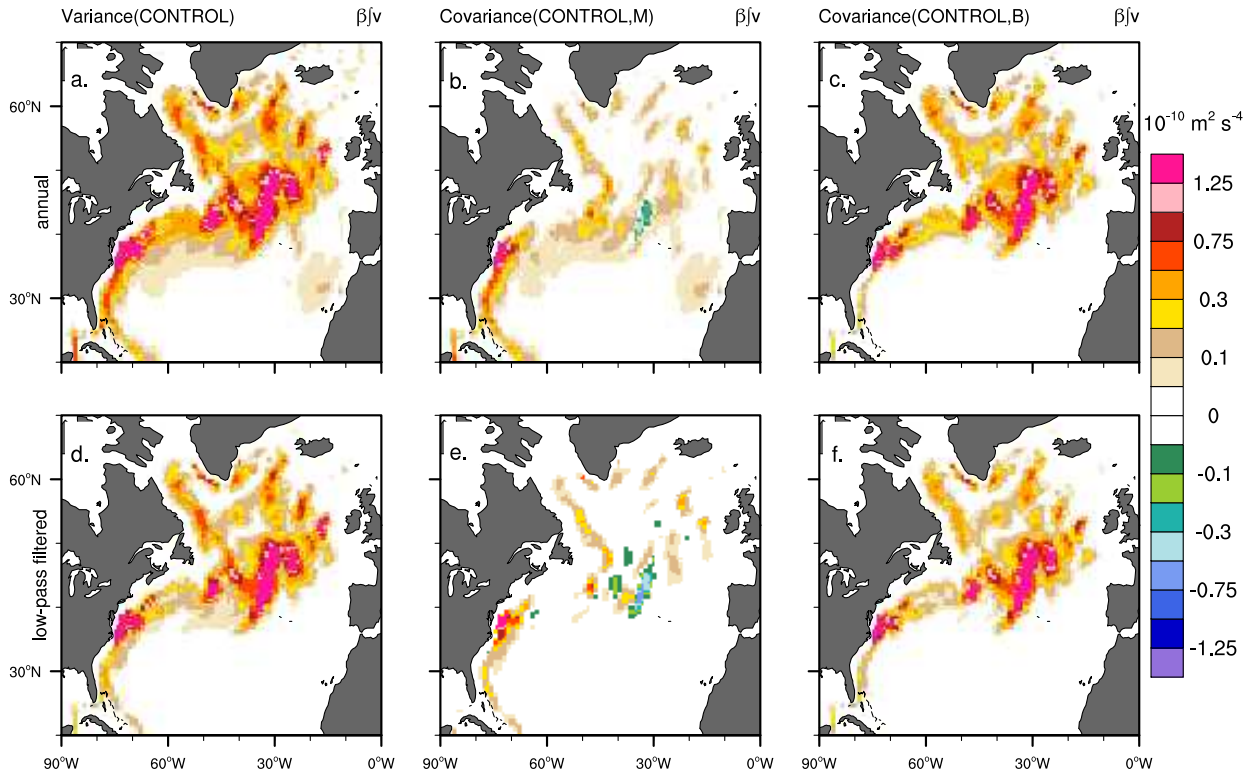

Figure 4.23: As in Figure 4.18, but for the vertically-integrated advection of planetary vorticity ($\beta \int v$) in the upper layer (z$\leq$1000m; including shelf flow).

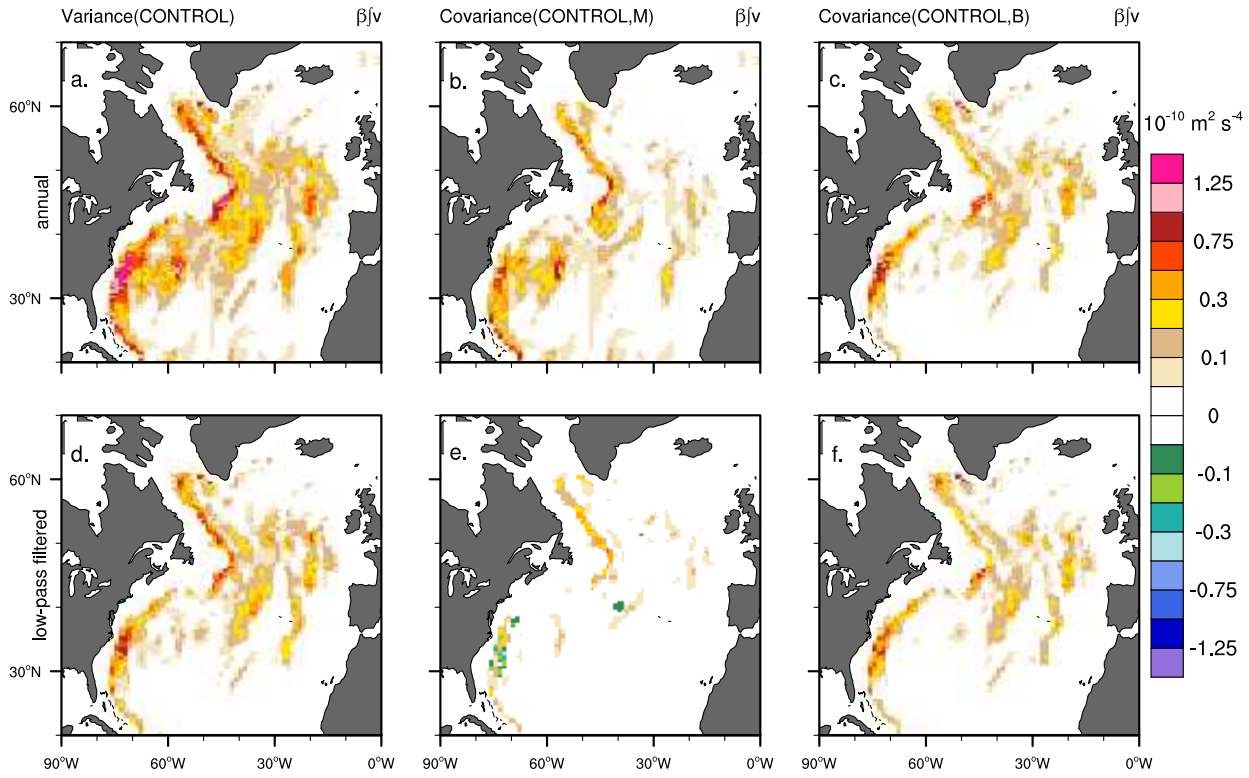

Figure 4.24: As in Figure 4.18, but for the vertically-integrated advection of planetary vorticity ($\beta \int v$) in the lower layer (z > 1000m).

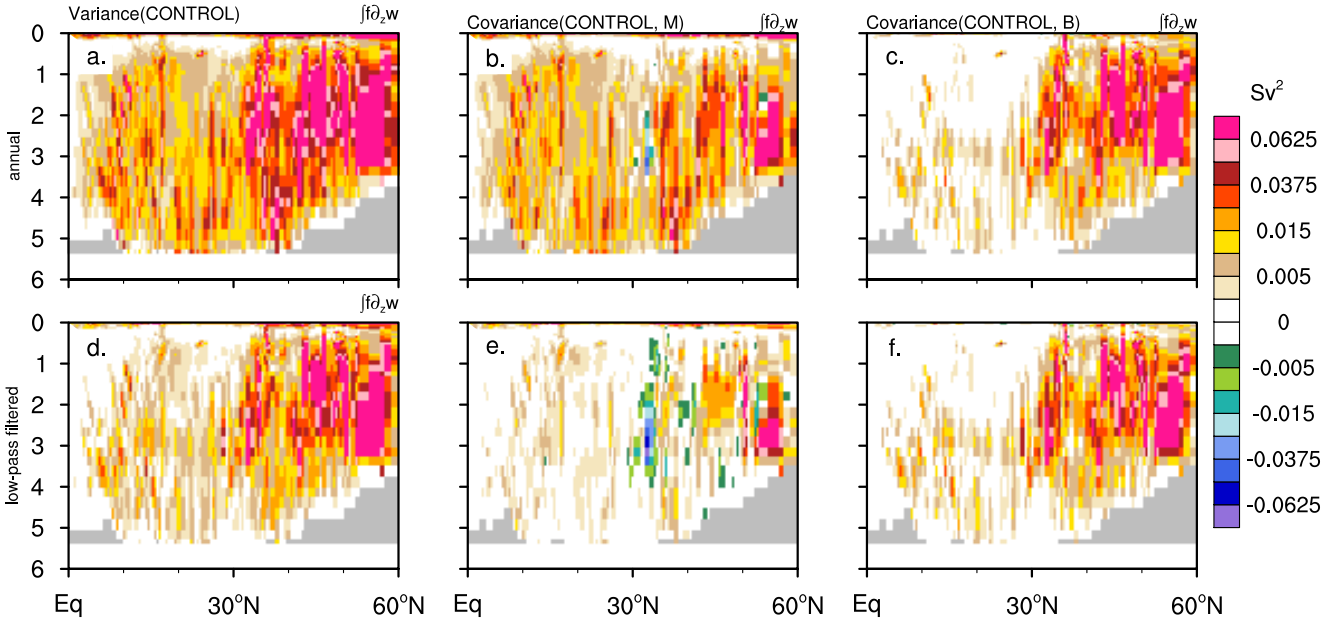

Figure 4.25: As in previous Figure, but for the zonally-integrated planetary vorticity stretching term: $\int f \frac{\partial w}{\partial z}$ (see Eqn 4.14, Fig. 4.11).

Chapter 5

Decadal prediction of North Atlantic SST

Nascent efforts to use historically-initialized CGCMs to predict near-term climate variations (with lead times of up to several decades) rely on two primary sources of skill: 1) the relatively well-constrained near-term trajectory of anthropogenic emissions and thus external forcing of the climate system, and 2) the memory of the climate system which largely resides in the ocean. In this chapter, we will show that the persistence of buoyancy-forced ocean density and circulation anomalies in the mid- to high-latitude North Atlantic is the most significant contributor to decadal prediction (DP) skill in that region in the CESM1 decadal prediction system. Furthermore, we will argue that skill in this region is mainly inhibited by poor heat flux prediction, and that this can be traced to fundamental errors in low-frequency air-sea coupling in CESM1.

5.1 Retrospective decadal prediction using initialized coupled ensembles of CESM1

Decadal climate prediction is a relatively new and burgeoning field of climate science made possible by improvements in CGCMs, advances in computing, and just as importantly, by developments in the Earth observing system and the techniques for transforming those observations into global climate (and in particular, ocean) state estimates (see Chapter 2). The Coupled Model Intercomparison Project Phase 5 (CMIP5) of the World Climate Research Programme (WCRP) proposed a set of coordinated initialized DP experiments for inclusion in the IPCC AR5. This has spurred international efforts to scope out the feasibility of providing advance notice of changes in

regional hurricane activity, rainfall, or the likelihood of extreme events such as severe heat waves (Meehl et al., 2009, 2013).

The premise behind DP is that there is potential to improve climate predictions, and in particular regional predictions, on timescales of up to a few decades by reducing the forecast uncertainty associated with intrinsic climate variability (Hawkins and Sutton, 2009). This can be achieved by initializing CGCM simulations with fields that reflect the current observed state of the Earth system, thereby synchronizing the slowly-evolving internal variability of the model with that of Nature. It has been shown that historical initialization does indeed increase model skill at predicting surface temperature change above the level that can be achieved using realistic external forcing alone, and that the increase in skill is particularly high in the North Atlantic region (e.g., Smith et al. (2007); Keenlyside et al. (2008); Pohlmann et al. (2009)).

Yeager et al. (2012) examined the North Atlantic evolution of a set of CMIP5 retrospective DP experiments which were run using the CESM1 model. The experiment set consisted of ten-member fully-coupled ensembles initialized at ten different start times separated by five year intervals (1961, 1966, 1971, ..., 2006). A total of 100 coupled simulations were analyzed, and all of these were integrated for at least 10 years. A CORE-forced ocean–sea-ice hindcast simulation (negligibly different from the CONTROL experiment of Appendix *B* but referred to in that paper as "CORE-IA") supplied the historical ocean and sea-ice initial conditions for the DP experiments. Ensembles were generated by slightly perturbing the atmospheric initial conditions.

The analysis focused on the abrupt warming of the SPG region of the North Atlantic Ocean in the 1990s (Figs. 2.18-2.20) as a case study of the CESM1 DP system. Ensemble mean SPG ocean heat content (HC) evolution showed a marked cooling trend for each of the 10 start dates (Fig. 5.1a) because the preferred mean upper ocean temperature of the CESM1 coupled model in the SPG region is much cooler than observed (Danabasoglu et al., 2012a). However, a striking visual impression of predictive skill in this region was obtained after removing the large, systematic drift common to each ensemble set (Fig. 5.1b).

Much of Yeager et al. (2012) was devoted to demonstrating that there was indeed real pre-

dictive skill of both heat content and SST in the SPG out to decadal timescales, and that this predictive skill was realized for sound physical reasons; namely, the successful reproduction of key historical changes in the SPG heat budget. A first-order autoregressive parametric bootstrop was used to compute 95% significance values for correlations of pentadal-mean anomalies (see Appendix of Yeager et al. (2012)). The DP correlations with various measures of historical truth for SPG HC and SST were thus determined to be highly significant, especially in the second pentad ($\tau = 6-10$) of prediction (Table 5.1). Surprisingly, the correlations with observed SST were even higher and more significant than HC, which may relate to the higher fidelity of gridded SST data products in this region.

The use of full-field (as opposed to anomaly) initialization for the CESM1 DP runs necessitated significant bias correction in order to interpret the coupled forecasts (Fig. 5.1), and this underscored the need for a mechanistic understanding of the origins of predictive skill. To that end, bias-corrected heat budgets of the SPG box region were computed for each of the DP ensembles, and these were compared term-by-term with the historical SPG heat budget diagnosed from the CORE-IA reconstruction (Fig. 2.20). Figure 5.2 shows the results for first pentad of the predictions. The high HC correlation partly reflects the large range in initial conditions, but it is significantly higher than would be expected from damped persistence of those initial conditions because of the significant skill in forecasting anomalous SPG HC tendency (TEND). Most of TEND skill derives from the advective heat transport convergence term (ADV), while surface heat flux (SFLX) is most responsible for degrading the TEND projection. The large range in ADV anomalies mostly reflects changes in advective heat flux through the south face, which Yeager et al. (2012) attribute to the low-frequency changes in the strength of the large-scale, buoyancy-driven ocean circulation in the ocean state reconstruction used for initialization (Chapters 2-4). The moderate success in predicting HC tendency early in the forecast translates into highly significant HC and SST skill even into the second pentad of prediction (Table 5.1).

The ensemble initialized in 1991 was scrutinized to show that the strength and timing of the predicted warming varied considerably amongst the ensemble members (Fig. 5.3). In experi-

ments which predicted NAO+ winter conditions between 1991 and 1995 (as in Nature), the abrupt warming of the SPG occurred later and was generally stronger than in experiments which predicted weak NAO, thus giving a better match to CORE-IA. However, none of the ensemble members was able to match the strength of the observed positive 1991-1995 NAO conditions, as measured by the zonal surface wind stress anomaly over the SPG region. The large ensemble mean rise in SPG HC in the 1991 experiment, and indeed the overall success of the CESM1 DP prediction of SPG HC and SST out to at least 10 years, was found to derive from the consistency across ensemble members of AMOC-related advective heat convergence, in spite of the generally poor and diverse SFLX prediction.

5.2 Uncoupled prediction of SPG SST

If correct air-sea coupling is not critical for prediction of SPG SST up to a decade in advance, because of the dominant influence of slow oceanic heat transport anomalies in this region, it begs the question whether coupled decadal prediction is in fact necessary. To test the hypothesis that damped persistence of AMOC anomalies generates predictive skill in this region without coupled air-sea interaction, we have replicated the DP analysis of Yeager et al. (2012) with a set of forced ocean–sea-ice experiments initialized in the same way as the coupled DP ensembles. These uncoupled DP experiments are forced at the surface with a repeating annual cycle of atmospheric fields (NYF; see Appendix *B*), and only one experiment is run for each start date, because an ensemble is not needed given the low internal variability of the non-eddy resolving ocean model. The results are shown in Figure 5.4.

In these experiments, there is much less bias correction because the mean ocean state in a NYF-forced simulation is not as different from that in the CONTROL simulation as it is in the coupled model. Some skill beyond damped persistence of HC anomalies is evident (e.g., in experiments initialized in 1971, 1991, and 1996), but in such forced OGCM experiments, the atmosphere has effectively an infinite heat capacity and this results in strong damping of the predicted HC anomalies. Part of the skill in the coupled system, therefore, derives from atmospheric

processes which tend to limit the heat exchange with the ocean. While not as skillful as the coupled DP system, the uncoupled results were obtained far more cheaply. Figure 5.4 was generated with 100 years of ocean–sea-ice simulation, while Figure 5.1 required 1000 years of fully coupled integration.

5.3 What is needed to advance decadal prediction of North Atlantic SST?

Extending decadal prediction beyond the timescale of damped persistence of anomalous oceanic heat convergence will require some ability to predict the anomalous water mass formation in the North Atlantic which precedes large-scale circulation changes. This amounts to predicting NAO and particularly, we have argued, the influence of NAO on storm track activity over the Lab Sea. A crucial ingredient would seem to be getting the correct atmospheric response to AMV, that is, a negative NAO reponse to positive AMV (Fig. 2.3). How does the CESM1 coupled model do in this regard?

Figure 5.5 shows the relationship between Q_{as} and SST in a 180-year segment of a fully coupled CESM1 control simulation for 1850 conditions. We see that on pentadal timescales, the model simulates a negative heat flux feedback in the Lab Sea and central SPG regions where observations suggest a moderate positive feedback is at work (Fig. 2.2). A positive feedback evident in the eastern SPG region is far removed from the site of model NADW formation and deep convection (Lab Sea). Qualitatively similar relationships are seen in CESM1 fully coupled simulations of the 20th century (not shown). The implication is that the model is not reproducing the coupled air-sea interaction which links AMV and NAO.

This might be attributable to any number of deficiencies in the component models of the coupled CESM1, but even when initialized from ocean conditions which bear a strong resemblance to observations (i.e., even in coupled DP experiments), the coupled system generates an incorrect response to high latitude SST anomalies. Yeager et al. (2012) show that the DP system does an excellent job of reproducing pentadal mean SST anomalies, but it does not get Q_{as} correct. This result is shown for the first pentad of prediction in Figure 5.6a,b. We are now able to perceive that the Q_{as} error in the DP experiments is associated with an incorrect atmospheric response to

pentadal SST anomalies. The CONTROL hindcast exhibits no relationship between pentadal SST anomalies and Q_{as} over the SPG region (Fig. 5.6c). This low correlation is itself a biased result and is due to the fact that the SPG region spans area of both positive and negative heat flux feedback in the forced CONTROL (see Fig. 3.12). Observations (HadleyOI SST and CORE-II fluxes) indicate there should be a modest positive correlation between pentadal Q_{as} and SST in the SPG (Figs. 2.2 and 5.7). However, the coupled system produces a strong negative feedback on SST anomalies in the SPG, both in the first pentad (Fig. 5.6d) and in the second (not shown).

The incorrect atmospheric response to SST does not strongly impact SPG prediction on timescales shorter than a decade, but it will likely contribute to poor prediction skill on longer timescales which will require some ability to anticipate NAO variations and anomalous WMF. The unrealistic nature of the low-frequency air-sea coupling in the coupled CESM1 model (Fig. 5.5) also calls into question the fidelity of AMV and AMOC variability mechanisms diagnosed from the model, which are likely overdamped by negative heat flux feedbacks on SST in water mass formation regions. Further work will be needed to explore the full ramifications of these results.

		$\tau = 1 - 5$	$\tau = 6 - 10$
Heat Content	CONTROL (CORE-IA)	0.95 (0.78)	0.92 (0.59)
	Levitus et al.	0.74 (0.77)	0.76 (0.60)
	Ishii and Kimoto	0.75 (0.77)	0.76 (0.60)
SST	CONTROL (CORE-IA)	0.93 (0.76)	0.94 (0.59)
	Hurrell et al.	0.88 (0.73)	0.89 (0.60)
	Ishii and Kimoto	0.80 (0.73)	0.84 (0.58)

Table 5.1: Table 1 from Yeager et al. (2012). First and second pentad correlations between regionally-averaged SPG ocean fields from DP and various representations of historical truth (by row; see text for references). Values in parantheses give the 95%-confidence level based on a first-order autoregressive parametric bootstrap (see appendix of Yeager et al. (2012) for details).

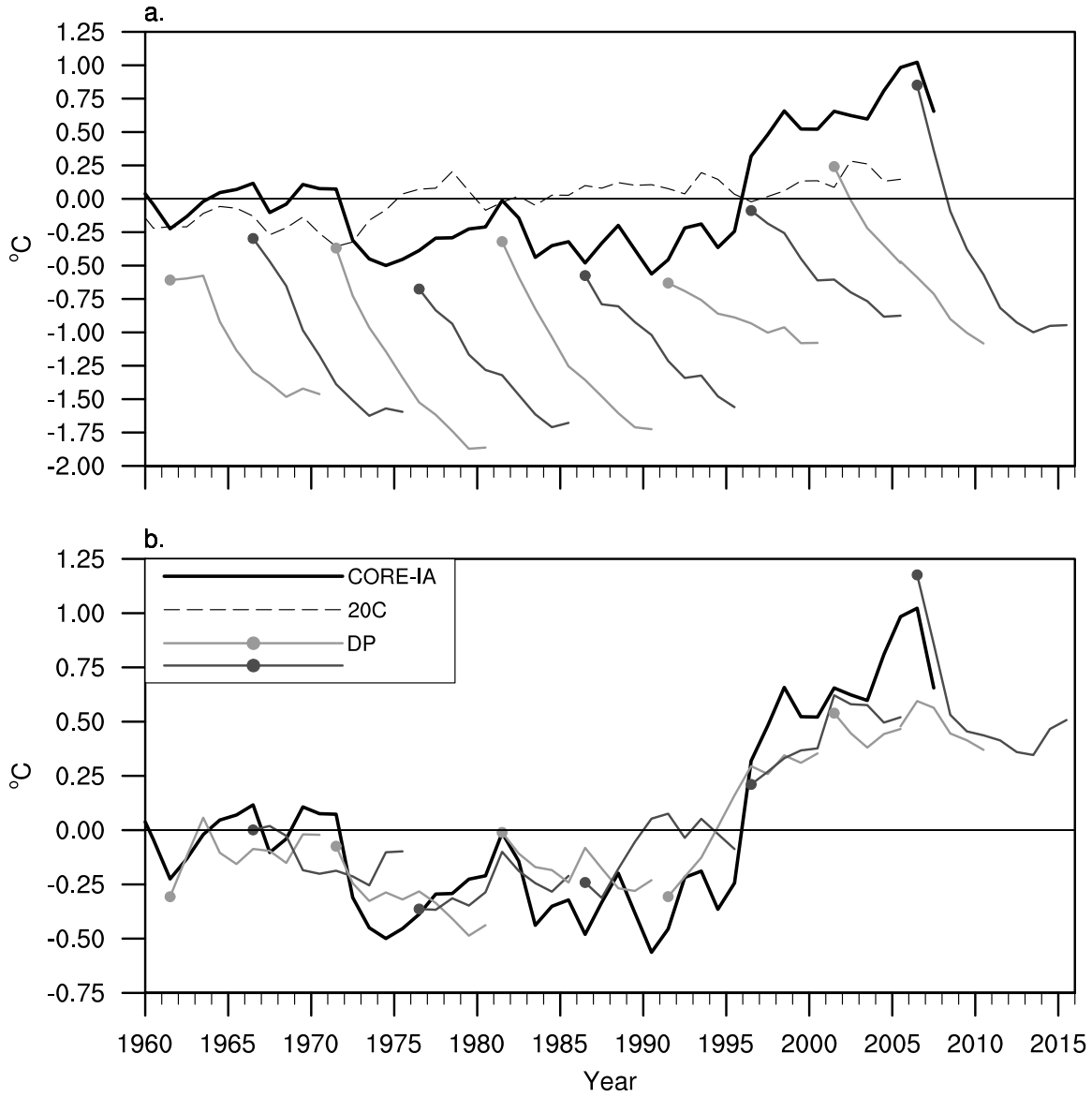

Figure 5.1: Figure 4 from Yeager et al. (2012). Annual mean 275-m heat content anomaly in the SPG box (in °C). Panel (a) shows CORE-IA (thick solid black), the 20C 6-member ensemble mean (thin dashed black), and the raw DP 10-member ensemble means (grey curves, alternating shades for clarity). Panel (b) shows CORE-IA and the bias-corrected DP ensemble means (note change in scale). Large circles indicate the first-year ($\tau = 1$) average of each DP ensemble. The CORE-IA and 20C anomalies are computed relative to climatologies over the reference periods 1961-2007 and 1961-2005, respectively; DP anomalies are computed relative to the CORE-IA climatology.

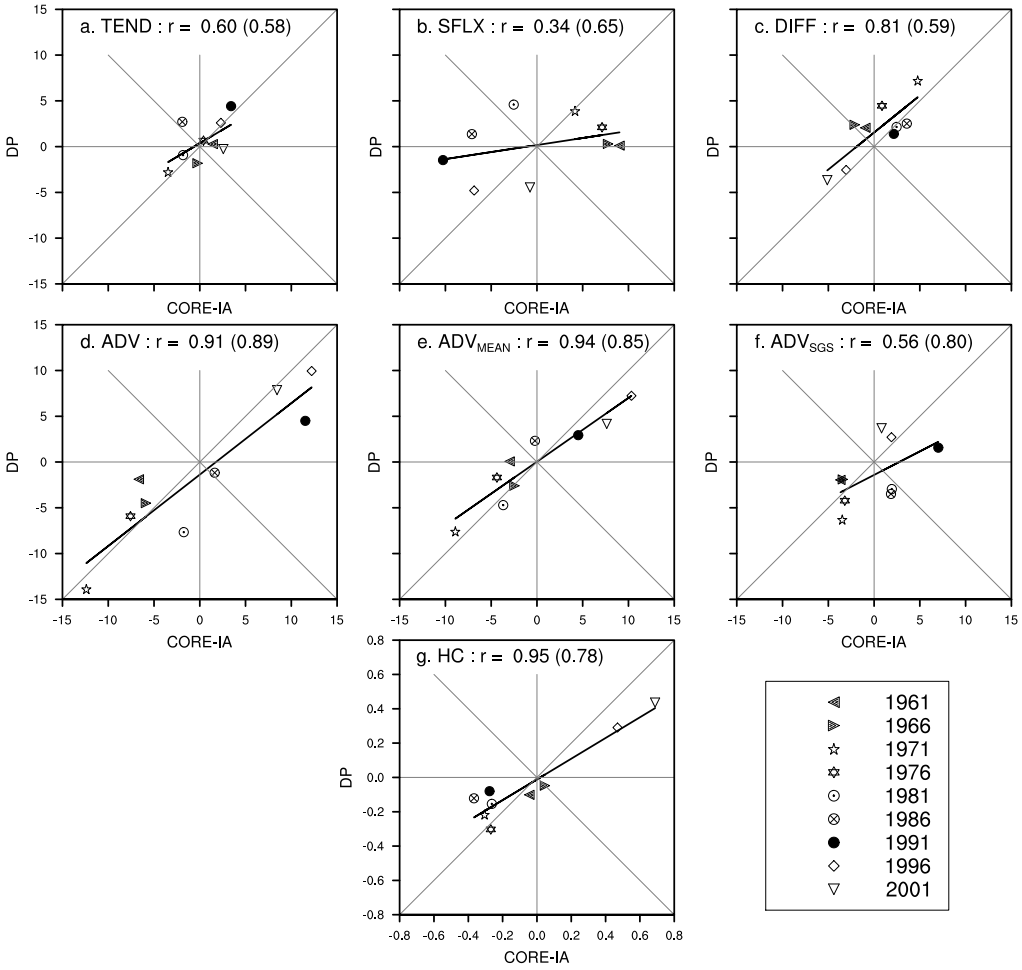

Figure 5.2: Figure 5 from Yeager et al. (2012). Comparison of mean SPG heat budget terms from the first pentad (τ = 1-5) of the DP predictions (y-axis) with the corresponding 5-year means from the CORE-IA ocean state (x-axis). All panels show anomalies relative to the 1961-2007 CORE-IA climatology. The terms plotted are (a) heat content tendency, (b) surface heat flux, (c) diffusive heat flux, (d) advective heat flux, (e) mean component of advective heat flux, (f) sub-gridscale component of advective heat flux. Panels (a)-(f) are in W m^{-2} and panel (g) is in °C. The symbols reflect the start year of a given DP ensemble and also the first year of the pentad. Correlation coefficients (r) and regression lines are indicated in each panel. Correlations in parantheses give the 95%-confidence level based on the null hypothesis that the predictive skill can be explained by a first-order autoregressive process (see Appendix of Yeager et al. (2012) for details).

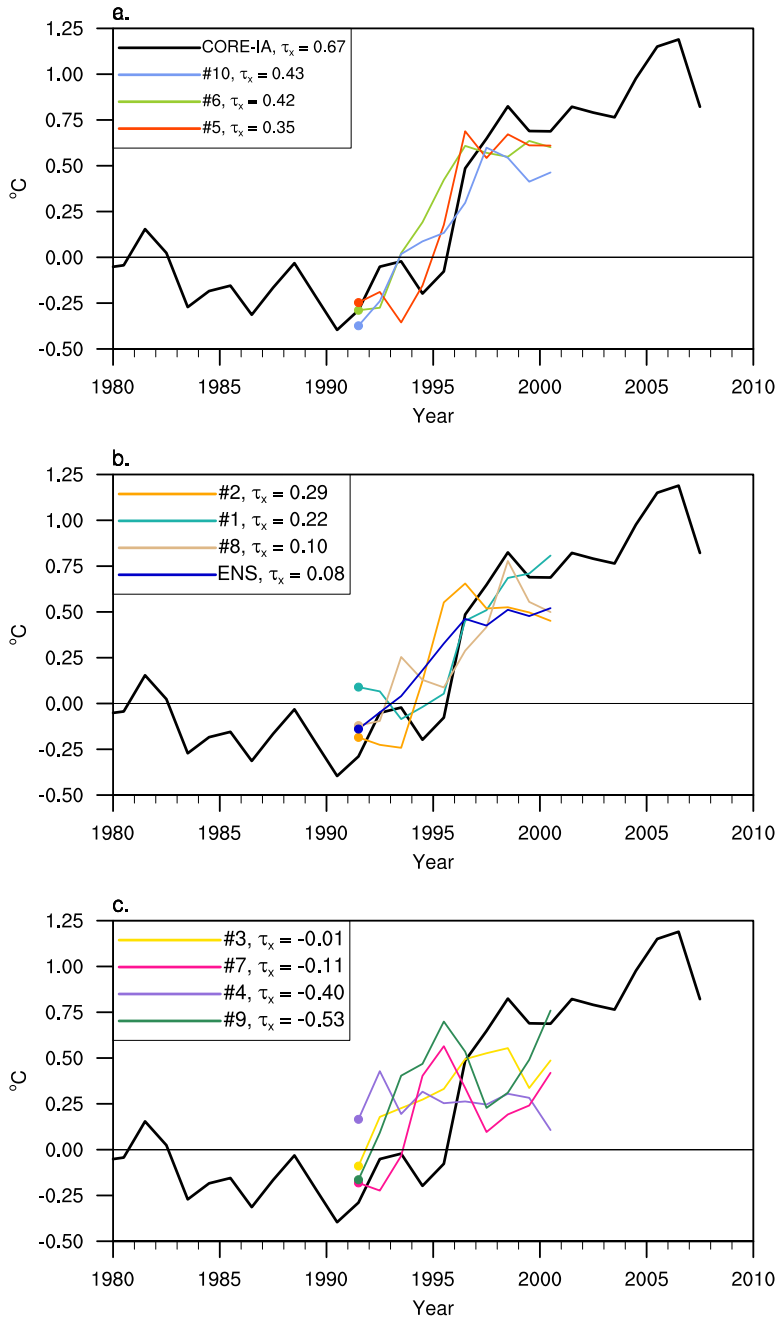

Figure 5.3: Figure 9 from Yeager et al. (2012). Annual mean time series of 275-m heat content anomaly in the SPG box from CORE-IA as well as from the ensemble of 1991-initialized DP simulations. The experiments are grouped according to the magnitude of the mean JFM zonal wind stress anomaly (τ_x, in N m^{-2}) between 1991-1995, regionally-averaged over the SPG box and computed relative to the CORE-IA 1961-2007 climatology. The panels are thus meant to correspond to a) strong, b) medium, and c) weak winter NAO conditions in the pentad leading up to the observed regime shift. The ensemble mean is included in panel b.

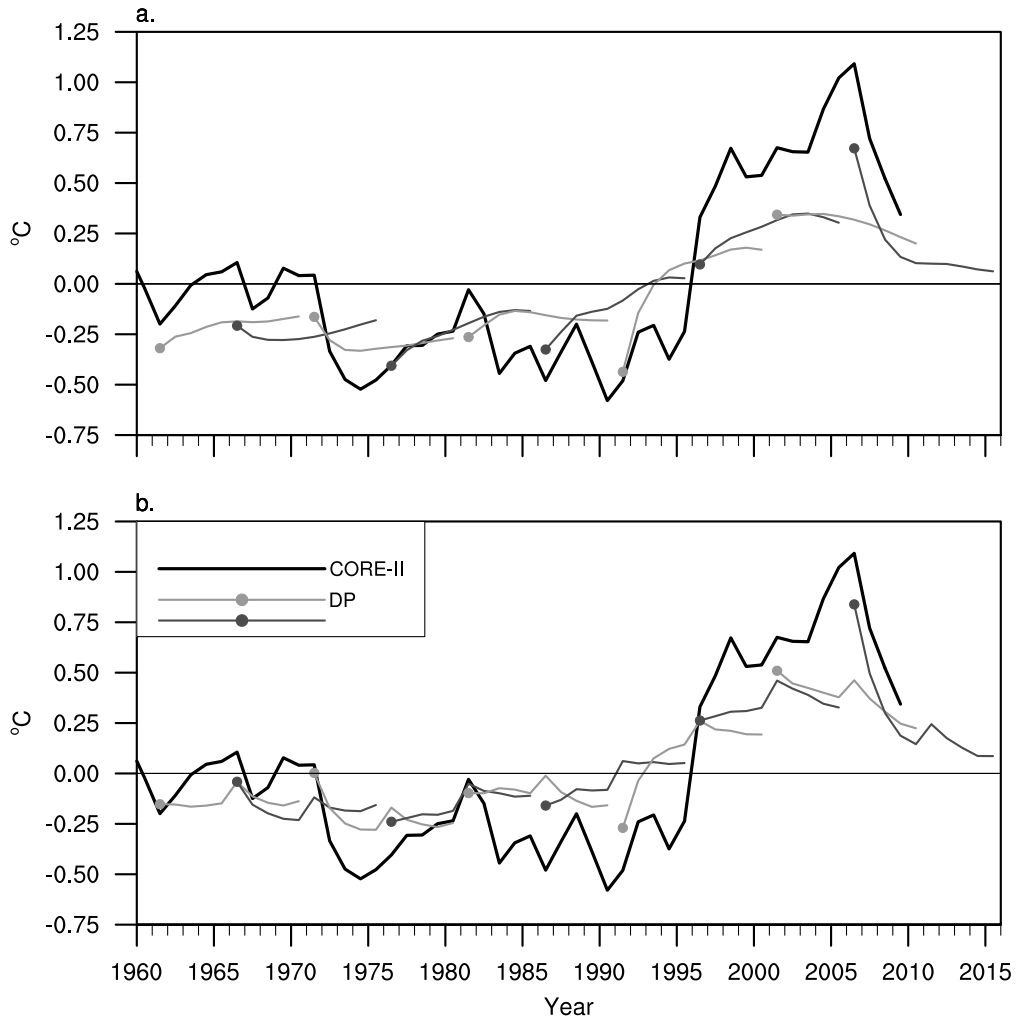

Figure 5.4: As in Figure 5.1, but computed from uncoupled, NYF-forced ocean–sea-ice configurations of CESM1 initialized from CONTROL.

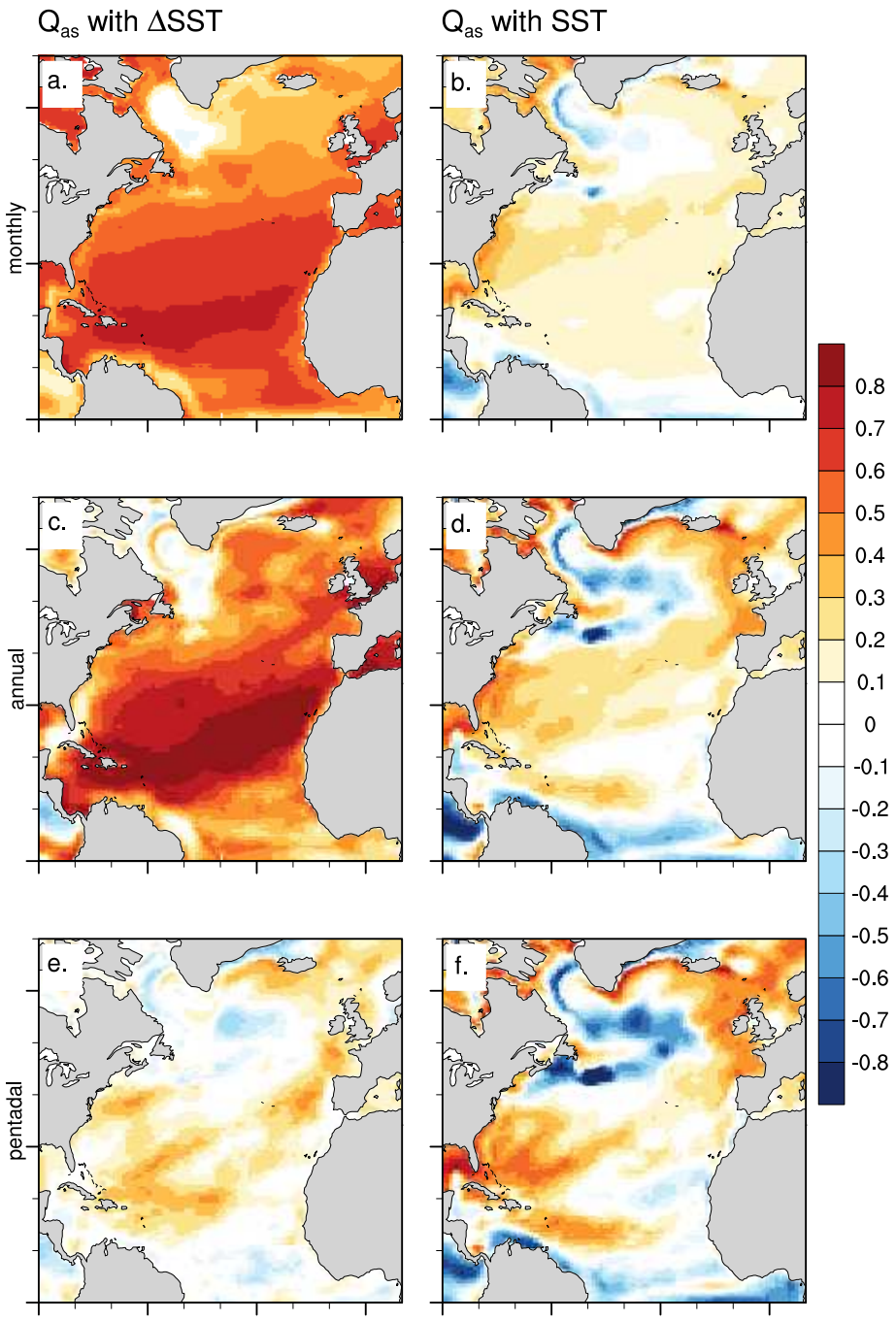

Figure 5.5: As in Figure 2.2, but computed from 180 years of a CESM1 1850 coupled control simulation.

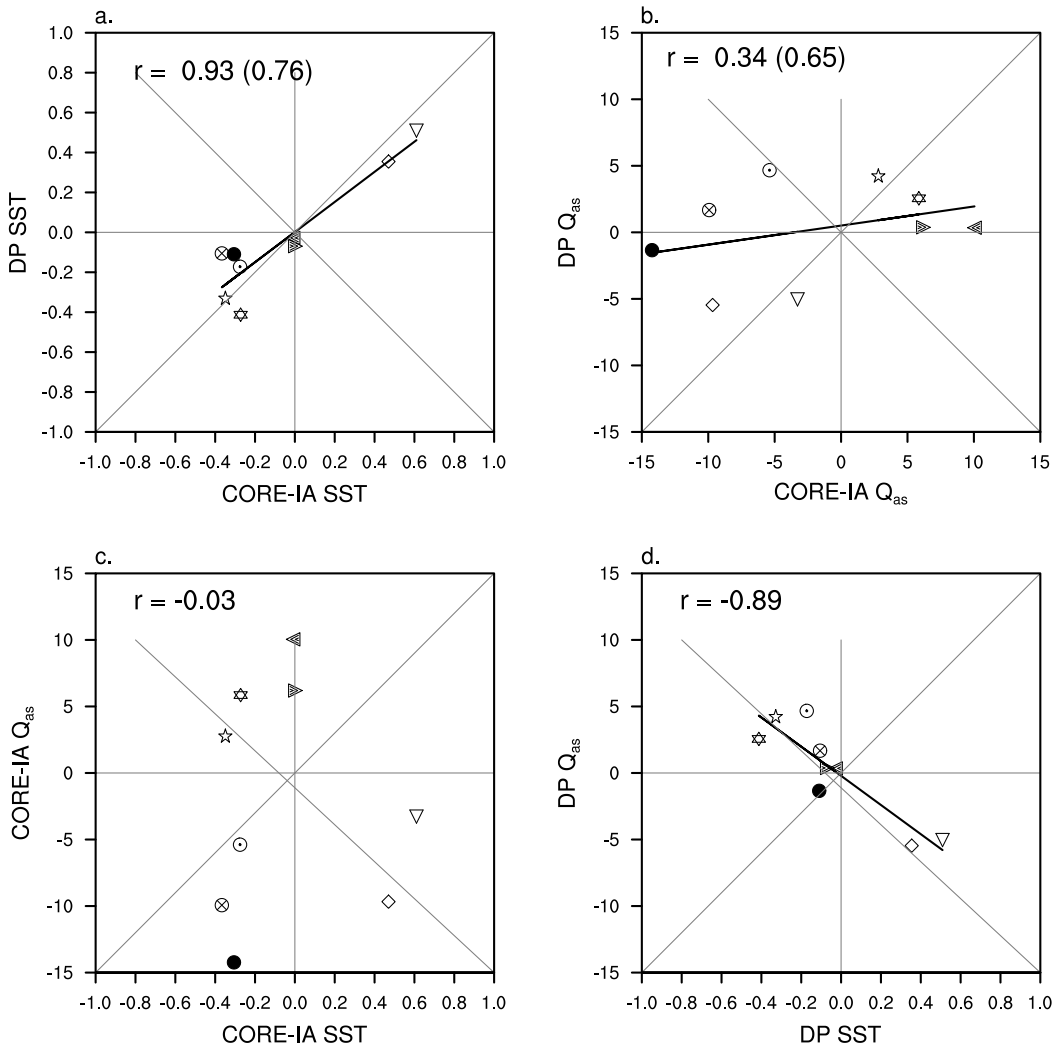

Figure 5.6: Comparison between CONTROL (CORE-IA) and the CESM1 DP ensemble means of pentadal mean SST and Q_{as} in the SPG region for the first pentad (τ = 1-5) of prediction. Refer to Figure 5.2 for the symbol legend. Correlation values are given with the 95%-confidence level in parantheses.

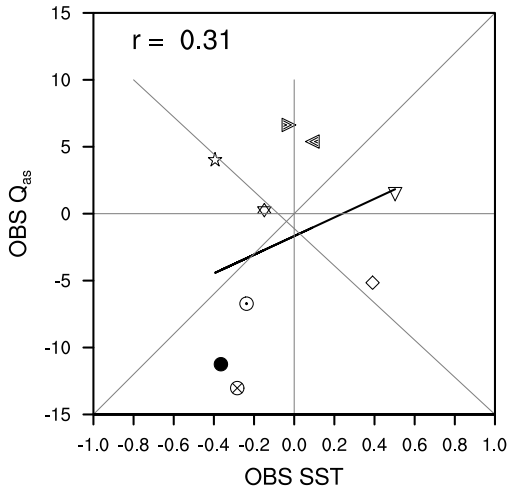

Figure 5.7: Same as Figure 5.6c, but using observed HadleyOI SST and observation-based CORE-II heat fluxes (see Chapter 2).

Chapter 6

Summary

The observational record alone yields substantial evidence for a coupled mechanism for AMV. The NADW formation changes implied by pairing the CORE-II flux data set with observed SST indicates that there were decadal variations in surface formation of LSW which were strongly linked to NAO. Lagged correlations of pentadal SST change with heat flux reveal a positive heat flux feedback in the SPG which suggests that observed SST anomalies induced a weakening of the storm track. This provides some measure of support to model-based results which show that positive AMOC anomalies generate a weak negative NAO response. The fact that NAO drove enhanced WMF and that slow SST variations in turn influenced NAO, are the necessary ingredients for coupled oscillatory behavior along the lines of Marshall et al. (2001a).

- We have produced new observation-based evidence for NAO-driven decadal AMOC variations over the late twentieth century.
- We have shown that the CORE-II flux data set is compatible with a coupled mechanism for AMV.

The CORE-II-forced POP hindcast corroborates the inferences drawn from the flux formation time series. Strong turbulent buoyancy forcing in the 1970s, 1980s, and 1990s generated anomalous model density fields which show a good correspondence with hydrographic time series in the central Labrador Sea. The positive density anomalies were the net result of intense storm forcing in high NAO winters. They were contemporaneous with anomalously deep convection, and while

they were mainly associated with the local heat flux forcing over and mixing within the Labrador Sea, forcing over the broader subpolar gyre region contributed to their strength. As the positive density perturbations propagated slowly into the interior, they induced changes in the large-scale circulation. The effects included a spinup of the barotropic subpolar gyre circulation, and enhanced baroclinic flow (AMOC) further south. Both the anomalous gyre and overturning circulations contributed to enhanced advective heat convergence into the subpolar region. The model indicates that the abrupt warming of the SPG in the mid-1990s, which is a dominant feature in the AMV regression, resulted from this advective heat convergence.

- We have demonstrated that a realistic model hindcast of the ocean state over the late twentieth century is characterized by decadal circulation variability that is in agreement with observation-based estimates of Atlantic THC variability.

- We have shown that the AMV signal associated with the mid-1990s warming of the SPG was driven largely by changes in ocean circulation.

The hypothesis that Southern Ocean wind forcing may have played a significant role in recent AMOC variability was shown to be false for the time period of 1948 to 2009. Although this does explain the decadal AMOC variability south of the Equator, almost all of the low-frequency gyre and overturning variability obtained in the CORE-II hindcast simulation in the North Atlantic is attributable to buoyancy forcing perturbations which changed NADW properties. The SSH field in the Labrador Sea was found to be driven largely by buoyancy forcing, and thus the hindcast indicates that AMOC variations at midlatitudes in the Atlantic may be anticipated up to 9 years in advance. The origins of the decadal circulation variability in this and other CORE-II-forced simulations was traced to the slow variation of atmospheric temperature and humidity over NADW formation regions. Modelling studies, as well as the CORE-II flux data set, suggest that this slow atmospheric variability arises, at least in part, through coupled air-sea interaction.

- We have clearly demonstrated that recent Southern Ocean wind forcing was only a minor contributor to AMOC variability of the recent past.

- We have demonstrated not only that North Atlantic buoyancy forcing drove most of the recent decadal variance in AMOC, but that the origin of the decadal timescale is found in the atmospheric temperature and humidity fields over WMF regions.
- We have established a link between Lab Sea SSH change and AMOC variability which may yield predictive skill.

We developed vorticity diagnostics for the POP ocean model in order to develop a deeper dynamical understanding of model circulation behaviors that have heretofore been analyzed largely descriptively (e.g., Yeager and Jochum, 2009; Yeager and Danabasoglu, 2012). The mean balance highlights the importance of flow interaction with bathymetry. This is a not a new finding, but it has not perhaps been widely enough appreciated by users and developers of this model, and it certainly has not been given much consideration in studies of climate dynamics. We have shown with this analysis that the Equator acts as a vorticity barrier which inhibits the communication of AMOC signals between the hemispheres. The combination of forcing perturbation experiments with the vorticity diagnostics is a powerful technique for understanding model mean behavior as well mechanisms of interannual variability in the ocean. We showed that buoyancy forcing drives gyre circulation variance through BVS effects and that this accounts for a significant fraction of intergyre-gyre variability and almost all of the NAC variability. The barotropic vorticity forcing associated with DWBC flow over the MAR contributes to the strength of the STG, whereas more DWBC west of the MAR contributes to the NRG. The latter contributes to GS separation whereas the former inhibits it. Although we cannot yet draw strong conclusions from this result, it is suggestive and we have laid the groundwork for GS separation studies using higher resolution models which will have better representation of potentially important nonlinear effects. Most surprisingly, we showed that BVS plays an important role in momentum-forced ocean variations. This effect is substantial in some regions where wind-induced abyssal flow anomalies generate large BVS anomalies, and we have argued that this may be a first order effect in wind-forced AMOC variations.

- We have shown how buoyancy-forced DWBC variations can have substantial impacts on the gyre circulation, even in midlatitudes.
- We have clarified the mean and time-dependent dynamics which underpin the Atlantic overturning circulation.
- We have shown that BVS plays a role in wind-driven circulation variations.

Finally, we demonstrated that slow, persistent, buoyancy-forced circulation anomalies explain the significant skill in predicting North Atlantic heat content and SST in initialized coupled decadal prediction experiments. Although prediction of air-sea heat exchange is poor, coupling enhances prediction skill by virtue of the finite heat capacity of the overlying atmospheric model. Advances in decadal prediction will require better simulation of the atmospheric response to slow SST change. In the CESM1 model, the heat flux feedback in the Labrador Sea and central SPG regions is of the wrong sign. This limits the predictive skill and calls into question AMV mechanisms diagnosed from this model.

- We have shown that skillful prediction of North Atlantic SST is possible out to at least a decade and the skill derives from the persistence of ocean heat transport convergence anomalies.
- We have presented evidence that unrealistic air-sea coupling in the North Atlantic in the CESM1 model may be the most significant limiting factor for extended prediction of AMV.

Bibliography

Antonov, J. I., et al., 2010: *World Ocean Atlas 2009, Volume 2: Salinity*, U.S. Government Printing Office, Washington, D. C.

Battisti, D. S., U. S. Bhatt, and M. A. Alexander, 1995: A modeling study of the interannual variability in the wintertime North Atlantic Ocean. *J. Climate*, **8**, 3067–3083.

Beismann, J.-O. and B. Barnier, 2004: Variability of the meridional overturning circulation of the North Atlantic: sensitivity to overflows of dense water masses. *Ocean Dynamics*, **54**, 92–106, doi:10.1007/s10236-003-0088-x.

Bell, M. J., 1999: Vortex stretching and bottom torques in the bryan-cox ocean circulation model. *J. Geophys. Res.*, **104**, 23 545–23 563.

Bentsen, M., H. Drange, T. Furevik, and T. Zhou, 2004: Simulated variability of the Atlantic meridional overturning circulation. *Clim. Dynam.*, **22**, 701–720, doi:10.1007/s00382-004-0397-x.

Biastoch, A., C. Böning, J. Getzlaff, J.-M. Molines, and G. Madec, 2008: Causes of Interannual-Decadal Variability in the Meridional Overturning Circulation of the Midlatitude North Atlantic Ocean. *J. Climate*, **21**, 6599–6615.

Bjerknes, J., 1959: The Recent Warming of the North Atlantic. *The Atmosphere and the Sea in Motion: The Rossby Memorial Volume*, B. Bolin, Ed., The Rockefeller Institute Press and Oxford University Press, 65–73.

Bjerknes, J., 1964: Atlantic air-sea interaction. *Adv. Geophys.*, **10**, 1–82.

Böning, C., M. Scheinert, J. Dengg, A. Biastoch, and A. Funk, 2006: Decadal variability of subpolar gyre transport and its reverberation in the North Atlantic overturning. *Geophys. Res. Lett.*, **33**, L21S01, doi:10.1029/2006GL026906.

Bower, A. S., M. S. Lozier, S. F. Gary, and C. W. Böning, 2009: Interior pathways of the north atlantic meridional overturning circulation. *Nature*, **459**, 243–247, doi:10.1038/nature07979.

Brambilla, E., L. D. Talley, and P. E. Robbins, 2008: Subpolar Mode Water in the northeastern Atlantic: 2. Origin and transformation. *J. Geophys. Res.*, **113**, doi:10.1029/2006JC004063.

Brauch, J. P. and R. Gerdes, 2005: Response of the northern north atlantic and arctic oceans to a sudden change of the north atlantic oscillation. *J. Geophys. Res.*, **110**, C11018, doi: 10.1029/2004JC002436.

Briegleb, B. P., G. Danabasoglu, and W. G. Large, 2010: An overflow parameterization for the ocean component of the community climate system model. NCAR Tech. Note NCAR/TN-481+STR, National Center for Atmospheric Research, 72 pp.

Brooks, I. H. and P. P. Niiler, 1977: Energetics of the florida current. *J. Mar. Res.*, **35**, 163–191.

Bryan, F. O., G. Danabasoglu, N. Nakashiki, Y. Yoshida, D. H. Kim, J. Tsutsui, and S. C. Doney, 2006: Response of the north atlantic thermohaline circulation and ventilation to increasing carbon dioxide in CCSM3. *J. Climate*, **19**, 2382–2397.

Bryan, K., S. Manabe, and R. C. Pacanowski, 1975: A global ocean-atmosphere climate model. part ii. the oceanic circulation. *J. Phys. Oceanogr.*, **5**, 30–46.

Cayan, D. R., 1992: Latent and Sensible Heat Flux Anomalies over the Northern Oceans: Driving the Sea Surface Temperature. *J. Phys. Oceanogr.*, **22**, 859–881.

Chanut, J., B. Barnier, W. Large, L. Debreu, T. Penduff, J. M. Molines, and P. Mathiot, 2008: Mesoscale eddies in the Labrador Sea and their contribution to convection and restratification. *J. Phys. Oceanogr.*, **38**, 1617–1643, doi:10.1175/2008JPO3485.1.

Cheng, W., R. Bleck, and C. Rooth, 2004: Multi-decadal thermohaline variability in an ocean-atmosphere general circulation model. *Clim. Dynam.*, **22**, 573–590.

Clark, P. U., N. G. Pisias, T. F. Stocker, and A. J. Weaver, 2002: The role of the thermohaline circulation in abrupt climate change. *Nature*, **415**, 863–869.

Collins, M., A. Carril, H. Drange, H. Pohlmann, R. Sutton, and L. Terray, 2003: North atlantic decadal predictability. 6-7 pp.

Comiso, J., 2000: Bootstrap sea ice concentrations from Nimbus-7 SMMR and DMSP SSM/I-SSMIS, Version 2. updated 2012. National Snow and Ice Data Center, Boulder, Colorado, USA.

Cunningham, S. A., et al., 2007: Temporal variability of the Atlantic meridional overturning circulation at 26.5°N. *Science*, **317**, 935–938.

Curry, R. G. and M. S. McCartney, 2001: Ocean gyre circulation changes associated with the north atlantic oscillation. *J. Phys. Oceanogr.*, **31**, 3374–3400.

Czaja, A. and C. Frankignoul, 1999: Influence of the North Atlantic SST on the atmospheric circulation. *Geophys. Res. Lett.*, **26**, 2969–2972.

Czaja, A. and C. Frankignoul, 2002: Observed Impact of Atlantic SST Anomalies on the North Atlantic Oscillation. *J. Climate*, **15**, 606–623.

Czaja, A. and J. Marshall, 2001: Observations of atmosphere-ocean coupling in the North Atlantic. *Quart. J. Roy. Meteor. Soc.*, **127**, 1893–1916.

Dai, A., A. Hu, G. A. Meehl, W. M. Washington, and W. G. Strand, 2005: Atlantic thermohaline circulation in a coupled general circulation model: Unforced variations versus forced changes. *J. Climate*, **18**, 3270–3293.

Dai, A., T. Qian, K. Trenberth, and J. Milliman, 2009: Changes in continental freshwater discharge from 1948-2004. *J. Climate*, **22**, 2773–2791.

Danabasoglu, G., 2008: On multidecadal variability of the atlantic meridional overturning circulation in the community climate system model version 3. *J. Climate*, **21**, 5524–5544.

Danabasoglu, G., S. C. Bates, B. P. Briegleb, S. R. Jayne, M. Jochum, W. G. Large, S. Peacock, and S. G. Yeager, 2012a: The CCSM4 ocean component. *J. Climate*, **25**, 1361–1389, doi:10.1175/JCLI-D-11-00091.1.

Danabasoglu, G., W. G. Large, and B. P. Briegleb, 2010: Climate impacts of parameterized Nordic Sea overflows. *J. Geophys. Res.*, **115**, C11005, doi:10.1029/2010JC006243.

Danabasoglu, G., S. G. Yeager, and coauthors, 2013: North Atlantic simulations in Coordinated Ocean-ice Reference Experiments phase II (COREII). part I: Mean States. *Ocean Modelling*, **submitted**.

Danabasoglu, G., S. G. Yeager, Y.-O. Kwon, J. Tribbia, A. Phillips, and J. Hurrell, 2012b: Variability of the Atlantic meridional overturning circulation in CCSM4. *J. Climate*, **25**, 5153–5172, doi:10.1175/JCLI-D-11-00463.1.

Delworth, T. and R. J. Greatbatch, 2000: Multidecadal thermohaline circulation variability driven by atmospheric surface flux forcing. *J. Climate*, **13**, 1481–1495.

Delworth, T., S. Manabe, and R. J. Stouffer, 1993: Interdecadal variations of the thermohaline circulation in a coupled ocean-atmosphere model. *J. Climate*, **6**, 1993–2011.

Delworth, T., R. Zhang, and M. E. Mann, 2007: Decadal to Centennial Variability of the Atlantic from Observations and Models. *Ocean Circulation: Mechanisms and Impacts*, AGU, Washington, D. C., Geophysical Monograph Series, Vol. 173, 131–148, doi:10.1029/173GM10.

Delworth, T. L. and M. E. Mann, 2000: Observed and simulated multidecadal variability in the Northern Hemisphere. *Clim. Dynam.*, **16**, 661–676.

Delworth, T. L. and F. Zeng, 2008: Simulated impact of altered Southern Hemisphere winds on the Atlantic overturning circulation. *Geophys. Res. Lett.*, **35**, 1–5, doi:10.1029/2008GL035166.

Dengg, H., A. Beckmann, and R. Gerdes, 1996: The gulf stream seperation problem. *The Warmwatersphere of the North Atlantic Ocean*, W. Krauss, Ed., Gebrüder Borntraeger, 253–290.

Deser, C. and M. Blackmon, 1993: Surface climate variations over the North Atlantic Ocean during winter: 1900-1989. *J. Climate*, **6**, 1743–1753.

Dickson, B., I. Yashayaev, J. Meincke, B. Turrell, S. Dye, and J. Holfort, 2002: Rapid freshening of the deep North Atlantic ocean over the past four decades. *Nature*, **416**, 832–836.

Dickson, R. R., W. J. Gould, T. J. Müller, and C. Maillard, 1985: Estimates of the mean circulation in the deep (¿2000m) layer of the Eastern North Atlantic. *Prog. Oceanogr.*, **14**, 103–127.

Doney, S. C., S. G. Yeager, W. G. Large, and J. C. McWilliams, 2003: Modeling global oceanic interannual variability (1958-1997): Simulation design and model-data evaluation. NCAR Tech. Note NCAR/TN-452+STR, National Center for Atmospheric Research, 48 pp.

Dukowicz, J. and R. Smith, 1994: Implicit free-surface formulation of the bryan-cox-semtner ocean model. *J. Geophys. Res.*, **99**, 7991–8014.

Eden, C. and J. Willebrand, 2001: Mechanism of interannual to decadal variability of the North Atlantic circulation. *J. Climate*, **14**, 2266–2280.

Edwards, C. A. and J. Pedlosky, 1998: Dynamics of Nonlinear Cross-Equatorial Flow. Part i: Potential Vorticity Transformation. *J. Phys. Oceanogr.*, **28**, 2382–2406.

Farneti, R. and T. L. Delworth, 2010: The role of mesoscale eddies in the remote oceanic response to altered Southern Hemisphere winds. *J. Phys. Oceanogr.*, **40**, 2348–2354, doi: 10.1175/2010JPO4480.1.

Farneti, R., T. L. Delworth, A. J. Rosati, S. M. Griffies, and F. Zeng, 2010: The role of mesoscale eddies in the rectification of the Southern Ocean response to climate change. *J. Phys. Oceanogr.*, **40**, 1539–1557, doi:10.1175/2010JPO4353.1.

Farneti, R. and P. R. Gent, 2011: The effects of the eddy-induced advection coefficient in a coarse-resolution coupled climate model. *Ocean Modelling*, **39**, 135–145, doi: 10.1016/j.ocemod.2011.02.005.

Farneti, R. and G. K. Vallis, 2009: Mechanisms of interdecadal climate variability and the role of ocean-atmosphere coupling. *Clim. Dynam.*, doi:10.1007/s00382-009-0674-9.

Flatau, M. K., L. Talley, and P. P. Niiler, 2003: The north atlantic oscillation, surface current velocities, and sst changes in the subpolar north atlantic. *J. Climate*, **16**, 2355–2369.

Foreman, M. G. G. and A. F. Bennett, 1989: On calculating vorticity balances in primitive equation models. *J. Phys. Oceanogr.*, **19**, 1407–1411.

Fox-Kemper, B., R. Ferrari, and R. W. Hallberg, 2008: Parameterization of mixed layer eddies. part i: Theory and diagnosis. *J. Phys. Oceanogr.*, **38**, 1145–1165.

Fox-Kemper, B. and J. Pedlosky, 2004a: Wind-driven barotropic gyre i: Circulation control by eddy vorticity fluxes to an enhanced removal region. *J. Mar. Res.*, **62**, 169–193.

Fox-Kemper, B. and J. Pedlosky, 2004b: Wind-driven barotropic gyre ii: Effects of eddies and low interior viscosity. *J. Mar. Res.*, **62**, 195–232.

Fox-Kemper, B., et al., 2011: Parameterization of mixed layer eddies. iii: Implementation and impact in global ocean climate simulations. *Ocean Modelling*, **39**, 61–78.

Ganachaud, A. and C. Wunsch, 2000: Improved estimates of global ocean circulation, heat transport and mixing from hydrographic data. *Nature*, **408**, 453–458.

Ganachaud, A. and C. Wunsch, 2003: Large-scale Ocean Heat and Freshwater Transports during the World Ocean Circulation Experiment. *J. Climate*, **16**, 696–705.

Gastineau, G., F. D'Andrea, and C. Frankignoul, 2012: Atmospheric response to the North Atlantic Ocean variability on seasonal to decadal time scales. *Clim. Dynam.*, doi:10.1007/s00382-012-1333-0.

Gastineau, G. and C. Frankignoul, 2012: Cold-season atmospheric response to the natural variability of the atlantic meridional overturning circulation. *Clim. Dynam.*, **39**, 37–57, doi: 10.1007/s00382-011-1109-y.

Gent, P. R. and G. Danabasoglu, 2011: Response to increasing Southern Hemisphere winds in CCSM4. *J. Climate*, **24**, 4992–4998, doi:10.1175/JCLI-D-10-05011.1.

Gent, P. R., et al., 2011: The Community Climate System Model version 4. *J. Climate*, **24**, 4973–4991, doi:10.1175/2011JCLI4083.1.

Griffies, S. M. and K. Bryan, 1997: Predictability of north atlantic multidecadal climate variability. *Science*, **275**, 181–184.

Griffies, S. M. and E. Tziperman, 1995: A Linear Thermohaline Oscillator Driven by Stochastic Atmospheric Forcing. *J. Climate*, **8**, 2440–2453.

Grist, J. P., et al., 2010: The roles of surface heat flux and ocean heat transport convergence in determining atlantic ocean temperature variability. *Ocean Dynamics*, **60**, 771–790, doi:10.1007/s10236-010-0292-4.

Gulev, S. K., B. Barnier, H. Knochel, J.-M. Molines, and M. Cottet, 2003: Water Mass Transformation in the North Atlantic and its Impact on the Meridional Circulation: Insights from an Ocean Model Forced by NCEP-NCAR Reanalysis Surface Fluxes. *J. Climate*, **16**, 3085–3110.

Häkkinen, S., 1999: Variability of the simulated meridional heat transport in the North Atlantic for the period 1951-1993. *J. Geophys. Res.*, **104**, 10 991–11 007.

Häkkinen, S. and P. B. Rhines, 2004: Decline of subpolar north atlantic circulation during the 1990s. *Science*, **304**, 555–559.

Hatun, H., et al., 2009: Large bio-geographical shifts in the north-eastern atlantic ocean: From the subpolar gyre, via plankton, to blue whiting and pilot whales. *Prog. Oceanogr.*, **80**, 149–162.

Hawkins, E. and R. Sutton, 2009: The potential to narrow uncertainty in regional climate predictions. *Bull. Amer. Meteor. Soc.*, **90**, 1095–1107.

Holland, D. M., R. H. Thomas, B. de Young, M. H. Ribergaard, and B. Lyberth, 2008: Acceleration of jakobshavn isbrae triggered by warm subsurface waters. *Nature*, **1**, 659–664.

Holland, M. M., D. A. Bailey, B. P. Briegleb, B. Light, and E. Hunke, 2012: Improved sea ice shortwave radiation physics in CCSM4: the impact of melt ponds and aerosols on Arctic sea ice. *J. Climate*, **25**, 1413–1430, doi:10.1175/JCLI-D-11-00078.1.

Holland, W. R., 1973: Baroclinic and topographic influences on the transport in western boundary currents. *Geophys. Fl. Dyn.*, **4**, 187–210.

Hughes, C. W. and B. A. de Cuevas, 2001: Why western boundary currents in realistic oceans are inviscid: A link between form stress and bottom pressure torques. *J. Phys. Oceanogr.*, **31**, 2871–2885.

Hunke, E. C. and W. H. Lipscomb, 2008: CICE: The Los Alamos sea ice model, documentation and software, version 4.0. Los Alamos National Laboratory Tech. Rep. LA-CC-06-012, Los Alamos, NM.

Hurrell, J. W., 1995: Decadal trends in the north atlantic oscillation: Regional temperatures and precipitation. *Science*, **269**, 676–679.

Hurrell, J. W., J. J. Hack, D. Shea, J. M. Caron, and J. Rosinski, 2008: A new sea surface temperature and sea ice boundary data set for the Community Atmosphere Model. *J. Climate*, **21**, 5145–5153, doi:10.1175/2008JCLI2292.1.

Hurrell, J. W. and H. Van Loon, 1997: Decadal Variations in Climate associated with the North Atlantic Oscillation. *Climatic Change*, **36**, 301–326.

Hurrell, J. W., et al., 2006: Atlantic climate variability and predictability: A clivar perspective. *J. Climate*, **19**, 5100–5121.

Ishii, M. and M. Kimoto, 2009: Reevaluation of historical ocean heat content variations with time-varying xbt and mbt depth bias corrections. *J. Oceanogr.*, **65**, 287–299.

Jayne, S. R. and J. Marotzke, 2001: The Dynamics of Ocean Heat Transport Variability. *Rev. Geophys.*, **39**, 385–412.

Jochum, M., G. Danabasoglu, M. Holland, Y.-O. Kwon, and W. G. Large, 2008: Ocean viscosity and climate. *J. Geophys. Res.*, **113**, C06017, doi:10.1029/2007JC004515.

Johns, W. E., T. J. Shay, J. M. Bane, and D. R. Watts, 1995: Gulf stream structure, transport, and recirculation near 68°w. *J. Geophys. Res.*, **100**, 817–838.

Johns, W. E., et al., 2011: Continuous, array-based estimates of the atlantic ocean heat transport at 26.5○n. *J. Climate*, **24**, 2429–2449.

Jungclaus, J. H., H. Haak, M. Latif, and U. Mikolajewicz, 2005: Arctic-north atlantic interactions and multidecadal variability of the meridional overturning circulation. *J. Climate*, **18**, 4013–4031.

Kanzow, T., et al., 2010: Seasonal variability of the atlantic meridional overturning circulation at 26.5○n. *J. Climate*, **accepted**, .

Keenlyside, N., M. Latif, J. Jungclaus, L. Kornbleuh, and E. Roeckner, 2008: Advancing decadal-scale climate prediction in the north atlantic sector. *Nature*, **453**, 84–88.

Kerr, R. A., 2000: A north atlantic climate pacemaker for the centuries. *Science*, **288**, 1984–1985.

Khatiwala, S., P. Schlosser, and M. Visbeck, 2002: Rates and mechanisms of water mass transformation in the labrador sea as inferred from tracer observations. *J. Phys. Oceanogr.*, **32**, 666–686.

Killworth, P. D., 1991: Cross-equatorial Geostrophic Adjustment. *J. Phys. Oceanogr.*, **21**, 1581–1601.

Kistler, R., et al., 2001: The NCEP-NCAR 50-year reanalysis: Monthly means cd-rom and documentation. *Bull. Amer. Meteor. Soc.*, **82**, 247–267.

Klinger, B. A. and C. Cruz, 2009: Decadal response of global circulation to Southern Ocean zonal wind stress perturbation. *J. Phys. Oceanogr.*, **39**, 1888–1904, doi:10.1175/2009JPO4070.1.

Knight, J. R., R. J. Allan, C. K. Folland, M. Vellinga, and M. E. Mann, 2005: A signature of persistant natural thermohaline cirulation cycles in observed climate. *Geophys. Res. Lett.*, **32**, L20708, doi:10.1029/2005GL024233.

Knight, J. R., C. K. Folland, and A. A. Scaife, 2006: Climate impacts of the Atlantic Multidecadal Oscillation. *Geophys. Res. Lett.*, **33**, L17706, doi:10.1029/2006GL026242.

Kuhlbrodt, T., A. Griesel, M. Montoya, A. Levermann, M. Hofmann, and S. Rahmstorf, 2007: On the driving processes of the Atlantic meridional overturning circulation. *Rev. Geophys.*, **45**, doi:10.1029/2004RG000166.

Kushnir, Y., 1994: Interdecadal Variations in North Atlantic Sea Surface Temperature and Associated Atmospheric Conditions. *J. Climate*, **7**, 141–157.

Kwon, Y.-O. and C. Frankignoul, 2012: Stochastically-driven multidecadal variability of the Atlantic meridional overturning circulation in CCSM3. *Clim. Dynam.*, **38**, 859–876.

Large, W. G. and G. Danabasoglu, 2006: Attribution and impacts of upper-ocean biases in CCSM3. *J. Climate*, **19**, 2325–2346.

Large, W. G., G. Danabasoglu, J. C. McWilliams, P. R. Gent, and F. O. Bryan, 2001: Equatorial circulation of a global ocean climate model with anisotropic horizontal viscosity. *J. Phys. Oceanogr.*, **31**, 518–536.

Large, W. G. and G. Nurser, 2001: Chapter 5.1 ocean surface water mass transformation. *Ocean Circulation and Climate – Observing and Modelling the Global Ocean*, Academic Press, International Geophysics, Vol. 77, 317–336, doi:10.1016/S0074-6142(01)80126-1.

Large, W. G. and S. G. Yeager, 2004: Diurnal to decadal global forcing for ocean and sea ice models: the data sets and climatologies. NCAR Tech. Note NCAR/TN-460+STR, National Center for Atmospheric Research, 105 pp.

Large, W. G. and S. G. Yeager, 2009: The global climatology of an interannually-varying air-sea flux data set. *Clim. Dynam.*, **33**, 341–364.

Large, W. G. and S. G. Yeager, 2012: On the observed trends (1984-2006) and changes in global sea surface temperature and air-sea heat fluxes. *J. Climate*, **25**, 6123–6135, doi:10.1175/JCLI-D-11-00148.1.

Lavender, K. L., R. E. Davis, and W. B. Owens, 2002: Observations of open-ocean deep convection in the Labrador Sea from subsurface floats. *J. Phys. Oceanogr.*, **32**, 511–526.

Lee, S.-K., W. Park, E. van Sebille, M. O. Baringer, C. Wang, D. B. Enfield, S. G. Yeager, and B. P. Kirtman, 2011: What caused the significant increase in Atlantic Ocean heat content since the mid-20th century? *Geophys. Res. Lett.*, **38**, 1–6, doi:10.1029/2011GL048856.

Levitus, S., J. I. Antonov, T. P. Boyer, R. A. Locarnini, H. E. Garcia, and A. V. Mishonov, 2009: Global ocean heat content 1955-2008 in light of recently revealed instrumentation problems. *Geophys. Res. Lett.*, **36**, 1–5, doi:10.1029/2008GL037155.

Levitus, S., et al., 1998: World Ocean Database vol. 1, introduction. NOAA Atlas NESDIS 18, National Oceanic and Atmospheric Administration, 346 pp.

Liu, Z., 2012: Dynamics of interdecadal climate variability: A historical perspective. *J. Climate*, **25**, 1963–1995, doi:10.1175/2011JCLI3980.1.

Lohmann, K., H. Drange, and M. Bentsen, 2009a: A possible mechanism for the strong weakening of the north atlantic subpolar gyre in the mid-1990s. *Geophys. Res. Lett.*, **36**, 1–5, doi: 10.1029/2009GL039166.

Lohmann, K., H. Drange, and M. Bentsen, 2009b: Response of the north atlantic subpolar gyre to persistent north atlantic oscillation like forcing. *Clim. Dynam.*, **32**, 273–285, doi:10.1007/s00382-008-0467-6.

Lozier, M. S., 2010: Deconstructing the conveyor belt. *Science*, **328**, 1507–1511, doi: 10.1126/science.1189250.

Lozier, M. S., S. Leadbetter, R. G. Williams, V. Roussenov, M. S. C. Reed, and N. J. Moore, 2008: The spatial pattern and mechanisms of heat-content change in the north atlantic. *Science*, **319**, 800–803, doi:10.1126/science.1146436.

Manabe, S. and R. J. Stouffer, 1999: The role of thermohaline ciruclation in climate. *Tellus*, **51A-B**, 91–109.

Marsh, R., 2000: Recent variability of the north atlantic thermohaline circulation inferred from surface heat and freshwater fluxes. *J. Climate*, **13**, 3239–3260.

Marshall, J., H. Johnson, and J. Goodman, 2001a: A study of the interaction of the north atlantic oscillation with ocean circulation. *J. Climate*, **14**, 1399–1421.

Marshall, J., et al., 1998: The Labrador Sea deep convection experiment. *Bull. Amer. Meteor. Soc.*, **79**, 2033–2058.

Marshall, J., et al., 2001b: North Atlantic Climate Variability: Phenomena, Impacts, and Mechanisms. *Int. J. Climatol.*, **21**, 1863–1898.

Meehl, J., et al., 2009: Decadal prediction: Can it be skillful? *Bull. Amer. Meteor. Soc.*, **90**, 1467–1485.

Meehl, J., et al., 2013: Decadal prediction: An Update from the Trenches. *Bull. Amer. Meteor. Soc.*, in press.

Mertz, G. and D. G. Wright, 1992: Interpretations of the JEBAR term. *J. Phys. Oceanogr.*, **22**, 301–305.

Msadek, R., K. W. Dixon, T. L. Delworth, and W. Hurlin, 2010: Assessing the predictability of the Atlantic meridional overturning circulation and associated fingerprints. *Geophys. Res. Lett.*, **37**, doi:10.1029/2010GL044517.

Msadek, R., W. E. Johns, S. G. Yeager, G. Danabasoglu, T. L. Delworth, and A. Rosati, 2013: The Atlantic Meridional Heat Transport at 26.5°N and its relationship with the MOC in the RAPID array and the GFDL and NCAR coupled models. *J. Climate*, **in press.**, doi:10.1175/JCLI-D-12-00081.1.

Munk, W., 1950: On the wind-driven ocean circulation. *J. Meteor.*, **7**, 79–93.

Nikurashin, M. and G. Vallis, 2012: A theory of the interhemispheric meridional overturning circulation and associated stratification. *J. Phys. Oceanogr.*, **42**, 1652–1667, doi:10.1175/JPO-D-11-0189.1.

Nurser, A. J. G., R. Marsh, and R. G. Williams, 1999: Diagnosing Water Mass Formation from Air-Sea Fluxes and Surface Mixing. *J. Phys. Oceanogr.*, **29**, 1468–1487.

Pedlosky, J., 1996: *Ocean Circulation Theory*. Springer-Verlag, 453 pp.

Pickart, R. S., D. J. Torres, and R. A. Clarke, 2002: Hydrography of the Labrador Sea during active convection. *J. Phys. Oceanogr.*, **32**, 428–457.

Pohlmann, H., J. H. Jungclaus, A. Köhl, D. Stammer, and J. Marotzke, 2009: Initializing decadal climate predictions with the gecco oceanic synthesis: Effects on the north atlantic. *J. Climate*, **22**, 3926–3938.

Rahmstorf, S., 2002: Ocean circulation and climate during the past 120,000 years. *Nature*, **419**, 207–214.

Rayner, N. A., D. E. Parker, E. B. Horton, C. K. Folland, L. V. Alexander, D. P. Rowell, E. C. Kent, and A. Kaplan, 2003: Global analyses of sea surface temperature, sea ice, and night marine air temperature since the late nineteenth century. *J. Geophys. Res.*, **108**, doi:10.1029/2002JD002670.

Robson, J. I., R. Sutton, K. Lohmann, D. Smith, and M. D. Palmer, 2012a: Causes of the rapid warming of the North Atlantic Ocean in the mid-1990s. *J. Climate*, **25**, 4116–4134, doi: 10.1175/JCLI-D-11-00443.1.

Robson, J. I., R. T. Sutton, and D. M. Smith, 2012b: Initialized decadal predictions of the rapid warming of the north atlantic ocean in the mid 1990s. *Geophys. Res. Lett.*, **39**, 1–6, doi: 10.1029/2012GL053370.

Roemmich, D. and C. Wunsch, 1985: Two transatlantic sections: meridional circulation and heat flux in the subtropical north atlantic ocean. *Deep-Sea Res. I*, **32**, 619–664.

Saenko, O. A. and A. J. Weaver, 2004: What drives heat transport in the Atlantic: Sensitivity to mechanical energy supply and buoyancy forcing in the Southern Ocean. *Geophys. Res. Lett.*, **31**, 1–4, doi:10.1029/2004GL020671.

Schmitt, R. W., P. S. Bogden, and C. E. Dorman, 1989: Evaporation Minus Precipitation and Density Fluxes for the North Atlantic. *J. Phys. Oceanogr.*, **19**, 1208–1221.

Schott, F. A., J. Fischer, M. Dengler, and R. Zantopp, 2006: Variability of the deep western boundary current east of the Grand Banks. *GRL*, doi:10.1029/2006GL026563.

Schott, F. A., R. Zantopp, L. Stramma, M. Dengler, J. Fischer, and M. Wibaux, 2004: Circulation and Deep-Water Export at the Western Exit of the Subpolar North Atlantic. *JPO*, **34**, 817–843.

Seager, R., Y. Kushnir, M. Visbeck, N. Naik, J. Miller, G. Krahmann, and H. Cullen, 2000: Causes of atlantic ocean climate variability between 1958 and 1998. *J. Climate*, **13**, 2845–2862.

Selten, F. M., R. J. Haarsma, and J. D. Opsteegh, 1999: On the Mechanism of North Atlantic Decadal Variability. *J. Climate*, **12**, 1956–1973.

Shaffrey, L. and R. Sutton, 2006: Bjerknes compensation and the decadal variability of the energy transports in a coupled climate model. *J. Climate*, **19**, 1167–1181.

Sijp, W. P. and M. H. England, 2009: Southern Hemisphere westerly wind control over the ocean's thermohaline circulation. *J. Climate*, **22**, 1277–1286, doi:10.1175/2008JCLI2310.1.

Smith, D., S. Cusack, A. W. Colman, C. K. Folland, G. R. Harris, and J. M. Murphy, 2007: Improved surface temperature prediction for the coming decade from a global climate model. *Science*, **317**, 796–799, doi:10.1126/science.1139540.

Smith, D. M., R. Eade, N. J. Dunstone, D. Fereday, J. M. Murphy, H. Pohlmann, and A. A. Scaife, 2010a: Skilful multi-year predictions of Atlantic hurricane frequency. *Nature Geoscience*, **3**, 846849, doi:10.1038/NGEO1004.

Smith, R., et al., 2010b: The Parallel Ocean Program (POP) reference manual, ocean component of the Community Climate System Model (CCSM). LANL Tech. Report LAUR-10-01853, Los Alamos National Laboratory, 141 pp.

Speer, K. and E. Tziperman, 1992: Rates of Water Mass Formation in the North Atlantic Ocean. *J. Phys. Oceanogr.*, **22**, 93–104.

Speer, K. G., H.-J. Isemer, and A. Biastoch, 1995: Water Mass Formation from Revised COADS Data. *J. Phys. Oceanogr.*, **25**, 2444–2457.

Spence, P., O. A. Saenko, W. Sijp, and M. England, 2012: The role of bottom pressure torques on the interior pathways of north atlantic deep water. *J. Phys. Oceanogr.*, **42**, 110–145, doi: 10.1175/2011JPO4584.1.

Srokosz, M., M. Baringer, H. Bryden, S. Cunningham, T. Delworth, S. Lozier, J. Marotzke, and R. Sutton, 2012: Past, present, and future change in the Atlantic meridional overturning circulation. *Bull. Amer. Meteor. Soc.*, **93**, 1663–1676, doi:10.1175/BAMS-D-11-00151.1.

Steele, M., R. Morley, and W. Ermold, 2001: PHC: A global ocean hydrography with a high-quality Arctic Ocean. *J. Climate*, **14**, 2079–2087.

Stevenson, J. W. and P. P. Niiler, 1983: Upper ocean heat budget during the Hawaii-to-Tahiti Shuttle Experiment. *J. Phys. Oceanogr.*, **13**, 1894–1907.

Stommel, H., 1948: The westward intensification of wind-driven ocean currents. *Trans. Amer. Geophys. Union*, **29**, 202–206.

Stramma, L., D. Kieke, M. Rhein, F. Schott, I. Yashayaev, and K. P. Koltermann, 2004: Deep water changes at the western boundary of the subpolar North Atlantic during 1996 to 2001. *Deep-Sea Res. I*, **51**, 1033–1056.

Sutton, R. T. and D. L. R. Hodson, 2005: Atlantic ocean forcing of North American and European summer climate. *Science*, **309**, 115–118.

Taylor, K. E., R. J. Stouffer, and G. A. Meehl, 2009: A summary of the cmip5 experimental design. Tech. rep., World Climate Research Programme, 32 pp., [Available from http://cmip-pcmdi.llnl.gov/cmip5/].

Thompson, D. W. J. and S. Solomon, 2002: Interpretation of recent Southern Hemisphere climate change. *Science*, **296**, 895–899, doi:10.1126/science.1069270.

Timmermann, A. and H. Goosse, 2004: Is the wind stress forcing essential for the meridional overturning circulation? *Geophys. Res. Lett.*, **31**, 1–4, doi:10.1029/2003GL018777.

Timmermann, A. and M. Latif, 2005: Northern hemisphere interdecadal variability: A coupled air-sea mode. *J. Climate*, **11**, 1906–1931.

Toggweiler, J. R. and B. Samuels, 1995: Effect of Drake Passage on the global thermohaline circulation. *Deep-Sea Res. I*, **42**, 477–500.

Toggweiler, J. R. and B. Samuels, 1998: On the ocean's large-scale circulation near the limit of no vertical mixing. *J. Phys. Oceanogr.*, **28**, 1832–1852.

Trenberth, K. E. and J. M. Caron, 2001: Estimates of Meridional Atmosphere and Ocean Heat Transports. *J. Climate*, **14**, 3433–3443.

Trenberth, K. E. and J. T. Fasullo, 2008: An Observational Estimate of Inferred Ocean Energy Divergence. *J. Phys. Oceanogr.*, **38**, 984–999.

Tziperman, E., 1986: On the Role of Interior Mixing and Air-Sea Fluxes in Determining the Stratification and Circulation of the Oceans. *J. Phys. Oceanogr.*, **16**, 680–693.

Vallis, G., 2006: *Atmospheric and Oceanic Fluid Dynamics*. Cambridge University Press, 378 pp.

Vellinga, M. and P. Wu, 2004: Low-latitude freshwater influence on centennial variability of the atlantic thermohaline circulation. *J. Climate*, **17**, 4498–4511.

Visbeck, M., E. P. Chassignet, R. Curry, T. Delworth, B. Dickson, and G. Krahmann, 2003: The ocean's response to north atlantic oscillation variability. *The North Atlantic Oscillation: Climate Significance and Environmental Impact*, AGU, Washington, D. C., Geophysical Monograph Series, Vol. 134, 113–146, doi:10.1029/GM134.

Vonder Haar, T. H. and A. H. Oort, 1973: New Estimate of Annual Poleward Energy Transport by Northern Hemisphere Oceans. *J. Phys. Oceanogr.*, **3**, 169–172.

Walin, G., 1982: On the relation between sea-surface heat flow and thermal circulation in the ocean. *Tellus*, **34**, 187–195.

Wolfe, C. L. and P. Cessi, 2010: What sets the strength of the middepth stratification and overturning circulation in eddying ocean models? *J. Phys. Oceanogr.*, **40**, 1520–1538, doi: 10.1175/2010JPO4393.1.

Woollings, T., J. M. Gregory, J. G. Pinto, M. Reyers, and D. J. Brayshaw, 2012: Response of the North Atlantic storm track to climate change shaped by ocean-atmosphere coupling. *Nature Geoscience*, **5**, 313–317, doi:10.1038/NGEO1438.

Wunsch, C., 2005: The Total Meridional Heat Flux and Its Oceanic and Atmospheric Partition. *J. Climate*, **18**, 4374–4380.

Wunsch, C., 2006: Abrupt climate change: An alternative view. *Quat. Res.*, **65**, 191–203.

Wunsch, C. and R. Ferrari, 2004: Vertical mixing, energy, and the general circulation of the oceans. *Annu. Rev. Fluid Mech.*, **36**, 281–314, doi:10.1146/annurev.fluid.36.050802.122121.

Wunsch, C. and D. Roemmich, 1985: Is the North Atlantic in Sverdrup Balance? *J. Phys. Oceanogr.*, **15**, 1876–1880.

Xu, X., H. E. Hurlburt, W. J. SchmitzJr, R. Zantopp, J. Fischer, and P. J. Hogan, 2013: On the currents and transports connected with the Atlantic meridional overturning circulation in the subpolar North Atlantic. *J. Geophys. Res. Oceans*, **118**, 1–15, doi:10.1002/jgrc.20065.

Yashayaev, I., 2007: Hydrographic changes in the Labrador Sea, 1960-2005. *Prog. Oceanogr.*, **73**, 242–276, doi:10.1016/j.pocean.2007.04.015.

Yashayaev, I. and J. W. Loder, 2009: Enhanced production of Labrador Sea water in 2008. *Geophys. Res. Lett.*, **36**, 1–7, doi:10.1029/2008GL036162.

Yeager, S. and G. Danabasoglu, 2012: Sensitivity of Atlantic meridional overturning circulation variability to parameterized Nordic Sea overflows in CCSM4. *J. Climate*, **25**, 2077–2103, doi: 10.1175/JCLI-D-11-00149.1.

Yeager, S. and G. Danabasoglu, 2013: What drove decadal ocean circulation changes in the North Atlantic in the late 20th century? *J. Climate*, **submitted**.

Yeager, S. and M. Jochum, 2009: The connection between Labrador Sea buoyancy loss, deep western boundary current strength, and Gulf Stream path in an ocean circulation model. *Ocean Modelling*, **30**, 207–224, doi:10.1016/j.ocemod.2009.06.014.

Yeager, S., A. Karspeck, G. Danabasoglu, J. Tribbia, and H. Teng, 2012: A decadal prediction case study: Late 20th century North Atlantic ocean heat content. *J. Climate*, **25**, 5173–5189, doi:10.1175/JCLI-D-11-00595.1.

Zhang, R., 2010: Latitudinal dependence of Atlantic meridional overturning circulation (AMOC) variations. *Geophys. Res. Lett.*, **37**, L16703, doi:10.1029/2010GL044474.

Zhang, R. and T. Delworth, 2006: Impact of Atlantic multidecadal oscillations on India/Sahel rainfall and Atlantic hurricanes. *Geophys. Res. Lett.*, **33**, L17712, doi:10.1029/2006GL026267.

Zhang, R. and G. K. Vallis, 2007: The role of bottom vortex stretching on the path of the north atlantic western boundary current and on the northern recirculation gyre. *J. Phys. Oceanogr.*, **37**, 2053–2080.

Appendix A

Frequently Used Abbreviations

AABW Antarctic Bottom Water

AMOC Atlantic Meridional Overturning Circulation

AMV Atlantic Multidecadal Variability

AR5 Assessment Report 5; the IPCC report scheduled for publication in September 2013

BSF Barotropic Streamfunction

BVS Bottom Vortex Stretching

CCSM4 Community Climate System Model, version 4

CESM1 Community Earth System Model, version 1

CGCM Coupled General Circulation Model

CORE-II Coordinated Ocean-ice Reference Experiments, phase II (see Appendix *B*)

CMIP5 Coupled Model Intercomparison Project Phase 5; a coordinated effort of the WCRP's WGCM

DP Decadal Prediction

DWBC Deep Western Boundary Current

EOF Empirical Orthogonal Function

GCM General Circulation Model

GS Gulf Stream

HC Heat Content

IPCC Intergovernmental Panel on Climate Change

JAS July-August-September

JFM January-February-March

LHS Left Hand Side

LSW Labrador Sea Water

MAR Mid-Atlantic Ridge

MHT Meridional Heat Transport

MLD Mixed Layer Depth

NHT Northward Heat Transport

NAC North Atlantic Current

NADW North Atlantic Deep Water

NAO North Atlantic Oscillation

NCAR National Center for Atmospheric Research

NRG Northern Recirculation Gyre

NSOW Nordic Seas Overflow Water

NYF Normal Year Forcing (see Appendix *B*)

OGCM Ocean General Circulation Model

POP Parallel Ocean Program; (Smith et al., 2010b)

PV Potential Vorticity

RAPID The observational program to monitor AMOC at 26.5°N, http://www.noc.soton.ac.uk/rapidmoc

RHS Right Hand Side

S Salinity

SPG Subpolar Gyre

SAM Southern Annular Mode

SGS Sub-grid Scale

SPMW Subpolar Mode Water

SSD Sea Surface Density

SSH Sea Surface Height

SSS Sea Surface Salinity

SST Sea Surface Temperature

STG Subtropical Gyre

T Temperature

THC Thermohaline Circulation

VIV Vertically-Integrated Vorticity

VS Vortex Stretching

WCRP World Climate Research Programme

WOA World Ocean Atlas

WGOMD Working Group on Ocean Model Development

WGCM Working Group on Coupled Modelling

WMF Water Mass Formation

WMT Water Mass Transformation

ZIV Zonally-Integrated Vorticity

Appendix B

CORE-II Forced Ocean-Ice Experiments

This appendix provides details about specific forced ocean–sea-ice simulations which are discussed throughout the thesis.

B.1 Experimental Setup

B.1.1 The Model

All of the simulations documented in this appendix are coupled ocean–sea-ice configurations of the CESM1 whose general description is given in Gent et al. (2011). The ocean model is the Parallel Ocean Program version 2 (POP2; Smith et al., 2010b) at nominal 1° horizontal resolution with 60 vertical levels. This is coupled to the Los Alamos sea ice model version 4 (CICE4; Hunke and Lipscomb, 2008) which runs on the same horizontal grid as the ocean. Further details regarding the POP2 and CICE4 models as implemented in CESM1 can be found in Danabasoglu et al. (2012a) and Holland et al. (2012), respectively.

B.1.2 The Forcing

The coupled ocean–sea-ice model is forced at the surface with the CORE-II historical atmospheric data sets, which are freely distributed together with release notes and support code by the WGOMD. This data set, which currently spans 1948 to 2009, is based primarily on the NCEP/NCAR reanalysis (Kistler et al., 2001) but includes flux parameters and prescribes adjustments based on other sources in an attempt to assemble the best forcing suite for ocean and sea ice modelling (Large and Yeager, 2004, 2009). No temperature restoring is used, but there is a very weak global restoring of model surface salinity to observed climatology with a piston velocity of 50 m/4 years to prevent salinity drift. The model uses a virtual salinity flux at the surface as opposed to true freshwater flux. Further details of the model configuration and how the NCAR submission to CORE-II differs from other comparably forced models can be found in Danabasoglu et al. (2013). We have extended the CORE-II forcing through 2011, although historical radiation data are lacking for years 2010-2011. Some analyses will include the extension of hindcast simulations through 2011.

We will be referring to the effects of specific fluxes, and so it is useful to review here the ocean model forcing methodology outlined in detail in Large and Yeager (2004) and Large and Yeager (2009). The fluxes of momentum ($\vec{\tau}$), freshwater (F), and heat (Q) which drive the ocean model are partitioned into air-sea ("as") and ice-ocean ("io") fluxes depending on the fraction of ice-free ocean (f_o) within a particular ocean grid cell:

$$\vec{\tau} \;=\; f_o\,\vec{\tau}_{as} \;+(1-f_o)\,\vec{\tau}_{io},$$

$$\begin{aligned} F &= f_o\, F_{as} \;+\; (1 - f_o)\, F_{io} \;+\; R, \\ Q &= f_o\, Q_{as} \;+\; (1 - f_o)\, Q_{io}. \end{aligned} \tag{B.1}$$

In the CORE-II data set, a monthly, interannually-varying continental discharge data set (Dai et al., 2009) is used to prescribe a river runoff flux (R). This continental runoff is distributed as a surface freshwater flux over ocean cells in the vicinity of river mouths. We will account for it in this study by including it in the F_{as} term even though it is not an air-sea flux (and in particular, is not masked in sea ice regions). It is important to note that the data set used for river runoff in CORE-II (Dai et al., 2009) uses model-derived regression relationships to specify runoff from Greenland, rather than actual measured discharge rates, and so any freshwater flux variation associated with the melting of glaciers on Greenland is absent in these experiments. A similar partitioning could be written for the fluxes which drive the ice model.

Our experiments are performed in a coupled ocean–sea-ice configuration, and so f_o, $\vec{\tau}_{io}$, F_{io}, and Q_{io} will in general be unconstrained, prognostic fields. Our focus will be on exploring controlled perturbations to $\vec{\tau}_{as}$, F_{as}, Q_{as}, which have the following dependence on the atmospheric and oceanic states:

$$\begin{aligned} \vec{\tau}_{as} &= \rho\, C_D \mid \Delta\vec{U}\mid \Delta\vec{U}, \\ F_{as} &= P \;+\; E \;+\; R, \\ &= P \;+\; \rho\, C_E\, (q - q_{sat}(SST))\, |\Delta\vec{U}| \;+\; R, \\ Q_{as} &= Q_S \;+\; Q_L \;+\; Q_E \;+\; Q_H, \\ &= Q_S \;+\; Q_L^{up}(SST) \;+\; Q_L^{down} \;+\; \Lambda_v\, E + \rho\, c_p\, C_H\, (\theta - SST)\, |\Delta\vec{U}|, \end{aligned} \tag{B.2}$$

where P is precipitation, E is evaporation, Q_S is shortwave radiation, Q_L is longwave radiation, and Q_E and Q_H are the latent and sensible heat fluxes, respectively. The longwave radiation splits into downward (Q_L^{down}) and upward (Q_L^{up}) components, with the latter solely a function of the SST. Bulk formulae parameterize the turbulent fluxes ($\vec{\tau}_{as}$, E, Q_E, and Q_H) as functions of differences between the prescribed near surface atmospheric state (wind $\vec{U}$, potential temperature θ, specific humidity q, and density ρ) and the evolving oceanic state (horizontal surface velocity $\vec{U}_o$ and SST). All of the turbulent fluxes depend on the wind speed through the term $|\Delta\vec{U}| = |\vec{U} - \vec{U}_o|$, and they require specification of transfer coefficients for drag (C_D), sensible heat (C_H), and evaporation (C_E). The computation of evaporation relies on the assumption that the specific humidity of air at the ocean surface is saturated at $q_{sat}(SST)$, and the latent heat flux is related to the evaporation through the latent heat of vaporization, Λ_v. Finally, c_p is the specific heat of air.

It is important to note that not all forcing fields in the CORE-II data set vary interannually over the full period 1948-2009. While the atmospheric state fields ($\vec{U}$, θ, q, ρ) are available at 6-hourly resolution over the full time period, monthly precipitation is available only after 1979, and daily downward shortwave and longwave radiation are available only after 1984. Furthermore, the lack of adequate observations of high latitude precipitation obliges us to use a monthly climatology for each year north of 68°N. Climatological values are used to fill in years for which historical values are lacking for a particular field (see Large and Yeager (2009) and CORE-II release notes).

Finally, some sensitivity experiments make use of the "normal year" forcing (NYF) data set described in Large and Yeager (2004), which is a single repeatable annual cycle of forcing fields at the same temporal resolution as in the full multi-year data set. This single cycle is climatological, but it is not a simple average of forcing parameters. In particular, it is designed to preserve the high frequency variance (frequencies of annual period and higher) present in the full data set as well as preserve the coherent propagation of weather signals.

B.1.3 The Experiments

The initial condition of the control experiment (CONTROL) was a state of rest and the January-mean potential temperature and salinity climatology from the Polar Science Center Hydrographic Climatology (PHC2), a blending of the Levitus et al. (1998) data set with Arctic Ocean modifications based on Steele et al. (2001). It was then spun up through 5 consecutive 60-year cycles of 1948-2007 forcing such that after every 60 years of model integration, the atmospheric state transitioned from December 2007 directly into January 1948, and then the cycle was repeated. The fifth cycle was extended through 2011, as mentioned above. Our analysis mainly focuses on a 50 year segment of the final cycle of integration (simulation years 251-300, forcing years 1958-2007). We ignore the first ten years in order to avoid some of the transient model response to the forcing transition (Doney et al., 2003).

Flux perturbation experiments which isolate the momentum-forced and buoyancy-forced interannual variability, referred to as experiments M and B, respectively (Table $B.1$), were branched from CONTROL at the start of simulation year 242 (near the start of the fifth forcing cycle) and integrated through simulation year 300. In these sensitivity experiments, normal year forcing was used to greatly suppress interannual variability in the fluxes of either buoyancy or momentum, although the dependence on the time-evolving ocean state in the turbulent fluxes as well as the upward longwave means that the use of NYF for these flux components does not completely eliminate interannual variability (see Table $B.1$ caption). This effect is small compared to the signals of interest here.

Variations on the M and B experiments were run to assess the impacts of particular fluxes and to probe regional effects. The relative impacts of surface-forced temperature (T) and salinity (S) variability are isolated in experiments B.Q and B.F, which make use of interannually-varying forcing only for the buoyancy fluxes of heat and freshwater, respectively. Experiment B.1 examines the ocean response to variations in the turbulent buoyancy fluxes, and B.2 probes the effects of turbulent buoyancy forcing within a Lab Sea box region (60°W-45°W, 53°N-65°N). We examine one variant of the M experiment in which interannual wind variability is restricted to Southern Ocean latitudes south of 35°S (experiment M.SO).

A pure normal year forcing case (NYF) was also branched from CONTROL at year 242 in order to quantify the drift associated with forward integration with NYF buoyancy forcing, because the initial condition obtained after 4 cycles of CORE-II forcing is quite different from the state that would correspond to a NYF forcing equilibrium. It is found that there is a non-negligible trend in AMOC in the NYF experiment which results from the adjustment of the ocean density structure to NYF buoyancy forcing. Although the precise origin of this drift remains unclear, we suspect it results from the use of NYF state fields for computing turbulent heat fluxes. We presume that a similar drift signal is present in all experiments which predominately use NYF forcing for turbulent heat fluxes (M, M.SO, B.F, and B.2). Therefore, we remove a drift diagnosed from the NYF experiment before plotting anomaly time series from these experiments (the drift in AMOC strength in experiment NYF is shown in Fig. 3.8). Unless otherwise indicated, a 20 year segment of the simulations (corresponding to 1988-2007) is used when considering time mean fields.

Experiment	$\vec{\tau}_{as}$	F_{as}	Q_{as}
CONTROL	$\boldsymbol{\vec{\tau}}$	$\boldsymbol{P+E+R}$	$\boldsymbol{Q_S+Q_L+Q_E+Q_H}$
M	$\boldsymbol{\vec{\tau}}$	$P+E+R$	$Q_S+Q_L+Q_E+Q_H$
B	$\vec{\tau}$	$\boldsymbol{P+E+R}$	$\boldsymbol{Q_S+Q_L+Q_E+Q_H}$
NYF	$\vec{\tau}$	$P+E+R$	$Q_S+Q_L+Q_E+Q_H$
B.Q	$\vec{\tau}$	$P+E+R$	$\boldsymbol{Q_S+Q_L+Q_E+Q_H}$
B.F	$\vec{\tau}$	$\boldsymbol{P+E+R}$	$Q_S+Q_L+Q_E+Q_H$
B.1	$\vec{\tau}$	$P+\boldsymbol{E}+R$	$Q_S+Q_L+\boldsymbol{Q_E}+\boldsymbol{Q_H}$
B.2	$\vec{\tau}$	$P+\boldsymbol{E}+R$, Lab Box $P+E+R$, elsewhere	$Q_S+Q_L+\boldsymbol{Q_E}+\boldsymbol{Q_H}$, Lab Box $Q_S+Q_L+Q_E+Q_H$, elsewhere
M.SO	$\vec{\tau}$, $\phi > 35°S$ $\boldsymbol{\vec{\tau}}$, $\phi \leq 35°S$	$P+E+R$	$Q_S+Q_L+Q_E+Q_H$

Table B.1: Guide to the forcings used in each experiment. Boldface type indicates that the variables in question are interannually-varying between 1948-2009 to the extent permitted by the CORE-II data set (e.g., $\boldsymbol{Q_E = Q_E(\rho, \Delta q, \Delta \vec{U})}$implies that atmospheric $\boldsymbol{\rho}$, $\boldsymbol{q}$, and $\boldsymbol{\vec{U}}$are all fully-varying as in CONTROL), while normal type indicates that normal year fluxes and/or state fields were used. Note that there will be some interannual variation in normal year fluxes which are functions of the ocean state, since: $\Delta\vec{U} = \vec{U} - \boldsymbol{\vec{U}_o}$, $\Delta\theta = \theta - \boldsymbol{SST}$, $\Delta q = q - \boldsymbol{q_{SAT}(SST)}$, and $Q_L = Q_L^{down} + \boldsymbol{Q_L^{up}(SST)}$. The Lab Box is defined as the region between 60°W-45°W and 53°N-65°N.

Appendix C

The vorticity budget of the POP ocean model

This appendix describes some of the nuances and practical considerations associated with computing vorticity budget diagnostics for the POP ocean model.

C.1 The momentum balance

The POP model solves the Boussinesq, hydrostatic primitive equations for a thin fluid on a sphere. The horizontal momentum equation in vector form is:

$$\frac{\partial \mathbf{u}}{\partial t} + \mathbf{v} \cdot \nabla \mathbf{u} + \mathbf{f} \times \mathbf{u} = -\frac{\nabla p}{\rho_o} + \mathbf{F}_H(\mathbf{u}) + \mathbf{F}_V(\mathbf{u}) \tag{C.1}$$

where $\mathbf{v} = (u, v, w) = (\mathbf{u}, w)$, $\mathbf{f} = (0, 0, f)$ is the Coriolis parameter, $\mathbf{F}_H(\mathbf{u}) = (F_H^x(u,v), F_H^y(u,v))$ is the horizontal viscous forcing, $\mathbf{F}_V(\mathbf{u}) = (F_V^x(u), F_V^y(v))$ is the vertical viscous forcing, p is pressure, and ρ_o is the background ocean density.

The time-average $(\overline{\cdot})$ model momentum balance is easily obtained if each term in Eqn $C.1$ is accumulated during model integration:

$$\overline{\frac{\partial \mathbf{u}}{\partial t}} + \overline{\mathbf{v} \cdot \nabla \mathbf{u}} + \overline{\mathbf{f} \times \mathbf{u}} = -\frac{\overline{\nabla p}}{\rho_o} + \overline{\mathbf{F}_H(\mathbf{u})} + \overline{\mathbf{F}_V(\mathbf{u})} \tag{C.2}$$

In practice, this requires accumulation of the momentum forcing terms in the baroclinic portion of the model's split barotropic-baroclinic momentum advance (for details, see Smith et al., 2010b). The baroclinic momentum equation is equivalent to Eqn $C.1$, but without the surface pressure (p_s) included, where:

$$\begin{aligned} p(x,y,z) &= p_s(x,y) + p_h(x,y,z) \\ &= \rho_o g \eta(x,y) + \int_z^0 dz' g \rho(x,y,z') \end{aligned} \tag{C.3}$$

and η is the surface height from the implicit free-surface formulation of the barotropic mode (Dukowicz and Smith, 1994). The momentum balance is thus computed offline from time-average model outputs as:

$$\begin{aligned} R_x &= -\overline{\mathbf{v} \cdot \nabla u} + f\overline{v} - g\partial_x \overline{\eta} - \frac{\overline{\partial_x p_h}}{\rho_o} + \overline{F_H^x(u,v)} + \overline{F_V^x(u)} \\ R_y &= -\overline{\mathbf{v} \cdot \nabla v} - f\overline{u} - g\partial_y \overline{\eta} - \frac{\overline{\partial_y p_h}}{\rho_o} + \overline{F_H^y(u,v)} + \overline{F_V^y(v)} \end{aligned} \tag{C.4}$$

The time-mean momentum tendency (LHS) is computed as the residual and is generally small on annual and longer timescales (Fig. *C*.1), but large residuals persist at all depths at particular grid cells in the Nordic and Weddell Seas. These locations are associated with the model overflow parameterization (Danabasoglu et al., 2010). At this time, it remains unclear why the momentum residuals are so large at these locations.

A brief aside Apart from $\overline{\mathbf{v}}$ and $\overline{\eta}$, the terms on the RHS of Eqn *C*.4 have not traditionally been saved as standard model output. The question arises whether useful momentum and vorticity budgets can be diagnosed from past CESM model simulations which may still be of scientific interest (e.g., simulations run for the IPCC AR4). Errors arise from the advection, vertical viscosity, and pressure gradient terms in Eqn *C*.1. If prognostic variables are decomposed in the usual way into time-mean (say, monthly) values plus deviations at each timestep (e.g. $u = \overline{u} + u'$), then it is straightforward to show that:

$$\begin{aligned} \overline{\mathbf{v} \cdot \nabla \mathbf{u}} &= \overline{\mathbf{v}} \cdot \nabla \overline{\mathbf{u}} + \overline{\mathbf{v}' \cdot \nabla \mathbf{u}'} \\ \overline{\mathbf{F}_V(\mathbf{u})} &= \frac{\partial}{\partial z} \overline{\mu} \frac{\partial}{\partial z} \overline{\mathbf{u}} + \overline{\frac{\partial}{\partial z} \mu' \frac{\partial}{\partial z} \mathbf{u}'} \end{aligned} \tag{C.5}$$

where μ is the vertical viscosity coefficient which varies in space and time. The horizontal viscosity term, $\mathbf{F}_H(\mathbf{u})$, is not problematic in its current formulation because it is linear in $\mathbf{u}$ and the horizontal viscosity coefficients vary in space but not in time (Jochum et al., 2008). Thus, an offline application of the model horizontal viscosity operator on $\overline{\mathbf{u}}$ should exactly reproduce the corresponding mean momentum tendency, $\overline{\mathbf{F}_H(\mathbf{u})}$, to within roundoff error. From the above, it is clear that a reconstruction of the model momentum budget based on the time-mean outputs $\overline{\mathbf{v}}$ and $\overline{\mu}$ will lack the contributions from the unresolved temporal correlations. The neglect of the covariance component of the advection term is probably tolerable, because it is a small term in the momentum balance of the laminar models used up to now in the CESM. A larger error is introduced by approximating the vertical momentum convergence with time-mean output, particularly in the upper ocean where μ' and $\partial_z \mathbf{u}'$ are large and highly-correlated (not shown). However, vertically-integrated momentum (and hence vorticity) budgets are still tenable since μ is held fixed for the computation of vertical momentum flux at the surface and bottom of the ocean column:

$$\begin{aligned} \int_{-H}^{0} \overline{\mathbf{F}_V(\mathbf{u})} &= \int_{-H}^{0} \left[\mathbf{F}_V(\overline{\mathbf{u}}, \overline{\mu}) + \mathbf{F}_V(\mathbf{u}', \mu') \right] \\ &= \left[\overline{\mu} \partial_z \overline{\mathbf{u}} + \overline{\mu' \partial_z \mathbf{u}'} \right]_{-H}^{0} \\ &= \left[\overline{\mu} \partial_z \overline{\mathbf{u}} \right]_{-H}^{0} \\ &= \left[\overline{\tau_s} - \overline{\tau_b} \right] / \rho_o \end{aligned} \tag{C.6}$$

Thus, the difference between the surface stress and bottom drag is recovered even if the vertical viscosity operator is applied offline to time-mean $\overline{\mu}$ and $\overline{\mathbf{u}}$. Finally, double-precision output is required to accurately reconstruct the pressure gradient term from historically-archived $\overline{\eta}$ and $\overline{\rho}$, using Eqn *C*.3. With single-precision ρ, the pressure error grows with depth, resulting in large, spurious residuals. Historical output is generally not saved to double-precision, but reasonable momentum budgets can still be obtained by assuming zero tendency and computing the pressure gradient term as the residual for all depths below the surface mixed layer (e.g. below 500m), where errors in the two terms in Eqn *C*.5 will be small. Essentially, this amounts to imposing a geostrophic balance in the deep ocean.

C.2 The vorticity balance

In the POP model, the discretized primitive equations are solved on an Arakawa B-grid (Smith et al., 2010b), and so the momentum equation terms of Eqn $C.4$ are located at the corners of tracer grid cells (i.e., they are defined at the U-grid vertices of the T-grid). A straightforward application of the model vertical curl operator on Eqn $C.4$ yields a 3-D, time-mean vertical vorticity balance, with vorticity[1] terms now defined on the T-grid. There is subtlety, however, in relating the resulting terms to familiar terms in the continuous vorticity equation, and in the interpretation of the various forms of vertically-integrated vorticity (Mertz and Wright, 1992; Bell, 1999).

First, consider the $\hat{k} \cdot \nabla \times ()$ operator applied in turn to each of the terms of Eqn $C.1$ for both a continuous fluid and a finite difference (FD) representation. The B-grid curl operator is (refer to Smith et al., 2010b):

$$\hat{k} \cdot \nabla \times \mathbf{u} = \frac{1}{\Delta y} \partial_x (\overline{v \Delta y}^y) - \frac{1}{\Delta x} \partial_y (\overline{u \Delta x}^x) \tag{C.7}$$

where Δx and Δy are grid cell lengths on the U-grid, the overbar here denotes spatial averaging of adjacent points in the grid-x and grid-y directions, and ∂_x, ∂_y are the standard FD derivative operators. In the above example, relative vorticity on the T-grid is calculated from grid and velocity information at the four surrounding points. The grid cell length weighting vanishes in the case of constant grid spacing, but must be kept for operations on the curvilinear POP mesh. In the continuous case, the curl of the nonlinear advection term (on the RHS) results in stretching/tilting and advection of relative vorticity ($\boldsymbol{\omega}$):

$$\hat{k} \cdot \nabla \times (-\mathbf{v} \cdot \nabla \mathbf{u}) = \boldsymbol{\omega} \cdot \nabla w - \mathbf{v} \cdot \nabla \xi, \qquad \boldsymbol{\omega} = (\omega_x, \omega_y, \xi) \tag{C.8}$$

For present purposes, we ignore this decomposition. The FD vertical curl operator applied to the time-mean nonlinear advection term in the momentum equation will be referred to as "ADV_ξ". Likewise, the horizontal and vertical viscous torques are computed by straightforward application of the Eqn $C.7$ operator to time-mean viscous momentum tendencies and will be referred to as "$\mathrm{F}_{H\xi}$" and "$\mathrm{F}_{V\xi}$", respectively:

$$ADV_\xi = \hat{k} \cdot \nabla \times (-\overline{\mathbf{v} \cdot \nabla \mathbf{u}}) \tag{C.9}$$

$$F_{H\xi} = \hat{k} \cdot \nabla \times (\overline{\mathbf{F}_H(\mathbf{u})}) \tag{C.10}$$

$$F_{V\xi} = \hat{k} \cdot \nabla \times (\overline{\mathbf{F}_V(\mathbf{u})}) \tag{C.11}$$

The curl of the Coriolis term merits special attention. In the continuous case, continuity implies a breakdown into stretching and advection of planetary vorticity:

$$\hat{k} \cdot \nabla \times (-\mathbf{f} \times \mathbf{u}) = f \frac{\partial w}{\partial z} - \beta v \tag{C.12}$$

We wish to obtain a similar breakdown in the FD formulation. Although tedious, it is useful to document here the derivation used for POP ocean model vorticity diagnostics. The notation is based on Fig. $C.2$ for an arbitrarily rotated grid cell with spatially-varying Δx and Δy. A Taylor expansion is used to approximate the Coriolis parameter at grid cell vertices in terms of its value at the cell center:

$$f_1 = f_0 + \frac{\beta}{2}(-\Delta x_0 sin(\alpha) + \Delta y_0 cos(\alpha)) = f_0 + \beta R_1, \tag{C.13}$$

[1] Unless otherwise noted, we henceforth use "vorticity" to refer to the $\hat{k}$-component of the vorticity vector

$$f_2 = f_0 + \frac{\beta}{2}(\Delta x_0 sin(\alpha) + \Delta y_0 cos(\alpha)) = f_0 + \beta R_2, \quad (C.14)$$

$$f_3 = f_0 + \frac{\beta}{2}(\Delta x_0 sin(\alpha) - \Delta y_0 cos(\alpha)) = f_0 + \beta R_3, \quad (C.15)$$

$$f_4 = f_0 + \frac{\beta}{2}(-\Delta x_0 sin(\alpha) - \Delta y_0 cos(\alpha)) = f_0 + \beta R_4 \quad (C.16)$$

where numeric (and below, letter) subscripts indicate location. The FD curl can then be expanded as follows:

$$\hat{k} \cdot \nabla \times (-\mathbf{f} \times \mathbf{u}) = -\frac{1}{\Delta y}\partial_x(\overline{fu\Delta y}^y) - \frac{1}{\Delta x}\partial_y(\overline{fv\Delta x}^x) \quad (C.17)$$

$$\begin{aligned}
\frac{1}{\Delta y}\partial_x(\overline{fu\Delta y}^y) &= \frac{1}{2\Delta x_0 \Delta y_0}\left[\Delta y_2 u_2 f_2 + \Delta y_3 u_3 f_3 - \Delta y_1 u_1 f_1 - \Delta y_4 u_4 f_4\right] \\
&= \frac{f_0}{\Delta y_0}\partial_x(\overline{u\Delta y}^y) + \frac{1}{2\Delta x_0 \Delta y_0}\left[\Delta y_2 u_2 \beta R_2 + \Delta y_3 u_3 \beta R_3 - \Delta y_1 u_1 \beta R_1 - \Delta y_4 u_4 \beta R_4\right] \\
&= \frac{f_0}{\Delta y_0}\partial_x(\overline{u\Delta y}^y) + \frac{\beta sin(\alpha)}{4\Delta y_0}\left[\Delta y_2 u_2 + \Delta y_3 u_3 + \Delta y_1 u_1 + \Delta y_4 u_4\right] + \\
&\qquad \frac{\beta cos(\alpha)}{4\Delta x_0}\left[\Delta y_2 u_2 - \Delta y_3 u_3 - \Delta y_1 u_1 + \Delta y_4 u_4\right] \\
&= \frac{f_0}{\Delta y_0}\partial_x(\overline{u\Delta y}^y) + \frac{\beta sin(\alpha)}{\Delta y_0}(\overline{u\Delta y}^{xy}) + \frac{\beta cos(\alpha)}{4\Delta x_0}\left[\Delta y_B \partial_y(u\Delta y)|_B - \Delta y_D \partial_y(u\Delta y)|_D\right] \\
\frac{1}{\Delta x}\partial_y(\overline{fv\Delta x}^x) &= \frac{f_0}{\Delta x_0}\partial_y(\overline{v\Delta x}^x) + \frac{\beta cos(\alpha)}{\Delta x_0}(\overline{v\Delta x}^{xy}) + \frac{\beta sin(\alpha)}{4\Delta y_0}\left[\Delta x_A \partial_x(v\Delta x)|_A - \Delta x_C \partial_x(v\Delta x)|_C\right]
\end{aligned}$$

Combing terms and noting the FD form of the divergence operator, then gives:

$$\begin{aligned}
\hat{k} \cdot \nabla \times (-\mathbf{f} \times \mathbf{u}) &= -f_0 \nabla \cdot \mathbf{u} - \beta\left[\frac{\overline{u\Delta y}^{xy} sin(\alpha)}{\Delta y_0} + \frac{\overline{v\Delta x}^{xy} cos(\alpha)}{\Delta x_0}\right] \\
&\quad -\frac{\beta}{4}\left[cos(\alpha)\partial_x(\Delta y \partial_y(u\Delta y)) + sin(\alpha)\partial_y(\Delta x \partial_x(v\Delta x))\right] \quad (C.18)
\end{aligned}$$

The first two terms in Eqn $C.18$ represent the FD analogs of Eqn $C.12$, with the advection of planetary vorticity associated with the true North projection of the grid-length-weighted average velocity vector. The additional term in Eqn $C.18$ is a numerical artifact of the FD formulation which vanishes in the limit $\Delta x, \Delta y \to 0$. We have derived this term for the general case of a non-uniform, rotated grid, but if $\alpha = 0$, then this term reduces to the form cited in Bell (1999); if $\alpha = 0$ and grid spacing is uniform, then the form from Foreman and Bennett (1989) is recovered. The sum of the RHS terms of Eqn $C.18$ equals the LHS to within roundoff error when computed offline from time-mean $\mathbf{u}$. In our vorticity analysis, we refer to the FD terms above as "$f\frac{\partial w}{\partial z}$" (computed using the FD divergence operator) and "$-\beta v$", with the small (see Fig. $C.3$) numeric term included in the latter:

$$f\frac{\partial w}{\partial z} = -f \nabla \cdot \overline{\mathbf{u}} \quad (C.19)$$

$$\begin{aligned}
-\beta v &= -\beta\left[\frac{\overline{\overline{u}\Delta y}^{xy} sin(\alpha)}{\Delta y_0} + \frac{\overline{\overline{v}\Delta x}^{xy} cos(\alpha)}{\Delta x_0}\right] \\
&\quad -\frac{\beta}{4}\left[cos(\alpha)\partial_x(\Delta y \partial_y(\overline{u}\Delta y)) + sin(\alpha)\partial_y(\Delta x \partial_x(\overline{v}\Delta x))\right] \quad (C.20)
\end{aligned}$$

Finally, we consider the vertical curl of the pressure gradient term. This is not identically zero in the FD case if grid-spacing is non-uniform Bell (1999), but in practice we find it to be negligible in the ocean interior (Fig. $C.3$). It is, however, large for ocean grid cells adjacent to land, because no-slip boundary conditions imply that ∇p must vanish on the sidewalls of the ocean domain (Eqn. $C.1$). Consider the ocean grid cell in Fig. $C.2$ adjacent to a sidewall along face D such that the momentum, momentum tendency, and pressure gradient are all zero at points 1 and 4:

$$\begin{aligned}
\hat{k} \cdot \nabla \times (\nabla p) &= -\frac{1}{\Delta y}\partial_x(\overline{\partial_y p \Delta y}^y) - \frac{1}{\Delta x}\partial_y(\overline{\partial_x p \Delta x}^x) \\
\frac{1}{\Delta y}\partial_x(\overline{\partial_y p \Delta y}^y) &= \frac{1}{2\Delta x_0 \Delta y_0}\left[\Delta y_2 \partial_y p_2 + \Delta y_3 \partial_y p_3\right] \\
\frac{1}{\Delta x}\partial_y(\overline{\partial_x p \Delta x}^x) &= \frac{1}{2\Delta x_0 \Delta y_0}\left[\Delta x_2 \partial_x p_2 - \Delta x_3 \partial_x p_3\right] \\
\Rightarrow \hat{k} \cdot \nabla \times (\nabla p) &\approx -\frac{\partial_y p|_B}{\Delta x}
\end{aligned} \tag{C.21}$$

Thus, the pressure torque is primarily a function of the interior pressure gradient parallel to the sidewall face (i.e., geostrophic flow normal to the sidewall). The term is diagnostically computed by applying the FD curl operator to the time-mean pressure gradient term in the momentum equation and will referred to as "GRADP$_\xi$":

$$GRADP_\xi = \hat{k} \cdot \nabla \times (-\frac{\overline{\nabla p}}{\rho_o}) \tag{C.22}$$

Note that other terms in the vorticity equation will likewise tend to be large in cells adjacent to land.

To summarize, vorticity diagnostics computed from time-mean POP model output yield the following 3D balance of terms defined at model T-grid points:

$$R_\xi = ADV_\xi + f\frac{\partial w}{\partial z} - \beta v + GRADP_\xi + F_{H\xi} + F_{V\xi} \tag{C.23}$$

Figure $C.3$ demonstrates the terms in this balance at 250m-depth, computing by averaging 50 years of annual mean vorticity diagnostics. The large momentum residuals associated with overflow points produce large vorticity residuals in these locations.

C.3 Vertically-integrated vorticity

As discussed in (Bell, 1999), flow interaction with bathymetry in vertically-integrated vorticity equations takes a variety of forms depending on whether the curl is taken before or after the integral. The curl of the vertically-averaged momentum equation yields a so-called JEBAR term ("joint effect of baroclinicity and relief"); the curl of the vertically-integrated momentum equation yields a bottom pressure torque term; and the vertical integral of the curl of the momentum equations yields bottom vortex stretching. Computing the latter in a Bryan-Cox type ocean model does not give a clear analogy to the continuous equations since the model vertical velocity at the ocean bottom is zero. Instead of bottom vortex stretching, the vertical integral of model vorticity yields a term associated with the non-zero pressure torque due to interaction with sidewalls (see above). Bell (1999) shows that a close analogy with the continous equations can be achieved by integrating the model vorticity equation (here, Eqn $C.23$) from the ocean bottom to the bottom of

the first ocean interior grid cell (where an interior cell is defined as one which is not adjacent to any sidewalls):

$$\begin{aligned} -fw_I &\approx \int_{z=-H}^{z=-z_I(x,y)} [ADV_\xi + -\beta v + GRADP_\xi + F_{H\xi} + F_{V\xi}] \\ -fw_I &\approx \int ADV_\xi + -\beta \int v + \int GRADP_\xi + \int F_{H\xi} + \int F_{V\xi}, \quad \textit{topographic} \end{aligned} \tag{C.24}$$

where we have neglected the residual and where z_I is a function of location, closely resembling the model bathymetry. The limits of integration of vertically-integrated vorticity terms will be made clear from the context. The above equation makes it possible to consider the dynamical effects of topography solely in terms of vortex stretching, since GRADP_ξ vanishes in the interior. The vertically-integrated model vorticity balance is thus split into a balance adjacent to sidewalls (Eqn *C*.24; hereafter referred to as the "topographic" balance) and a balance in the ocean interior:

$$\begin{aligned} \int_{z=-z_I(x,y)}^{z=0} R_\xi &= \int_{z=-z_I(x,y)}^{z=0} \left[ADV_\xi + f\frac{\partial w}{\partial z} - \beta v + GRADP_\xi + F_{H\xi} + F_{V\xi} \right] \\ \int R_\xi &= \int ADV_\xi - fw_I - \beta \int v + \int F_{H\xi} + \int F_{V\xi}, \quad \textit{interior} \end{aligned} \tag{C.25}$$

Our primary focus will be on this interior vorticity balance (referred to frequently as the "barotropic" balance), because it allows us to ignore the balance of large terms on the RHS of Eqn *C*.24. These topographic terms are only significant for the large-scale circulation insofar as they produce residual stretching along the sidewalls.[2] This results in a bottom vortex stretching term (-fw_I) in the interior vorticity balance which forces the barotropic flow. The GRADP_ξ term is the primary driver of stretching along model sidewalls (Fig. *C*.4), and thus the continuous relation between bottom pressure torque and vertical velocity at the ocean bottom (e.g., Holland, 1973) is recovered (approximately) in the FD formulation.

[2] However, the $\int F_{V\xi}$ term in Eqn *C*.25 includes an effect associated with topographic shear at z=z_I. See discussion in Chapter 4.

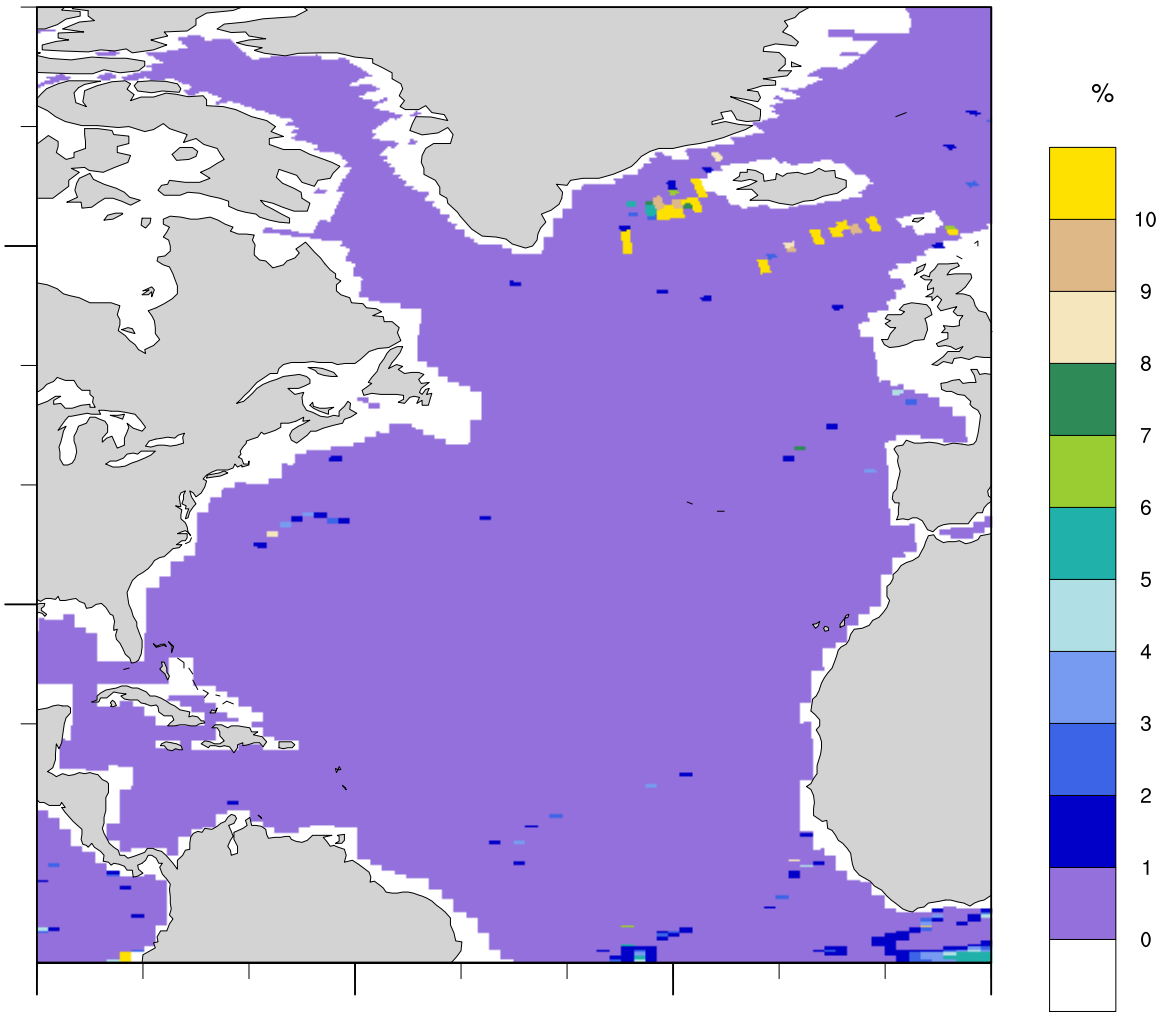

Figure C.1: Relative magnitude (in %) of R_x compared to the largest term on the RHS of Eqn $C.4$ from 50-year mean POP model output, at 250m depth.

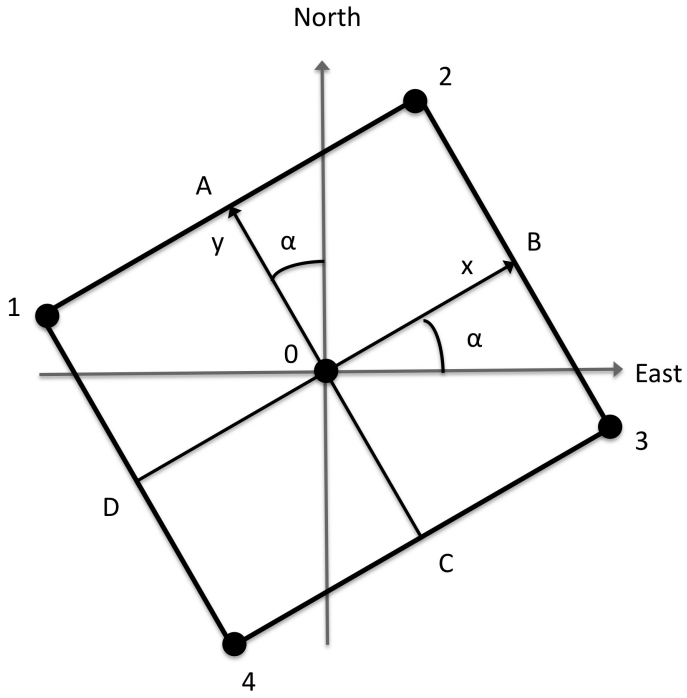

Figure C.2: Schematic of a generic POP ocean grid cell with tracers and vorticity defined at point 0, and velocity defined at points 1, 2, 3, and 4. The grid curvature introduces a local angle α (defined at 0) between the model x-direction and true East. The tracer grid cell dimensions are Δx_0 (length of line segment DB), and Δy_0 (length of line segment AC).

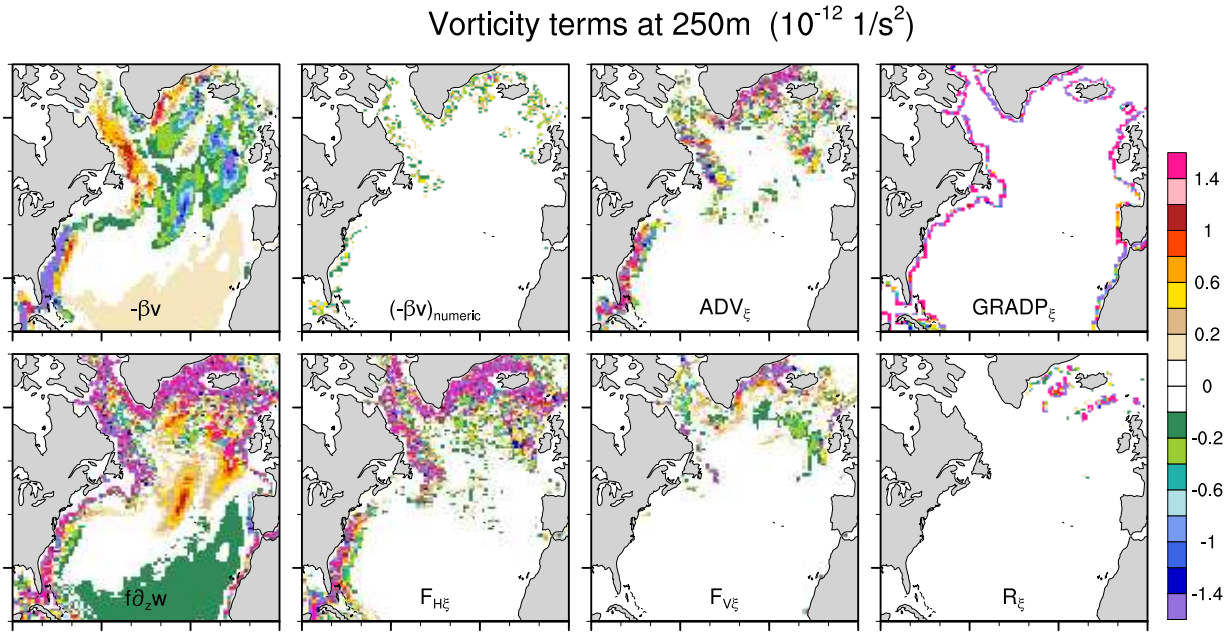

Figure C.3: Vorticity terms at 250m depth computed from 50-year mean POP model output.

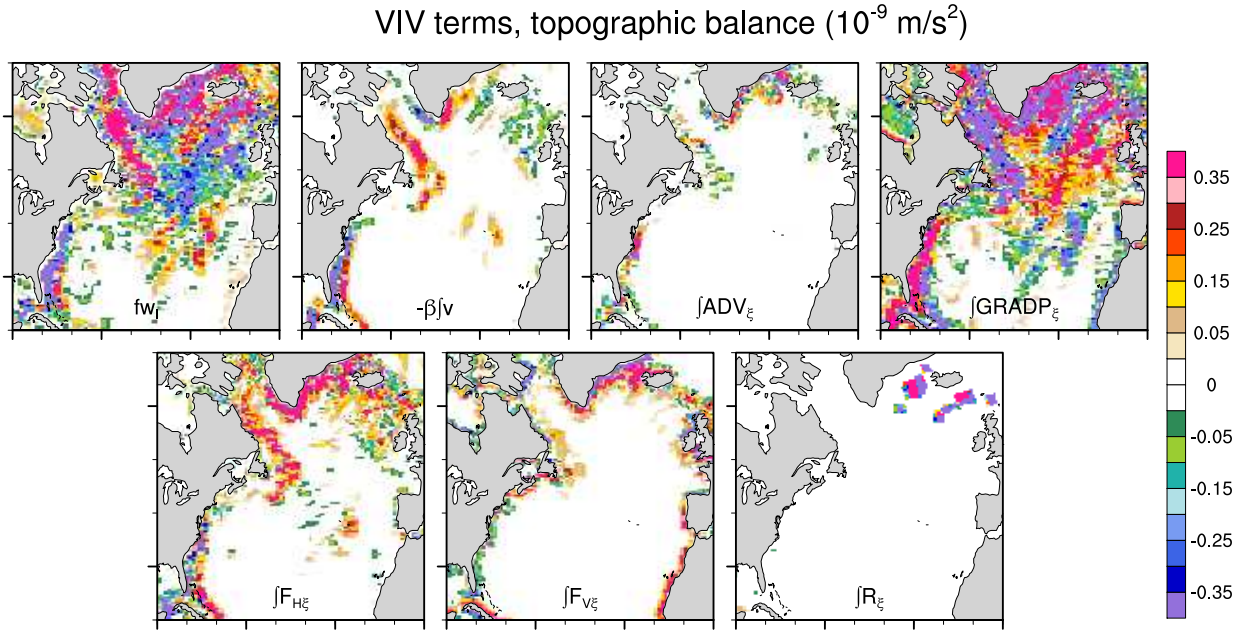

Figure C.4: Terms in the vertically-integrated vorticity (VIV) balance (Eqn *C*.24) between the bottom (z=-H) and the ocean interior (z=-z_I) computed from 50-year mean POP model output. All terms are plotted as RHS values except R_ξ. All fields have been smoothed with a 9-point spatial filter.

Appendix D

The connection between Labrador Sea buoyancy loss, deep western boundary current strength, and Gulf Stream path in an ocean circulation model

This appendix contains the text of Yeager and Jochum (2009), which was published in *Ocean Modelling*. The full text may be found at http://dx.doi.org/10.1016/j.ocemod.2009.06.014

Abstract The sensitivity of the North Atlantic gyre circulation to high latitude buoyancy forcing is explored in a global, non eddy resolving ocean general circulation model. Increased buoyancy forcing strengthens the Deep Western Boundary Current, the Northern Recirculation Gyre, and the North Atlantic Current, which leads to a more realistic Gulf Stream path. High latitude density fluxes and surface water mass transformation are strongly dependent on the choice of sea ice and salinity restoring boundary conditions. Coupling the ocean model to a prognostic sea ice model results in much greater buoyancy loss in the Labrador Sea compared to simulations in which the ocean is forced by prescribed sea ice boundary conditions. A comparison of bulk flux forced hindcast simulations which differ only in their sea ice and salinity restoring forcings reveals the effects of a mixed thermohaline boundary condition transport feedback whereby small, positive temperature and salinity anomalies in subpolar regions are amplified when the gyre spins up as a result of increased buoyancy loss and convection. The primary buoyancy flux effects of the sea ice which cause the simulations to diverge are ice melt, which is less physical in the diagnostic sea ice model, and insulation of the ocean, which is less physical with the prognostic sea ice model. Increased salinity restoring ensures a more realistic net winter buoyancy loss in the Labrador Sea, but it is found that improvements in the Gulf Stream simulation can only be achieved with the excessive buoyancy loss associated with weak salinity restoring.

Appendix E

Sensitivity of Atlantic Meridional Overturning Circulation variability to parameterized Nordic Sea overflows in CCSM4

This appendix contains the text of Yeager and Danabasoglu (2012), which was published in *Journal of Climate*. The full text may be found at http://dx.doi.org/10.1175/JCLI-D-11-00149.1

Abstract The inclusion of parameterized Nordic Sea overflows in the ocean component of the Community Climate System Model version 4 (CCSM4) results in a much improved mean representation of North Atlantic Deep Water (NADW) tracer and velocity distributions compared to a control CCSM4 simulation without this parameterization. As a consequence, the variability of the Atlantic Meridional Overturning Circulation (AMOC) on decadal and longer timescales is generally lower, but the reduction is not uniform in latitude, depth, or frequency-space. While there is dramatically less variance in the overall AMOC maximum (at about 35°N), AMOC variance at higher latitudes is only slightly lower, and it is somewhat enhanced in the deep ocean and at low latitudes (south of about 30°N). The complexity of overturning reponse to overflows is related to the fact that, in both simulations, the AMOC spectrum changes substantially with latitude and depth, reflecting a variety of driving mechanisms which are impacted in different ways by the overflows. The usefulness of reducing AMOC to a single index is thus called into question. We identify two main improvements in the ocean mean state associated with the overflow parameterization which tend to damp AMOC variability: enhanced stratification in the Labrador Sea due to the injection of dense overflow waters, and a deepening of the deep western boundary current. Direct driving of deep AMOC variance by overflow transport variations is found to be a second order effect.

Appendix F

A Decadal Prediction Case Study: Late 20th Century North Atlantic Ocean Heat Content

This appendix contains the text of Yeager et al. (2012), which was published in *Journal of Climate*. The full text may be found at http://dx.doi.org/10.1175/JCLI-D-11-00595.1

Abstract An ensemble of initialized decadal prediction (DP) experiments using the Community Climate System Model, version 4 (CCSM4) shows considerable skill at forecasting changes in North Atlantic upper ocean heat content and surface temperature up to a decade in advance. Coupled model ensembles were integrated forward from each of 10 different start dates spanning 1961 to 2006 with ocean and sea-ice initial conditions obtained from a forced historical experiment (CORE-IA), which exhibits a good correspondence with late 20^{th} century ocean observations from the North Atlantic subpolar gyre (SPG) region. North Atlantic heat content anomalies from the DP ensemble correlate highly with those from the CORE-IA simulation after correcting for a drift bias. In particular, the observed large, rapid rise in SPG heat content in the mid 1990s is successfully predicted in the ensemble initialized in January of 1991. A budget of SPG heat content from the CORE-IA experiment sheds light on the origins of the 1990s regime shift, and it demonstrates the extent to which low-frequency changes in ocean heat advection related to the Atlantic meridional overturning circulation dominate temperature tendencies in this region. Similar budgets from the DP ensembles reveal varying degrees of predictive skill in the individual heat budget terms, with large advective heat flux anomalies from the south exhibiting the highest correlation with CORE-IA. The skill of the DP in this region is thus tied to correct initialization of ocean circulation anomalies, while external forcing is found to contribute negligibly (and for incorrect reasons) to predictive skill in this region and over this time period.